

Waveguide Quantum Electrodynamics in Superconducting Circuits

Thesis by
Eun Jong Kim

In Partial Fulfillment of the Requirements for the
Degree of
Doctor of Philosophy

The logo for the California Institute of Technology (Caltech), featuring the word "Caltech" in a bold, orange, sans-serif font.

CALIFORNIA INSTITUTE OF TECHNOLOGY
Pasadena, California

2022
Defended February 11th, 2022

© 2022

Eun Jong Kim

ORCID: 0000-0003-4879-8819

All rights reserved

To my wife Eunjin Hong and my daughter Hayden
without whom I could not have put a successful end to this journey.

And to my parents Meewon Park and Sunsuk Kim
who made me who I am today.

ACKNOWLEDGEMENTS

Now has been the moment long awaited since the first day I came to Caltech, a hot summer day of Southern California in 2016 when my long journey towards PhD began. I am feeling grateful for many of whom I had the privilege to interact with along this adventure, which I would like to acknowledge here.

I want to first thank my advisor Prof. Oskar Painter for the endless support, encouragement, trust, and guidance you constantly showed me during the course of my PhD. No words can express how much I feel indebted to you. In particular, I appreciate for being open to trying out new things in the lab and supporting all of my research from the heart. From you, I learned to enjoy scientific research, not being overwhelmed by technical difficulties, and to be confident of my skills and knowledge when dealing with projects.

Also, I would like to express special gratitude to my colleague Xueyue (Sherry) Zhang who I spent the most time with in the lab and the office. I enjoyed numerous hours we spent in the lab and the enlightening discussions we had, which were crucial to moving the experiments forward and coming up with new ideas for the projects. I believe your sharpness and patience in approaching research will pay off, and I wish you the best of luck in completing your PhD.

Painter group class of 2022, Vinicius Ferreira and Jash Banker, I want to thank you guys for being nice friends and colleagues along the long journey to PhD. After coming through numerous ups and downs (usually more downs than ups), including the first publication of papers, struggles and successes in projects, and the outbreak of pandemic, I am truly happy that we finally made it to the end. I want to congratulate you all and hope you have a great start of your future careers after graduation.

I cannot help mentioning how I fortunate I was to learn from the most brilliant mentors, the former postdocs of Painter group Mohammad Mirhosseini (now faculty at Caltech EE), Andrew Keller (now at AWS Center for Quantum Computing), and Alp Sipahigil (now faculty at UC Berkeley), from an early stage of my PhD. I owe you countless cups of coffee for the instruction of various theoretical and experimental techniques, skills to overcome technical challenges, and the academic mindsets.

I also want to acknowledge our technical staff Barry Baker and former senior graduate students Mahmoud Kalae, Gregory MacCabe, Hengjiang (Jared) Ren, Jie (Roger)

Luo, and Michael Fang for their help in keeping up the lab in shape and training various tools used for my research. I would like to thank the postdocs Srujan Meesala, Clai Owens, Mo Chen, David Lake and graduate students Steven Wood, Gihwan Kim, Andreas Butler, Piero Sameer Sonar, and Utku Hatipoglu who joined the group during the latter part of my PhD for helpful discussions and everyday chitchats. Best of luck in your future endeavors!

Outside of Caltech, I want to thank wonderful collaborators I worked with during my PhD. I learned a lot from discussion with theory collaborators Prof. Ana Asenjo-Garcia (Columbia University) and Prof. Darrick Chang (ICFO) who helped us in the magic cavity project, Dr. Miguel Bello and Prof. Alejandro González-Tudela (CSIC) who helped out with quickly ramping up the topological waveguide QED project. Also, I am feeling grateful to Daniel Mark and Prof. Soonwon Choi at MIT for the discussions we had about the on-going project on studying quantum many-body physics in our quantum processor. I believe that our collaboration will come to fruition very soon. Also, special thanks to my Israeli friends Niv Drucker, Yonatan Cohen, and colleagues from Quantum Machines for endless technical support on the OPX.

Last but not least, I want to thank my family members for their unconditional encouragement and support. To my parents Meewon Park and Sunsuk Kim, who should've been waiting for this moment more than I did from 6000 miles away full of heart. You're not only great parents but also the greatest people I've ever known. Thank you for making me believe that I can do anything and everything in life. To my wonderful wife Eunjin Hong, who bravely ventured into becoming my lifelong companion and always stayed with through all the goods and hardships. I am so lucky to have a wife like you, and I love you with all of myself. To my soon-to-be-born daughter Hayden, who responded to my calling from Eunjin's tummy with a lot of fetal movement. I'm so excited to meet you soon!

ABSTRACT

Achieving an efficient interface of light and matter has been a principal goal in the field of quantum optics. A burgeoning paradigm in the study of light-matter interface is waveguide quantum electrodynamics (QED), where quantum emitters are coupled to a common one-dimensional waveguide channel. In this scenario, cooperative effects among quantum emitters emerge as a result of real and virtual exchange of photons, giving rise to new ways of controlling matter.

Superconducting quantum circuits offer an exciting platform to study quantum optics in the microwave domain with artificial quantum emitters interfaced to engineered photonic structures on chip. Beyond revisiting the experiments performed in atom-based platforms, superconducting circuits enable exploration of novel regimes in quantum optics that are otherwise prohibitively challenging to achieve. Moreover, the unprecedented level of control over individual quantum degrees of freedom and good scalability of the system provided by state-of-the-art circuit QED toolbox set a promising direction towards the study of quantum many-body phenomena.

In this thesis, I discuss waveguide QED experiments performed in superconducting quantum circuits where transmon qubits are coupled to engineered microwave waveguides. Employing the high flexibility and controllability of superconducting quantum circuits, we realize and explore various schemes for generating waveguide-mediated interactions between superconducting qubits. We also demonstrate an intermediate-scale quantum processor based on a dispersive waveguide QED system involving ten superconducting qubits, exploring quantum many-body dynamics in a highly controllable fashion. The work described in the thesis marks an important step towards the construction of scalable architectures for quantum simulation of many-body models and realization of efficient coupling schemes for quantum computation.

PUBLISHED CONTENT AND CONTRIBUTIONS

- [1] V. S. Ferreira, J. Banker, A. Sipahigil, M. H. Matheny, A. J. Keller, E. Kim, M. Mirhosseini, and O. Painter, “Collapse and revival of an artificial atom coupled to a structured photonic reservoir,” *Phys. Rev. X* **11**, 041043 (2021) [10.1103/PhysRevX.11.041043](https://doi.org/10.1103/PhysRevX.11.041043),
E.K. participated in the conception of the project and contributed to the writing of the manuscript.
- [2] E. Kim, X. Zhang, V. S. Ferreira, J. Banker, J. K. Iverson, A. Sipahigil, M. Bello, A. González-Tudela, M. Mirhosseini, and O. Painter, “Quantum electrodynamics in a topological waveguide,” *Phys. Rev. X* **11**, 011015 (2021) [10.1103/PhysRevX.11.011015](https://doi.org/10.1103/PhysRevX.11.011015),
E.K. came up with the concept and planned the experiment, performed the device design and fabrication, performed the measurements, analyzed the data, and participated in the writing of the manuscript. E.K. and X.Z. contributed equally to this work.
- [3] M. Mirhosseini, E. Kim, X. Zhang, A. Sipahigil, P. B. Dieterle, A. J. Keller, A. Asenjo-Garcia, D. E. Chang, and O. Painter, “Cavity quantum electrodynamics with atom-like mirrors,” *Nature* **569**, 692–697 (2019) [10.1038/s41586-019-1196-1](https://doi.org/10.1038/s41586-019-1196-1),
E.K. came up with the concept and planned the experiment, performed the device design and fabrication, performed the measurements, analyzed the data, and participated in the writing of the manuscript. E.K. and M.M. contributed equally to this work.
- [4] M. Mirhosseini, E. Kim, V. S. Ferreira, M. Kalae, A. Sipahigil, A. J. Keller, and O. Painter, “Superconducting metamaterials for waveguide quantum electrodynamics,” *Nat. Commun.* **9**, 3706 (2018) [10.1038/s41467-018-06142-z](https://doi.org/10.1038/s41467-018-06142-z),
E.K. carried out the device design and fabrication, performed the measurements, analyzed the data, and contributed to the writing of the manuscript.

CONTENTS

Acknowledgements	iv
Abstract	vi
Published Content and Contributions	vii
Contents	vii
List of Figures	x
List of Tables	xii
Chapter I: Introduction	1
1.1 Quantum light-matter interface	2
1.2 Quantum computation	6
1.3 Quantum many-body physics	9
1.4 Outline of the thesis	10
Chapter II: Waveguide Quantum Electrodynamics	12
2.1 From cavity QED to waveguide QED	12
2.2 Quantum emitters coupled to a waveguide with linear dispersion	13
2.3 Waveguide QED in a dispersive photonic channel	21
2.4 Experimental realizations of waveguide QED	27
Chapter III: Device Fabrication and Experimental Techniques	31
3.1 Fabrication of superconducting quantum circuits	31
3.2 Microwave packaging of quantum devices	32
3.3 Cryogenic setup	35
3.4 Room-temperature electronics and signal processing	38
Chapter IV: Waveguide-mediated Cooperative Interactions of Superconducting qubits	46
4.1 Introduction	46
4.2 Strong-coupling regime of waveguide QED: cavity QED with atom-like mirrors	47
4.3 Spectroscopic characterizations	50
4.4 Time-domain characterizations	52
4.5 Compound atomic mirrors	56
4.6 Conclusion	58
4.7 Methods	58
Chapter V: Development of Superconducting Metamaterials for Waveguide QED	65
5.1 Introduction	65
5.2 Band-structure analysis and spectroscopy	69
5.3 Physical realization using lumped-element resonators.	70
5.4 Disorder and Anderson localization	71
5.5 Anomalous Lamb shift near the band-edge	71
5.6 Enhancement and suppression of spontaneous emission	73

5.7 Discussion	76
Chapter VI: Quantum Electrodynamics in a Topological Waveguide	77
6.1 Introduction	77
6.2 Description of the topological waveguide	78
6.3 Properties of quantum emitters coupled to the topological waveguide	81
6.4 Quantum state transfer via topological edge states	88
6.5 Discussion and outlook	90
Chapter VII: An Intermediate-Scale Quantum Processor Based on Dispersive Waveguide QED	92
7.1 Introduction	92
7.2 Metamaterial quantum processor	94
7.3 Single-qubit characterization	97
7.4 Interaction between qubit-photon bound states	98
7.5 High-fidelity single-shot readout	100
7.6 Quantum many-body dynamics	102
7.7 Discussion and outlook	104
Chapter VIII: Outlook and Future Directions	105
8.1 Opportunities for studying many-body physics	105
8.2 New directions for scaling up quantum processors	107
Bibliography	108
Appendix A: Fabrication Details	140
Appendix B: Designing Josephson Junctions for Transmon Qubits	147
Appendix C: Supplementary Information for Chapter 4	151
Appendix D: Supplementary Information for Chapter 5	165
Appendix E: Supplementary Information for Chapter 6	183

LIST OF FIGURES

<i>Number</i>	<i>Page</i>
1.1 Quantum light-matter interface	2
1.2 Cavity quantum electrodynamics	3
1.3 Stages of quantum information processing	8
1.4 Overview of our work	10
2.1 Transition from cavity QED to waveguide QED	12
2.2 Single quantum emitter coupled to a waveguide	14
2.3 Multiple quantum emitters coupled to a waveguide	16
2.4 Superradiance and subradiance of two quantum emitters	17
2.5 Coherent waveguide-mediated exchange interaction	19
2.6 Exchange interaction between two quantum emitters	21
2.7 Emitter-photon bound state	22
2.8 Waveguide-mediated interactions between emitter-photon bound states	25
2.9 Examples of experimental platforms for waveguide QED	28
3.1 Microwave packaging of quantum devices	32
3.2 Cryogenic Setup	36
3.3 Microwave synthesis	39
3.4 Downconversion and demodulation	42
4.1 Waveguide-QED setup	48
4.2 Single-qubit spectroscopy	51
4.3 Vacuum Rabi splitting	52
4.4 Vacuum Rabi oscillations	53
4.5 Characterization of the dark-state cavity	55
4.6 Compound atomic mirrors, $N = 4$	57
4.7 Scanning electron microscope image of the fabricated device	59
4.8 Schematic of the measurement chain inside the dilution refrigerator	62
5.1 Microwave metamaterial waveguide	67
5.2 Disorder effects and qubit-waveguide coupling	68
5.3 Measured dispersive and dissipative qubit dynamics	72
5.4 State-selective enhancement and inhibition of radiative decay	74
6.1 Topological waveguide	79
6.2 Directionality of qubit-photon bound states	82

6.3	Probing band topology with qubits	85
6.4	Qubit interaction with topological edge modes	87
7.1	Metamaterial waveguide	94
7.2	Description of the metamaterial quantum processor	96
7.3	Single-qubit characterization	97
7.4	Qubit-qubit interactions	99
7.5	Multi-qubit readout characterization	101
7.6	Quantum walk of two photons along qubit-photon bound states . . .	103
B.1	Scanning electron micrograph of a Josephson junction	150
C.1	Effect of thermal occupancy on extinction	153
C.2	Level structure of the atomic cavity and linear cavity	154
D.1	Circuit diagram of metamaterial waveguide	165
D.2	Characterization of lumped element resonators	174
D.3	Circuit diagram for a transmon qubit coupled to a metamaterial waveguide	177
D.4	Qubit lifetime as a function of resonance frequency	178
E.1	Modeling of the topological waveguide	183
E.2	Band structure of the realized topological waveguide under various assumptions discussed in App. E.2	191
E.3	Eigenspectrum of the finite-sized topological circuit	192
E.4	Eigenfrequencies of the system under 100 disorder realizations in coupling elements	195
E.5	Optical micrograph of Device I (false-colored)	197
E.6	Schematic of the measurement setup inside the dilution refrigerator for Device I	198
E.7	Tapering section of Device I	200
E.8	Understanding the directionality of qubit-photon bound states	202
E.9	External coupling rate of qubit-photon bound states away from the reference frequency	203
E.10	Understanding the swirl pattern	205
E.11	Topology-dependent photon scattering on various qubit pairs	207
E.12	Optical micrograph of Device II (false-colored)	208
E.13	Schematic of the measurement setup inside the dilution refrigerator for Device II	209

LIST OF TABLES

<i>Number</i>		<i>Page</i>
2.1	Experimental platforms for studying waveguide QED	28
4.1	Qubit characteristics	59
C.1	Parameters used for fitting Rabi oscillation curves	159
C.2	Decay rate and decoherence rate of dark states	159
D.1	Measured resonance parameters for metamaterial waveguide	172
E.1	Qubit coherence in the middle bandgap.	196
E.2	Qubit parameters on Device II	208

Chapter 1

INTRODUCTION

Since its inception in the 20th century, quantum mechanics had a profound impact on humans, revolutionizing the physical understanding of nature. Starting from Planck's quantum hypothesis to explain the black-body radiation [1]—a mere heuristic correction to the classical mechanics at that point—the quantum mechanics became a major theory in fundamental science, permeating through a broad range of disciplines such as atomic, molecular, and optical (AMO) physics, condensed matter physics, particles physics, and even quantum chemistry. Not only of fundamental importance, the quantum theory also spawned major technological developments such as lasers [2, 3] and transistors which are integral to modern telecommunication and digital electronics we use in everyday life.

While the counter-intuitive aspects of quantum theory, often exemplified by the famous thought experiments such as Schrödinger's cat [4] and Bell's inequality [5], were considered purely theoretical in the early days, the unprecedented ability to control and measure individual quantum degrees of freedom, such as atoms, photons, and even macroscopic objects, developed in modern era of physics has placed such exotic quantum nature within the experimental reach. This has sparked new directions in quantum physics where information theoretic tools are utilized for understanding complex quantum many-body phenomena and strongly correlated states of matter. In particular, such approach can open the door to novel and powerful technologies that can benefit from truly quantum mechanical effects such as quantum superposition and quantum entanglement beyond the semi-classical description.

The burgeoning interest in quantum science we see in recent years, highlighted by industry-fueled efforts to build a practical quantum computer [6–10] and a variety of quantum simulators [11–16], is expected to again transform the world in many ways. Numerous ways to systematically control, measure, and understand quantum systems await further explorations and are anticipated to give birth to practical quantum applications. We present a step towards this goal by demonstrating quantum control experiments in a new platform. In the following, I will provide a gentle introduction to the thesis by explaining the historical context on relevant scientific disciplines and providing an outline of the remaining chapters.

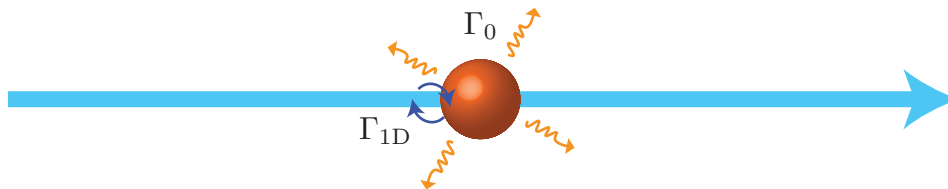


Figure 1.1: Quantum light-matter interface. A one-dimensional photonic channel (light blue) is coupled to an atom (orange) at a rate Γ_{1D} . The atom has a spontaneous emission rate Γ_0 to free space.

1.1 Quantum light-matter interface

Interaction between electromagnetic field and matter lies at the heart of various phenomena we observe in nature. The basic optical processes such as reflection of light and dispersion of materials originate from the interplay between oscillating fields and charged particles (e.g., electrons) governed by laws of classical electrodynamics [17]. In the quantum regime, the same problem is mapped to the interaction between a single photon and a single atom [18] which results in non-classical phenomena such as anti-bunching of photons emitted by an atom [19] and quantum beat of Rabi oscillation [20]. In this respect, engineering an efficient interface of light and matter in a controllable fashion has been a central goal in atomic physics [21] and quantum optics [22], and is of fundamental significance.

Coupling of an atom to a 1D photonic channel

The general picture of quantum light-matter interface can be understood in terms of the simplest scenario of coupling a 1D photonic channel with a single atom, as described in Fig. 1.1. In this case, the useful rate that couples the atom to the desired channel is represented by the decay rate Γ_{1D} , which is often compared with the rate Γ_0 of spontaneous emission. The ratio Γ_{1D}/Γ_0 of the two rates is a key figure of merit quantifying the efficiency of atom-photon coupling and is known to depend on the following relation [23]:

$$\frac{\Gamma_{1D}}{\Gamma_0} \propto \left(\frac{\sigma_0}{A}\right) \times \left(\frac{c}{v_g}\right). \quad (1.1)$$

Here, the first factor is the ratio of the scattering cross-section σ_0 of the atom to the effective mode area A . The second factor is the group index of the introduced photonic channel given by the ratio of speed of light c in vacuum to the group velocity v_g of the desired mode.

Achieving a strong atom-photon coupling is naturally a challenging task. An atom in free space has the resonant scattering cross-section of $\sigma_0 = 3\lambda_0^2/(2\pi)$, where

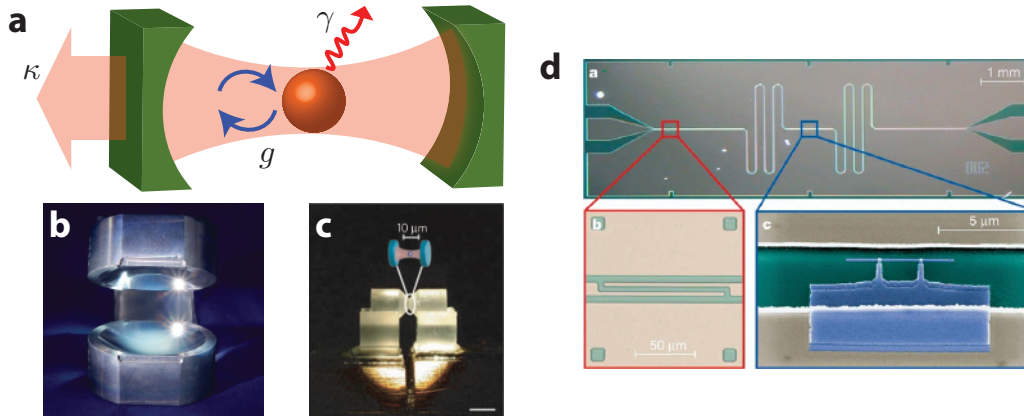


Figure 1.2: Cavity quantum electrodynamics. **a**, A cavity QED setup, consisting of an atom (orange, decay rate γ) coupled to photons inside a cavity (green, leakage rate κ) with a coupling rate g . **b**, A microwave cavity made of two superconducting niobium mirrors used in Prof. Serge Haroche's group. **c**, An optical cavity used in Prof. Jeff Kimble's group. **d**, A circuit QED setup consisting of a coplanar waveguide resonator coupled to a superconducting qubit (blue inset) on chip. The panels **b**, **c**, and **d** are adapted from Refs. [25], [26], and [27], respectively.

λ_0 is the linewidth of the atomic transition [21]. This means that the area A of the coupled mode has to be very small (on the order of λ_0^2) in order to achieve an appreciable atom-photon coupling according to Eq. (1.1). One could imagine using tightly focused beam to reduce the mode area [24], but the diffraction limit makes it challenging to accomplish σ_0/A on the order of unity.

Cavity quantum electrodynamics

One successful method to overcome this challenge is by utilizing an electromagnetic mode confined in a resonator such as a Fabry-Pérot cavity. In this case, the efficiency of coupling is enhanced by the number of passes that a photon makes across the atom before leaking out of the cavity. Also, the placement of a resonator alters the photonic vacuum of the environment for the atom, greatly modifying the rate of spontaneous emission. This field where an atom is interfaced with photons inside a cavity is known as the cavity quantum electrodynamics (QED) [28, 29], illustrated in Fig. 1.2. A cavity QED system is described by the Jaynes-Cummings Hamiltonian [30]

$$\hat{H} = \hbar g(\hat{a}\hat{\sigma}^+ + \hat{a}^\dagger\hat{\sigma}^-) \quad (1.2)$$

where g is the coupling between an atom and a cavity photon, \hat{a} (\hat{a}^\dagger) is the annihilation (creation) operator of cavity photons, and $\hat{\sigma}^-$ ($\hat{\sigma}^+$) is the lowering (raising) operator of atomic pseudospin-1/2. In addition to the Hamiltonian, the cavity QED

system is further described by the the decay rate γ of the atom and the photon leakage rate κ of the cavity. In this case, the figure of merit Γ_{1D}/Γ_0 can be mapped to the cooperativity

$$C = \frac{(2g)^2}{\kappa\gamma}. \quad (1.3)$$

Achieving cooperativity exceeding the unity (i.e., $C > 1$) where the atom-field interaction overwhelms the dissipative processes, known as the strong-coupling regime of cavity QED, is the key to observing exotic quantum phenomena, which has been successfully demonstrated in a variety of platforms.

The field of cavity QED was pioneered by Prof. Serge Haroche at Ecole Normale Supérieure in the microwave domain by using Rydberg atoms with superconducting cavities [31] (see Fig. 1.2b). A parallel endeavor in the group of Prof. Jeff Kimble at Caltech [32] was pursued in the optical domain by employing high-finesse optical Fabry-Pérot cavities [33] (see Fig. 1.2c) and microtoroidal resonators [34]. The implementation of cavity QED is not restricted to atomic systems but more generally achievable with artificially engineered quantum emitters such as quantum dots, color centers in diamond, rare-earth ions, or superconducting qubits. In particular, the cavity QED framework revisited in systems of superconducting qubits and microwave resonators was specifically named the *circuit QED* [35–38] (see Fig. 1.2d), laying the groundwork for numerous efforts to build a quantum computer.

Alternative approaches to realize a strong atom-photon interaction

While cavity QED has been the predominant approach for achieving strong atom-photon interactions at the single-photon level, there are several drawbacks to this approach as the system size grows. First, cavities are intrinsically finite-sized objects as they are physically confined the electromagnetic structure. Represented as a zero-dimensional object (node) in a graph, scaling up such systems will require envisioning a network of quantum nodes [26, 39]. Another consideration is related to applications where a high bandwidth is necessary for inducing photon-photon interactions [40], which will inevitably degrade the cooperativity defined in Eq. (1.3). Various 1D-scalable approaches to build strongly coupled quantum light-matter interfaces ensued for these reasons.

One alternative method is to utilize the cooperative enhancement of coupling of an ensemble of atoms [41]. From the early days in quantum physics, it has been shown that the radiation of a collection of emitters much faster and stronger than that of a single atom, known as the Dicke superradiance [42, 43]. Utilizing the collective

excitation of an atomic ensemble it is possible to realize the cooperative Γ_{1D} scaling linearly with the number of atoms.

Another promising approach is based on utilizing guided modes of an engineered waveguide, called the *waveguide QED* [44, 45], which is being investigated in a variety of physical platforms including atoms coupled to optical nanofiber or nanophotonic structures. Our approach to waveguide QED experiments in superconducting quantum circuits is realized by employing superconducting qubits coupled to on-chip microwave transmission lines or engineered superconducting metamaterial waveguides. This topic will be discussed in a greater depth in Chapter 2.

Novel types of light-matter interface

In addition to the directions mentioned above, there has been various efforts to realize exotic types of quantum light-matter interface employing novel properties of photonic baths [46, 47]. Here, I enumerate a few interesting examples related to this approach.

First, the spin-momentum locking of strongly confined guided modes in nanophotonic structures are being studied as chiral light-matter interfaces [46]. This was experimentally investigated in cold atoms coupled to a nanofiber [48] or coupled via whispering-gallery mode of a microsphere resonator [49] and quantum dots coupled to a nanophotonic waveguide [50]. In such settings, the unidirectional coupling of quantum emitters to a 1D photonic mode realizes a cascaded quantum system [51] which can be used to perform steady-state generation of entangled states of emitters with driven-dissipative methods [52].

Second, there has been novel efforts to synthesize strongly-correlated quantum matter in topological photonic structures that breaks the time-reversal symmetry. For example, a twisted optical cavity where photons experience artificial gauge field together with Rydberg atom-mediated photon-photon interactions were employed to create fractional quantum Hall states of light [53]. In line with this, a Chern insulator made of a two-dimensional array of 3D superconducting cavities with superconducting qubits are being investigated [54].

Finally, the topological property of photonic bath can alter the properties of quantum emitters, which can be used to imprint novel types of interaction leading to an exotic quantum many-body state [55, 56]. Our work on the topological waveguide QED will be discussed in this context in Chapter 6.

1.2 Quantum computation

The emergence of the field of quantum computation [57] dates back to 1982 when Richard Feynman discussed the problem of simulating quantum systems [58]. He explained the infeasibility of simulating quantum systems with a classical computer and postulated a computer based on quantum systems to achieve this. It is an interdisciplinary field of science associated with the convergence of three major scientific areas that appeared in the 20th century—quantum theory, computer science, and information theory.

Power of quantum computation

The fact that quantum systems are hard to simulate with a classical computer implies that quantum computers capable of solving certain kinds of classically intractable problems (NP-hard), the most trivial example of which is the simulation of quantum many-body systems discussed in Sec. 1.3. However, the power of quantum computation was not generally appreciated until 1994 when Peter Shor discovered an efficient algorithm for prime factorization on a quantum computer [59], which is otherwise prohibitively hard to tackle to date. This was soon followed by the discovery of another important quantum algorithm for search of unstructured database, known as the Grover's algorithm [60], which drew a wider attention to the field. Even today, many applications of quantum computing are being envisioned, further strengthening the potentials of quantum computers.

Quantum error correction

Contrary to the optimistic perspectives on quantum computing from its potential computational power, there has been many skeptical views associated with its feasibility [61]. Practically, quantum computation is experimentally a daunting task due to the conflicting requirement that qubits strongly interact with each other while the interaction of qubits to the environment has to be greatly suppressed except when we interrogate qubits for control and measurement. The inevitable build-up of coherent and incoherent errors during quantum computation will make the approach unscalable, making the sophisticated quantum algorithms ineffectual.

In order to resolve this issue, ideas on quantum error correction were conceived from the early days in the field of quantum computation [62, 63]. The basic principles of quantum error correction is to encode logical quantum information in a subspace of Hilbert space of a larger number of physical qubits, thereby using quantum entanglement to introduce sufficient redundancy. Measurement of error syndromes (few

combinations of multi-qubit Pauli operators) allows one to detect and correct bit-flips (X -type errors) and phase-flips (Z -type errors) without destroying the original quantum information. However, one needs to consider the errors associated with the error correction process itself. Fault-tolerant protocols are proven to allow reliable quantum computation even with errors provided the error rate per physical gate or time step is below some constant threshold value, known as the threshold theorem [64]. Therefore, quantum error correction serves as an important foundation for a scalable quantum computation.

A widely accepted viable approach for quantum error correction is the *surface code* [65, 66], which is based on topological error correcting codes named toric code invented by Sergey Bravyi and Alexei Kitaev [67]. This scheme utilizes physical qubits laid out in a 2D checkerboard pattern alternating between data qubits and measure qubits. The measure qubits themselves alternates between X syndrome and Z syndrome qubits for measurement of $XXXX$ and $ZZZZ$ operators of adjacent data qubits, respectively, and the $+1$ eigenspace of all syndrome operators define the logical code space. The surface code is considered the most feasible direction in quantum error correction, requiring only nearest-neighbor connectivity between large number of physical qubits and tolerating high error rate on the order of $\sim 1\%$ [66] compared with other error-correcting codes.

Another interesting direction is to encode a logical quantum bit of information in levels of a harmonic oscillator, known as the *bosonic error correction* [68, 69]. A harmonic oscillator has an infinite number of evenly spaced levels and in principle can provide hardware-efficient redundancy for encoding in contrast to approaches involving multiple physical qubits described above. In addition, the dominant error in harmonic oscillators is the photon loss error a , further simplifying the kind of error that needs to be corrected. Examples of well-known bosonic codes include the Gottesman-Kitaev-Preskill (GKP) code [70] (analog of quadrature-amplitude modulation), the cat code [71] (analog of phase-shift keying), and the binomial code [72] where a logical quantum bit of information is encoded in superposition of position/momentum eigenstates, coherent states, and Fock states, respectively. In particular, assisted by the low error rates of 3D circuit QED architectures, bosonic error correction with cat code has reached a milestone of break-even [73] where the lifetime of logical qubit was comparable to that of the physical constituent (cavity photon).

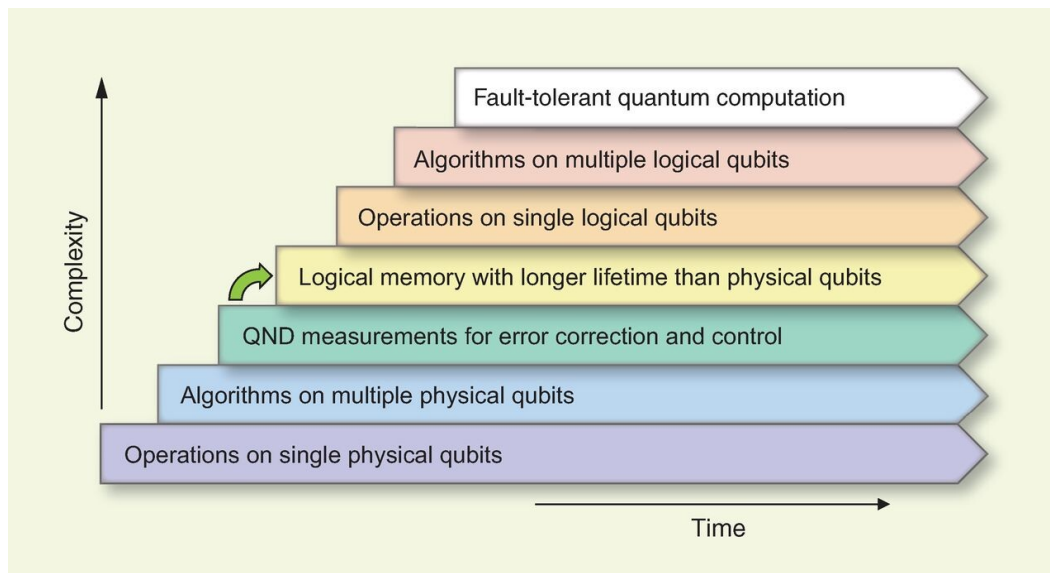


Figure 1.3: Stages of quantum information processing. Seven stages of quantum information processing described by Devoret and Schoelkopf. The figure is taken from Ref. [74].

Experimental approaches to quantum computation

Experimental efforts to build a quantum computer started with technical development of building blocks of quantum computation and proof-of-principle experiments to demonstrate quantum algorithms in a variety of platforms including nuclear magnetic resonance (NMR), trapped ions, superconducting qubits, neutral atoms, and photons, to name a few. In 2013, pioneers in superconducting qubits Michel Devoret and Robert Schoelkopf at Yale University presented their perspectives on the development stages of quantum information processing [74], illustrated in Fig. 1.3. They argued that the three first stages associated with single- and multi-qubit operations as well as the quantum non-demolition measurement has been achieved but the next step—demonstrating a logical qubit with a lifetime greater than the underlying physical qubits—poses significant technical challenges.

Systematic efforts to accomplish an error-corrected logical qubit are under way in both the academic and industrial fronts, but realizing a logical qubit outperforming physical qubits persists to be a difficult task due to technical challenges associated with various error processes. In this respect, Prof. John Preskill at Caltech coined the term *noisy intermediate-scale quantum (NISQ)* to describe [75] the current progress of the field with quantum processors of ~ 100 qubits without error correction. The NISQ devices will be complicated enough to be simulated with the most powerful classical computers in the world, best represented by the quantum supremacy ex-

periment [76], but nevertheless limited by noise to harness the full computational power of quantum computers.

In parallel with the frontier to push the boundary of quantum error correction, new types of building blocks for quantum computation are continually being developed. Examples of this include multi-mode circuit QED [77, 78] and schemes for scaling up error-corrected bosonic systems [79]. In line with this, we will describe a waveguide-based high-bandwidth approach to realize a scalable long-range interactions between qubits in Chapter 7, which remains relatively unexplored.

1.3 Quantum many-body physics

Understanding strongly correlated phases of matter has been a long-standing goal in the field of condensed matter physics, with the famous examples of fractional quantum Hall effect [80] and high- T_c superconductivity [81], first discovered in the 1980s, still lacking established microscopic theories. Coherent control over engineered quantum systems provides a novel alternative approach for tackling such formidable tasks by enabling the quantum simulation of many-body phenomena [82, 83]. In addition, quantum control experiments are central to the study of fundamental topics ranging from quantum thermalization [84, 85] and dynamics of quantum entanglement [86] to novel quantum phases of matter.

Pioneering experiments in quantum simulation utilized laser-cooled and trapped cold neutral atoms to study Bose- and Fermi-Hubbard models [87]. Quantum gas microscopes with in-situ imaging at single-atom and single-site resolution [88, 89] enabled explorations of quantum correlations of many-body systems [90–92], followed by a bottom-up approach to assemble arrays of atoms trapped in optical tweezers [12, 15]. In parallel, various quantum simulation experiments were performed using trapped ions [93, 94], resulting in numerous impressive studies in quantum information propagation [95], dynamical quantum phase transition [96], and discrete time crystals [97, 98], to name a few.

Superconducting quantum circuits have recently emerged as a promising platform to study quantum many-body physics. Compared to the traditional AMO systems, superconducting qubits offer new possibilities to study higher-order quantum many-body effects at a high repetition rate, with fully arbitrary local qubit control, quantum non-demolition readout, and real-time feedback control without technical difficulties associated with cooling and trapping atoms. Investigations of quantum many-body physics in superconducting circuits took place in architectures with cou-

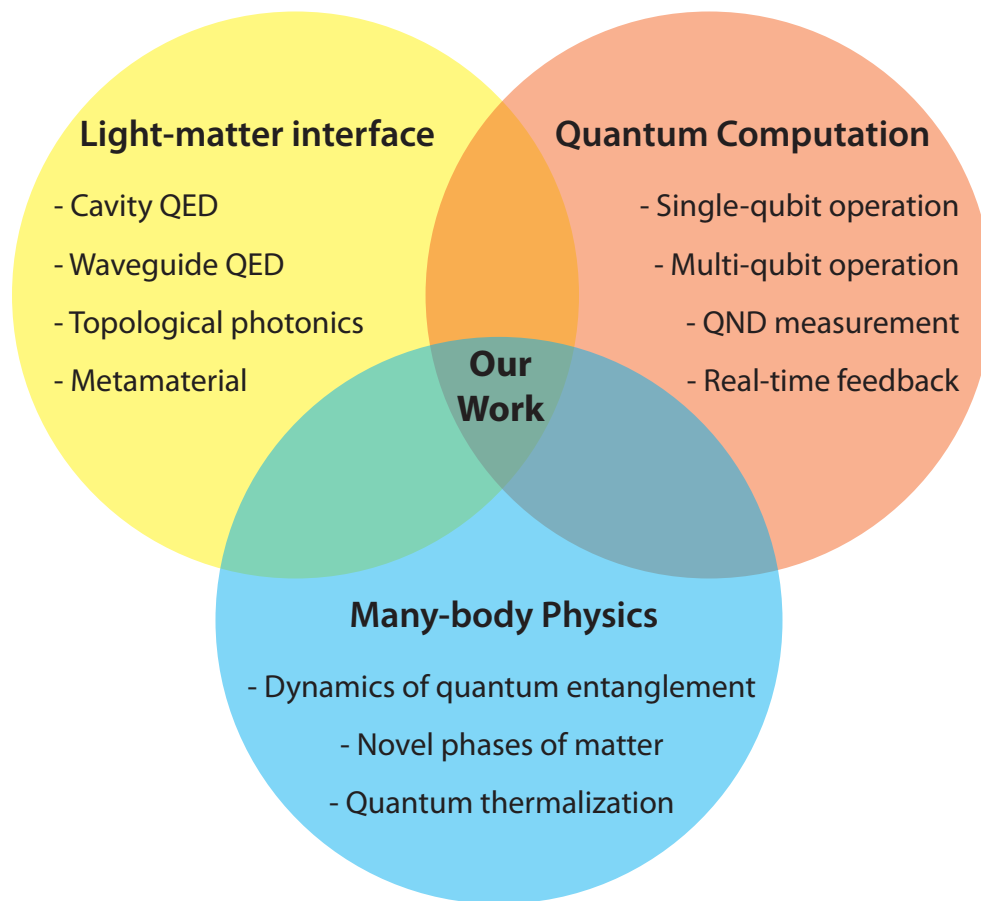


Figure 1.4: Overview of our work. The work in the thesis is viewed from a broad context of quantum light-matter interface, quantum computation, and quantum many-body physics, described in Secs. 1.1-1.3.

pling limited to nearest neighbor in 1D [99–101] and 2D [102, 103] lattice or with resonator-mediated all-to-all coupling [104–106] which is not scalable. Our quantum processor based on superconducting metamaterials discussed in Chapter 7 goes beyond this by realizing a scalable approach to create tunable long-range interaction between qubits.

1.4 Outline of the thesis

My doctoral research at Caltech lies at the intersection of broad disciplines of science discussed above, as illustrated in Fig. 1.4. In particular, we perform experimental studies of the burgeoning field of waveguide QED by utilizing micro-fabricated superconducting quantum devices. Below, I provide a brief description on the organization of the thesis.

First, I will begin the thesis by introducing the field of waveguide QED. Specifically, I will motivate the transition from cavity QED to waveguide QED and discuss the basic concepts and various physical realizations of waveguide QED in Chapter 2.

Next, I will describe the experimental techniques which have been employed throughout the work in the thesis in Chapter 3. This includes the device fabrication procedure, microwave packaging of device, cryogenic setup, and room-temperature electronics that are standard in the field of superconducting quantum circuits [107] or newly developed in the lab.

In the remaining parts of the thesis, I will provide detailed descriptions on the experiments performed during my PhD:

- In Chapter 4, I discuss the interaction between superconducting qubits mediated by a common waveguide channel in the strong-coupling regime, which is published in Ref. [108].
- In Chapter 5, a new approach to scaling up quantum processors with a compact waveguide QED architecture based on superconducting metamaterials is explored, which is published in Ref. [109].
- In Chapter 6, we utilize our ability to engineer a novel topological photonic structure and demonstrate an exotic type of qubit-qubit interaction mediated by this structure, which is published in Ref. [56].
- In Chapter 7, I will describe our current progress on building a large-scale quantum processor based on superconducting metamaterials.

Finally, I will conclude the thesis by discussing the implications of our work to the field and by providing an outlook and future directions in Chapter 8.

WAVEGUIDE QUANTUM ELECTRODYNAMICS

We have discussed the historical context and overview of quantum-light matter interfaces in Sec. 1.1 with a gentle introduction to the field of waveguide QED. In this chapter, we provide a more detailed description of waveguide QED systems by explaining the theory and the experimental realizations.

2.1 From cavity QED to waveguide QED

Cavity quantum electrodynamics (QED) studies the interaction of a quantum emitter with a single electromagnetic mode of a high-finesse cavity with a discrete spectrum [28, 29]. In this canonical setting, a large emitter–photon coupling is achieved by repeated interaction of the emitter with a single photon bouncing many times between the cavity mirrors. Coupling multiple quantum emitters to a common cavity is also shown to induce exchange-type photon-mediated interactions between the emitters [110–112], realizing a quantum information processing architecture with all-to-all connectivity. The cavity is formed by confining the electromagnetic field

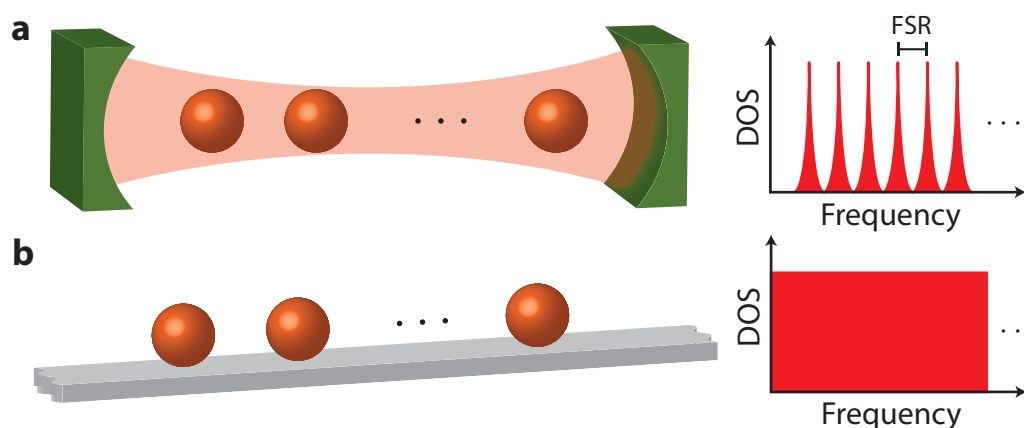


Figure 2.1: Transition from cavity QED to waveguide QED. **a**, Left: a cavity QED system where quantum emitters are coupled to a common cavity. Right: the density of states (DOS) inside a cavity plotted against the frequency shows a set of peaks associated with discrete modes spaced by free spectral range (FSR). The FSR is inversely proportional to the physical length scale of the cavity and hence the size of the cavity cannot grow indefinitely while maintaining the single-mode picture. **b**, Left: a waveguide QED system where quantum emitters are coupled to a common 1D waveguide channel. Right: the DOS of a waveguide plotted against the frequency shows a continuum of modes.

into a small volume and therefore has a finite length scale L that limits the number of quantum emitters that can be simultaneously coupled to the cavity. Increasing the size L of the cavity inevitably comes at the expense of breakdown of the single-mode picture due to the decrease in free spectral range (FSR), which is inversely proportional to the system size (Fig. 2.1a). Therefore, one needs to consider an alternative strategy of connecting multiple cavity QED systems in order to scale up, outlined in Prof. Jeff Kimble’s description of quantum internet [26].

Recently, there has been much interest in achieving strong light–matter interaction in a cavity-free system such as a waveguide [40, 44, 45]. Waveguide QED refers to a system where a chain of quantum emitters are coupled to a common 1D photonic channel with a continuum of electromagnetic modes over a large bandwidth, visualized in Fig. 2.1b. While it is more challenging to achieve strong emitter-photon interaction than the cavity QED scenario, utilizing waveguide-based architectures provides a natural solution for scaling up the system in 1D. Also, the high bandwidth of the system enables using propagating photons as the basis for quantum information processing [40, 113].

2.2 Quantum emitters coupled to a waveguide with linear dispersion

A canonical waveguide QED system consists of an array of quantum emitters which are interfaced with a common 1D waveguide channel with linear dispersion. In this scenario, the quantum emitters are characterized by the decay rate Γ_{1D} to the desired waveguide channel and the parasitic decay rate Γ' , as illustrated in Fig. 2.2a. The most important figure of merit in such systems representing the strength of emitter-photon coupling is the *Purcell factor* [114, 115], given by

$$P_{1D} \equiv \frac{\Gamma_{1D}}{\Gamma'}, \quad (2.1)$$

which characterizes the collection efficiency of the emitter’s radiation to the desired waveguide channel. In the following, I provide a heuristic overview of the basic processes in this setting. A more general description of the system in the form of input-output theory is discussed in Refs. [116, 117].

Single quantum emitter coupled to a waveguide

The simplest scenario in waveguide QED is when a single quantum emitter is coupled to the waveguide as illustrated in Fig. 2.2a. Even in this simple setting, the interaction between the emitter and photons in the waveguide can give rise to various output fields depending on photon statistics of the incident field.

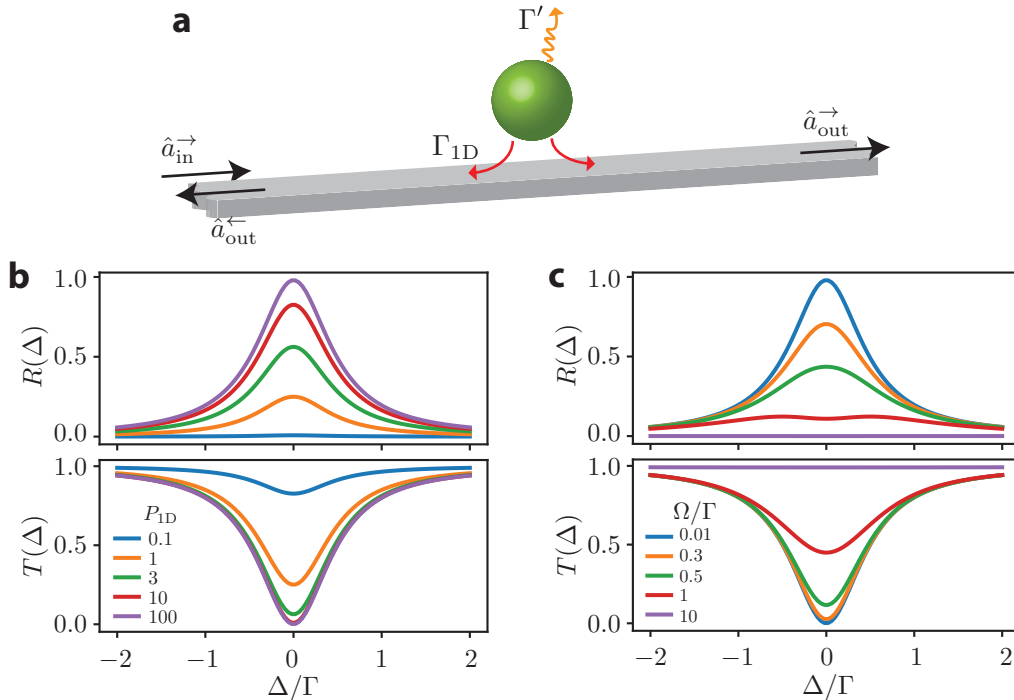


Figure 2.2: Single quantum emitter coupled to the waveguide. **a**, A quantum emitter is coupled to a 1D waveguide channel with decay rates Γ_{1D} to the waveguide and Γ' to other spurious channels. **b**, The reflectance $R(\Delta)$ and transmittance $T(\Delta)$ associated with single-photon scattering are plotted as a function of detuning Δ normalized to the total decay rate $\Gamma = \Gamma_{1D} + \Gamma'$, for a few different values of Purcell factor $P_{1D} = \{0.1, 1, 3, 10, 100\}$. **c**, The reflectance $R(\Delta)$ and transmittance $T(\Delta)$ of coherent field are plotted against normalized detuning Δ/Γ with Purcell factor of $P_{1D} = 100$, for a few different values of drive amplitude $\Omega/\Gamma = \{0.01, 0.3, 0.5, 1, 10\}$.

Single-photon scattering

We first consider the effects in the linear regime where the saturation of quantum emitters is negligible, which can be realized by using a single-photon wavepacket or a weak coherent field as input to the system. The reflectivity and transmittivity in this case can be written as [115, 118, 119]

$$r(\Delta) = \frac{\Gamma_{1D}/2}{i\Delta - (\Gamma_{1D} + \Gamma')/2}, \quad t(\Delta) = 1 + r(\Delta), \quad (2.2)$$

where $\Delta = \omega - \omega_0$ is the detuning of the probe photon from the resonant frequency ω_0 of the emitter. The transmission and reflection spectrum, represented by reflectance $R(\Delta) \equiv |r(\Delta)|^2$ and transmittance $T(\Delta) \equiv |t(\Delta)|^2$, have the Lorentzian lineshapes centered at the emitter's resonance as illustrated in Fig. 2.2b. On resonance $\Delta = 0$ ($\omega = \omega_0$), the reflectance and the transmittance can be simplified into

$$R(\Delta = 0) = \left(\frac{P_{1D}}{1 + P_{1D}} \right)^2, \quad T(\Delta = 0) = \frac{1}{(1 + P_{1D})^2}, \quad (2.3)$$

indicating that the emitter becomes reflective $R \approx 1$ ($T \approx 0$) in the regime of high Purcell factor $P_{1D} \gg 1$. In other words, a single quantum emitter with high Purcell factor can act as a near-perfect mirror for a single photon resonant to the emitter propagating along the waveguide. This can be attributed to the destructive interference of the incident photonic wavepacket with the emitter's radiation in the forward direction. The on-resonance extinction measured from low-power spectroscopy of a single quantum emitter offers a simple method to extract the Purcell factor from experiments. It is interesting to note that the mirror-like property of quantum emitters at the single-photon level can be leveraged to create a cavity-like confinement of photonic excitation in a finite segment of the waveguide, allowing us to revisit cavity QED-like effects in a waveguide QED setting [109, 120] (see also Chapter 4).

Multi-photon scattering

Using a multi-photon input to the system can result in various non-trivial effects due to the interference of emitter's radiation with the incident field from which the emitter can absorb only one photon at a time. For example, it has been shown that a degenerate two-photon state input results in three possible cases of strongly correlated output photon pairs consisting of (i) a pair of anti-bunched photons that are reflected, (ii) a pair of bunched photons that are transmitted (two-photon bound state), and (iii) a pair of transmitted and reflected photons propagating in the opposite directions [121, 122].

Inputting a coherent state to the system, the reflection and transmission spectrum in Eq. (2.2) are also modified, collecting a factor associated with the saturation of the emitter [115]:

$$r(\Delta) = -\frac{\Gamma_{1D}}{2} \frac{i\Delta + \frac{\Gamma_{1D} + \Gamma'}{2}}{\Delta^2 + \left(\frac{\Gamma_{1D} + \Gamma'}{2}\right)^2 + \frac{\Omega^2}{2}}, \quad t(\Delta) = 1 + r(\Delta). \quad (2.4)$$

Here, Ω denotes the Rabi frequency, the rate at which the emitter is driven by the input field. The effect of saturation is shown in Fig. 2.2c. Setting $\Omega = 0$ reduces Eq. (2.4) into the earlier case of single-photon scattering in Eq. (2.2), while larger spectroscopy power increases the effective linewidth of Lorentzian curve due to saturation.

Cooperative effects in waveguide QED

When multiple quantum emitters are coupled to a common waveguide channel, the exchange of photons in the waveguide between emitters result in cooperative

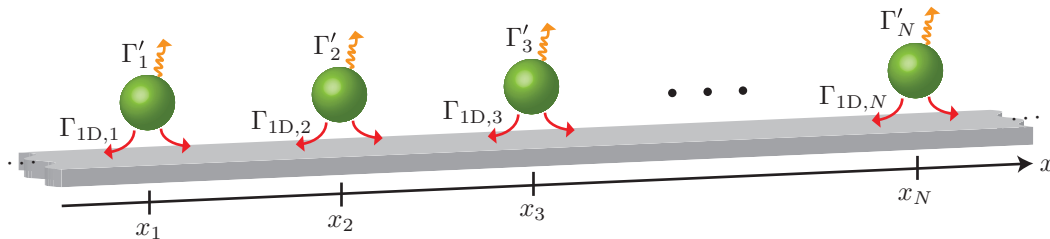


Figure 2.3: Multiple quantum emitters coupled to a waveguide. Quantum emitters are coupled to a waveguide channel at positions $x = x_j$ along the waveguide, with waveguide decay rate $\Gamma_{\text{ID},j}$ and spurious decay rate Γ'_j ($1 \leq j \leq N$).

effects such as correlated decay and exchange interaction [116, 120]. For simplicity, we consider the case where quantum emitters are placed along the waveguide at position $x = x_j$, with identical transition frequency ω_0 , waveguide decay rates $\Gamma_{\text{ID},j}$, and spurious decay rate Γ'_j , as illustrated in Fig. 2.3 ($j = 1, 2, \dots, N$). The photons propagating along the waveguide is assumed to have group velocity v (i.e., wavelength of $\lambda = 2\pi v/\omega_0$ or wavevector $k = \omega_0/v$). In cases where propagation delay is negligible compared to the timescale of radiation of emitters, i.e., $v \gg \Gamma_{\text{ID}}L$ where L is the length scale associated with the largest distance between emitters, the Born-Markov approximation holds and we can describe these processes with a Lindblad master equation after tracing out the photonic degrees of freedom [116, 120]:

$$\frac{d}{dt}\rho = -\frac{i}{\hbar}[\hat{H}, \rho] + \mathcal{L}[\rho]. \quad (2.5)$$

Here, ρ is the density operator in the subspace of emitters, \hat{H} is the Hamiltonian describing the coherent processes and \mathcal{L} is the Liouville superoperator specifying the incoherent processes.

Correlated decay

The correlated decay is caused by the cooperative emission of real photons to the waveguide channel from an ensemble of emitters. For example, a photon emitted from a quantum emitter can propagate to the other emitter at a distance d along the waveguide by collecting a phase factor e^{ikd} before interacting with the second emitter, and vice versa. Since the emitters share the same waveguide bath of photons, the emission from multiple emitters can be coherently added, resulting in interference of emission processes. A prime example of the correlated decay is the Dicke superradiance [42, 43] where the emission of an ensemble of excited emitters distributed within distances much smaller than the resonant wavelength ($d \ll \lambda$) radiates at a rate much faster than that of a single emitter. Such processes

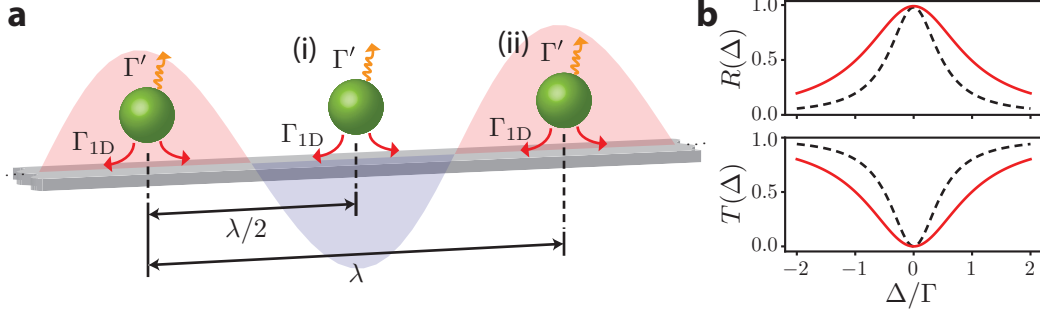


Figure 2.4: Superradiance and subradiance of two quantum emitters. **a**, Two quantum emitters are coupled to a waveguide with a separation of (i) $d = \lambda/2$ or (ii) $d = \lambda$. The electric field of a resonant photon propagating along the waveguide is illustrated, with regions of positive (negative) value shaded in red (blue). Due to the phase associated with photon propagation, the anti-symmetric (symmetric) superposition of single excitation states of emitters is superradiant to the waveguide when $d = \lambda/2$ ($d = \lambda$). The other superposition state with opposite symmetry is subradiant to the waveguide, having zero waveguide decay rate. **b**, The reflectance $R(\Delta)$ and transmittance $T(\Delta)$ of such two-emitter waveguide QED system plotted against the detuning Δ normalized to the total decay rate $\Gamma = \Gamma_{1D} + \Gamma'$ of a single emitter (red solid lines). The black dashed lines represent the spectra for a single-emitter waveguide QED system. Here, it is assumed that the Purcell factor is $P_{1D} = 100$.

in waveguide QED can be described by a Liouville superoperator \mathcal{L}_c given by

$$\mathcal{L}_c[\rho] = \sum_{i,j} \Gamma_{ij} \left[\hat{\sigma}_i^- \rho \hat{\sigma}_j^+ - \frac{1}{2} \{ \hat{\sigma}_j^+ \hat{\sigma}_i^-, \rho \} \right] \quad (2.6)$$

where

$$\Gamma_{ij} = \sqrt{\Gamma_{1D,i} \Gamma_{1D,j}} \cos(k|x_i - x_j|). \quad (2.7)$$

The diagonal terms ($i = j$) in Eq. (2.7) correspond to the self-decay of an emitter to the waveguide that was present in the case of single emitter, i.e., $\Gamma_{ii} = \Gamma_{1D,i}$. The off-diagonal terms ($i \neq j$) in Eq. (2.7) represent the rate of correlated decay which is proportional to the geometric mean of waveguide decay rates Γ_{1D} of a pair of emitters and a sinusoidal function dependent on the phase $\phi_{ij} = k|x_i - x_j|$ associated with propagation of a photon along the waveguide between the emitters.

Restricting our analysis to the case of two emitters with identical waveguide decay rate $\Gamma_{1D,j} = \Gamma_{1D}$ and spurious decay rate $\Gamma'_j = \Gamma'$ for $j = 1, 2$, it can be shown that the magnitude of correlated decay rate is maximized if the emitters are separated by a integer multiple of half-wavelength, i.e., $d = |x_1 - x_2| = n\lambda/2$ where n is an integer (equivalently, $kd = n\pi$). In this case, Equation (2.6) can be rewritten as

$$\mathcal{L}_c[\rho] = \sum_{\mu=B,D} \Gamma_{1D,\mu} \left[\hat{\sigma}_\mu^- \rho \hat{\sigma}_\mu^+ - \frac{1}{2} \{ \hat{\sigma}_\mu^+ \hat{\sigma}_\mu^-, \rho \} \right] \quad (2.8)$$

in terms of new operators

$$\hat{\sigma}_B^\pm = \frac{\hat{\sigma}_1^\pm + (-1)^n \hat{\sigma}_2^\pm}{\sqrt{2}}, \quad \hat{\sigma}_D^\pm = \frac{\hat{\sigma}_1^\pm - (-1)^n \hat{\sigma}_2^\pm}{\sqrt{2}} \quad (2.9)$$

and modified waveguide decay rates $\Gamma_{1D,B} = 2\Gamma_{1D}$ and $\Gamma_{1D,D} = 0$. This means that an entangled single-excitation state

$$|B\rangle \equiv \hat{\sigma}_B^+ |g\rangle_1 |g\rangle_2 = \frac{|e\rangle_1 |g\rangle_2 + (-1)^n |g\rangle_1 |e\rangle_2}{\sqrt{2}} \quad (2.10a)$$

has a superradiantly enhanced decay rate equal to the sum of decay rates of emitters, hence the name *bright state* (also referred to as superradiant state). It can be shown that the effective Purcell factor of the two-emitter bright state $|B\rangle$ is $P_{1D,B} = 2\Gamma_{1D}/\Gamma'$, two times the single-emitter Purcell factor¹. On the other hand, the other state with the opposite symmetry

$$|D\rangle \equiv \hat{\sigma}_D^+ |g\rangle_1 |g\rangle_2 = \frac{|e\rangle_1 |g\rangle_2 - (-1)^n |g\rangle_1 |e\rangle_2}{\sqrt{2}}, \quad (2.10b)$$

named *dark state* (also referred to as subradiant state), is effectively decoupled from the waveguide channel and therefore has zero waveguide decay rate. The subspace of Hilbert space composed of such non-radiative states to the waveguide channel is referred to as the decoherence-free subspace, consisting of the only long-lived states in a waveguide QED system which could be used as resources for quantum information processing [123]. Note that the bright (dark) state has the same (opposite) symmetry as a photon propagating along the waveguide, collecting a phase factor $e^{ik \cdot n\lambda/2} = (-1)^n$, as illustrated in Fig. 2.4a. It can be also shown that the coherent exchange interaction between the emitters is zero at such distances $d = n\lambda/2$ (see below), so the self and the correlated decay alone are sufficient to describe the full picture.

The signature of superradiance can be measured with spectroscopic methods at low enough probe power. It can be shown that the transmission and reflection spectrum of such two-qubit system shows a Lorentzian lineshape with full-width half-maximum linewidth of $2\Gamma_{1D}$ corresponding to the bright state $|B\rangle$, as shown in Fig. 2.4b. The dark state $|D\rangle$, decoupled from the waveguide channel, cannot be probed by using the waveguide channel and therefore cannot be easily accessed. A novel scheme to utilize waveguide-mediated coherent interaction to perform coherent control over the inaccessible dark state $|D\rangle$, proposed by Darrick Chang and colleagues [120], will be experimentally investigated in Chapter 4 [108].

¹More generally, the Purcell factor of the most superradiant state of an array of quantum emitters is proportional to the number of emitters N .

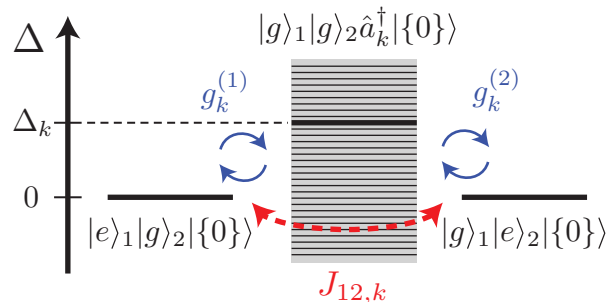


Figure 2.5: Coherent waveguide-mediated exchange interaction. Energy level diagram of single-excitation subspace of a system involving two quantum emitters (state labeled by subscript indices 1, 2) and a waveguide (state labeled by mode index k). The single-emitter excited state $|e\rangle_1|g\rangle_2|\{0\}\rangle$ ($|g\rangle_1|e\rangle_2|\{0\}\rangle$) of emitter 1 (2) is coupled to a single-photon state $|g\rangle_1|g\rangle_2\hat{a}_k^\dagger|\{0\}\rangle$ of mode k at detuning Δ_k from the frequency of the emitters with coupling rate $g_k^{(1)}$ ($g_k^{(2)}$) (blue, solid). This induces virtual exchange between the two single-emitter excited states at a rate $J_{12,k} = -g_k^{(1)}g_k^{(2)}/\Delta_k$ (red, dashed) for each off-resonant mode k , without transfer of real photons.

Exchange interaction

There also exists a mechanism to induce coherent interactions between emitters coupled to a common waveguide channel, known as the exchange interaction. This process arises from virtual exchange of photons mediated by off-resonant modes of the waveguide which form a continuum without transferring real photons to the dissipative waveguide, as illustrated in Fig. 2.5.

The coherent exchange interaction can be described by a Hamiltonian \hat{H}_c written as

$$\hat{H}_c = \sum_{i,j} J_{ij} \hat{\sigma}_i^+ \hat{\sigma}_j^-, \quad (2.11)$$

where

$$J_{ij} = \frac{1}{2} \sqrt{\Gamma_{1D,i} \Gamma_{1D,j}} \sin(k|x_i - x_j|). \quad (2.12)$$

The diagonal terms ($i = j$) in Eq. (2.12) correspond to the self-interaction of an emitter with itself which is zero $J_{ii} = 0$. The off-diagonal terms ($i \neq j$) in Eq. (2.12) represent the rate of exchange interaction which is proportional to the geometric

²While the Eq. (2.12) predicts that the waveguide-mediated exchange interaction is infinite-ranged, this form is obtained under the Born-Markov approximation in the limit where the propagation delay is small compared to the inverse of relevant bandwidth for waveguide photons. At long distances, the non-negligible propagation delay will significantly invalidate the assumption, resulting in non-Markovian phenomena that cannot be described by a simple effective master equation in Eq. (2.5).

mean of waveguide decay rates Γ_{1D} of a pair of emitters and a sinusoidal function dependent on the phase $\phi_{ij} = k|x_i - x_j|$ associated with propagation of a photon along the waveguide between the emitters. It is interesting to note that the form of J_{ij} is purely sinusoidal without reduction at large inter-emitter distances, providing potential for realizing long-range coherent interactions².

Restricting our analysis to the case of two emitters with identical waveguide decay rate $\Gamma_{1D,j} = \Gamma_{1D}$ for $j = 1, 2$, it can be shown that the magnitude of exchange interaction rate is maximized if the emitters are separated by a half-integer multiple of half-wavelength, i.e., $d = |x_1 - x_2| = (n+1/2)\lambda/2$ where n is an integer (equivalently, $kd = n\pi + \pi/2$) as illustrated in Fig. 2.6a. In this case, Equation (2.11) can be rewritten as

$$\hat{H}_c = (-1)^n \frac{\Gamma_{1D}}{2} (\hat{\sigma}_1^+ \hat{\sigma}_2^- + \hat{\sigma}_2^+ \hat{\sigma}_1^-), \quad (2.13)$$

giving the maximal achievable interaction rate of $J = (-1)^n \Gamma_{1D}/2$ between the two emitters. Note that the correlated decay rate Γ_{12} vanishes to zero in this configuration, while the self decay of each emitter to the waveguide at the rate Γ_{1D} remains. Since the magnitude of coherent coupling rate cannot exceed the total decay rate of individual emitter, i.e., $2|J| \leq \Gamma = \Gamma_{1D} + \Gamma'$, it is intrinsically forbidden to realize a strong coherent coupling of two emitters in waveguide QED, which would have resulted in vacuum Rabi splitting in spectroscopic characterization. Instead, the transmission and reflection spectrum of such a system shows the interference of coherent coupling and strong decay, giving rise to a non-Lorentzian lineshape illustrated in Fig. 2.6b.

Such intrinsic limitations forbid us from efficiently utilizing the long-range interactions, which could be useful for performing non-local gates in quantum computation and also for the study of many-body physics. There has been two major ways to overcome this challenge. The first approach is to only use states that are non-radiative to the waveguide channel, the decoherence-free subspace, with precise positioning of emitters along the waveguide. The second method is to make the emitters themselves non-dissipative, which makes the protocol for controlling emitters much simpler. One example of this is to utilize an emitter coupled to a waveguide at multiple locations to allow the emitter's radiation from multiple coupling points to destructively interfere, known as the *giant atom* [124]. The other example is to utilize emitter-photon bound states inside the bandgap regime of a dispersive waveguide [125], discussed in Sec. 2.3

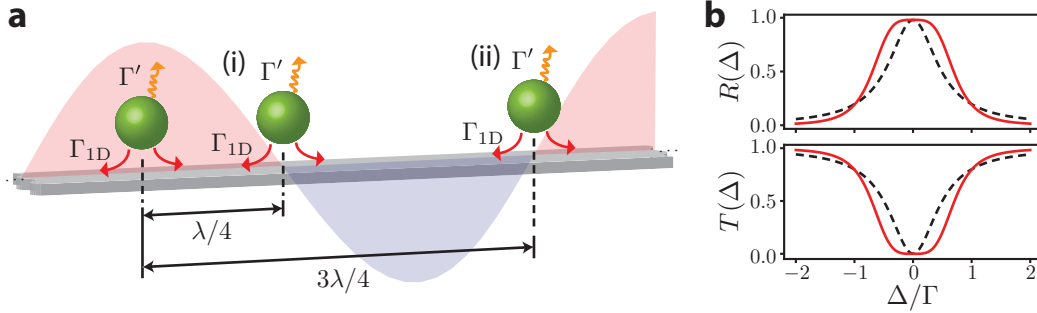


Figure 2.6: Exchange interaction between two quantum emitters. **a**, Two quantum emitters are coupled to a waveguide with a separation of (i) $d = \lambda/4$ or (ii) $d = \lambda/3$. The electric field of a resonant photon propagating along the waveguide is illustrated, with regions of positive (negative) value shaded in red (blue). Due to the phase associated with photon propagation, the coupling of second emitter with a mode at a positive detuning from the emitters' frequency, having a shorter wavelength, will have a sign opposite (identical) to that of the first emitter when $d = \lambda/4$ ($d = 3\lambda/4$), resulting in a positive (negative) exchange interaction. **b**, The reflectance $R(\Delta)$ and transmittance $T(\Delta)$ of such two-emitter waveguide QED system plotted against the detuning Δ normalized to the total decay rate $\Gamma = \Gamma_{1D} + \Gamma'$ of a single emitter (red solid lines). The spectra for a single-emitter waveguide QED system is plotted with black dashed lines as a reference. Here, it is assumed that the Purcell factor is $P_{1D} = 100$.

2.3 Waveguide QED in a dispersive photonic channel

While the original concept of waveguide QED revolved around coupling quantum emitters to a waveguide inside a transmission band, a new paradigm to induce long-range photon-mediated interactions between quantum emitters inside a photonic bandgap was proposed in Ref. [125]. In this scheme, photonic structures are engineered to host a bandgap where the propagation of photons are prohibited. Tuning the emitters' frequencies inside the bandgap, the emitters cannot radiate to the waveguide channel while the coherent interaction between distant emitters are still allowed by means of exchange of virtual photons. Compared to the case when the emitters are tuned inside the transmission band discussed in Sec. 2.2, the bandgap regime offers a practical direction to achieve strong and long-range coupling between emitters without suffering from significant dissipation to the photonic band. In this section, I introduce the basic concepts of this direction to achieve a scalable quantum many-body system with long-range connectivity.

Emitter-photon bound states

When the transition frequency of a quantum emitter is tuned inside a photonic bandgap of an electromagnetic structure, the spontaneous emission of the emitter is forbidden due to the absence of resonant photonic modes to absorb the emitted

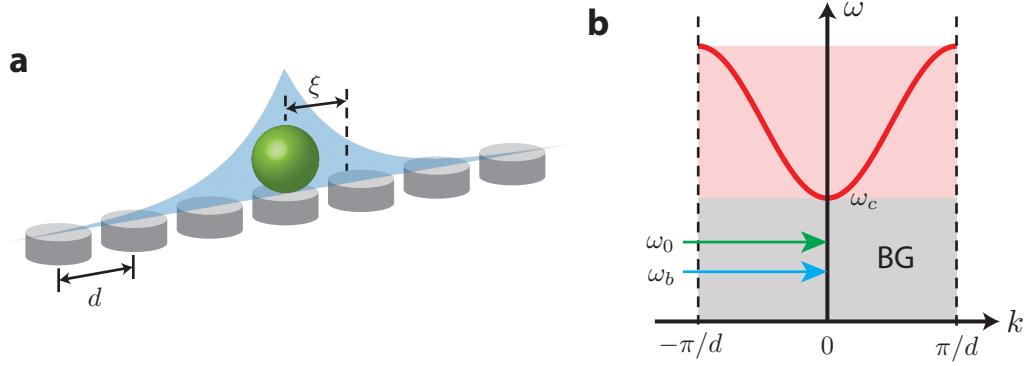


Figure 2.7: Emitter-photon bound state. **a**, Illustration of a quantum emitter (green circle) coupled to a 1D dispersive waveguide channel (gray) represented as a periodic electromagnetic structure with lattice constant d . The emitter's frequency is tuned inside the bandgap of the waveguide, inducing an emitter-photon bound state exponentially localized at a length scale ξ , shaded in blue. **b**, An example of photonic bandstructure of a dispersive waveguide. The transmission band (bandgap) is shaded in red (gray). Tuning the bare transition frequency ω_0 of the emitter (green arrow) below the frequency ω_c of band-edge, the emitter-photon bound state exists at a frequency ω_b lower than that of the emitter (blue arrow).

photons. Instead, the emitted photon is scattered back to the original emitter, resulting in a coupled eigenstate of photonic modes of the electromagnetic structure and the emitter. This is known as the *emitter-photon bound state*³, first predicted by Sajeev John and Jian Wang in 1990 [126] in the context of Anderson localization of light [127]. In the emitter-photon bound state, the emitter is dressed with a photonic tail exponentially localized with respect to the emitter, gaining a spatial extent. This length scale of the emitter-photon bound state can be adjusted by controlling the detuning of the emitter from the edge of the photonic band.

The Hamiltonian of a quantum emitter coupled to such 1D photonic structure, a dispersive waveguide (an example illustrated in Fig. 2.7), can be written as

$$\hat{H} = \hbar\omega_0|e\rangle\langle e| + \sum_k \hbar\omega_k \hat{a}_k^\dagger \hat{a}_k + \sum_k \hbar \left(g_k \hat{a}_k^\dagger |g\rangle\langle e| + g_k^* \hat{a}_k |e\rangle\langle g| \right), \quad (2.14)$$

where ω_0 is the transition frequency of the emitter, \hat{a}_k (\hat{a}_k^\dagger) is the annihilation (creation) operator of photonic mode at wavevector k satisfying the canonical commutation relation $[\hat{a}_k, \hat{a}_{k'}^\dagger] = \delta_{k,k'}$, and g_k is the momentum-space coupling between the emitter and the waveguide photons. Here, $|g\rangle$ and $|e\rangle$ denote the ground state and the excited state of the emitter, respectively. Limiting our analysis to the single-

³Also known as the atom (qubit)-photon bound state if an atom (a qubit) plays the role of a two-level emitter.

excitation manifold, we look for a emitter-photon bound state of the following form

$$|\phi_b\rangle = \cos\theta|\{0\}\rangle|e\rangle + \sin\theta \sum_k c_k \hat{a}_k^\dagger |\{0\}\rangle|g\rangle \quad (2.15)$$

that satisfies the time-independent Schrödinger equation $\hat{H}|\phi_b\rangle = \hbar\omega_b|\phi_b\rangle$. Here, $|\{0\}\rangle$ represents the vacuum state of photon modes and the coefficients c_k are normalized by $\sum_k |c_k|^2 = 1$. Writing out the algebraically independent terms in the equation we get

$$\omega_0 \cos\theta + \left(\sum_k g_k^* c_k \right) \sin\theta = \omega_b \cos\theta \quad (2.16a)$$

$$\omega_k c_k \sin\theta + g_k \cos\theta = \omega_b c_k \sin\theta \quad (2.16b)$$

From equating the coefficients in Eq. (2.16b), we obtain the probability amplitudes at wavevector k to be

$$c_k = \frac{g_k}{(\omega_b - \omega_k) \tan\theta}. \quad (2.17)$$

Substituting the Eq. (2.17) into Eq. (2.16a), we get a transcendental equation for evaluating the energy of the emitter-photon bound state

$$\omega_b = \omega_0 + \sum_k \frac{|g_k|^2}{\omega_b - \omega_k} \quad (2.18a)$$

subjected to the normalization condition

$$\tan^2\theta = \sum_k \frac{|g_k|^2}{(\omega_b - \omega_k)^2}. \quad (2.18b)$$

For a generic 1D waveguide with a quadratic dispersion relation, a simple analytical relation to describe the emitter-photon bound state can be derived. We specifically consider the dispersion relation of the form

$$\omega_k = \omega_c + \alpha(k - k_0)^2, \quad (2.19)$$

where ω_c is the frequency of the band-edge, $\alpha > 0$ is the curvature of the photonic band, and k_0 is the wavevector at which the band-edge occurs.

Assuming that the coupling of emitter and the waveguide locally occurs at position $x = x_0$ with the strength g , the emitter-photon interaction Hamiltonian takes the form $\hat{H}_{\text{int}} = g(\hat{a}_{x_0}^\dagger|g\rangle\langle e| + \hat{a}_{x_0}|e\rangle\langle g|)$ in terms of real-space annihilation operator $\hat{a}_{x_0} = \frac{1}{\sqrt{N}} \sum_k e^{ikx_0} \hat{a}_k$ where N is the number of modes inside the band. This is

translated into the last term in Eq. (2.14) with momentum-space coupling given by $g_k = g e^{-ikx_0}/\sqrt{N}$. In this case, the Eqs. (2.18a)-(2.18b) are simplified into⁴

$$\omega_0 - \omega_b = \frac{g^2 d}{2\sqrt{\alpha}(\omega_c - \omega_b)} \quad (2.20a)$$

and

$$\tan^2 \theta = \frac{g^2 d}{4\sqrt{\alpha}(\omega_c - \omega_b)^3} = \frac{\omega_0 - \omega_b}{2(\omega_c - \omega_b)}. \quad (2.20b)$$

Here, d is the shortest length scale (lattice constant) of the waveguide that determines the first Brillouin zone. It can be seen from Eq. (2.20a) that the emitter-photon bound state inside the bandgap ($\omega_b < \omega_c$) has a frequency lower than the bare emitter frequency ($\omega_b < \omega_0$) due to the negative Lamb shift from hybridization with photonic modes at higher frequencies. Also, combining Eqs. (2.20a)-(2.20b), it can be shown that the photonic component of the bound state becomes

$$\sin^2 \theta = \left[1 + \frac{4\sqrt{\alpha}}{g^2 d} (\omega_c - \omega_b)^{3/2} \right]^{-1}. \quad (2.21)$$

This means that the emitter-photon bound state becomes more photon (emitter)-like as the frequency get closer to (farther from) the band-edge frequency ω_c .

One can also evaluate the real-space coefficients $c_x = \frac{1}{\sqrt{N}} \sum_k e^{ikx} c_k$ of photonic part of the wavefunction $|\phi_b\rangle$ using Eq. (2.17)⁵:

$$c_x = -\frac{gd}{\sqrt{2\alpha}(\omega_0 - \omega_b)} e^{ik_0(x-x_0)} e^{-|x-x_0|/\xi} \quad (2.22)$$

where

$$\xi = \sqrt{\frac{\alpha}{\omega_c - \omega_b}} \quad (2.23)$$

⁴In the derivation, the summation \sum_k over the first Brillouin zone was replaced with the integral $\frac{d}{2\pi} \int dk$ in the thermodynamic limit ($N \rightarrow \infty$) whose upper and lower limits are extended from $\pm\pi$ to $\pm\infty$ assuming that the integration performed at high $|k|$ values are negligible. Also, the integral identities

$$\int \frac{dx}{a^2 + x^2} = \frac{1}{a} \tan^{-1} \left(\frac{x}{a} \right), \quad \int \frac{dx}{a^2 + x^2}^2 = \frac{1}{2a^3} \frac{ax}{a^2 + x^2} + \frac{1}{2a^3} \tan^{-1} \left(\frac{x}{a} \right)$$

are employed.

⁵Here, the integral identity

$$\int_{-\infty}^{\infty} dx \frac{e^{iax}}{x^2 + 1} = \pi e^{-|a|}$$

is used.

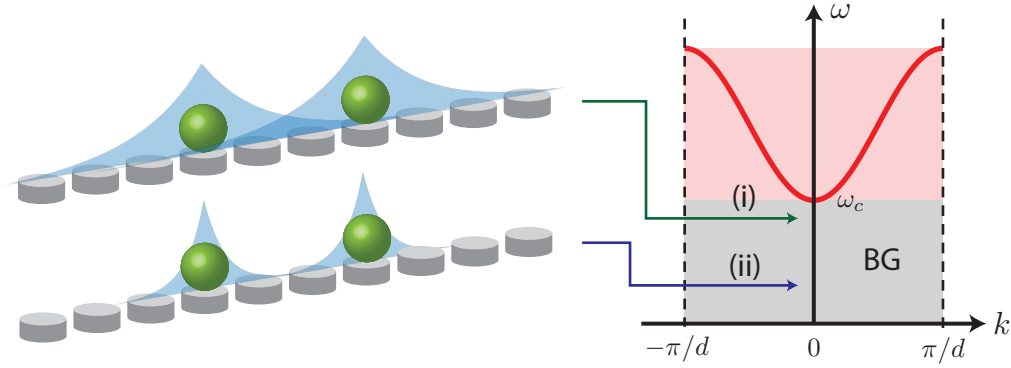


Figure 2.8: Waveguide-mediated interactions between emitter-photon bound states. When two quantum emitters are tuned inside the bandgap, the spatial overlap of corresponding emitter-photon bound states induces emitter-emitter interaction. The range of interaction depends on the localization length ξ which is long when the emitters are tuned close to the band-edge frequency ω_c (i, green arrow), while the interaction is short-ranged deep inside the bandgap (ii, blue arrow).

is the localization length. Equations (2.22)-(2.23) directly shows a few important properties of the photonic component of the bound state. First, the magnitude of c_x exponentially decays at a length scale ξ with respect to the location $x = x_0$ of the emitter. The localization length ξ characterizes the effective spatial extent of the emitter-photon bound state. Second, the probability amplitude c_x collects an additional factor $e^{ik_0(x-x_0)}$ associated with propagation with wavevector $k = k_0$ of the band-edge. Also, the localization length is inversely proportional to the detuning of bound state from the band-edge, i.e., $\xi \propto (\omega_c - \omega_b)^{-1/2}$, diverging as $\omega_b \rightarrow \omega_c$. This means that the spatial extent of the emitter-photon bound state can take a wide range of values depending on the frequency tuning of the emitter inside the bandgap.

Waveguide-mediated interactions between emitter-photon bound states

The spatially extended nature of the emitter-photon bound state has been viewed as a method to induce effective interactions between emitters not long since the first theoretical investigation of emitter-photon bound states [128, 129]. When two resonant emitters are tuned inside the bandgap of a common photonic structure, it was shown that the photonic band off-resonantly mediates exchange interaction between the emitters in a way similar to how each emitter is dressed by photonic modes to form the emitter-bound state (self-interaction). Such interaction takes a special form that falls off exponentially with the distance between the emitters, whose length scale ξ can be tuned by adjusting the frequency of the emitters inside

the bandgap (see Fig. 2.8).

The Hamiltonian of two quantum emitters (labeled by $j = 1, 2$) coupled to a common 1D dispersive waveguide is given by

$$\hat{H} = \sum_j \hbar\omega_0^{(j)} |e\rangle\langle e|_j + \sum_k \hbar\omega_k \hat{a}_k^\dagger \hat{a}_k + \sum_{j,k} \hbar \left[g_k^{(j)} \hat{a}_k^\dagger |g\rangle\langle e|_j + g_k^{(j)*} \hat{a}_k |e\rangle\langle g|_j \right], \quad (2.24)$$

where $\omega_0^{(j)}$ is the frequency of the emitter j , \hat{a}_k (\hat{a}_k^\dagger) is the annihilation (creation) operator of photonic mode at wavevector k satisfying the canonical commutation relation $[\hat{a}_k, \hat{a}_{k'}^\dagger] = \delta_{k,k'}$, and $g_k^{(j)}$ is the momentum-space coupling between the emitter j and the waveguide. Here, $|g\rangle_j$ and $|e\rangle_j$ denote the ground state and the excited state of the emitter j , respectively.

Again, we look for a emitter-photon bound state in the single-excitation manifold of the following form

$$|\phi_b\rangle = \cos\theta |\{0\}\rangle \left[c_q^{(1)} |e\rangle_1 |g\rangle_2 + c_q^{(2)} |g\rangle_1 |e\rangle_2 \right] + \sin\theta \sum_k c_k \hat{a}_k^\dagger |\{0\}\rangle |g\rangle_1 |g\rangle_2 \quad (2.25)$$

that satisfies the time-independent Schrödinger equation $\hat{H}|\phi_b\rangle = \hbar\omega_b |\phi_b\rangle$. Here, $|\{0\}\rangle$ represents the vacuum state of photon modes and the coefficients c_k are normalized by $\sum_k |c_k|^2 = 1$ and c_q by $\sum_j |c_q^{(j)}|^2 = 1$. Writing out the algebraically independent terms in the equation we get

$$\omega_0^{(j)} c_q^{(j)} \cos\theta + \left(\sum_k g_k^{(j)*} c_k \right) \sin\theta = \omega_b c_q^{(j)} \cos\theta, \quad (2.26a)$$

$$\left(\sum_j g_k^{(j)} c_q^{(j)} \right) \cos\theta + \omega_k c_k \sin\theta = \omega_b c_k \sin\theta. \quad (2.26b)$$

Equation (2.26b) can be simplified into an expression for coefficients c_k of photonic modes:

$$c_k = \frac{\sum_j g_k^{(j)} c_q^{(j)}}{(\omega_b - \omega_k) \tan\theta}. \quad (2.27)$$

Substituting Eq. (2.27) into Eq. (2.26a), we obtain an eigenequation for probability amplitudes $c_q^{(j)}$ of quantum emitters given by

$$\omega_b \begin{pmatrix} c_q^{(1)} \\ c_q^{(2)} \end{pmatrix} = \begin{pmatrix} \omega_0^{(1)} + J_{11} & J_{12} \\ J_{21} & \omega_0^{(2)} + J_{22} \end{pmatrix} \begin{pmatrix} c_q^{(1)} \\ c_q^{(2)} \end{pmatrix}, \quad (2.28)$$

where

$$J_{ij} = \sum_k \frac{g_k^{(i)*} g_k^{(j)}}{\omega_b - \omega_k}. \quad (2.29)$$

The matrix J_{ij} is Hermitian and represents the effective interaction between the emitters mediated by photons of the transmission band. The diagonal terms ($i = j$) correspond to self-interaction of a quantum emitter with itself, also known as the Lamb shift identical to Eq. (2.18a).

Considering again a 1D waveguide with a quadratic dispersion relation described in Eq. (2.19) where each emitter j is coupled at position $x = x_j$ of the waveguide (resulting in momentum-space coupling $g_k^{(j)} = g e^{-ikx_j} / \sqrt{N}$), we can readily evaluate the sum over k in the thermodynamic limit. Following procedures similar to the derivation of Eq. (2.22), Equation (2.29) reduces to

$$J_{ij} = -\frac{g^2 d}{2\sqrt{\alpha}(\omega_c - \omega_b)} e^{ik_0(x_i - x_j)} e^{-|x_i - x_j|/\xi}, \quad (2.30)$$

where ξ is the localization length defined in (2.23). It can be easily seen that the interaction between emitters mediated by the dispersive waveguide in Eq. (2.30) follows the spatial shape of emitter-photon bound state in Eq. (2.22), collecting a phase factor $e^{ik_0\Delta x}$ and an attenuation factor $e^{-|\Delta x|/\xi}$ associated with suppressed propagation of a photon inside the bandgap along the displacement $\Delta x = x_i - x_j$ between the emitters.

2.4 Experimental realizations of waveguide QED

The physical processes discussed in Secs. 2.2-2.3 are applicable to a generic system consisting of two-level quantum emitters coupled to a 1D photonic waveguide channel. This paradigm of waveguide QED has been experimentally realized in various combinations of emitters and waveguides such as atoms coupled to a tapered nanofiber [130, 131] or a nanophotonic waveguide [44], artificial atoms such as quantum dots coupled to a nanophotonic waveguide [132], and superconducting qubits coupled to a transmission line in the microwave domain, as illustrated in Fig. 2.9. In this section, I will provide a brief introduction to various platforms for waveguide QED experiments and compare the characteristics of the platforms, summarized in Table 2.1.

Cold atoms

Experiments in waveguide QED were first performed in cold atomic systems by tightly focusing a probe field toward a single trapped atom [24], where it was shown that a single atom could cause an extinction of $\sim 10\%$ in transmission spectrum of the field. However, as noted in Sec. 1.1 and in Eq. (1.1), achieving strong atom-photon interactions with this approach is challenging due to a small atomic

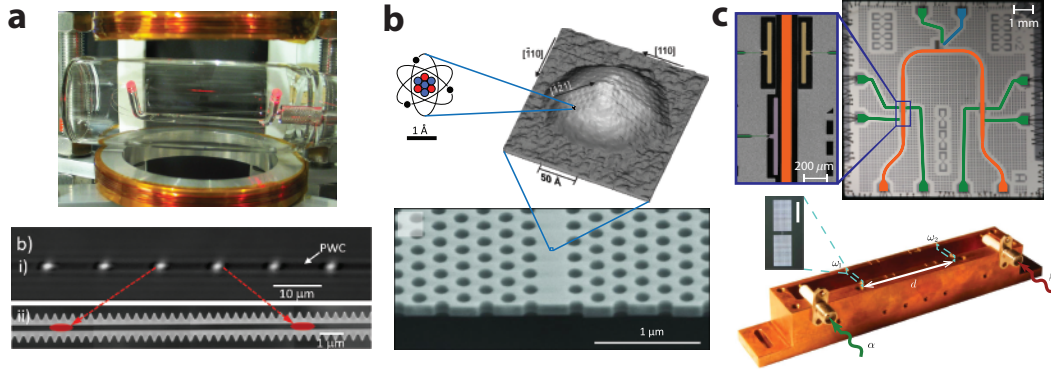


Figure 2.9: Examples of experimental platforms for waveguide QED. **a**, Atoms are interfaced with tapered optical nanofiber (top) or an alligator photonic crystal waveguide (bottom). **b**, A quantum dot is interfaced with a photonic crystal waveguide. **c**, Superconducting qubits are interfaced with a coplanar waveguide transmission line (top) or a machined 3D waveguide (bottom). The panel **a** is adapted from Refs. [133, 134]; **b** is adapted from Ref. [132]; **c** is adapted from Refs. [108, 135].

Quantum Emitter	Waveguide	P_{1D}	N	Ref.
Atom	Nanofiber	$\sim 10^{-2}-10^{-1}$	$\sim 10^3$	[136]
	PhC waveguide	$\sim 10^{-1}-10^0$	< 5	[137]
Quantum dot	Plasmonic waveguide	$\sim 10^1-10^2$	1	[132]
	PhC waveguide	$\sim 10^0-10^1$	1	[138]
SC qubit	On-chip TL	$\sim 10^2$	~ 10	[108]
	3D waveguide	$\sim 10^2$	< 5	[135]

Table 2.1: Experimental platforms for studying waveguide QED. State-of-the-art experiments in waveguide QED, performed in various combinations of quantum emitters and waveguides, are summarized. Here, typical values of the highest achieved Purcell factor P_{1D} and the number of resonant quantum emitters N are compared between platforms. PhC: photonic crystal, SC: superconducting, TL: transmission line.

scattering cross section $\sigma_0 = 3\lambda_0^2/(2\pi)$ at best comparable to the focused mode area $A \sim \lambda_0^2$ (diffraction limit). Also, this technique cannot be extended to the case of many atoms since the beam waist diverges rapidly under tight focusing.

For these reasons, alternative approaches to achieve strong atom-photon interactions were investigated using guided modes of 1D photonic structures which realizes small mode area. Optical nanofibers with radius of few hundred nanometers were first used to couple atoms to the evanescent tail of guided nanofiber mode [139]. Trapped atoms near the nanofiber, it was shown that $N \sim 10^3$ atoms could be coupled to the photonic mode [140]. However, suboptimal mode overlap between atoms and photons at the evanescent tail result in small single-atom Purcell factor. To overcome this challenge, a novel direction to employ engineered nanophotonic waveguides was

pursued. In particular, a Purcell factor on the order of unity was achieved for the first time with atoms by interfacing with a photonic crystal waveguide engineered to have the highest mode intensity at the atoms' position [137, 141]. Also, a similar structure was utilized to study atom-atom interactions inside the bandgap regime discussed in Sec. 2.3, especially near the band-edge [142]. An outstanding challenge in this approach is to trap the atoms near the nanophotonic structures [134, 143], which has been difficult due to strong attractive forces at the dielectric surface [144].

Quantum dots

There has been numerous investigations to interface quantum dots with nanophotonic structures [132] such as a photonic crystal waveguide or a plasmonic waveguide [138], realizing single-emitter Purcell factors on the order of 10–100. However, most of the studies to date were limited to the case of a single quantum dot with photons being conceived as resources for quantum applications [145].

Superconducting qubits

Superconducting circuits offer a promising platform to study waveguide QED in the microwave domain due to strong emitter-photon coupling and a wide variety of microwave photonic structures that could be fabricated on chip with high flexibility. In superconducting circuits, the strong sub-wavelength confinement of electromagnetic modes in transverse direction and large transition dipole moment of superconducting qubits themselves result in high Purcell factors. The first notable waveguide QED experiment in superconducting circuits was performed by Astafiev and colleagues [146] where they have used a superconducting flux qubit coupled to a transmission line on chip. The resonance fluorescence showed strong extinction in transmission spectrum of 94 %, indicating a Purcell factor beyond unity $P_{ID} > 1$. Experiments involving multiple qubits [147] were also investigated, demonstrating strong cooperative interactions between qubits mediated by the waveguide channel [108]. There has also been new efforts to utilize machined 3D microwave waveguides together with multiple qubit chips placed along the waveguide [135, 148].

The current limitations of superconducting qubit platform is related to the scalability. The wavelength at microwave frequencies (few GHz) is on the order of a few centimeters and therefore channeling qubits with a microwave waveguide requires a large footprint on chip or a large 3D enclosure. Therefore, a compact microwave structure for waveguide QED must be envisioned [109] in order to increase the effective size of the system. Also, additional wiring for individual addressing of

qubits is necessary to harness the full power of superconducting qubits, which makes the scale-up more challenging. Nevertheless, with the technology developed for state-of-the-art quantum processors [6, 76], realizing a waveguide QED system with $N \sim 10^2$ superconducting qubits is expected to be feasible.

*Chapter 3***DEVICE FABRICATION AND EXPERIMENTAL TECHNIQUES**

Performing experiments with superconducting quantum circuits requires a broad technical knowledge ranging from fabrication of device, designing packaging of the device, engineering of cryogenic setup and microwave electronics, and experimental methods to control and read out qubits. In this chapter, I will summarize the techniques developed and utilized in the experiments described in the remaining chapters.

3.1 Fabrication of superconducting quantum circuits

The devices used in the thesis are fabricated on 500 μm -thick high-resistivity ($> 10 \text{ k}\Omega \cdot \text{cm}$) silicon (Si) wafers diced into $1 \text{ cm} \times 1 \text{ cm}$ or $2 \text{ cm} \times 1 \text{ cm}$ chips¹. As the first step, alignment markers (positive 20 μm square) are created by performing electron-beam lithography on Zeon ZEP520A resist, development in Zeon ZED-N50 developer, and electron-beam evaporation of 150 nm-thick niobium (Nb). Next, the ground plane, waveguides, resonators and qubit capacitors are patterned by electron-beam lithography with the same resist and development procedure as above, followed by electron-beam evaporation of 120 nm aluminum (Al). The Josephson junctions for qubits are then patterned on MMA(8.5)MAA EL11 and 950 PMMA A4² bilayer resist stack and fabricated using double-angle electron-beam evaporation on suspended Dolan bridges [149], where 60 nm and 120 nm Al evaporation are intervened by controlled exposure to oxygen. We then perform 5 min argon (Ar) ion mill and 140 nm Al evaporation to form a bandage layer [150] that electrically contacts the Al layers defined in previous steps. Finally, the airbridges are patterned using grayscale electron-beam lithography on a trilayer resist stack consisting of 950 PMMA A9³, MMA(8.5)MAA EL11⁴, and 950 PMMA A9 and developed in a mixture of isopropyl alcohol (IPA) and deionized (DI) water [151]. After 2 hr of resist reflow at 105 °C, electron-beam evaporation of 140 nm Al is performed at a rate of 1 nm/s following 5 min of Ar ion milling. The bandage and the airbridge steps are often combined into a single-layer process when only a small number of

¹The wafers are diced from Silicon Valley Microelectronics, Inc.

²Polymethyl methacrylate with molecular weight of 950k, 4 % in Anisole.

³Polymethyl methacrylate with molecular weight of 950k, 9 % in Anisole.

⁴Mixture of PMMA and 8.5 % methacrylic acid, 11 % in Etyl Lactate.

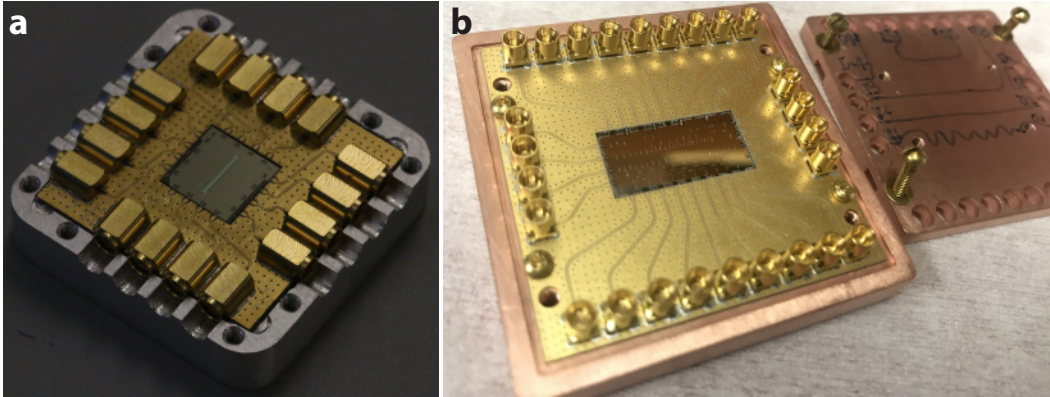


Figure 3.1: Microwave packaging of quantum devices. **a**, A device is packaged in 16-port packaging for $1\text{ cm} \times 1\text{ cm}$ chips developed in 2017, consisting of a printed circuit board (PCB) soldered to MMPX connectors and a machined aluminum enclosure. **b**, A device is packaged in 26-port packaging for $2\text{ cm} \times 1\text{ cm}$ chips developed in 2021, consisting of a printed circuit board (PCB) soldered to SMPM connectors and a machined copper enclosure.

airbridges are necessary. Liftoff processes are performed at the end of each layer in N-methyl-2-pyrrolidone at 160°C for at least 1.5 hr. For detailed descriptions on each fabrication step, refer to App. A. We also implement additional calibrations involving few rounds of test fabrication and imaging prior to fabrication of the junction layer for accurate fabrication of Josephson junctions, which is outlined in App. B.

3.2 Microwave packaging of quantum devices

The fabricated devices are wire-bonded to a printed circuit board (PCB) for electrical connection to external control wiring and packaged inside a metal enclosure for electromagnetic shielding and good thermalization. For high-fidelity control of multiple qubits, it is crucial for microwave packaging to have low crosstalk and to accommodate high wiring density without spurious modes [152]. Also, the packaging must be mechanically robust and thermally stable to be able to undergo multiple rounds of experiments with reconfiguration and thermal cycling. In this section, I will introduce the microwave packages used for experiments described in the thesis.

16-port packaging for $1\text{ cm} \times 1\text{ cm}$ chips

The 16-port device packaging system illustrated in Fig. 3.1a was developed by former undergraduate student Paul Dieterle in 2017 and has enabled a multitude of successful experiments in Refs. [56, 108, 109, 153].

The core of the PCB in this packaging is Arlon AD1000 (dielectric constant $\epsilon_r = 10.2$ and loss tangent $\tan \delta = 0.0023$ at 10 GHz) with the thickness of 20 mils ($508 \mu\text{m}$), 0.5 oz ($18 \mu\text{m}$) copper electrodeposited on the top surface, 2 oz ($72 \mu\text{m}$) copper electrodeposited on the bottom surface. The top and bottom copper films of the PCB are connected by a large number of copper vias of diameter 10 mil ($254 \mu\text{m}$) which are periodically arranged in a two-dimensional grid spaced by 1 mm, in order to minimize stray resonances. Planar microwave transmission lines in the form of conductor-backed coplanar waveguide (CBCPW) [154] are patterned on the PCB to interface the chip's input and output ports to end-launch surface mount MMPX connectors (Huber+Suhner 92_MMPX-S50-0-1/111_NM) with operating frequencies up to 65 GHz. The PCB is electroplated with $50 \mu\text{in}$ ($1.27 \mu\text{m}$) of wire-bondable soft gold without nickel (i.e., non-magnetic) to prevent oxidation and to improve thermal contact with the enclosure. The designed PCB was manufactured by Hughes Circuits, Inc. The MMPX connectors are soldered to the PCB by using low-temperature Sn42/Bi57.6/Ag0.4 solder paste⁵ and a heat gun.

The enclosure (commonly referred to as “box”) for the chip and the PCB is manufactured by machining either oxygen-free high-conductivity (OFHC) copper (C101) for best thermalization or aluminum alloy (6061-T651) for shielding against external magnetic field⁶. It consists of a top part (cover) and a bottom part (mount plate) joined with UNC #2-56 brass screws. The cover has a $11.4 \text{ mm} \times 11.4 \text{ mm} \times 1.5 \text{ mm}$ rectangular opening above the chip surface. The mount plate was initially designed without opening but a pocket of $8 \text{ mm} \times 8 \text{ mm} \times 3 \text{ mm}$ was milled out in later revisions to suppress cavity resonances formed by the mount plate and the ground plane of the chip due to high dielectric constant $\epsilon_r = 11.65$ of the Si substrate.

While many experiments were conducted in this packaging, there has been several issues found over time. First, there is no mechanism to tightly mount the PCB to the enclosure. This made the wirebonding of the chip to PCB challenging and is also expected to make the thermalization of PCB inefficient. Second, there were many cases when the MMPX connectors soldered to PCB “pop out” due to mechanical force unintentionally acting on the connectors when closing the lid of the box, making the assembly process very challenging. This is due to the over-constrained design of

⁵Chip Quik SMDLTLFP, melting point 138°C .

⁶Aluminum becomes a superconductor at temperatures below $\sim 1 \text{ K}$ and can repel magnetic field due to the Meissner effect.

the assembly associated with mating of connectors, PCB, and the enclosure. Finally, MMPX connectors are costly relative to other kinds of RF connectors to be used as consumables. These issues are addressed in the new packaging design which is described below.

26-port and 16-port packaging for 2 cm × 1 cm chips

In 2021, we have developed a new packaging standard illustrated in Fig. 3.1b to enable larger-scale experiments and to accommodate larger number of control lines. In particular, packaging for 2 cm × 1 cm chips was conceived to enable fabrication of longer superconducting metamaterial waveguides for constructing 10-qubit system to study quantum many-body physics.

The PCB has a large footprint of 45 mm × 45 mm to allow for up to 26 RF connectors along its perimeter. We use the same PCB core (Arlon AD1000 with 2 oz/0.5 oz electrodeposited copper) as the old packaging version and pattern similar CBCPW transmission lines to connect on-chip launchers to RF connectors. We place vias of diameter 10 mil (254 μm) as “fences” surrounding each waveguide trace and the footprint of each RF connector to suppress spurious resonances. Also, the vias are placed along the inner edges of the PCB and in a two-dimensional grid spaced by 1 mm automatically positioned according to the PCB fabrication rules. We decided to use the SMPM connector⁷, a miniature version of the well-known SMP connector considered the availability and the cost. We use full-detent through-hole connectors (Amphenol RF 925-138J-51P) soldered to the PCB rather than surface mount ones to achieve mechanically robust connections. Stub resonances caused by ~ 2 mm extruded pins of this connector are expected to lie above ~ 38 GHz which will not cause problems in the experiments. The PCB is gold-plated in a similar manner as described above. The SMPM connectors are soldered to the PCB from the bottom side by using eutectic Sn63/Pb37 solder paste⁸ and a heat gun.

The machined OFHC copper enclosure consists of the cover and the mount plate. The cover has an opening of 21.4 mm × 11.4mm × 1.6mm above the top surface of the chip. The mount plate has a 20 mm × 10 mm wide and 3 mm deep pocket to be placed under the chip to suppress the resonances above 10 GHz. Also, pedestals at the corners of the pocket provide mechanical support of the chip. The top cover and the mount plate are assembled using four UNC #2-56 brass screws.

⁷SMPM is also known as mini-SMP or Corning Gilbert GPPO, with maximum operating frequency of 65 GHz.

⁸Chip Quik SMD291AX10, melting point 183 °C

During the test of this packaging, we have observed degradation of mating between the PCB connectors and right-angled cable connectors with thermal cycling. To prevent this, we have later added another copper piece to the assembly for cable connectors to be tightly clamped to the PCB connectors, which solved the problems.

Assembly procedure

The PCB is soldered to RF connectors and then sonicated in acetone and IPA in order to remove residues of solder paste. The enclosure parts made of aluminum (copper) are cleaned with Transene Aluminum Etchant A (1.0M citric acid) followed by rinse in DI water and IPA prior to the assembly.

After cleaning, the PCB and the fabricated chip is placed on top of the mount plate and wire-bonded. In case of the new packaging, the fabricated chip is bonded to the pedestals by using GE Varnish (VGE-7031) to provide strong mechanical support prior to wire-bonding and cryogenic heatsink [155]. Also, the PCB is tightly attached to the mount plate by using four UNC #1-64 brass screws with a thin layer of Apiezon N grease [156] applied at the interface to maintain good thermal conductance at cryogenic temperatures. The box is then closed by joining the cover and the mount plate with brass screws.

The packaging assembly is then installed vertically to the sample mount machined with OFHC copper and mounted to the mixing chamber plate of the dilution refrigerator. We use non-magnetic semi-flexible coaxial cables (Micro-Coax UT-085C-FORM) to route input/output signals between the PCB connectors and the cryogenic semi-rigid coaxial cables discussed in Sec. 3.3. After this, we enclose the packaging assembly with two 1.5 mm-thick cylindrical Cryophy magnetic shields of outer diameters 70 mm and 90 mm and heights 185 mm and 200 mm, respectively. Finally, there exists a large cylindrical mu-metal shield (thickness 1 mm, inner diameter 395 mm, height 750 mm) placed inside the vacuum can of the dilution refrigerator for additional protection from external magnetic field.

3.3 Cryogenic setup

The packaged devices are cooled down to low temperatures for deposited metals to become superconductors [$T_c = 1.2\text{ K}$ (9.26 K) for Al (Nb)] and more importantly for quantum effects to appear. The devices in the thesis are characterized in Bluefors LD-250 dilution refrigerator (named “DF2”) with a base temperature of $T \lesssim 7\text{ mK}$. Proper engineering and placement of cryogenic microwave components [157–160] cannot be overlooked as thermal photons due to bad thermalization at milli-Kelvin

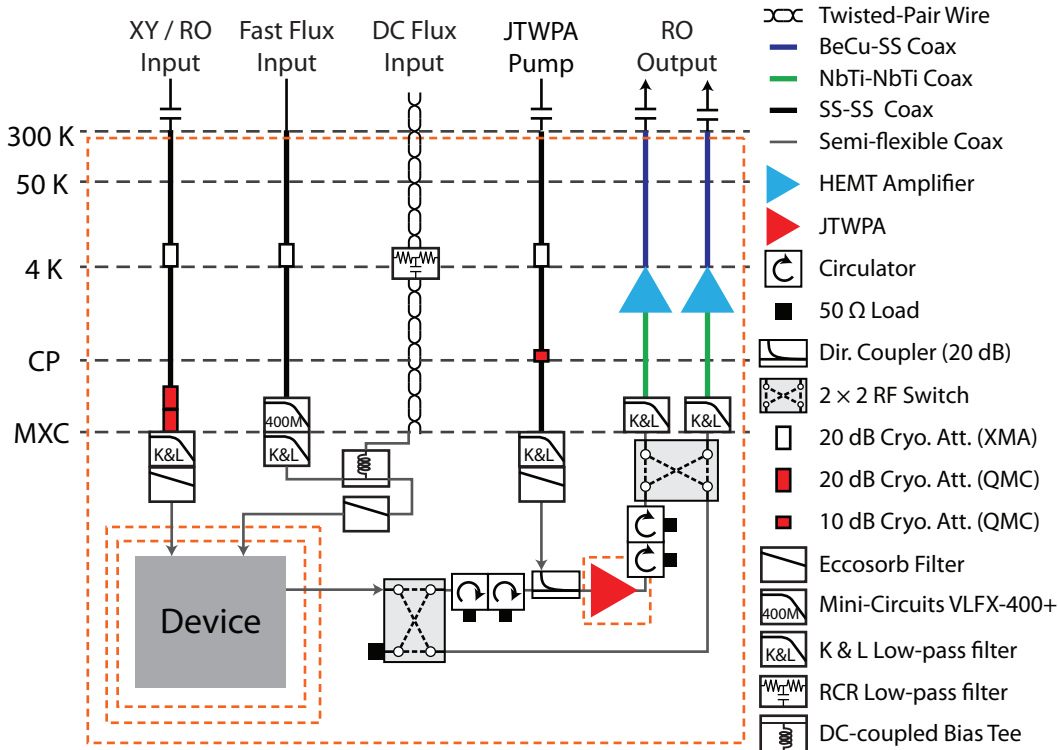


Figure 3.2: Cryogenic Setup. A typical wiring diagram of our dilution refrigerator, where the meaning of symbols are enumerated on the right. Orange dashed boxes indicate magnetic shields. The capacitor symbol represents inner/outer DC blocks for breaking ground loops.

temperatures [161, 162] can result in thermal excitation of qubits [163, 164] or dephasing associated with residual thermal photons in readout resonators [165, 166]. Here, I will provide detailed description of the cryogenic setup in DF2, illustrated in Fig. 3.2. For a general introduction to cryogenic engineering and operating principles of dilution refrigerator, I refer the readers to Refs. [167, 168].

Input lines

The input coaxial cables are thermalized at each stage of the refrigerator with a series of cryogenic attenuators⁹ to reduce the thermal noise from the room-temperature environment. To be specific, for input drive lines for XY control and readout resonators, we place 1 dB at 50 K plate, 20 dB at 4 K plate, 1 dB at still plate, 10 dB

⁹We use cryogenic attenuators 2082-6418-□□-CRYO with stainless steel (SS) enclosure from XMA Corporation at stages with temperature above 100 mK (50 K, 4 K, Still). For stages with temperature below 100 mK (CP, MXC), we try to use attenuators made with OFHC copper enclosure for best thermalization. Examples of such cold attenuators include ones from Prof. B. S. Palmer's lab [157] and QMC-CRYOATT-□□ from Quantum Microwave. Here, □□ is the value of attenuation in units of dB.

at cold plate (CP), and 30 dB at mixing chamber (MXC) plate with stages connected by semi-rigid SS-SS coaxial cables (Micro-Coax UT-085-SS-SS). Along the input coaxial lines for fast flux control, we only place 20 dB at 4 K plate and 0 dB at other stages. Each fast flux line is additionally filtered with a reflective low-pass filter with passband width of 400 MHz (Mini-Circuits VLFX-400+). in order to prevent high-frequency noise from entering the device while keeping full analog bandwidth offered by arbitrary waveform generators with sample rate of 1 GSa/s. For DC flux inputs, we use low-Ohmic twisted-pair wiring consisting of copper from room temperature to 4 K and NbTi/CuNi (superconducting) from 4K to MXC manufactured by Bluefors. The DC wiring goes through a cryogenic RCR low-pass filter¹⁰ thermalized to the 4 K plate via a copper braid. The DC and the fast flux signals are combined with a DC-coupled bias tee¹¹ anchored to the MXC plate.

Output lines

The output signal is directed through a pair of cryogenic isolators¹² thermally anchored to the MXC plate of the dilution refrigerator and is subsequently sent into an amplifier chain consisting of a high electron mobility transistor (HEMT) amplifier¹³ at the 4 K stage via a series of semi-rigid superconducting NbTi–NbTi coaxial cables (KEYCOM NbTiNbTi085A). Note that good thermalization of HEMT amplifiers by a direct contact with machined OFHC copper parts (rather than braided copper straps) is crucial to achieving the smallest added noise. After the HEMT amplifier we use semi-rigid beryllium copper (BeCu)–SS coaxial cables (Micro-Coax UT-085B-SS) to establish a low-loss connection to higher-temperature stages at the expense of a slightly higher thermal conductivity than the SS–SS ones used for the input lines.

For rapid single-shot readout of qubits, it is necessary to employ near quantum-limited parametric amplifiers such as Josephson parametric amplifier (JPA) [169] or Josephson traveling-wave parametric amplifier (JTWPA) [170, 171] at the first amplification stage before the HEMT amplifier. To that end, we install JTWPA pro-

¹⁰The RCR filter is manufactured by Aivon and consists of two series resistors (SMD 499 Ω \pm 1 %, giving total series resistance of 1 k Ω) and a shunt capacitance of 10.2 nF to the ground. This gives the cutoff frequency of $f_c \approx 33$ kHz assuming source resistance $R_S = 10$ k Ω and zero load resistance.

¹¹Mini-Circuits ZFBT-4R2GW+ is modified by replacing the series capacitor between the RF and RF+DC ports with a short.

¹²Low-Noise Factory 4–12 GHz cryogenic circulator LNF-CICIC4_12A terminated with Quantum Microwave QMC-CRYOTERM-0412.

¹³Low-Noise Factory LNF-LNC4_8C for lowest-noise amplification in typical readout frequencies 4–8 GHz or LNF-LNC0.3_14A for wideband amplification across 0.3–14 GHz.

vided by Prof. William Oliver’s group at MIT Lincoln Laboratory on the MXC plate with a cryogenic directional coupler (Quantum Microwave QMC-CRYOCOUPLER-20) and a pair of wideband dual-junction cryogenic isolators¹² for 50 Ω impedance matching at the signal, idler, and pump frequencies. While the addition of cryogenic isolators between the sample and the JTWPA results in insertion loss reducing the quantum efficiency of readout, at least 30 dB of isolation was necessary in order to prevent pump leakage and spurious JTWPA tones from reaching the device which caused unintended driving of readout resonators and ac Stark shift of qubits. In addition, well-thermalized cryogenic isolators are necessary in order to attenuate the residual room-temperature thermal photons propagating backwards from the output lines without need for attenuators. The JTWPA is enclosed inside a Cryoperm shield to prevent critical current suppression arising from external magnetic field.

Infrared filtering

Infrared (IR) radiation is known to generate excess quasiparticles in superconductors by breaking Cooper pairs [172, 173], acting as a loss mechanism in superconducting circuits. In order to prevent IR light from entering the device we take several measures in the cryogenic setup. First, we place low-pass clean-up filters (K&L Microwave 6L250-12000/T26000-OP/O) with the cutoff frequency of 12 GHz and guaranteed 50 dB rejection up to 26 GHz along all the input/output lines to reflect off any high-frequency radiation transmitted to the device via coaxial cables. For the same purpose, coaxial absorptive Eccosorb filters [174–176] were manufactured in lab or acquired from AWS Center for Quantum Computing and additionally installed along the input lines. Finally, the interior of the radiation shield for the MXC stage was painted with IR-blocking absorptive materials (a mixture of silica powder, fine carbon powder, and 1 mm silicon carbide grains in Stycast 1266 epoxy) described in Refs. [172, 177] to shield against stray IR radiation.

3.4 Room-temperature electronics and signal processing

The quantum device cooled down to cryogenic temperatures is interrogated with various electronic circuitry and instruments. In this section, we introduce the main electronic components at the room-temperature for controlling and measuring superconducting qubits.

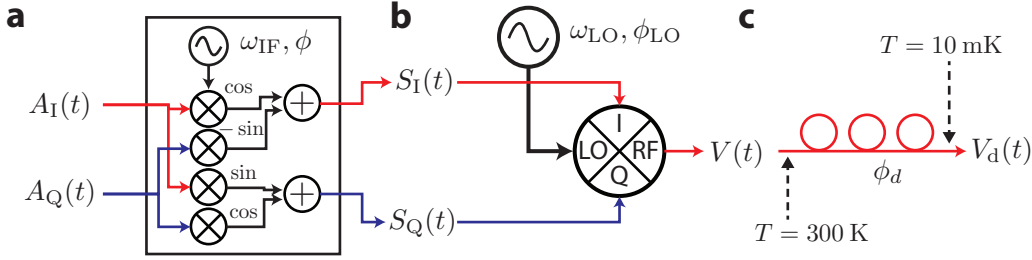


Figure 3.3: Microwave synthesis. **a**, The baseband waveforms $A_I(t)$ and $A_Q(t)$ are multiplied to phase-shifted copies of oscillating signals (\cos , $-\sin$, \sin , \cos) at intermediate frequency (IF) ω_{IF} with phase ϕ and summed, resulting in upconverted IF waveforms $S_I(t)$ and $S_Q(t)$. The IF waveforms are output from DAC channels of a controller instrument (represented as box). **b**, The IF waveforms are multiplied to a local oscillator (LO) signal with frequency ω_{LO} and phase ϕ_{LO} at a IQ mixer, resulting in RF signal $V(t)$. **c**, The RF signal $V(t)$ synthesized at room temperature propagates to the device via a series of cryogenic coaxial cables and components, acquiring a phase ϕ_d associated with the delay and response. The final voltage arriving at the device is denoted as $V_d(t)$. Throughout the figure, the signals corresponding to the real (imaginary) part of the corresponding complex phasor representation is colored red (blue).

Synthesis of microwave pulses for qubit control and readout

We synthesize microwave pulses for driving superconducting qubits and readout resonators with electronics at the room temperature and the resulting voltage signal propagates to the device inside the dilution refrigerator.

Generation of IF signals from baseband waveforms

The first stage of synthesis of microwave signals happens inside the controller instruments as illustrated in Fig. 3.3a. We specify the real-valued baseband waveforms $A_I(t)$ and $A_Q(t)$, which act as envelope functions for real-valued intermediate-frequency (IF) voltage signals $S_I(t)$ and $S_Q(t)$ that are analog outputs from the instrument. The relation between the specified baseband waveforms and the outputs from digital-to-analog converter (DAC) channels are given by

$$\begin{pmatrix} S_I(t) \\ S_Q(t) \end{pmatrix} = \begin{pmatrix} \cos(\omega_{\text{IF}}t + \phi) & -\sin(\omega_{\text{IF}}t + \phi) \\ \sin(\omega_{\text{IF}}t + \phi) & \cos(\omega_{\text{IF}}t + \phi) \end{pmatrix} \begin{pmatrix} A_I(t) \\ A_Q(t) \end{pmatrix}, \quad (3.1)$$

where ω_{IF} is the angular frequency of the IF signal and ϕ is the angle of frame rotation. An equivalent representation of Eq. (3.1) using complex variables $\mathbf{S}(t) \equiv S_I(t) + iS_Q(t)$ and $\mathbf{A}(t) \equiv A_I(t) + iA_Q(t)$ is given by

$$\mathbf{S}(t) = e^{i(\omega_{\text{IF}}t + \phi)} \mathbf{A}(t). \quad (3.2)$$

This process can be done completely in the software by uploading the computed IF waveform $S_{I/Q}(t)$ of a full sequence of pulses to arbitrary waveform generators

(AWGs). In architectures based on field-programmable gate array (FPGA), we only specify the baseband envelope $A_{I/Q}(t)$ at the pulse level and this computation is done at the hardware in real time. In our experiments, we have used Keysight M3202A PXIe AWG in the former case and Quantum Machines Operator-X (OPX) in the latter case. Both systems have the DAC sample rate of $f_s = 1$ GSa/s and has the analog bandwidth of 400 MHz.

Upconversion of signals from IF to RF

The IF signals from the DAC channels are multiplied with local oscillator (LO) signal at the IQ mixer and are upconverted into radio frequency (RF) signal as shown in Fig. 3.3b. The upconverted real-valued voltage signal $V(t)$ from the IQ mixer can be written as

$$\begin{aligned} V(t) &= S_I(t) \cos(\omega_{LO}t + \phi_{LO}) - S_Q(t) \sin(\omega_{LO}t + \phi_{LO}) \\ &= A_I(t) \cos(\omega t + \phi + \phi_{LO}) - A_Q(t) \sin(\omega t + \phi + \phi_{LO}) \end{aligned} \quad (3.3)$$

Here, $\omega = \omega_{LO} + \omega_{IF}$ is the upconverted frequency. An equivalent complex variable representation with $V(t) = \text{Re} [\mathbf{V}(t)]$ is given by

$$\mathbf{V}(t) = e^{i(\omega_{LO}t + \phi_{LO})} \mathbf{S}(t) = e^{i(\omega t + \phi + \phi_{LO})} \mathbf{A}(t). \quad (3.4)$$

In our setup, the pair of IF outputs $S_{I/Q}(t)$ from DAC channels are filtered by a low-pass filter (Mini-Circuits VLFX-400+) to reject any possible spurious signals above the Nyquist frequency ($f_s/2 = 500$ MHz) and are plugged into I/Q ports of an IQ mixer¹⁴ mounted to the microwave chassis for temperature stability. We place microwave attenuators on the I/Q ports (i) to limit the power into the IQ mixer ~ 6 dB to below the 1 dB compression point in order to avoid non-linearity and (ii) to provide good matching. We use Rohde & Schwarz SMB100A microwave signal generators to synthesize LO signals for IQ mixers. The RF output $V(t)$ from the IQ mixers are amplified by a low-noise linear amplifier (Mini-Circuits ZX60-83LN-S+) and sent into the microwave input lines of the dilution refrigerator. In practice, this upconversion process with IQ mixers generates spurious tones due to various imperfections in the mixing process, which needs to be calibrated [178]. For a general introduction to microwave mixers, refer to Refs. [179–182]. While the

¹⁴We use IQ mixers manufactured from Marki Microwave. Specifically, the legacy models IQ-0307 (3–7 GHz) and IQ-4509 (4.5–9 GHz), and more recently monolithic microwave integrated circuit (MMIC) IQ mixers MMIQ-0218LXPC (2–18 GHz) were used in the experiments described in the thesis.

analog bandwidth of each IF signal is 400 MHz, the IQ-combined single-sideband upconversion to RF allows for frequencies in the range $[-400, +400]$ MHz with respect to the LO frequency (i.e., bandwidth of 800 MHz).

Propagation to the device

The RF signal $V(t)$ synthesized at room temperature propagates to a XY drive line of qubits or a feedline of readout resonators inside the dilution refrigerator after passing through multiple coaxial cables and various microwave components such as amplifiers, attenuators, and filters as illustrated in Fig. 3.3c. The ideal net effect of propagation is frequency-dependent group delay t_d resulting in a phase shift. Then, the qubit drive voltage $V_d(t)$ can be written in the form

$$V_d(t) = V(t - t_d) = A_I(t) \cos(\omega t + \phi + \phi_d) - A_Q(t) \sin(\omega t + \phi + \phi_d).$$

where ϕ_d is the sum of phases that we don't have control over.

Equivalent complex variable representation with $V_d(t) = \text{Re}[V_d(t)]$ is given by

$$\mathbf{V}_d(t) = e^{i\phi_d} \mathbf{V}(t) = e^{i(\omega t + \phi + \phi_{LO} + \phi_d)} \mathbf{A}(t).$$

In practice, the propagation of room-temperature RF signal to the device can be affected by impedance mismatch of various microwave components inside the cryostat, adding undesirable response to the pulse. Proper engineering of cryogenic microwave components is thus necessary in order to achieve high-fidelity qubit control [183].

Example: amplitude- and phase-modulated baseband waveforms

Let us consider the most general case of baseband waveforms $A_I(t) = a(t) \cos[\theta(t)]$ and $A_Q(t) = a(t) \sin[\theta(t)]$ [complex representation $\mathbf{A}(t) = a(t)e^{i\theta(t)}$], which represents amplitude modulation with $a(t)$ and phase modulation with $\theta(t)$. The resulting IF outputs from DAC channels are given by

$$\begin{aligned} S_I(t) &= a(t) \cos[\omega_{IF}t + \phi + \theta(t)] \\ S_Q(t) &= a(t) \sin[\omega_{IF}t + \phi + \theta(t)] \end{aligned} \quad \text{or} \quad \mathbf{S}(t) = a(t)e^{i[\omega_{IF}t + \phi + \theta(t)]}.$$

After upconversion to RF, the signal becomes

$$V(t) = a(t) \cos[\omega t + \phi + \theta(t) + \phi_{LO}] \quad \text{or} \quad \mathbf{V}(t) = a(t)e^{i[\omega_{IF}t + \phi + \theta(t) + \phi_{LO}]}.$$

After propagation to the device, the drive voltage is given by

$$V_d(t) = a(t) \cos[\omega t + \varphi(t)], \tag{3.5}$$

where $\varphi(t) = \phi + \theta(t) + \phi_{LO} + \phi_d$ is the sum of all phases.

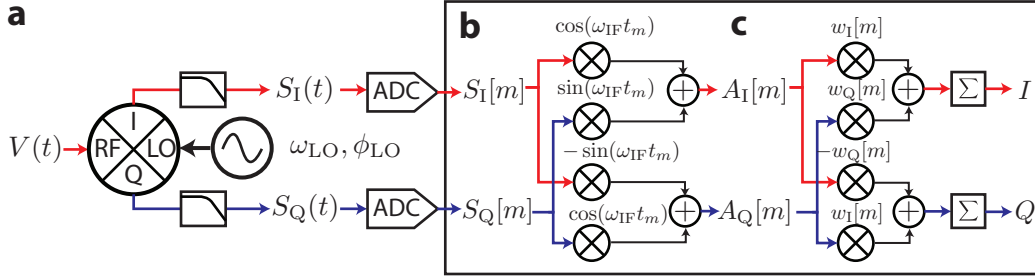


Figure 3.4: Downconversion and demodulation. **a**, The RF output signal $V(t)$ is mixed with LO signal and downconverted to a pair of IF signals $S_I(t)$ and $S_Q(t)$ at a IQ mixer. A low-pass filter is placed after the downconversion to reject spurious high-frequency components above the LO frequency. **b**, The IF signals are digitized at ADC channels and transformed into discrete-time signals $S_I[m]$ and $S_Q[m]$. The discrete-time signals are multiplied to phases-shifted copy of IF signals and summed, resulting in discrete-time baseband waveforms $A_I[m]$ and $A_Q[m]$. **c**, The baseband waveforms are summed with integration weights specified by $w_I[m]$ and $w_Q[m]$, resulting in scalars I and Q . Throughout the figure, the signals corresponding to the real (imaginary) part of the corresponding complex phasor representation is colored red (blue).

Downconversion of readout signal and state discrimination

The output readout signals from the cryostat pass through a variety of microwave components and are digitized to be further processed for qubit state discrimination. Prior to the first room-temperature amplification, it is necessary to remove the JTWPA pump leakage tone (dominant spurious tone from JTWPA) in order to avoid saturation of subsequent amplifiers and mixers. To that end, the output readout signals are passed through a room-temperature isolator¹⁵ followed by a Yttrium iron garnet (YIG)-tuned band-reject filter (Micro Lambda Wireless MLBFR-0212) whose rejection frequency set to that of the JTWPA pump. Then, we place a high-gain room-temperature amplifier¹⁶ and a tunable microwave attenuator (Vaunix LabBrick LDA-133) to adjust the power to sufficiently below 1 dB compression points of subsequent microwave components while utilizing the full dynamic range.

Downconversion of signals from RF to IF

The RF output $V(t) = b(t) \cos[\omega t + \varphi(t)]$ is multiplied to two copies of the LO signal with relative phase of 90° at the IQ mixer and downconverted into IF signal as shown in Fig. 3.4a. The downconverted real-valued voltage signals $S_{I/Q}(t)$ at I/Q

¹⁵Fairview Microwave dual-junction circulator FMCR1019 terminated with Mini-Circuits ANNE-50L+ matched loads.

¹⁶Narda-MITEQ AFS42-00101200-22-10P-42

ports of an IQ mixer are given by

$$\begin{aligned}
S_I(t) &\propto V(t) \cos(\omega_{LO}t) \\
&= \frac{b(t)}{2} \{ \cos[(2\omega_{LO} + \omega_{IF})t + \varphi(t)] + \cos[\omega_{IF}t + \varphi(t)] \}, \\
S_Q(t) &\propto -V(t) \sin(\omega_{LO}t) \\
&= \frac{b(t)}{2} \{ -\sin[(2\omega_{LO} + \omega_{IF})t + \varphi(t)] + \sin[\omega_{IF}t + \varphi(t)] \}.
\end{aligned}$$

After low-pass filtering (Mini-Circuits VLFX-400+), the fast-oscillating terms at frequency $2\omega_{LO} + \omega_{IF}$ are discarded, and the resulting IF signals at I and Q ports are written as

$$\begin{aligned}
S_I(t) &= b(t) \cos[\omega_{IF}t + \varphi(t)] \\
S_Q(t) &= b(t) \sin[\omega_{IF}t + \varphi(t)]
\end{aligned}
\quad \text{or} \quad
\mathbf{S}(t) = b(t)e^{i[\omega_{IF}t + \varphi(t)]}, \quad (3.6)$$

where $\mathbf{S}(t) = S_I(t) + iS_Q(t)$ is the complex representation of IF signals.

Digitization and Demodulation of IF signals

The downconverted IF waveforms $S_{I/Q}(t)$ are rescaled with attenuators and IF amplifiers (Mini-Circuits ZFL-500LNB+) to fit in the range of analog-to-digital converter (ADC) channels. In the experiments described in the thesis, we use ADC channels of AlazarTech ATS9870 PCIe digitizer or Quantum Machines OPX with the sample rate of 1 GSa/s for digitization of IF waveforms. In order to avoid aliasing, we additionally place a low-pass filter (Mini-Circuits VLFX-400+) to reject spurious signals above the Nyquist frequency of the ADC channels.

Upon digitization, the IF signals are converted to discrete-time signals $S_{I/Q}(t_m) \rightarrow S_{I/Q}[m]$ sampled at times $t = t_m$ ($m = 0, 1, 2, \dots, N - 1$). Each discrete-time sample recorded to ADC channels is multiplied to cosine and sine functions as

$$\begin{pmatrix} A_I[m] \\ A_Q[m] \end{pmatrix} = \begin{pmatrix} \cos(\omega_{IF}t_m) & \sin(\omega_{IF}t_m) \\ -\sin(\omega_{IF}t_m) & \cos(\omega_{IF}t_m) \end{pmatrix} \begin{pmatrix} S_I[m] \\ S_Q[m] \end{pmatrix}, \quad (3.7)$$

and downconverted to the baseband discrete-time samples $A_{I/Q}[m]$ (Fig. 3.4b), which are summed with integration weights $w_{I/Q}[m]$ to reduce to scalars (Fig. 3.4c)

$$\begin{pmatrix} I \\ Q \end{pmatrix} = \sum_{m=0}^{N-1} \begin{pmatrix} w_I[m] & w_Q[m] \\ -w_Q[m] & w_I[m] \end{pmatrix} \begin{pmatrix} A_I[m] \\ A_Q[m] \end{pmatrix}. \quad (3.8)$$

Using the complex notation for the baseband waveforms $\mathbf{A}[m] \equiv A_I[m] + iA_Q[m]$, the integration weights $\mathbf{w}[m] \equiv w_I[m] + iw_Q[m]$, and the demodulated scalar

variables $\mathbf{Z} \equiv I + iQ$, equations (3.7)-(3.8) can be simplified into

$$\mathbf{Z} = \sum_{m=0}^{N-1} \mathbf{w}^*[m]A[m] = \sum_{m=0}^{N-1} e^{-i\omega_{\text{IF}}t_m} \mathbf{w}^*[m]S[m]. \quad (3.9)$$

Given the IF signals in Eq. (3.6), the demodulated IQ variables are given by

$$I = \sum_{m=0}^{N-1} b(t_m) \{w_I[m] \cos \varphi(t_m) + w_Q[m] \sin \varphi(t_m)\}, \quad (3.10a)$$

$$Q = \sum_{m=0}^{N-1} b(t_m) \{-w_Q[m] \cos \varphi(t_m) + w_I[m] \sin \varphi(t_m)\}, \quad (3.10b)$$

or equivalently,

$$\mathbf{Z} = \sum_{m=0}^{N-1} \mathbf{w}^*[m]b(t_m)e^{i\varphi(t_m)}. \quad (3.10c)$$

In the simplest case of readout with uniform integration weights ($w_I[m], w_Q[m] = (\cos \phi_0, \sin \phi_0)$), we obtain

$$I = \sum_{m=0}^{N-1} b(t_m) \cos [\varphi(t_m) - \phi_0], \quad Q = \sum_{m=0}^{N-1} b(t_m) \sin [\varphi(t_m) - \phi_0], \quad (3.11a)$$

or equivalently,

$$\mathbf{Z} = \sum_{m=0}^{N-1} b(t_m)e^{i[\varphi(t_m) - \phi_0]}. \quad (3.11b)$$

If the readout duration is long enough compared to the ringdown time $1/\kappa$ of the readout resonator, the readout resonator stays in the steady state most of the time during the on-time of the readout pulse, giving near-constant readout signal with magnitude $b_{\text{ss}} \approx b(t_m)$ and phase $\varphi_{\text{ss}} \approx \varphi(t_m)$. This further simplifies Eq. (3.11a)-(3.11b) into

$$I \approx Nb_{\text{ss}} \cos (\phi_{\text{ss}} - \phi_0), \quad Q \approx Nb_{\text{ss}} \sin (\phi_{\text{ss}} - \phi_0). \quad (3.12a)$$

or equivalently,

$$\mathbf{Z} \approx Nb_{\text{ss}}e^{i(\phi_{\text{ss}} - \phi_0)}. \quad (3.12b)$$

Qubit state discrimination

An ensemble of demodulated readout signals $\{\mathbf{Z}_{|i\rangle}\}$ corresponding to each qubit state $|i\rangle$ ($i = g, e, f, \dots$) form a blob of points in the IQ -plane following a Gaussian distribution centered at $\boldsymbol{\mu}_{|i\rangle}$ and standard deviation $\sigma_{|i\rangle}$ in the ideal case. It is common to perform qubit state discrimination by drawing boundaries on the IQ

plane and classifying according to the region each point fall into. Misclassified points count towards readout infidelity and the boundaries for state discrimination should be chosen to minimize the infidelity.

In the simplest case, a line passing through the midpoint of means $\bar{\mathbf{Z}}_{|i\rangle}$ and $\bar{\mathbf{Z}}_{|j\rangle}$ that is perpendicular to the difference vector $\bar{\mathbf{Z}}_{|i\rangle} - \bar{\mathbf{Z}}_{|j\rangle}$ for classification between states $|i\rangle$ and $|j\rangle$. Another well-known method to find the classification boundary is to fit the histogram with a multi-mode Gaussian distribution [184, 185]. This assumes that the ensemble of readout signals with preparation of each qubit state follows a superposition of multiple Gaussian distributions corresponding to qubit states to take into account the non-ideal effects during state preparation and measurement. Machine learning-based classification methods [186] are also being widely used due to the high-performance and simplicity. We use linear discriminant analysis (LDA) trained with the collection of readout signals and corresponding state preparation labels, linear map This only requires allows for real-time state discrimination in Quantum Machines OPX.

WAVEGUIDE-MEDIATED COOPERATIVE INTERACTIONS OF SUPERCONDUCTING QUBITS

The simplest scheme to engineer interactions between qubits using a waveguide is to utilize modes inside the transmission band. In Sec. 2.2, it was shown that strong coherent interaction between two quantum emitters are intrinsically forbidden due to the fact that the maximum waveguide-mediated exchange interaction rate cannot exceed the rate of decay of emitters. A novel approach to circumvent this problem was proposed in Ref. [120], by creating a cavity-like configuration of emitters where subradiant states can coherently interact with another precisely positioned emitter without significant decay to the waveguide. In this chapter, I will introduce our experimental work on this topic, which is published in Ref. [108].

4.1 Introduction

It has long been recognized that atomic emission of radiation is not an immutable property of an atom, but is instead dependent on the electromagnetic environment [187], and in the case of ensembles, also on the collective interactions between the atoms [42, 43, 111, 112, 188]. In an open radiative environment, the hallmark of collective interactions is enhanced spontaneous emission—super-radiance [42]—with non-dissipative dynamics largely obscured by rapid atomic decay [189]. Here, we observe the dynamical exchange of excitations between a single artificial atom and an entangled collective state of an atomic array [120] through the precise positioning of artificial atoms realized as superconducting qubits [190] along a one-dimensional waveguide. This collective state is dark, trapping radiation and creating a cavity-like system with artificial atoms acting as resonant mirrors in the otherwise open waveguide. The emergent atom-cavity system is shown to achieve a large interaction-to-dissipation ratio (cooperativity exceeding 100), reaching the regime of strong coupling, in which coherent interactions dominate dissipative and decoherence effects. Achieving strong coupling with interacting qubits in an open waveguide provides a means of synthesizing multi-photon dark states with high efficiency and paves the way for exploiting correlated dissipation and decoherence-free subspaces of quantum emitter arrays at the many-body level [191–194].

The collective interaction of atoms in the presence of a radiation field has been

studied since the early days of quantum physics. As first studied by Dicke [42], the interaction of resonant atoms in such systems results in the formation of super- and sub-radiant states in the spontaneous emission. While Dicke’s central insight—that atoms interact coherently even through an open environment—was used to understand the radiation properties of an idealized, point-like atomic gas, the dynamical properties of ordered, distant atoms coupled to open environments also exhibit novel physics. In their most essential form, such systems can be studied within the canonical waveguide quantum electrodynamics (QED) model [40]: atoms coupled to a one-dimensional (1D) continuum realized by an optical fiber or a microwave waveguide [132, 195]. Within this model, a diverse and rich set of phenomena await experimental study. For instance, one can synthesize an artificial cavity QED system [120], distill exotic many-excitation dark states with fermionic spatial correlations [191], and use classical light sources to generate entangled and quantum many-body states of light [192–194].

4.2 Strong-coupling regime of waveguide QED: cavity QED with atom-like mirrors

A central technical hurdle common to these research avenues—reaching the so-called *strong coupling regime*, in which atom-atom interactions dominate decay—is experimentally difficult, especially in waveguide QED, because while the waveguide facilitates infinite-range interactions between the atoms [196, 197], it also provides a dissipative channel [198]. Decoherence through this and other sources destroys the fragile many-body states of the system, which has limited the experimental state-of-the-art to spectroscopic probes of waveguide-mediated interactions [142, 147, 199]. However, by utilizing collective dark states, where the precise positioning of atoms protects them from substantial waveguide-emission decoherence, the strong coupling limit is predicted to be within reach [120]. Additionally, if the timescale of single-atom emission into the waveguide is long enough to permit measurement and manipulation of the system, the coherent dynamics can be driven and probed at the single-atom level. Here, we overcome these hurdles with a waveguide QED system consisting of transmon qubits coupled to a common microwave waveguide, strengthening opportunities for a range of waveguide QED physics.

As a demonstration of this tool, we construct such an emergent cavity QED system and probe its linear and non-linear dynamics. The system features an ancillary probe qubit and a cavity-like mode formed by the dark state of two single-qubit mirrors. Using waveguide transmission and individual addressing of the probe qubit,

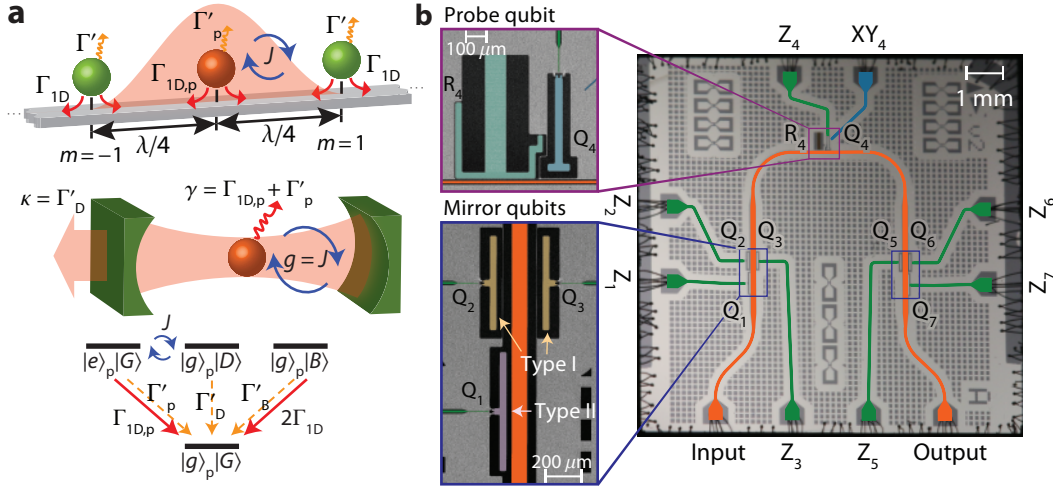


Figure 4.1: Waveguide-QED setup. **a**, The top schematic shows the cavity configuration of waveguide QED system consisting of an array of N mirror qubits ($N = 2$ shown; green) coupled to the waveguide with an inter-qubit separation of $\lambda_0/2$, with a probe qubit (red) at the center of the mirror array. The middle schematic shows the analogous cavity QED system with correspondence to waveguide parameters. The bottom panel shows the energy-level diagram of the system of three qubits (two mirror, one probe). The mirror dark state $|D\rangle$ is coupled to the excited state of the probe qubit $|e\rangle_p$ at a cooperatively enhanced rate of $2J = \sqrt{2\Gamma_{1D}\Gamma_{1D,p}}$. The bright state $|B\rangle$ is decoupled from the probe qubit. **b**, Optical image of the fabricated waveguide QED circuit. Tunable transmon qubits interact via microwave photons in a superconducting CPW (false-color orange trace). The CPW is used for externally exciting the system and is terminated in a $50\text{-}\Omega$ load. The insets show scanning electron microscope images of the different qubit designs used in our experiment. The probe qubit, designed to have $\Gamma_{1D,p}/2\pi = 1$ MHz, is accessible via a separate CPW (XY_4 ; false-color blue trace) for state preparation, and is also coupled to a compact microwave resonator (R_4 ; false-color cyan) for dispersive readout. The mirror qubits come in two types: type I, with $\Gamma_{1D}/2\pi = 20$ MHz and type II, with $\Gamma_{1D}/2\pi = 100$ MHz. The figure is adapted from Ref. [108].

we observe spectroscopic and time-domain signatures of the collective dynamics of the qubit array, including vacuum Rabi oscillations between the probe qubit and the cavity-like mode. These oscillations provide direct evidence of strong coupling between these modes as well as a natural method of efficiently creating and measuring dark states that are inaccessible through the waveguide. Unlike traditional cavity QED, our cavity-like mode is itself quantum nonlinear, as we show by characterizing the two-excitation dynamics of the array.

The collective evolution of an array of resonant qubits coupled to a 1D waveguide can be formally described by a master equation [116, 120] of the form

$$\dot{\hat{\rho}} = -\frac{i}{\hbar}[\hat{H}_{\text{eff}}, \hat{\rho}] + \sum_{m,n} \Gamma_{m,n} \hat{\sigma}_{ge}^m \hat{\rho} \hat{\sigma}_{eg}^n, \quad (4.1)$$

where $\hat{\sigma}_{ge}^m = |g_m\rangle\langle e_m|$, $|g\rangle$ and $\langle e|$ are a qubit's ground and excited states, respectively, and m and n represent the indices of the qubit array. Within the Born-Markov approximation, the effective Hamiltonian can be written in the interaction picture as

$$\hat{H}_{\text{eff}} = \hbar \sum_{m,n} \left(J_{m,n} - i \frac{\Gamma_{m,n}}{2} \right) \hat{\sigma}_{eg}^m \hat{\sigma}_{ge}^n, \quad (4.2)$$

where $\hbar = h/2\pi$ is the reduced Planck constant. Figure 4.1a depicts the waveguide QED system considered in this work. The system consists of an array of N qubits separated by distance $d = \lambda_0/2$ and a separate probe qubit centered in the middle of the array with one-dimensional waveguide decay rate $\Gamma_{1D,p}$, and where $\lambda_0 = c/f_0$ is the wavelength of the field in the waveguide at the transition frequency of the qubits f_0 . In this configuration, the effective Hamiltonian can be simplified in the single-excitation manifold to

$$\hat{H}_{\text{eff}} = -\frac{iN\hbar\Gamma_{1D}}{2} \hat{S}_B^\dagger \hat{S}_B - \frac{i\hbar\Gamma_{1D,p}}{2} \hat{\sigma}_{ee}^{(p)} + \hbar J \left(\hat{\sigma}_{ge}^{(p)} \hat{S}_D^\dagger + \text{H.c.} \right), \quad (4.3)$$

where $\hat{S}_B, \hat{S}_D = 1/\sqrt{N} \sum_{m>0} (\hat{\sigma}_{ge}^m \mp \hat{\sigma}_{ge}^{-m}) (-1)^m$ are the lowering operators of the bright collective state $|B\rangle$ and the fully-symmetric dark collective state $|D\rangle$ of the qubit array, as shown in Fig. 4.1a, and where $m > 0$ and $m < 0$ denote qubits to the right and left of the probe qubit, respectively. As shown by the last term in the Hamiltonian, the probe qubit is coupled to this dark state at a cooperatively enhanced rate $2J = \sqrt{N} \sqrt{\Gamma_{1D} \Gamma_{1D,p}}$. (H.c. is the Hermitian conjugate.) The bright state super-radiantly emits into the waveguide at a rate of $N\Gamma_{1D}$. The collective dark state has no coupling to the waveguide, and a decoherence rate Γ'_D which is set by parasitic damping and dephasing not captured in the simple waveguide QED model (see Sec. C.2 and Sec. C.3). In addition to the bright and dark collective states described above, there exist an additional $N - 2$ collective states of the qubit array with no coupling to either the probe qubit or the waveguide [120].

The subsystem consisting of a coupled probe qubit and symmetric dark state of the mirror qubit array can be described as an analog to a cavity QED system [120]. In this depiction, the probe qubit plays the role of a two-level atom and the dark state mimics a high-finesse cavity, with the qubits in the $\lambda_0/2$ -spaced array acting as atomic mirrors (see Fig. 4.1a). In general, provided that the fraction of excited array qubits remains small as N increases, \hat{S}_D stays nearly bosonic and the analogy to the Jaynes-Cummings model remains valid. By mapping the waveguide parameters to those of a cavity QED system, the cooperativity between probe qubit and atomic cavity can be written as $C = (2J)^2 / (\Gamma_{1D,p} + \Gamma'_D) \Gamma'_D \approx NP_{1D}$. Here $P_{1D} = \Gamma_{1D} / \Gamma'_D$ is

the single qubit Purcell factor, which quantifies the ratio of the waveguide emission rate to the parasitic damping and dephasing rates. Attaining $C > 1$ is a prerequisite for observing coherent quantum effects. Referring to the energy level diagram of Fig. 4.1a, by sufficiently reducing the waveguide coupling rate of the probe qubit one can also realize a situation in which $J > (\Gamma_{1D,p} + \Gamma'_p), \Gamma'_D$, corresponding to the strong coupling regime of cavity QED between excited state of the probe qubit ($|e\rangle_p|G\rangle$) and a single photon in the atomic cavity ($|g\rangle_p|D\rangle$) (see Sec. C.2). This mapping of a waveguide QED system onto a cavity QED analog therefore allows us to use cavity QED techniques to efficiently probe the dark states of the qubit array with single-photon precision.

The fabricated superconducting circuit used to realize the waveguide-QED system is shown in Fig. 4.1b. The circuit consists of seven transmon qubits (Q_j , where $j = 1-7$), all of which are side-coupled to the same coplanar waveguide (CPW). Each qubit's transition frequency is tunable via an external flux bias port (Z_1-Z_7). We use the top-center qubit in the circuit (Q_4) as a probe qubit. This qubit can be independently excited via a weakly coupled CPW drive line (XY_4), and is coupled to a lumped-element microwave cavity (R_4) for dispersive readout of its state. The other six qubits are mirror qubits. The mirror qubits come in two different types (I and II), which are designed with different waveguide coupling rates ($\Gamma_{1D,I}/2\pi = 20$ MHz and $\Gamma_{1D,II}/2\pi = 100$ MHz) in order to provide access to a range of Purcell factors. Type I mirror qubits also lie in pairs across the CPW waveguide and have rather large (~ 50 MHz) direct coupling.

4.3 Spectroscopic characterizations

We characterize the waveguide and parasitic coupling rates of each individual qubit by measuring the phase and amplitude of microwave transmission through the waveguide (see Fig. 4.2) [146]. Measurements are performed in a dilution refrigerator at a base temperature of 8 mK (see Sec. 4.7). For a sufficiently weak coherent drive the effects of qubit saturation can be neglected and the on-resonance extinction of the coherent waveguide tone relates to a lower bound on the individual qubit Purcell factor. Any residual waveguide thermal photons, however, can result in weak saturation of the qubit and a reduction of the on-resonance extinction. We find an on-resonance intensity transmittance as low as 2×10^{-5} for the type II mirror qubits, corresponding to an upper bound on the CPW mode temperature of 43 mK and a lower bound on the Purcell factor of 200. Further details of the design and measured parameters of probe and each mirror qubit are provided in Sec. 4.7.

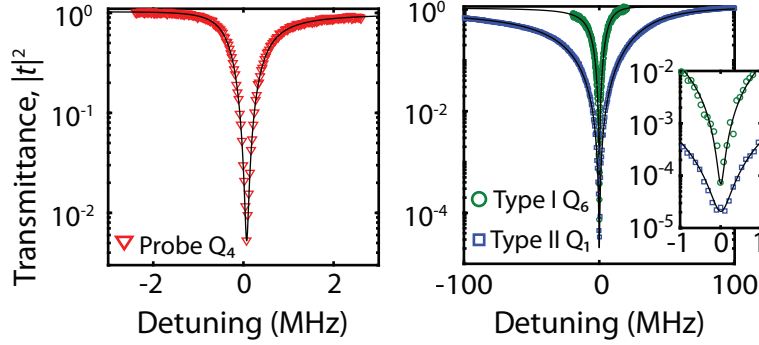


Figure 4.2: Single-qubit spectroscopy. Waveguide transmission spectrum across individual qubit resonances. The left panel shows the probe qubit (Q_4); the right panel shows type I (Q_6 , green curve) and type II (Q_1 , blue curve) mirror qubits). The inset shows a zoomed-in view of the center of the curves with the same axes. From a Lorentzian lineshape fit of the measured waveguide transmission spectra we infer Purcell factors of $P_{1D} = 11$ for the probe qubit and $P_{1D} = 98$ (219) for the type I (type II) mirror qubit. The figure is adapted from Ref. [108].

The transmission through the waveguide, in the presence of the probe qubit, can also be used to measure spectroscopic signatures of the collective dark state of the qubit array. As an example of this we utilize a single pair of type I mirror qubits (Q_2 and Q_6), which we tune to a frequency where their separation along the waveguide axis is $d = \lambda_0/2$. The remaining qubits on the CPW are decoupled from the waveguide input by tuning their frequency away from the measurement point. Figure 4.3a shows the waveguide transmission spectrum for a weak coherent tone in which a broad resonance dip is evident, corresponding to the bright state of the mirror qubit pair. We find a bright-state waveguide coupling rate of $\Gamma_{1D,B} \approx 2\Gamma_{1D} = 2\pi \times 26.8$ MHz by fitting a Lorentzian lineshape to the spectrum. The dark state of the mirror qubits is not observable in this waveguide spectrum, but it becomes observable when measuring the waveguide transmission with the probe qubit tuned into resonance with the mirror qubits (see Fig. 4.3b). In addition to the broad response from the bright state, in this case two spectral peaks appear near the center of the bright-state resonance (Fig. 4.3c). This pair of highly non-Lorentzian spectral features result from the Fano interference between the broad bright state and the hybridized polariton resonances formed between the dark state of the mirror qubits (the atomic cavity photon) and the probe qubit. The hybridized probe qubit and the atomic cavity eigenstates can be more clearly observed by measuring the transmission between the probe qubit drive line (XY_4) and the output port of the waveguide (see Fig. 4.3d). As the XY_4 line does not couple to the bright state owing to the symmetry of its positioning along the waveguide, we observe two well-resolved

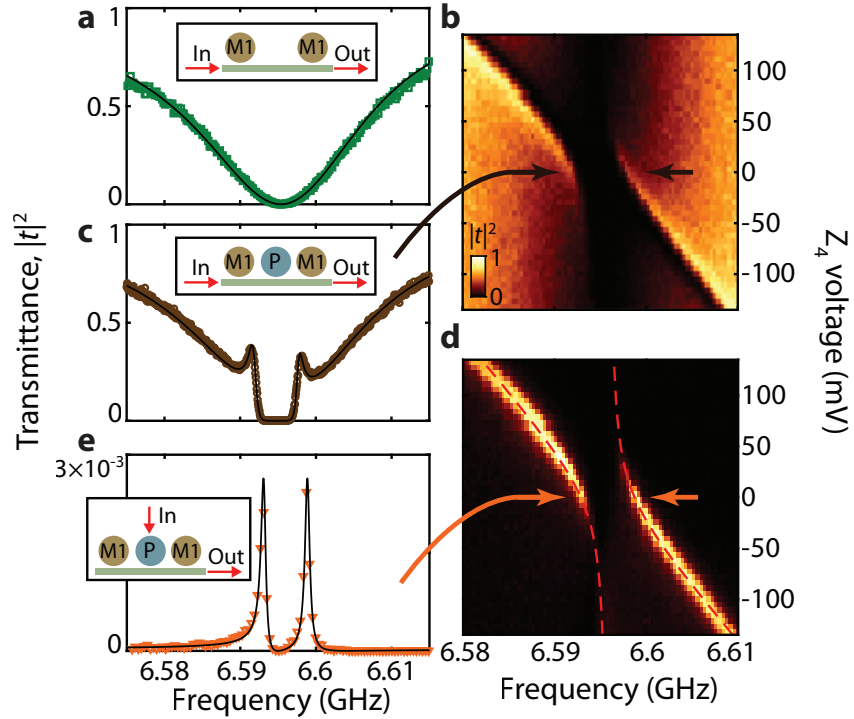


Figure 4.3: Vacuum Rabi splitting. **a**, Transmission through the waveguide for two type I mirror qubits (M1; Q_2 and Q_6) on resonance, with the remaining qubits on the chip tuned away from the measurement frequency range. **b**, Transmission through the waveguide as a function of the flux bias tuning voltage of the probe qubit (Q_4). **c**, Waveguide transmission spectrum for the probe qubit (P; Q_4) and the mirror qubits tuned to resonance. **d**, Transmission spectrum as measured between the probe qubit drive line XY_4 and the waveguide output as a function of flux bias tuning of the probe qubit. **e**, XY_4 -to-waveguide transmission spectrum for the three qubits tuned to resonance. The dashed red lines in **d** and solid black line in **e** are the predictions of a numerical model with experimentally measured qubit parameters. The prediction in **e** includes slight power broadening effects. The figure is adapted from Ref. [108].

resonances (Fig. 4.3e) with mode splitting $2J/2\pi \approx 6$ MHz, when the probe qubit is nearly resonant with the dark state. Observation of vacuum Rabi splitting in the hybridized atomic cavity-probe qubit polariton spectrum signifies operation in the strong coupling regime.

4.4 Time-domain characterizations

To further investigate the signatures of strong coupling we perform time-domain measurements in which we prepare the system in the initial state $|g\rangle_p|G\rangle \rightarrow |e\rangle_p|G\rangle$ using a 10-ns microwave π pulse applied at the XY_4 drive line. Following excitation of the probe qubit we use a fast (5 ns) flux bias pulse to tune the probe qubit into

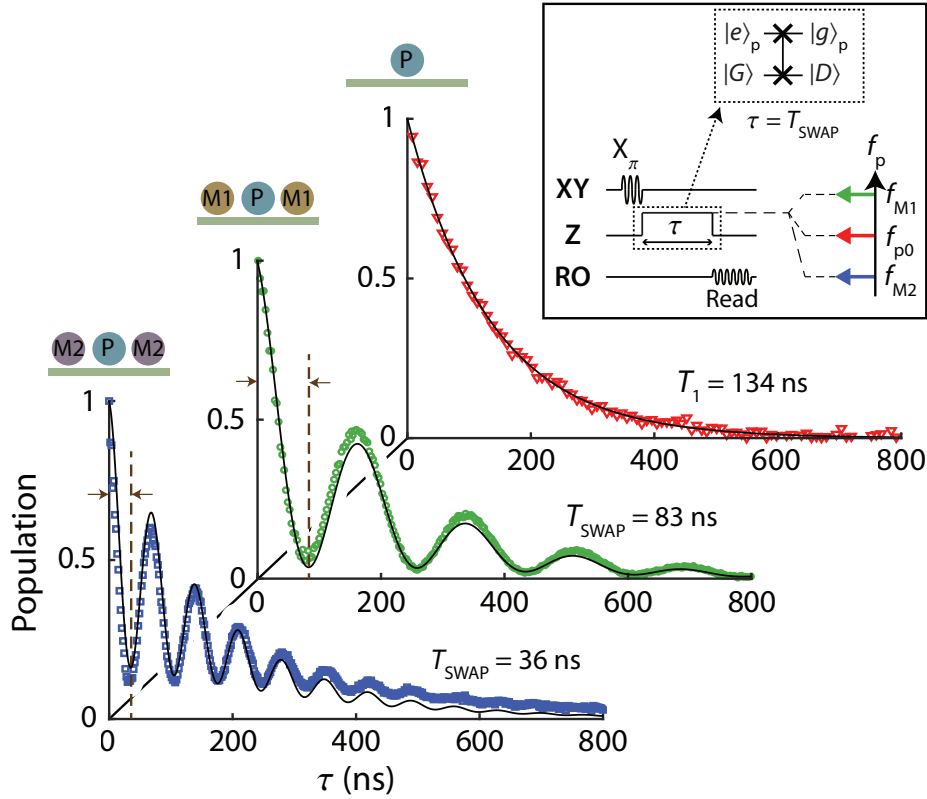


Figure 4.4: Vacuum Rabi oscillations. Measured population of the excited state of the probe qubit for three different scenarios. The top, red curve represents the probe qubit (P) tuned to $f_{p0} = 6.55$ GHz, with all mirror qubits tuned away, corresponding to free population decay. The middle, green curve represents the probe qubit tuned into resonance with a pair of type I mirror qubits (M1; Q₂ and Q₆) at frequency $f_{M1} = 6.6$ GHz corresponding to $d_I = \lambda_0/2$. The bottom, blue curve represents the probe qubit tuned into resonance with type II mirror qubits (M2; Q₁ and Q₇) at frequency $f_{M2} = 5.826$ GHz corresponding to population decay time and half the oscillation time period for the spontaneous decay curve and the vacuum Rabi oscillations, respectively. The figure is adapted from Ref. [108].

resonance with the collective dark state of the mirror qubits (the atomic cavity) for a desired interaction time τ . Upon returning to its initial frequency after the flux bias pulse, the excited-state population of the probe qubit is measured via the dispersively coupled readout resonator. In Fig. 4.4, we show a timing diagram and plot three measured curves of the probe qubit's population dynamics versus τ . The top red curve corresponds to the measured probe qubit's free decay, where the probe qubit is shifted to a detuned frequency f_{p0} to eliminate mirror qubit interactions. From an exponential fit to the decay curve we find a decay rate of $1/T_1 \approx 2\pi \times 1.19$ MHz, in agreement with the result from waveguide spectroscopy at f_{p0} . In the middle green and bottom blue curves we plot the measured probe qubit's population dynamics while interacting with an atomic cavity formed from

type I and type II mirror qubit pairs, respectively. In both cases the initially prepared state $|e\rangle_p|G\rangle$ undergoes vacuum Rabi oscillations with the dark state of the mirror qubits $|g\rangle_p|D\rangle$. Along with the measured data we plot a theoretical model where the waveguide coupling, parasitic damping, and dephasing rate parameters of the probe qubit and dark state are taken from independent measurements, and the detuning between probe qubit and dark state is left as a free parameter (see Sec. C.2). From the excellent agreement between measurement and model we infer an interaction rate of $2J/2\pi = 5.64$ MHz (13.0 MHz) and a cooperativity of $C = 94$ (172) for the type I (type II) mirror system. For both mirror types we find that the system is well within the strong coupling regime $J \gg \Gamma_{1D,p} + \Gamma'_p, \Gamma'_D$, with the photon-mediated interactions dominating the decay and dephasing rates by roughly two orders of magnitude.

The tunable interaction time in our measurement sequence also permits state transfer between the probe qubit and the dark state of the mirror qubits using an iSWAP gate. We measure the dark state's population decay in a protocol where we excite the probe qubit and transfer the excitation into the dark state (see Fig. 4.5a). From an exponential fit to the data we find a dark-state decay rate of $T_{1,D} = 757$ ns (274 ns) for type I (type II) mirror qubits, enhanced by approximately the cooperativity over the bright-state lifetime. In addition to the lifetime, we can measure the coherence time of the dark state with a Ramsey-like sequence (see Fig. 4.5b), yielding $T_{2,D}^* = 435$ ns (191 ns) for type I (type II) mirror qubits. The collective dark-state coherence time is slightly shorter than its population decay time, hinting at correlated sources of noise in the distantly entangled qubits forming the dark state (see discussion in Sec. C.3).

These experiments have so far probed the waveguide and the multi-qubit array with a single excitation, where the cavity QED analog is helpful for understanding the response. However, this analogy is not fully accurate for understanding multi-excitation dynamics, where the quantum nonlinear response of the qubits leads to a number of interesting phenomena. To observe this, we populate the atomic cavity with a single photon via an iSWAP gate and then measure the transmission of weak coherent pulses through the waveguide. Figure 4.5c shows transmission through the atomic cavity formed from type I mirror qubits before and after adding a single photon. The sharp change in the transmissivity of the atomic cavity is a result of trapping in the long-lived dark state of the mirror qubits. The dark state has no transition dipole to the waveguide channel (see Fig. 4.5d), and thus it cannot participate in absorption or emission of photons when probed via the

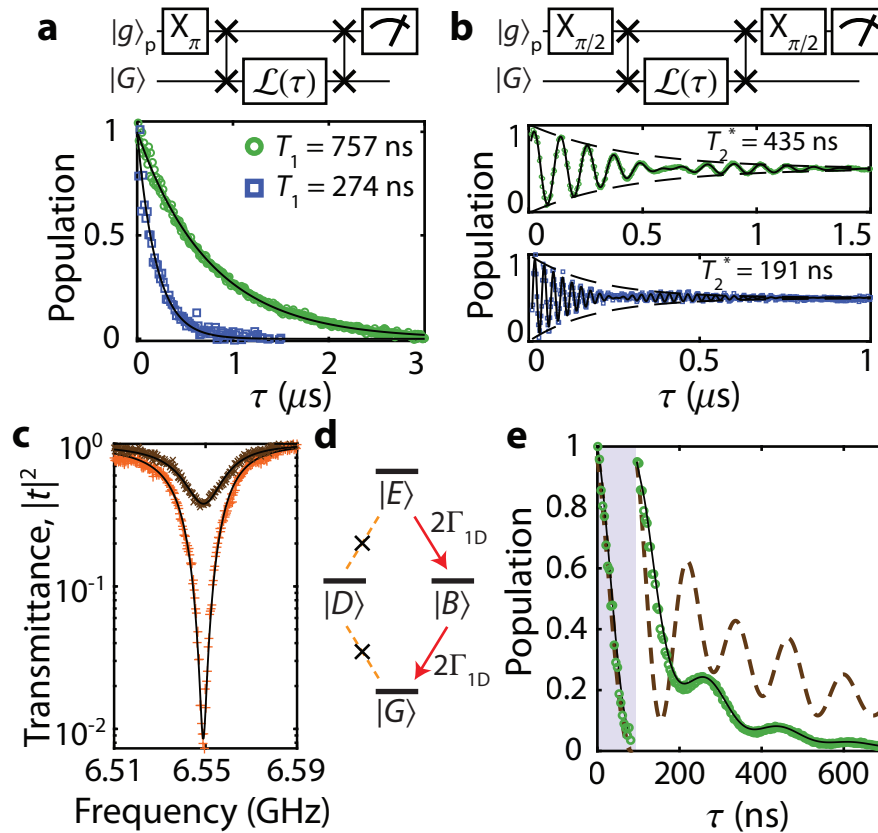


Figure 4.5: Characterization of the dark-state cavity **a**, Measurement of the population decay time ($T_{1,D}$) of the dark state of the type I (top, green) and type II (bottom, blue) mirror qubits. **b**, Corresponding Ramsey coherence time ($T_{2,D}^*$) of the type I (top, green) and type II (bottom, blue) dark states. **c**, Waveguide transmission spectrum through the atomic cavity without (brown data points) and with (orange data points) pre-population of the cavity. Here the atomic cavity is initialized in a single photon state by performing an iSWAP gate acting on the probe qubit followed by detuning of the probe qubit away from resonance. In both cases the transmission measurement is performed using coherent rectangular pulses with a duration of 260 ns and a peak power of $P \approx 0.03(\hbar\omega_0\Gamma_{1D})$. Solid lines show theory fits from numerical modeling of the system. **d**, Energy level diagram of the 0 ($|G\rangle$), 1 ($|D\rangle, |B\rangle$), and 2 ($|E\rangle$) excitation manifolds of the atomic cavity indicating waveguide-induced decay and excitation pathways. **e**, Rabi oscillation with two excitations in the system of the probe qubit and atomic cavity. The shaded region shows the first iSWAP step in which an initial probe qubit excitation is transferred to the atomic cavity. Populating the probe qubit with an additional excitation at this point results in strong damping of subsequent Rabi oscillations due to the rapid decay of state $|E\rangle$. The dashed brown curve is the predicted result for interaction of the probe qubit with an equivalent linear cavity. In (c)-(e) the atomic cavity is formed from type I mirror qubits Q_2 and Q_6 . The figure is adapted from Ref. [108].

waveguide. As a result, populating the atomic cavity with a single photon makes it nearly transparent to incoming waveguide signals for the duration of the dark-state lifetime. This is analogous to the electron shelving phenomenon, which leads to suppression of resonance fluorescence in three-level atomic systems [200]. As a further example, we use the probe qubit to prepare the cavity in the doubly excited state via two consecutive iSWAP gates. In this case, with only two mirror qubits and the rapid decay via the bright state of the two-excitation state $|E\rangle$ of the mirror qubits (refer to Fig. 4.5d), the resulting probe qubit population dynamics shown in Fig. 4.5e have a strongly damped response ($C < 1$) with weak oscillations occurring at the vacuum Rabi oscillation frequency. This is in contrast to the behavior of a linear cavity (shown as the dashed brown curve in Fig. 4.5e), where driving the second photon transition leads to persistent Rabi oscillations with a frequency that is $\sqrt{2}$ times larger than vacuum Rabi oscillations. Further analysis of the nonlinear behavior of the atomic cavity is provided in Sec. C.4.

4.5 Compound atomic mirrors

The waveguide QED chip of Fig. 4.1b can also be used to investigate the spectrum of sub-radiant states that emerge when $N > 2$ and there is direct interaction between mirror qubits. This situation can be realized by taking advantage of the capacitive coupling between co-localized pairs of type I qubits (Q_2 and Q_3 , or Q_5 and Q_6). Although in an idealized 1D waveguide model there is no cooperative interaction term between qubits with zero separation along the waveguide, we observe a strong coupling (with the measured interaction rate, $g/2\pi = 46$ MHz) between the co-localized pair of mirror qubits Q_2 and Q_3 , as shown in Fig. 4.6a. This coupling results from near-field components of the electromagnetic field that are excluded in the simple waveguide model. The non-degenerate hybridized eigenstates of the qubit pair effectively behave as a compound atomic mirror. The emission rate of each compound mirror to the waveguide can be adjusted by setting the detuning, Δ , between the pair. As illustrated in Fig. 4.6b, resonantly aligning the compound atomic mirrors on both ends of the waveguide results in a hierarchy of bright and dark states involving both near-field and waveguide-mediated cooperative coupling. Probing the system with a weak continuous tone via the waveguide, we identify the two super-radiant combinations of the compound atomic mirrors (Fig. 4.6c). Similar to the case of a two-qubit cavity, we can identify the collective dark states via the probe qubit. As evidenced by the measured Rabi oscillations shown in Fig. 4.6d, the combination of direct and waveguide-mediated interactions of mirror qubits in

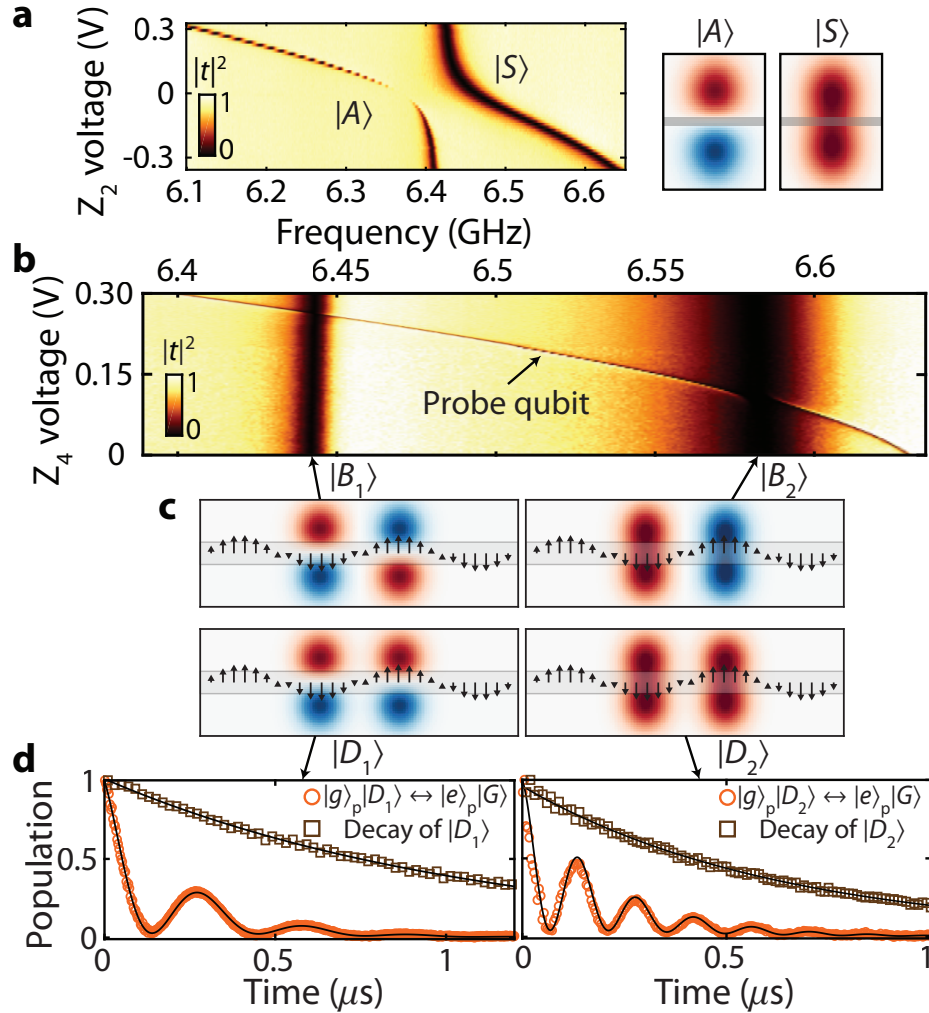


Figure 4.6: Compound atomic mirrors, $N = 4$. **a**, Avoided mode crossing of a pair of type I mirror qubits positioned on opposite sides of the CPW. Near the degeneracy point, the qubits form a pair of compound eigenstates consisting of symmetric ($|S\rangle$) and anti-symmetric ($|A\rangle$) states with respect to the waveguide axis. **b**, Measured transmission through the waveguide with the pair of compound atomic mirrors aligned in frequency. The two broad resonances correspond to super-radiant states $|B_1\rangle$ and $|B_2\rangle$ as indicated. As we tune the frequency of the probe qubit, we observe the (avoided-crossing-like) signatures of the interaction of the probe qubit with each dark state. **c**, Illustration of the single-excitation manifold of the collective states of $N = 4$ mirror qubits forming a pair of compound atomic cavities. The bright (super-radiant) and dark (sub-radiant) states can be identified by comparing the symmetry of the compound qubit states with the resonant radiation field pattern in the waveguide. **d**, Probe qubit measurements of the two dark states, $|D_1\rangle$ and $|D_2\rangle$. In these measurements the frequency of each dark state is shifted to ensure $\lambda_0/2$ separation between the two compound atomic mirrors. The figure is adapted from Ref. [108].

this geometry results in the emergence of a pair of collective entangled states of the four qubits acting as strongly-coupled atomic cavities with a frequency separation of $\sqrt{4g^2 + \Delta^2}$.

4.6 Conclusion

In conclusion, we have realized a synthetic cavity QED system in which to observe and drive the coherent dynamics that emerge from correlated dissipation in an open waveguide, paving the way for several exciting research avenues beyond the work presented here. Our current work has reached single-qubit Purcell factors exceeding 200, which is an order of magnitude larger than the experimental state of the art in planar superconducting quantum circuits and on par with the values achievable in less scalable three-dimensional architectures [135], but further improvement is theoretically possible. With better thermalization to the waveguide [157] and coherence times in line with the best planar superconducting qubits [201], Purcell factors in excess of 10^4 should be achievable. In this regime, with an already realized system size of $N = 4$, a universal set of quantum gates with fidelity above 0.99 could theoretically be realized by encoding information in decoherence-free subspaces [123]. Even without improved Purcell factors, the control demonstrated here over the sub-radiant states of an atomic chain enables studies of the formation of fermionic correlations between excitations and the power-law decay dynamics associated with a critical open system in a modestly-sized array ($N = 10$) [191]. Further, the demonstrated ability to measure the population decay time and coherence time for the entangled states of multiple distant qubits provides a valuable experimental tool with which to examine the sources of correlated decoherence in circuit QED. Finally, reducing the frequency disorder of transmon qubits beyond the values measured in our system ($\delta f \approx 60$ MHz) and using a slow-light metamaterial waveguide [109] would allow chip-scale waveguide QED experiments with a much larger number of fixed-frequency qubits, in the range $N = 10$ –100, where the full extent of the many-body dynamics of large quantum spin chains can be studied [192–194].

4.7 Methods

Qubits

We design and fabricate transmon qubits in three different variants for the experiment (see Fig. 4.7a-b): type I mirror qubits (Q_2, Q_3, Q_5, Q_6), type II mirror qubits (Q_1, Q_7), and the probe qubit (Q_4). The qubit frequency tuning range, waveguide

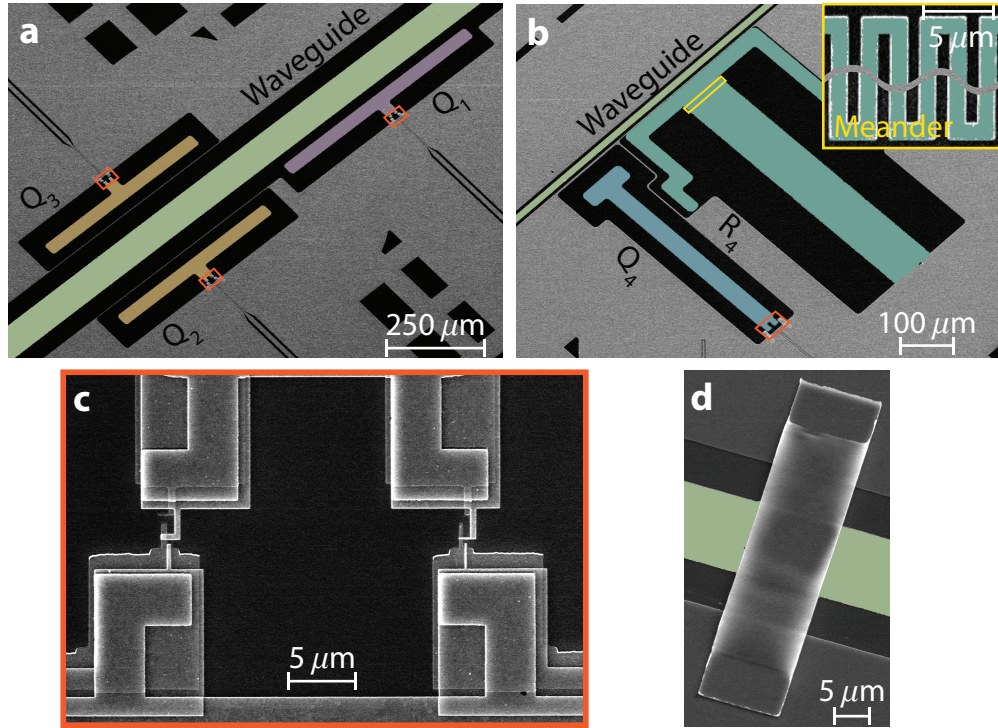


Figure 4.7: Scanning electron microscope image of the fabricated device. **a**, Type I (Q_2 , Q_3) and type II (Q_1) mirror qubits coupled to the coplanar waveguide (CPW). **b**, The central probe qubit (Q_4) and lumped-element readout resonator (R_4) coupled to CPW. The inset shows an inductive meander of the lumped-element readout resonator. **c**, A superconducting quantum interference device (SQUID) loop with asymmetric Josephson junctions used for qubits. **d**, An airbridge placed across the waveguide to suppress slotline mode.

	Q_1	Q_2	Q_3	Q_4	Q_5	Q_6	Q_7
f_{\max} (GHz)	6.052	6.678	6.750	6.638	6.702	6.817	6.175
f_{\min} (GHz)	4.861	5.373	5.389	5.431	5.157	5.510	4.972
$\Gamma_{1D}/2\pi$ (MHz)	94.1	16.5	13.9 ^{a,b}	0.91	18.4 ^b	18.1	99.5
$\Gamma'/2\pi$ (kHz)	430	< 341	< 760 ^{a,b}	81	375 ^b	185	998

^a Measured at 6.6 GHz

^b Measured without the cold attenuator

Table 4.1: Qubit characteristics. f_{\max} (f_{\min}) is the maximum (minimum) frequency of the qubit, corresponding to “sweet spots” with zero first-order flux sensitivity. Γ_{1D} is the qubit’s rate of decay into the waveguide channel and Γ' is its parasitic decoherence rate due to damping and dephasing from channels other than the waveguide at 0 temperature. All reported values are measured at the maximum frequency of each qubit, save for Q_3 in which case the values were measured at 6.6 GHz (marked with superscript ^a). With the exception of Q_3 and Q_5 (marked with superscript ^b), all the values are measured with the cold attenuator placed in the input line of the waveguide (see Sec. C.1).

uide coupling rate (Γ_{1D}), and parasitic decoherence rate (Γ') can be extracted from waveguide spectroscopy measurements of the individual qubits. The values for all the qubits inferred in this manner are listed in Table 4.1. Note that Γ' is defined as due to damping and dephasing from channels other than the waveguide at zero temperature. The inferred value of Γ' from waveguide spectroscopy measurements is consistent with this definition in the zero temperature waveguide limit (effects of finite waveguide temperature are considered in Sec. C.1). The standard deviation in maximum frequencies of the four identically designed qubits (type I) is found as 61 MHz, equivalent to $\sim 1\%$ qubit frequency disorder in our fabrication process. Asymmetric Josephson junctions are used in all qubits' superconducting quantum interference device (SQUID) loops (Fig. 4.7c) to reduce dephasing from flux noise, which limits the tuning range of qubits to around 1.3 GHz. For Q_4 , the Josephson energies of the junctions are extracted to be $E_{J1}/h = 18.4$ GHz and $E_{J2}/h = 3.5$ GHz, giving a junction asymmetry of $d \equiv \frac{E_{J1}-E_{J2}}{E_{J1}+E_{J2}} = 0.68$. The anharmonicity is measured to be $\eta/2\pi = -272$ MHz and $E_J/E_C = 81$ at maximum frequency for Q_4 .

Readout

We have fabricated a lumped-element resonator (shown in Fig. 4.7b) to perform dispersive readout of the state of central probe qubit (Q_4). The lumped-element resonator consists of a capacitive claw and an inductive meander with a pitch of about $1\ \mu\text{m}$, effectively acting as a quarter-wave resonator. The bare frequency of resonator and coupling to probe qubit are determined to be $f_r = 5.156$ GHz and $g/2\pi = 116$ MHz, respectively, giving dispersive frequency shift of $\chi/2\pi = -2.05$ MHz for Q_4 at maximum frequency. The resonator is loaded to the common waveguide in the experiment, and its internal and external quality factors are measured to be $Q_i = 1.3 \times 10^5$ and $Q_e = 980$ below single-photon level. It should be noted that the resonator-induced Purcell decay rate of Q_4 is $\Gamma_1^{\text{Purcell}}/2\pi \sim 70$ kHz, small compared to the decay rate into the waveguide $\Gamma_{1D,p}/2\pi \sim 1$ MHz. The compact footprint of the lumped-element resonator is critical for minimizing the distributed coupling effects that may arise from interference between direct qubit decay to the waveguide and the the Purcell decay of the qubit via the resonator path.

Suppression of spurious modes

In our experiment we use a coplanar transmission line for realizing a microwave waveguide. In addition to the fundamental propagating mode of the waveguide, which has even symmetry with respect to the waveguide axis, these structures

also support a set of modes with odd symmetry, known as slotline modes. The propagation of a slotline mode can be completely suppressed in a waveguide with perfectly symmetric boundary conditions. However, in practice perfect symmetry cannot be maintained over the full waveguide length, which unavoidably leads to presence of the slotline mode as a spurious loss channel for the qubits. Crossovers connecting ground planes across the waveguide are known to suppress propagation of slotline modes, and to this effect Al airbridges have been used in superconducting circuits with negligible impedance mismatch for the desired CPW mode [202].

In this experiment, we place airbridges (Fig. 4.7d) along the waveguide and control lines at specific distances set with the following considerations. Airbridges create reflecting boundary for slotline mode, and if placed by a distance d a discrete resonance corresponding to wavelength of $2d$ is formed. Therefore, placing airbridges over distances less than $\lambda/4$ apart, where λ is the wavelength of the mode resonant with the qubits, pushes the slotline resonances of the waveguide sections between the airbridges to substantially higher frequencies. In this situation, the dissipation rate of qubits via the spurious channel is substantially suppressed by the off-resonance Purcell factor $\Gamma_1^{\text{Purcell}} \sim (g/\Delta)^2 \kappa$, where Δ denotes detuning between the qubit transition frequency and the frequency of the odd mode in the waveguide section between the two airbridges, and where the parameters g and κ are the interaction rate of the qubit and the decay rate of the slot-line cavity modes, respectively. In addition, we place the airbridges before and after bends in waveguide, to ensure the fundamental waveguide mode is not converted to the slot-line mode upon propagation [203].

Crosstalk in flux biasing

We tune the frequency of each qubit by supplying a bias current to individual flux control lines (Z lines), which control the magnetic flux in the qubit's SQUID loop. In our system, the Z lines are attached to external wires in two forms with different configurations, which allows the qubit frequency to be tuned in 'slow' and 'fast' timescales (See Fig. 4.8). The bias currents were generated via independent bias voltages generated by seven arbitrary waveform generator channels, allowing for simultaneous tuning of all qubits. In practice, independent frequency tuning of each qubit needs to be accompanied by small changes in the flux bias of the qubits in the near physical vicinity of the qubit of interest, owing to cross-talk between adjacent Z control lines.

In this experiment, we characterized the crosstalk between bias voltage channels of

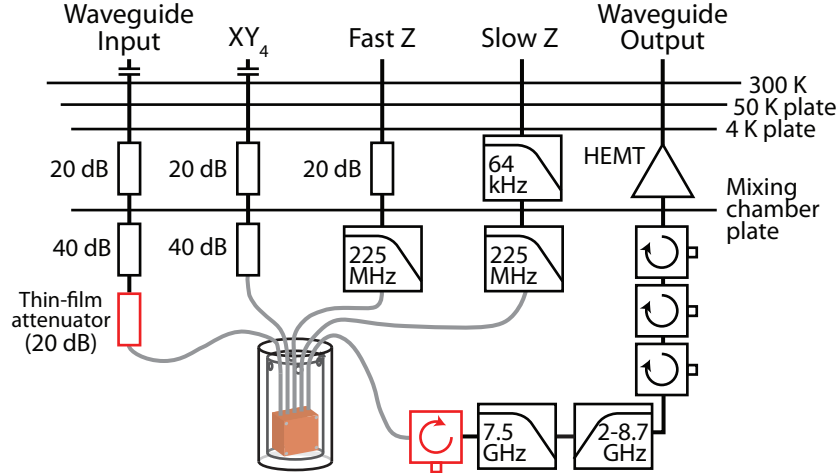


Figure 4.8: Schematic of the measurement chain inside the dilution refrigerator. The four types of input lines, the output line, and their connection to the device inside a magnetic shield are illustrated. Attenuators are expressed as rectangles with labeled power attenuation and capacitor symbols correspond to direct-current blocks. The thin-film attenuator and a circulator (colored red) are added to the waveguide input line and output line, respectively, in a second version of the setup and a second round of measurements to further protect the sample from thermal noise in the waveguide line. HEMT, high-electron-mobility-transistor.

the qubits in the following way. First, we tune the qubits not in use to frequencies more than 800 MHz away from the working frequency (which is set as either 5.83 GHz or 6.6 GHz). These qubits are controlled by fixed biases such that their frequencies, even in the presence of crosstalk from other qubits, remained far enough from the working frequency and hence were not considered for the rest of the analysis. Second, we tune the remaining in-use qubits to relevant frequencies within 100 MHz of the working frequency and record the array of biases ν_0 and frequencies f_0 of all qubits. Third, we varied the bias on only a single (j th) qubit and linearly interpolated the change in frequency (f_i) of the other (i th) qubits with respect to bias voltage ν_j on the j th qubit, finding the cross talk matrix component $M_{ij} = (\partial f_i / \partial \nu_j)_{\nu = \nu_0}$. Repeating this step, we obtained the following (approximately linearized) relation between the frequencies f and bias voltages ν of qubits:

$$f \approx f_0 + M(\nu - \nu_0).$$

Finally, we took the inverse of the above relation to find bias voltages ν that is required for tuning qubits to frequencies f :

$$\nu \approx \nu_0 + M^{-1}(f - f_0).$$

An example of such crosstalk matrix between Q_2 , Q_4 , and Q_6 near $f_0 = (6.6, 6.6, 6.6)$ GHz used in the experiment is given by

$$M = \begin{pmatrix} 0.2683 & -0.0245 & -0.0033 \\ -0.0141 & -0.5310 & 0.0170 \\ 0.0016 & 0.0245 & 0.4933 \end{pmatrix} \text{GHz/V}$$

This indicates that the crosstalk level between Q_4 and either Q_2 or Q_6 is about 5%, while that between Q_2 and Q_6 is less than 1%. We have repeated similar steps for other configurations in the experiment.

Measurement Setup

Figure 4.8 illustrates the outline of the measurement chain in our dilution refrigerator. The sample was enclosed in a magnetic shield that was mounted at the mixing chamber. We have outlined four different types of input lines used in our experiment. Input lines to the waveguide and XY_4 go through a direct-current block at room temperature and then were attenuated by 20 dB at the 4 K stage, followed by additional 40 dB of attenuation at the mixing chamber. The fast flux tuning lines (Z_3, Z_4) are attenuated by 20 dB and were filtered with a low-pass filter with corner frequency at 225 MHz to minimize thermal noise photons while maintaining short rise and fall time of pulses for fast flux control. The slow flux tuning lines (Z_1, Z_2, Z_5, Z_6, Z_7) are filtered by an additional low-pass filter with 64 kHz corner frequency at the 4K stage to further suppress noise photons. In addition, the waveguide signal output path contained a high electron mobility transistor (HEMT) amplifier at the 4K plate. Three circulators were placed between the HEMT and the sample to ensure (> 70 dB) isolation of the sample from the amplifier noise. In addition, a series of low-pass and band-pass filters on the output line suppressed noise sources outside the measurement spectrum.

A thin-film ‘cold attenuator’, developed by Palmer and colleagues at the University of Maryland [157], was added to the measurement path in order to achieve better thermalization between the microwave coaxial line and its thermal environment. Similarly, an additional circulator was added to the waveguide measurement chain in later setups to further protect the device against thermal photons (both the attenuator and circulator are highlighted in red in the schematic in Fig. 4.8). The effect of this change is discussed in Sec. C.1.

Dark state characterization

We characterized the collective dark state of mirror qubits with population decay time $T_{1,D}$ and Ramsey coherence time $T_{2,D}^*$ using the cooperative interaction with the probe qubit. For each configuration of mirror qubits, we obtain the Rabi oscillation curve (see Figs. 4.4a, 4.6d) using a fast flux-bias pulse on the probe qubit as explained in the main text. The half-period T_{SWAP} of Rabi oscillation results in a complete transfer of probe qubit population to the collective dark state and vice versa, hence defining an iSWAP gate.

To measure the population decay time $T_{1,D}$ of the dark state, we excited the probe qubit with a resonant microwave π -pulse, followed by applying an iSWAP gate. This prepared the collective dark state $|g\rangle_p|D\rangle$ off-resonantly decoupled from the probe qubit. After free evolution of the dark state for a variable duration τ , another iSWAP gate was applied to transfer the remaining dark state population back to the probe qubit. Finally, we measured the state of the probe qubit and performed an exponential fitting to the resulting decay curve.

Likewise, we measured Ramsey coherence time $T_{2,D}^*$ of the dark state as follows. First, we excited the probe qubit to a superposition $(|g\rangle + |e\rangle)_p|G\rangle$ of the ground and excited states by applying a detuned microwave $\pi/2$ -pulse. Next, application of an iSWAP gate maps this superposition to that of the dark state $|g\rangle_p(|G\rangle + |D\rangle)$. After a varying delay time τ , another iSWAP gate was applied, followed by a detuned $\pi/2$ -pulse on the probe qubit. Measurement of the state of the probe qubit resulted in a damped oscillation curve the decay envelope of which gives the Ramsey coherence time of the dark state involved in the experiment. Note that the fast oscillation frequency in this curve is determined by detuning of the dark state with respect to the frequency of the microwave pulses applied to the probe qubit.

DEVELOPMENT OF SUPERCONDUCTING METAMATERIALS FOR WAVEGUIDE QED

In the previous chapter, we observed that a waveguide having a linear dispersion relation close to transition frequencies of superconducting qubits can be harnessed to induce coherent long-range interaction in the strong-coupling regime. As noted in Secs. 2.2 and 2.3, there are several drawbacks of this approach associated with having to work with specific arrangement of qubit array in order to access decoherence-free subspace, the only states in a waveguide QED system protected from radiation to the waveguide channel, complicating the protocol for quantum information processing. We divert our attention to an alternative direction utilizing a dispersive waveguide for realizing long-range qubit-qubit interaction inside a photonic bandgap, while simultaneously protecting qubits from radiation to the waveguide. In this chapter, we introduce our work on the development of a compact and scalable microwave structure based on metamaterial concept and characterization of this structure utilizing a superconducting qubit, which is published in Ref. [109].

5.1 Introduction

Recently, there has been much interest in achieving strong light-matter interaction in a cavity-free system such as a waveguide [40, 195]. Slow-light photonic crystal waveguides are of particular interest in waveguide QED because the reduced group velocity near a bandgap preferentially amplifies the desired radiation of the atoms into the waveguide modes [137, 204, 205]. Moreover, in this configuration an interesting paradigm can be achieved by placing the resonance frequency of the atom inside the bandgap of the waveguide [126, 142, 206, 207]. In this case, the atom cannot radiate into the waveguide but the evanescent field surrounding it gives rise to a photonic bound state [126]. The interaction of such localized bound states has been proposed for realizing tunable spin-exchange interaction between atoms in a chain [125, 208], and also for realizing effective non-local interactions between photons [209, 210].

While achieving efficient waveguide coupling in the optical regime requires the challenging task of interfacing atoms or atomic-like systems with nanoscale dielectric structures [132, 140, 211–213], superconducting circuits provide an entirely differ-

ent platform for studying the physics of light-matter interaction in the microwave regime [35, 195]. Development of the field of circuit QED has enabled fabrication of tunable qubits with long coherence times and fast qubit gate times [190, 214]. Moreover, strong coupling is readily achieved in coplanar platforms due to the deep sub-wavelength transverse confinement of photons attainable in microwave waveguides and the large electrical dipole of superconducting qubits [27]. Microwave waveguides with strong dispersion, even “bandgaps” in frequency, can also be simply realized by periodically modulating the geometry of a coplanar transmission line [180]. Such an approach was recently demonstrated in a pioneering experiment by Liu and Houck [215], whereby a qubit was coupled to the localized photonic state within the bandgap of a modulated coplanar waveguide (CPW). Satisfying the Bragg condition in a periodically modulated waveguide requires a lattice constant on the order of the wavelength, however, which translates to a device size of approximately a few centimeters for complete confinement of the evanescent fields in the frequency range suitable for microwave qubits. Such a restriction significantly limits the scaling in this approach, both in qubit number and qubit connectivity.

An alternative approach for tailoring dispersion in the microwave domain is to take advantage of the metamaterial concept. Metamaterials are composite structures with sub-wavelength components which are designed to provide an effective electromagnetic response [216, 217]. Since the early microwave work, the electromagnetic metamaterial concept has been expanded and extensively studied across a broad range of classical optical sciences [218–220]; however, their role in quantum optics has remained relatively unexplored, at least in part due to the lossy nature of many sub-wavelength components. Improvements in design and fabrication of low-loss superconducting circuit components in circuit QED offer a new prospect for utilizing microwave metamaterials in quantum applications [221]. Indeed, high quality-factor superconducting components such as resonators can be readily fabricated on a chip [222], and such elements have been used as a tool for achieving phase-matching in near quantum-limited traveling wave amplifiers [170, 223] and for tailoring qubit interactions in a multimode cavity QED architecture [224].

In this work, we utilize an array of coupled lumped-element microwave resonators to form a compact bandgap waveguide with a deep sub-wavelength lattice constant ($\lambda/60$) based on the metamaterial concept. In addition to a compact footprint, these sort of structures can exhibit highly nonlinear band dispersion surrounding the bandgap, leading to exceptionally strong confinement of localized intra-gap photon

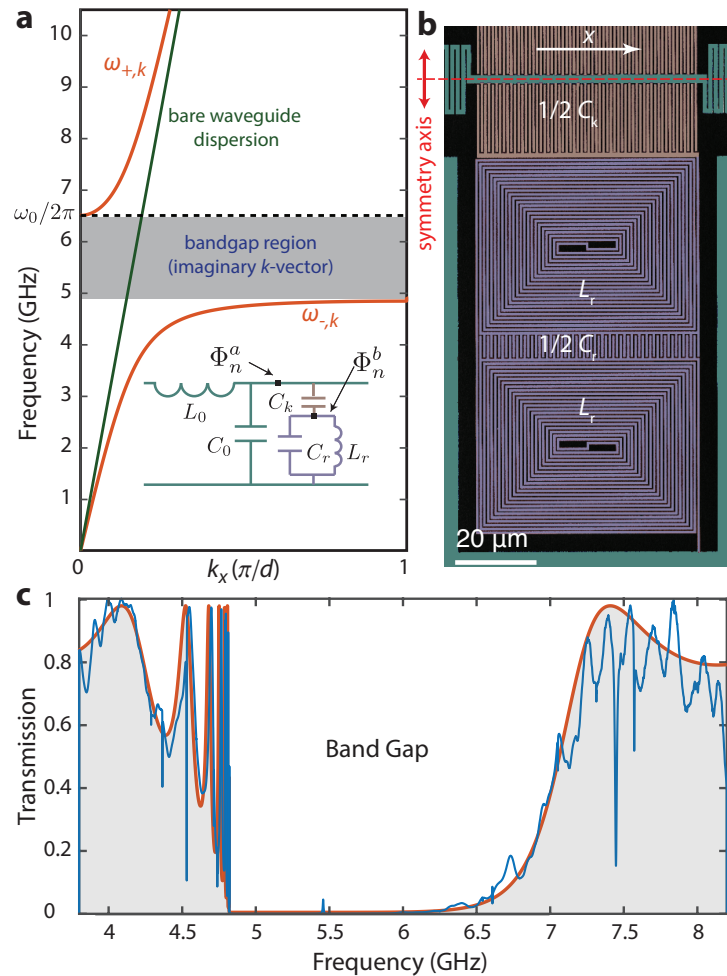


Figure 5.1: Microwave metamaterial waveguide. **a**, Dispersion relation of a CPW loaded with a periodic array of microwave resonators (red curve). The green line shows the dispersion relation of the waveguide without the resonators. Inset: circuit diagram for a unit cell of the periodic structure. **b**, Scanning electron microscope (SEM) image of a fabricated capacitively coupled microwave resonator, here with a wire width of 500 nm. The resonator region is false-colored in purple, the waveguide central conductor and the ground plane are colored green, and the coupling capacitor is shown in orange. We have used pairs of identical resonators symmetrically placed on the two sides of the transmission line to preserve the symmetry of the structure. **c**, Transmission measurement for the realized metamaterial waveguide made from 9 unit cells of resonator pairs with a wire width of $1\ \mu\text{m}$, repeated with a lattice constant of $d = 350\ \mu\text{m}$. The blue curve depicts the experimental data and the red curve shows the lumped-element model fit to the data.

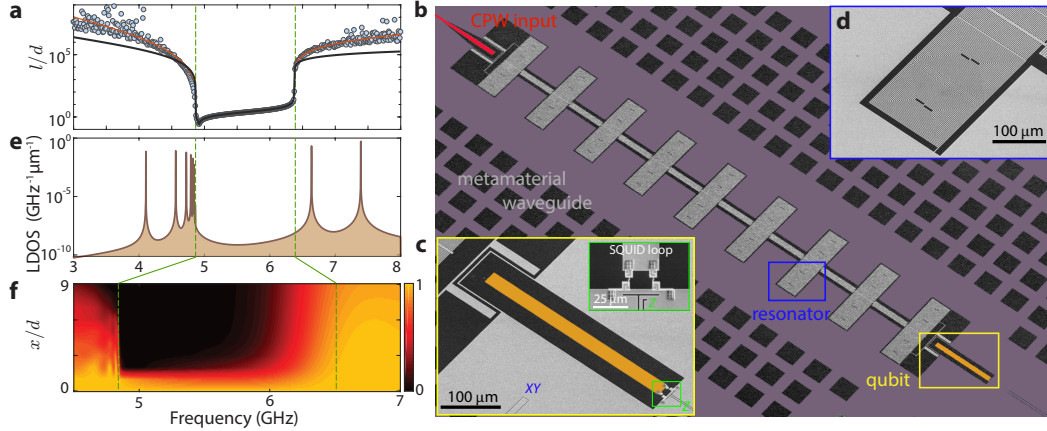


Figure 5.2: Disorder effects and qubit-waveguide coupling. **a**, Calculated localization length for a loss-less metamaterial waveguide with structural disorder (blue circles). The nominal waveguide parameters are determined from the fit to a lumped element model (including resonator loss) to the transmission data in Fig. 5.1. Numerical simulation has been performed for $N = 100$ unit cells, averaged over 10^5 randomly realized values of the resonance frequency ω_0 , with the standard deviation $\delta\omega_0/\omega_0 = 0.5\%$. The vertical green lines represent the extent of the bandgap region. The red curve outside the gap is an analytic model based on Ref. [225]. For comparison, the solid black curve shows the calculated effective localization length without resonator frequency disorder but including resonator loss. **b**, SEM image of the fabricated qubit-waveguide system. The metamaterial waveguide (gray) consists of 9 periods of the resonator unit cell. The waveguide is capacitively coupled to an external CPW (red) for reflective read-out. **c**, The transmon qubit is capacitively coupled to the resonator at the end of the array. The Z drive is used to tune the qubit resonance frequency by controlling the external flux bias in the superconducting quantum interference device (SQUID) loop. The XY drive is used to coherently excite the qubit. **d**, capacitively coupled microwave resonator. **e**, Calculated local density of states (LDOS) at the qubit position for a metamaterial waveguide with a length of 9 unit cells and open boundary conditions (experimental measurements of LDOS tabulated in Table D.1). The band-edges for the corresponding infinite structure are marked with vertical green lines. **f**, Normalized electromagnetic energy distribution along the waveguide versus qubit frequency for the coupled qubit-waveguide system. The vertical axis marks the distance from the qubit (x/d) in units of the lattice period d .

states. We present the design and fabrication of such a metamaterial waveguide, and characterize the resulting waveguide dispersion and bandgap properties via interaction with a tunable superconducting transmon qubit. We measure the Lamb shift and lifetime of the qubit in the bandgap and its vicinity, demonstrating the anomalous Lamb shift of the fundamental qubit transition as well as selective inhibition and enhancement of spontaneous emission for the first two excited states of the transmon qubit.

5.2 Band-structure analysis and spectroscopy

We begin by considering the circuit model of a CPW that is periodically loaded with microwave resonators as shown in the inset to Fig. 5.1a. The Lagrangian for this system can be constructed as a function of the node fluxes of the resonator and waveguide sections Φ_n^b and Φ_n^a [226]. Assuming periodic boundary conditions and applying the rotating wave approximation, we derive the Hamiltonian for this system and solve for the energies $\hbar\omega_{\pm,k}$ along with the corresponding eigenstates $|\pm, k\rangle = \hat{\alpha}_{\pm,k}|0\rangle$ as (see Sec. D.1)

$$\omega_{\pm,k} = \frac{1}{2} \left[(\Omega_k + \omega_0) \pm \sqrt{(\Omega_k - \omega_0)^2 + 4g_k^2} \right], \quad (5.1)$$

$$\hat{\alpha}_{\pm,k} = \frac{(\omega_{\pm,k} - \omega_0)}{\sqrt{(\omega_{\pm,k} - \omega_0)^2 + g_k^2}} \hat{a}_k + \frac{g_k}{\sqrt{(\omega_{\pm,k} - \omega_0)^2 + g_k^2}} \hat{b}_k. \quad (5.2)$$

Here, \hat{a}_k , and \hat{b}_k describe the momentum-space annihilation operators for the bare waveguide and bare resonator sections, the index k denotes the wavevector, and the parameters Ω_k , ω_0 , and g_k quantify the frequency of traveling modes of the bare waveguide, the resonance frequency of the microwave resonators, and coupling rate between resonator and waveguide modes, respectively. The operators $\hat{\alpha}_{\pm,k}$ represent quasi-particle solutions of the composite waveguide, where far from the bandgap the quasi-particle is primarily composed of the bare waveguide mode, while in the vicinity of ω_0 most of its energy is confined in the microwave resonators.

Figure 5.1a depicts the numerically calculated energy bands $\omega_{\pm,k}$ as a function of the wavevector k . It is evident that the dispersion has the form of an avoided crossing between the energy bands of the bare waveguide and the uncoupled resonators. For small gap sizes, the midgap frequency is close to the resonance frequency of uncoupled resonators ω_0 , and unlike the case of a periodically modulated waveguide, there is no fundamental relation tying the midgap frequency to the lattice constant in this case. The form of the band structure near the higher cut-off frequency ω_{c+} can be approximated as a quadratic function $(\omega - \omega_{c+}) \propto k^2$, whereas the band structure near the lower band-edge ω_{c-} is inversely proportional to the square of the wavenumber $(\omega - \omega_{c-}) \propto 1/k^2$. The analysis above has been presented for resonators which are capacitively coupled to a waveguide in a parallel geometry; a similar band structure can also be achieved using series inductive coupling of resonators (see Sec. D.1 and Fig. D.1).

5.3 Physical realization using lumped-element resonators.

A coplanar microwave resonator is often realized by terminating a short segment of a coplanar transmission line with a length set to an integer multiple of $\lambda/4$, where λ is the wavelength corresponding to the fundamental resonance frequency [180, 222]. However, it is possible to significantly reduce the footprint of a resonator by using components that mimic the behavior of lumped elements. We have used the design presented in Ref. [227] to realize resonators in the frequency range of 6-10 GHz. This design provides compact resonators by placing interdigitated capacitors at the anti-nodes of the charge waves and double spiral coils near the peak of the current waves at the fundamental frequency (see Fig. 5.1b). The symmetry of this geometry results in the suppression of the second harmonic frequency and thus the elimination of an undesired bandgap at twice the fundamental resonance frequency of the band-gap waveguide. A more subtle design criterion is that the resonators be of high impedance. Use of high impedance resonators allows for a larger photonic bandgap and greater waveguide-qubit coupling. For the waveguide QED application of interest this enables denser qubit circuits, both spatially and spectrally.

The impedance of the resonators scales roughly as the inverse square-root of the pitch of the wires in the spiral coils. Complicating matters is that smaller wire widths have been found to introduce larger resonator frequency disorder due to kinetic inductance effects [228]. Here we have selected an aggressive resonator wire width of $1 \mu\text{m}$ and fabricated a periodic array of $N = 9$ resonator pairs coupled to a CPW with a lattice constant of $d = 350 \mu\text{m}$. The resonators are arranged in identical pairs placed on opposite sides of the central waveguide conductor to preserve the symmetry of the waveguide. In addition, the center conductor of each CPW section is meandered over a length of $210 \mu\text{m}$ so as to increase the overall inductance of the waveguide section which also increases the bandgap. Further details of the design criteria and lumped element parameters are given in Sec. D.2. The fabrication of the waveguide is performed using electron-beam deposited Al film (See Methods). Figure 5.1c shows the measured power transmission through such a finite-length metamaterial waveguide. Here $50\text{-}\Omega$ CPW segments, galvanically coupled to the metamaterial waveguide, are used at the input and output ports. We find a midgap frequency of 5.83 GHz and a bandgap extent of 1.82 GHz for the structure. Using the simulated value of effective refractive index of 2.54, the midgap frequency gives a lattice constant-to-wavelength ratio of $d/\lambda \approx 1/60$.

5.4 Disorder and Anderson localization

Fluctuations in the electromagnetic properties of the metamaterial waveguide along its length, such as the aforementioned resonator disorder, results in random scattering of traveling waves. Such random scattering can lead to an exponential extinction of propagating photons in the presence of weak disorder and complete trapping of photons for strong disorder, a phenomenon known as the Anderson localization of light [229]. Similarly, absorption loss in the resonators results in attenuation of wave propagation which adds a dissipative component to the effective localization of fields in the metamaterial waveguide. Figure 5.2a shows numerical simulations of the effective localization length as a function of frequency when considering separately the effects of resonator frequency disorder and loss (see Sec. D.3 for details of independent resonator measurements used to determine frequency variation (0.5%) and loss parameters (intrinsic Q -factor of 7.2×10^4) for this model). In addition to the desired localization of photons within the bandgap, we see that the effects of disorder and loss also limit the localization length outside the bandgap. In the lower transmission band where the group index is largest, the localization length is seen to rapidly approach zero near the band-edge, predominantly due to disorder. In the upper transmission band where the group index is smaller, the localization length maintains a large value of 6×10^3 periods all the way to the band-edge. Within the bandgap the simulations show that the localization length is negligibly modified by the levels of loss and disorder expected in the resonators of this work, and is well approximated by the periodic loading of the waveguide alone which can be simply related to the inverse of the curvature of the transmission bands of a lossless, disorder-free structure [125]. These results indicate that, even with practical limitations on disorder and loss in such metamaterial waveguides, a range of photon length scales of nearly four orders of magnitude should be accessible for frequencies within a few hundred MHz of the band-edges of the gap (See Sec. D.4).

5.5 Anomalous Lamb shift near the band-edge

To further probe the electromagnetic properties of the metamaterial waveguide we couple it to a superconducting qubit. In this work we use a transmon qubit [190] with the fundamental resonance frequency $\omega_{ge}/2\pi = 7.9$ GHz and Josephson energy to single electron charging energy ratio of $E_J/E_C \approx 100$ at zero flux bias (details of our qubit fabrication methods can also be found in Ref. [230]). Figure 5.2b shows the geometry of the device where the qubit is capacitively coupled to one end of the waveguide and the other end is capacitively coupled to a 50- Ω CPW transmission

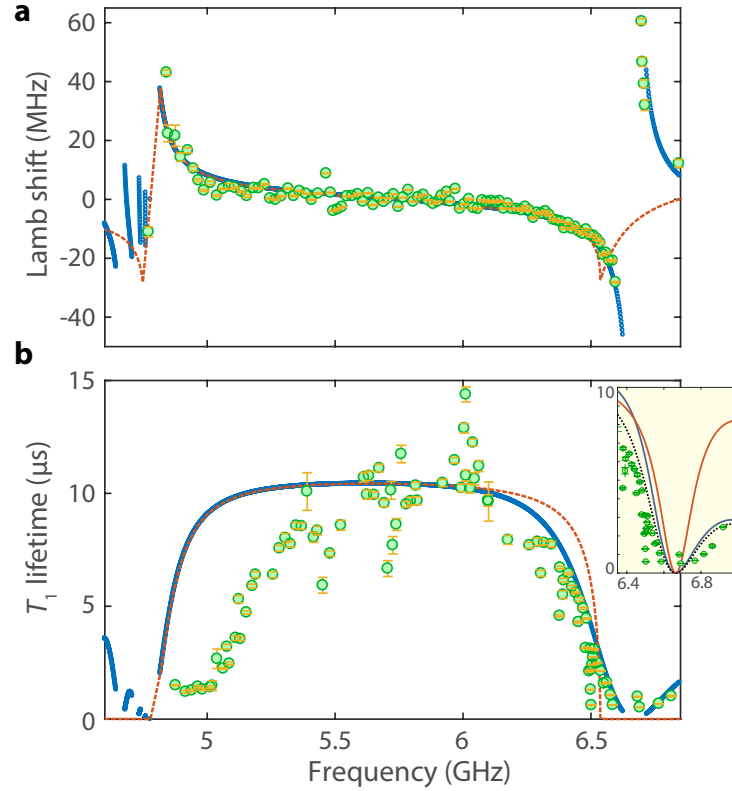


Figure 5.3: Measured dispersive and dissipative qubit dynamics. **a**, Lamb shift of the qubit transition versus qubit frequency. **b**, Lifetime of the excited qubit state versus qubit frequency. Open circles show measured data. The solid blue line (dashed red line) is theoretical curve from the circuit model of a finite (infinite) waveguide structure. For determining the Lamb shift from measurement, the bare qubit frequency is calculated as a function of flux bias Φ as $\hbar\omega_{ge} = \sqrt{8E_C E_J(\Phi)} - E_C$ using the extracted values of E_C , E_J , and assuming the symmetrical SQUID flux bias relation $E_J(\Phi) = E_{J,\max} \cos(2\pi\Phi/\Phi_0)$ [190]. The lifetime characterization is performed in the time domain where the qubit is initially excited with a π pulse through the XY drive. The excited state population, determined from the state-dependent dispersive shift of a close-by band-edge waveguide mode, is measured subsequent to a delay time during which the qubit freely decays. Inset to **b** shows a zoomed in region of the qubit lifetime near the upper band-edge. Solid blue (red) lines show the circuit model contributions to output port radiation (structural waveguide loss), adjusted to include a frequency independent intrinsic qubit life time of $10.86 \mu\text{s}$. The black dashed line shows the cumulative theoretical lifetime.

line. This geometry allows for forming narrow individual modes in the transmission band of the metamaterial, which can be used for dispersive qubit state read-out [231] from reflection measurements at the 50- Ω CPW input port (see Sec. D.2 and Table D.1). Figures 5.2e and 5.2f show the theoretical photonic LDOS and spatial photon energy localization versus frequency for this finite length qubit-waveguide system. Within the bandgap the qubit is self-dressed by virtual photons which are emitted and re-absorbed due to the lack of escape channels for the radiation. Near the band-edges surrounding the bandgap, where the LDOS is rapidly varying with frequency, this results in a large anomalous Lamb shift of the dressed qubit frequency [129, 207]. Figure 5.3a shows the measured qubit transition frequency shift from the expected bare qubit tuning curve as a function of frequency. Shown for comparison are the circuit theory model frequency shift of a finite structure with $N = 9$ periods (blue solid curve) alongside that of an infinite length waveguide (red dashed curve). It is evident that the qubit frequency is repelled from the band-edges on the two sides of the bandgap, a result of the strongly asymmetric density of states in these two regions. The measured frequency shift at the lower frequency band-edge is 43 MHz, in good agreement with the circuit theory model. Note that at the lower frequency band-edge where the localization length approaches zero due to the anomalous dispersion (see Fig. 5.2a), boundary-effects in the finite structure do not significantly alter the Lamb shift. Near the upper frequency band-edge, where finite-structure effects are non-negligible due to the weaker dispersion and corresponding finite localization length, we measure a qubit frequency shift as large as -28 MHz. This again is in good correspondence with the finite structure model; the upper band-edge of the infinite length waveguide occurs at a slightly lower frequency with a slightly smaller Lamb shift.

5.6 Enhancement and suppression of spontaneous emission

Another signature of the qubit-waveguide interaction is the change in the rate of spontaneous emission of the qubit. Tuning the qubit into the bandgap changes the localization length of the waveguide photonic state that dresses the qubit (see Fig. 5.2f). Since the finite waveguide is connected to an external port which acts as a dissipative environment, the change in localization length $\ell(\omega)$ is accompanied by a change in the lifetime of the qubit $T_{\text{rad}}(\omega) \propto e^{2x/\ell(\omega)}$, where x is the total length of the waveguide (See Sec. D.5). In addition to radiative decay into the output channel, losses in the resonators in the waveguide also contribute to the qubit's excited state decay. Using a low power probe in the single-photon regime we

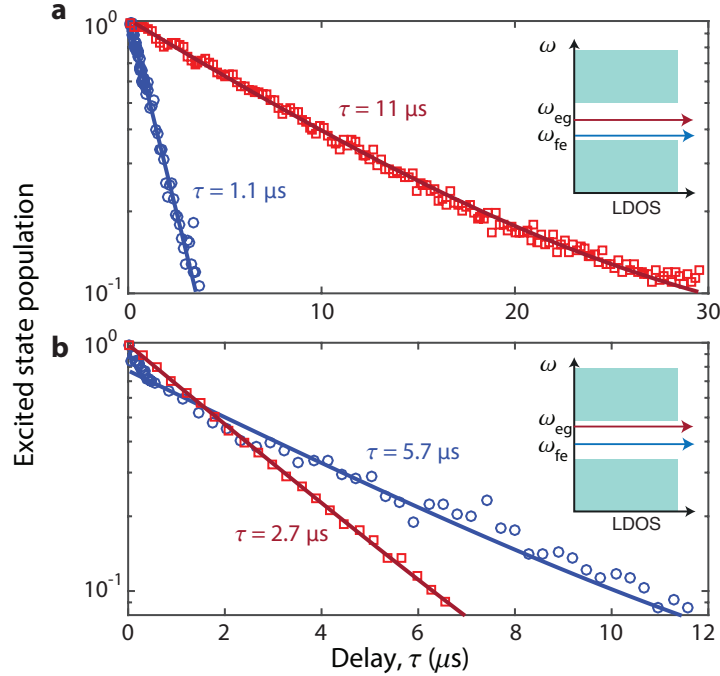


Figure 5.4: State-selective enhancement and inhibition of radiative decay. **a**, Measurement with the e-g transition tuned deep into the bandgap ($\omega_{eg}/2\pi = 5.37\text{GHz}$), with the f-e transition near the lower transmission band ($\omega_{fe}/2\pi = 5.01\text{GHz}$). **b**, Measurement with the e-g transition tuned near the upper transmission band ($\omega_{eg}/2\pi = 6.51\text{GHz}$), with the f-e transition deep in the bandgap ($\omega_{fe}/2\pi = 6.17\text{GHz}$). For measuring the f-e lifetime, we initially excite the third energy level $|f\rangle$ via a two-photon π pulse at the frequency of $\omega_{gf}/2$. Following the population decay in a selected time interval, the population in $|f\rangle$ is mapped to the ground state using a second π pulse. Finally the ground state population is read using the dispersive shift of a close-by band-edge resonance of the waveguide. g-e (f-e) transition data shown as red squares (blue circles)

have measured intrinsic Q -factors of $7.2 \pm 0.4 \times 10^4$ for the individual waveguide resonances between 4.6-7.4 GHz. Figure 5.3b shows the measured qubit lifetime (T_1) as a function of its frequency in the bandgap. The solid blue curve in Fig. 5.3b shows a fitted theoretical curve which takes into account the loss in the waveguide along with a phenomenological intrinsic lifetime of the qubit ($T_{1,i} = 10.8 \mu\text{s}$). The dashed red curve shows the expected qubit lifetime for an infinite waveguide length. Qualitatively, the measured lifetime of the qubit behaves as expected; the qubit lifetime drastically increases inside the bandgap region and is reduced in the transmission bands. More subtle features of the measured lifetime include multiple, narrow Fano-like spectral features deep within the bandgap. These features arise from what are believed to be interference between parasitic on-chip modes and low- Q modes of our external copper box chip packaging. In addition, while the measured lifetime near the upper band-edge is in excellent agreement with the finite waveguide

theoretical model, the data near the lower band-edge shows significant deviation. We attribute this discrepancy to the presence of low- Q parasitic resonances, observable in transmission measurements between the qubit XY drive line and the 50- Ω CPW port. Possible candidates for such spurious modes include the asymmetric “slotline” modes of the waveguide, which are weakly coupled to our symmetrically grounded CPW line but may couple to the qubit. Further study of the spectrum of these modes and possible methods for suppressing them will be a topic of future studies.

Focusing on the upper band-edge, we plot as an inset to Fig. 5.3b a zoom-in of the measured qubit lifetime along with theoretical estimates of the different components of qubit decay. Here the qubit decay results from two dominant effects: detuning-dependent coupling to the lossy resonances in the transmission band of the waveguide, and emission into the output port of the finite waveguide structure. The former effect is an incoherent phenomena arising from a multi-mode cavity-QED picture, whereas the latter effect arises from the coherent interference of band-edge resonances which can be related to the photon bound state picture and resulting localization length. Owing to the weaker dispersion at the upper band-edge, the extent of the photon bound state has an appreciable impact on the qubit lifetime in the $N = 9$ finite length waveguide. This is most telling in the strongly asymmetric qubit lifetime around the first waveguide resonance in the upper transmission band. Quantitatively, the slope of the radiative component of the lifetime curve in the bandgap near the band-edge can be shown to be proportional to the group delay (see Sec. D.6), $|\partial T_{\text{rad}}/\partial\omega| = T_{\text{rad}}\tau_{\text{delay}}$. The corresponding group index, $n_g \equiv \tau_{\text{delay}}/x$, is a property of the waveguide independent of its length x . Here we measure a slope corresponding to a group index $n_g \approx 450$, in good correspondence with the circuit model of the lossy metamaterial waveguide.

The sharp variation in the photonic LDOS near the metamaterial waveguide band-edges may also be used to engineer the multi-level dynamics of the qubit. A transmon qubit, by construct, is a nonlinear quantum oscillator and thus has a multilevel energy spectrum. In particular, a third energy level ($|f\rangle$) exists at the frequency $\omega_{gf} = 2\omega_{ge} - E_C/\hbar$. Although the transition g-f is forbidden by selection rules, the f-e transition has a dipole moment that is $\sqrt{2}$ larger than the fundamental transition [190]. This is consistent with the scaling of transition amplitudes in a harmonic oscillator and results in a second transition lifetime that is half of the fundamental transition lifetime for a uniform density of states in the electromagnetic environment of the oscillator. The sharply varying density of states in the metamaterial, on the

other hand, can lead to strong suppression or enhancement of the spontaneous emission for each transition. Figure 5.4 shows the measured lifetimes of the two transitions for two different spectral configurations. In the first scenario, we enhance the ratio of the lifetimes $T_{\text{eg}}/T_{\text{fe}}$ by situating the fundamental transition frequency deep inside in the bandgap while having the second transition positioned near the lower transmission band. The situation is reversed in the second configuration, where the fundamental frequency is tuned to be near the upper energy band while the second transition lies deep inside the gap. In our fabricated qubit, the second transition is about 300 MHz lower than the fundamental transition frequency at zero flux bias, which allows for achieving large lifetime contrast in both configurations.

5.7 Discussion

Looking forward, we anticipate that further refinement in the engineering and fabrication of the devices presented here should enable metamaterial waveguides approaching a lattice constant-to-wavelength ratio of $\lambda/1000$, with limited disorder and a bandgap-to-midgap ratio in excess of 50% (see Sec. D.7). Such compact, low loss, low disorder superconducting metamaterials can help realize more scalable superconducting quantum circuits with higher levels of complexity and functionality in several regards. They offer a method for densely packing qubits – both in spatial and frequency dimensions – with isolation from the environment and controllable connectivity achieved via bound qubit-waveguide polaritons [125, 199, 205]. Moreover, the ability to selectively modify the transition lifetimes provides simultaneous access to long-lived metastable qubit states as well as short-lived states strongly coupled to waveguide modes. This approach realizes a transmon qubit system with state-dependent bound state localization lengths, which can be used as a quantum nonlinear media for propagating microwave photons [210, 232, 233], or as recently demonstrated, to realize spin-photon entanglement and high-bandwidth itinerant single microwave photon detection [234, 235]. Combined, these attributes provide a unique platform for studying the many-body physics of quantum photonic matter [236–239].

*Chapter 6***QUANTUM ELECTRODYNAMICS IN A TOPOLOGICAL WAVEGUIDE**

We have introduced our first step to develop a scalable waveguide QED architecture based on engineered superconducting metamaterials in Chapter 5. By periodic placement of sub-wavelength resonant microwave elements, we were able to realize a dispersive and low-loss 1D waveguide channel which induces a huge anomalous Lamb shift of a superconducting qubit close to edges of photonic bands, a prerequisite for inducing strong and long-range photon-mediated interactions between qubit-photon bound states (see Sec. 2.3). This opens up opportunities to investigate quantum electrodynamical properties of quantum emitters coupled to numerous types of engineered photonic structures, which can be designed to induce exotic characters on the emitters depending on the dispersion relation and the topology. By utilizing the highly flexibility of waveguide QED tools we have developed in superconducting circuits, we demonstrate the physics of quantum emitters coupled to a dispersive waveguide with topological properties, which is published in Ref. [56].

6.1 Introduction

Harnessing the topological properties of photonic bands [47, 240, 241] is a burgeoning paradigm in the study of periodic electromagnetic structures. Topological concepts discovered in electronic systems [242, 243] have now been translated and studied as photonic analogs in various microwave and optical systems [47, 241]. In particular, symmetry-protected topological phases [202] which do not require time-reversal-symmetry breaking, have received significant attention in experimental studies of photonic topological phenomena, both in the linear and nonlinear regime [244]. One of the simplest canonical models is the Su-Schrieffer-Heeger (SSH) model [245, 246], which was initially used to describe electrons hopping along a one-dimensional dimerized chain with a staggered set of hopping amplitudes between nearest-neighbor elements. The chiral symmetry of the SSH model, corresponding to a symmetry of the electron amplitudes found on the two types of sites in the dimer chain, gives rise to two topologically distinct phases of electron propagation. The SSH model, and its various extensions, have been used in photonics to explore a variety of optical phenomena, from robust lasing in arrays

of microcavities [247, 248] and photonic crystals [249], to disorder-insensitive 3rd harmonic generation in zigzag nanoparticle arrays [250].

Utilization of quantum emitters brings new opportunities in the study of topological physics with strongly interacting photons [251–253], where single-excitation dynamics [254] and topological protection of quantum many-body states [255] in the SSH model have recently been investigated. In a similar vein, a topological photonic bath can also be used as an effective substrate for endowing special properties to quantum matter. For example, a photonic waveguide which localizes and transports electromagnetic waves over large distances, can form a highly effective quantum light-matter interface [29, 44, 132] for introducing non-trivial interactions between quantum emitters. Several systems utilizing highly dispersive electromagnetic waveguide structures have been proposed for realizing quantum photonic matter exhibiting tailorable, long-range interactions between quantum emitters [125, 199, 215, 256, 257]. With the addition of non-trivial topology to such a photonic bath, exotic classes of quantum entanglement can be generated through photon-mediated interactions of a chiral [46, 258] or directional nature [55, 259].

With this motivation, here we investigate the properties of quantum emitters coupled to a topological waveguide which is a photonic analog of the SSH model, following the theoretical proposal in Ref. [55]. Our setup is realized by coupling superconducting transmon qubits [190] to an engineered superconducting metamaterial waveguide [109, 153], consisting of an array of sub-wavelength microwave resonators with SSH topology. Combining the notions from waveguide quantum electrodynamics (QED) [40, 44, 132, 195] and topological photonics [47, 241], we observe qubit-photon bound states with directional photonic envelopes inside a bandgap and cooperative radiative emission from qubits inside a passband dependent on the topological configuration of the waveguide. Coupling of qubits to the waveguide also allows for quantum control over topological edge states, enabling quantum state transfer between distant qubits via a topological channel.

6.2 Description of the topological waveguide

The SSH model describing the topological waveguide studied here is illustrated in Fig. 6.1a. Each unit cell of the waveguide consists of two photonic sites, A and B, each containing a resonator with resonant frequency ω_0 . The intra-cell coupling between A and B sites is $J(1 + \delta)$ and the inter-cell coupling between unit cells is $J(1 - \delta)$. The discrete translational symmetry (lattice constant d) of this

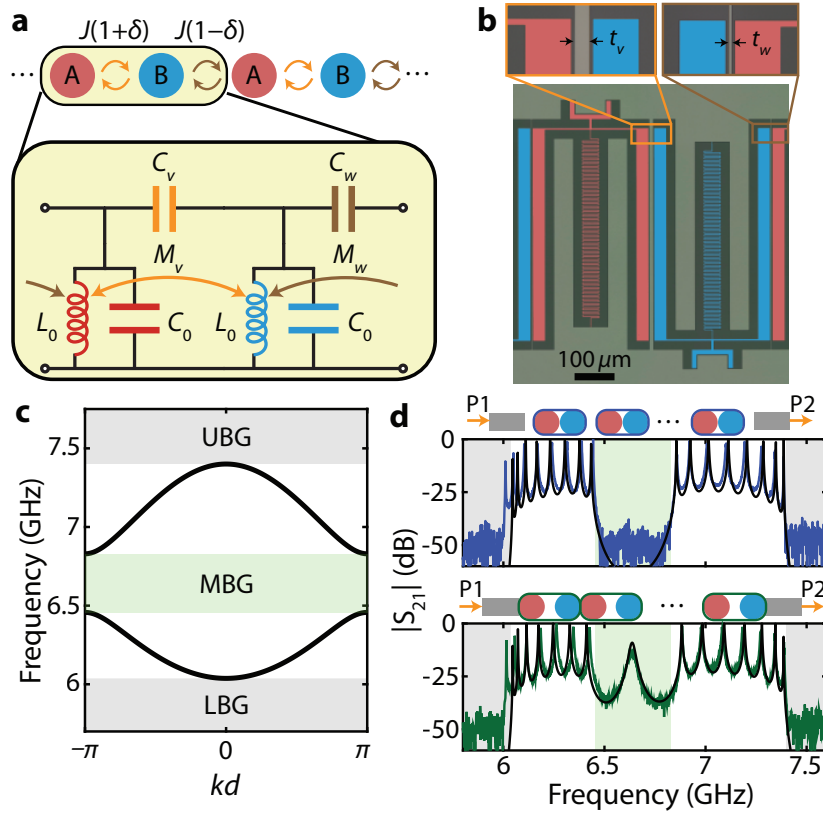


Figure 6.1: Topological waveguide. (a) Top: schematic of the SSH model. Each unit cell contains two sites A and B (red and blue circles) with intra- and inter-cell coupling $J(1 \pm \delta)$ (orange and brown arrows). Bottom: an analog of this model in electrical circuits, with corresponding components color-coded. The photonic sites are mapped to LC resonators with inductance L_0 and capacitance C_0 , with intra- and inter-cell coupling capacitance C_v , C_w and mutual inductance M_v , M_w between neighboring resonators, respectively (arrows). (b) Optical micrograph (false-colored) of a unit cell (lattice constant $d = 592 \mu\text{m}$) on a fabricated device in the topological phase. The lumped-element resonator corresponding to sublattice A (B) is colored in red (blue). The insets show zoomed-in view of the section between resonators where planar wires of thickness $(t_v, t_w) = (10, 2) \mu\text{m}$ (indicated with black arrows) control the intra- and inter-cell distance between neighboring resonators, respectively. (c) Dispersion relation of the realized waveguide according to the circuit model in panel (a). Upper bandgap (UBG) and lower bandgap (LBG) are shaded in gray, and middle bandgap (MBG) is shaded in green. (d) Waveguide transmission spectrum $|S_{21}|$ across the test structure with 8 unit cells in the trivial ($\delta > 0$; top) and topological ($\delta < 0$; bottom) phase. The cartoons illustrate the measurement configuration of systems with external ports 1 and 2 (denoted P1 and P2), where distances between circles are used to specify relative coupling strengths between sites and blue (green) outlines enclosing two circles indicate unit cells in the trivial (topological) phase. Black solid curves are fits to the measured data (see App. E.1 for details) with parameters $L_0 = 1.9 \text{ nH}$, $C_0 = 253 \text{ fF}$, coupling capacitance $(C_v, C_w) = (33, 17) \text{ fF}$ and mutual inductance $(M_v, M_w) = (-38, -32) \text{ pH}$ in the trivial phase (the values are interchanged in the case of topological phase). The shaded regions correspond to bandgaps in the dispersion relation of panel (c). The figure is adapted from Ref. [56].

system allows us to write the Hamiltonian in terms of momentum-space operators, $\hat{H}/\hbar = \sum_k (\hat{\mathbf{v}}_k)^\dagger \mathbf{h}(k) \hat{\mathbf{v}}_k$, where $\hat{\mathbf{v}}_k = (\hat{a}_k, \hat{b}_k)^T$ is a vector operator consisting of a pair of A and B sublattice photonic mode operators, and the k -dependent kernel of the Hamiltonian is given by,

$$\mathbf{h}(k) = \begin{pmatrix} \omega_0 & f(k) \\ f^*(k) & \omega_0 \end{pmatrix}. \quad (6.1)$$

Here, $f(k) \equiv -J[(1 + \delta) + (1 - \delta)e^{-ikd}]$ is the momentum-space coupling between modes on different sublattice, which carries information about the topology of the system. The eigenstates of this Hamiltonian form two symmetric bands centered about the reference frequency ω_0 with dispersion relation

$$\omega_{\pm}(k) = \omega_0 \pm J\sqrt{2(1 + \delta^2) + 2(1 - \delta^2)\cos(kd)},$$

where the $+$ ($-$) branch corresponds to the upper (lower) frequency passband. While the band structure is dependent only on the magnitude of δ , and not on whether $\delta > 0$ or $\delta < 0$, deformation from one case to the other must be accompanied by the closing of the middle bandgap (MBG), defining two topologically distinct phases. For a finite system, it is well known that edge states localized on the boundary of the waveguide at a $\omega = \omega_0$ only appear in the case of $\delta < 0$, the so-called *topological* phase [47, 246]. The case for which $\delta > 0$ is the *trivial* phase with no edge states. It should be noted that for an infinite system, the topological or trivial phase in the SSH model depends on the choice of unit cell, resulting in an ambiguity in defining the bulk properties. Despite this, considering the open boundary of a finite-sized array or a particular section of the bulk, the topological character of the bands can be uniquely defined and can give rise to observable effects.

We construct a circuit analog of this canonical model using an array of inductor-capacitor (LC) resonators with alternating coupling capacitance and mutual inductance as shown in Fig. 6.1a. The topological phase of the circuit model is determined by the relative size of intra- and inter-cell coupling between neighboring resonators, including both the capacitive and inductive contributions. Strictly speaking, this circuit model breaks chiral symmetry of the original SSH Hamiltonian [47, 246], which ensures the band spectrum to be symmetric with respect to $\omega = \omega_0$. Nevertheless, the topological protection of the edge states under perturbation in the intra- and inter-cell coupling strengths remains valid as long as the bare resonant frequencies

of resonators (diagonal elements of the Hamiltonian) are not perturbed, and the existence of edge states still persists due to the presence of inversion symmetry within the unit cell of the circuit analog, leading to a quantized Zak phase [260]. For detailed analysis of the modeling, symmetry, and robustness of the circuit topological waveguide see Apps. E.1 and E.2.

The circuit model is realized using fabrication techniques for superconducting metamaterials discussed in Refs. [109, 153], where the coupling between sites is controlled by the physical distance between neighboring resonators. Due to the near-field nature, the coupling strength is larger (smaller) for smaller (larger) distance between resonators on a device. An example unit cell of a fabricated device in the topological phase is shown in Fig. 6.1b (the values of intra- and inter-cell distances are interchanged in the trivial phase). We find a good agreement between the measured transmission spectrum and a theoretical curve calculated from a LC lumped-element model of the test structures with 8 unit cells in both trivial and topological configurations (Fig. 6.1c,d). For the topological configuration, the observed peak in the waveguide transmission spectrum at 6.636 GHz inside the MBG signifies the associated edge state physics in our system.

6.3 Properties of quantum emitters coupled to the topological waveguide

The non-trivial properties of the topological waveguide can be accessed by coupling quantum emitters to the engineered structure. To this end, we prepare Device I consisting of a topological waveguide in the trivial phase with 9 unit cells, whose boundary is tapered with specially designed resonators before connection to external ports (see Fig. 6.2a). The tapering sections at both ends of the array are designed to reduce the impedance mismatch to the external ports ($Z_0 = 50 \Omega$) at frequencies in the upper passband (UPB). This is crucial for reducing ripples in the waveguide transmission spectrum in the passbands [153]. Every site of the 7 unit cells in the middle of the array is occupied by a single frequency-tunable transmon qubit [190] (the device contains in total 14 qubits labeled Q_i^α , where $i = 1-7$ and $\alpha = A, B$ are the cell and sublattice indices, respectively). Properties of Device I and the tapering section are discussed in further detail in Apps. E.3 and E.4, respectively.

Directional qubit-photon bound states

For qubits lying within the middle bandgap, the topology of the waveguide manifests itself in the spatial profile of the resulting qubit-photon bound states. When the qubit transition frequency is inside the bandgap, the emission of a propagating photon from

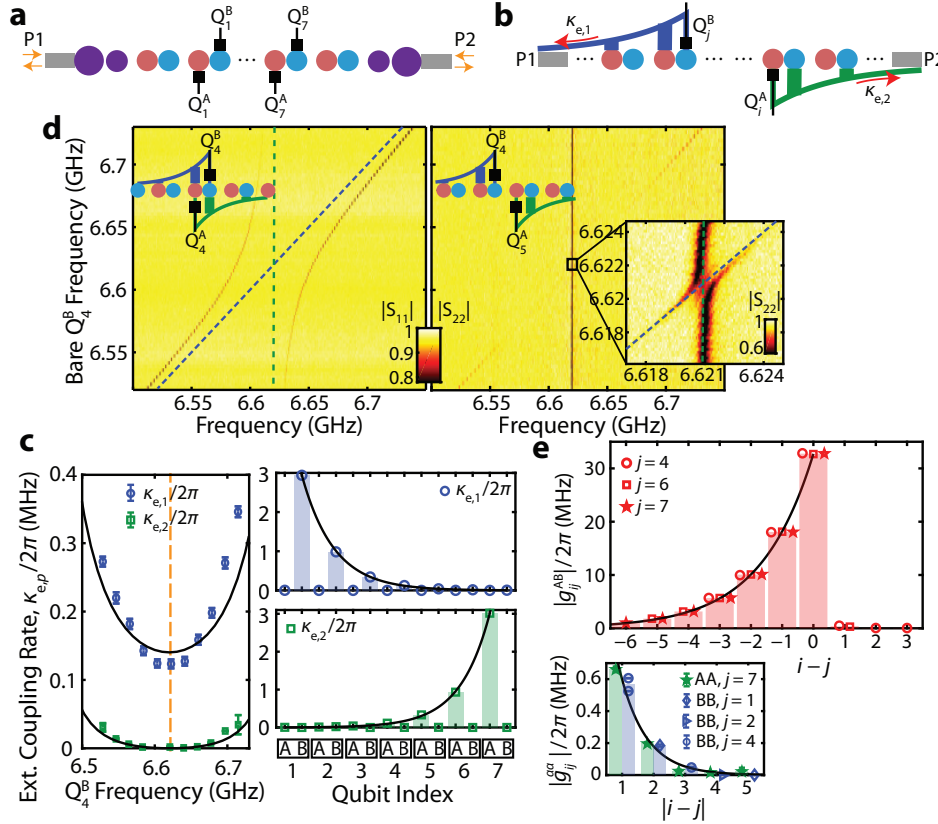


Figure 6.2: Directionality of qubit-photon bound states. (a) Schematic of Device I, consisting of 9 unit cells in the trivial phase with qubits (black lines terminated with a square) coupled to every site on the 7 central unit cells. The ends of the array are tapered with additional resonators (purple) with engineered couplings designed to minimize impedance mismatch at upper passband frequencies. (b) Theoretical photonic envelope of the directional qubit-photon bound states. At the reference frequency ω_0 , the qubit coupled to site A (B) induces a photonic envelope to the right (left), colored in green (blue). The bars along the envelope indicate photon occupation on the corresponding resonator sites. (c) Measured coupling rate $\kappa_{e,p}/2\pi$ (MHz) to external port numbers, $p = 1, 2$, of qubit-photon bound states. Left: external coupling rate of qubit Q_4^B to each port as a function of frequency inside the MBG. Solid black curve is a model fit to the measured external coupling curves. The frequency point of highest directionality is extracted from the fit curve, and is found to be $\omega_0/2\pi = 6.621$ GHz (vertical dashed orange line). Top (Bottom)-right: external coupling rate of all qubits tuned to $\omega = \omega_0$ measured from port P1 (P2). The solid black curves in these plots correspond to exponential fits to the measured external qubit coupling versus qubit index. (d) Two-dimensional color intensity plot of the reflection spectrum under crossing between a pair of qubits with frequency centered around $\omega = \omega_0$. Left: reflection from P1 ($|S_{11}|$) while tuning Q_4^B across Q_4^A (fixed). An avoided crossing of $2|g_{44}^{AB}|/2\pi = 65.7$ MHz is observed. Right: reflection from P2 ($|S_{22}|$) while tuning Q_4^B across Q_5^A (fixed), indicating the absence of appreciable coupling. Inset to the right shows a zoomed-in region where a small avoided crossing of $2|g_{54}^{AB}|/2\pi = 967$ kHz is measured. The bare qubit frequencies from the fit are shown with dashed lines. (e) Coupling $|g_{ij}^{\alpha\beta}|$ ($\alpha, \beta \in \{A, B\}$) between various qubit pairs (Q_i^α, Q_j^β) at $\omega = \omega_0$, extracted from the crossing experiments similar to panel (d). Solid black curves are exponential fits to the measured qubit-qubit coupling rate versus qubit index difference (spatial separation). Error bars in all figure panels indicate 95% confidence interval, and are omitted on data points whose marker size is larger than the error itself. The figure is adapted from Ref. [56].

the qubit is forbidden due to the absence of photonic modes at the qubit resonant frequency. In this scenario, a stable bound state excitation forms, consisting of a qubit in its excited state and a waveguide photon with exponentially localized photonic envelope [126, 128]. Generally, bound states with a symmetric photonic envelope emerge due to the inversion symmetry of the photonic bath with respect to the qubit location [215]. In the case of the SSH photonic bath, however, a directional envelope can be realized [55] for a qubit at the centre of the MBG (ω_0), where the presence of a qubit creates a domain wall in the SSH chain and the induced photonic bound state is akin to an edge state (refer to App. E.5 for a detailed description). For example, in the trivial phase, a qubit coupled to site A (B) acts as the last site of a topological array extended to the right (left) while the subsystem consisting of the remaining sites extended to the left (right) is interpreted as a trivial array. Mimicking the topological edge state, the induced photonic envelope of the bound state faces right (left) with photon occupation only on B (A) sites (Fig. 6.2b), while across the trivial boundary on the left (right) there is no photon occupation. The opposite directional character is expected in the case of the topological phase of the waveguide. The directionality reduces away from the center of the MBG, and is effectively absent inside the upper or lower bandgaps.

We experimentally probe the directionality of qubit-photon bound states by utilizing the coupling of bound states to the external ports in the finite-length waveguide of Device I (see Fig. 6.2c). The external coupling rate $\kappa_{e,p}$ ($p = 1, 2$) is governed by the overlap of modes in the external port p with the tail of the exponentially attenuated envelope of the bound state, and therefore serves as a useful measure to characterize the localization [109, 215, 261]. To find the reference frequency ω_0 where the bound state becomes most directional, we measure the reflection spectrum S_{11} (S_{22}) of the bound state seen from port 1 (2) as a function of qubit tuning. We extract the external coupling rate $\kappa_{e,p}$ by fitting the measured reflection spectrum with a Fano lineshape [262]. For Q_4^B , which is located near the center of the array, we find $\kappa_{e,1}$ to be much larger than $\kappa_{e,2}$ at all frequencies inside MBG. At $\omega_0/2\pi = 6.621$ GHz, $\kappa_{e,2}$ completely vanishes, indicating a directionality of the Q_4^B bound state to the left. Plotting the external coupling at this frequency to both ports against qubit index, we observe a decaying envelope on every other site, signifying the directionality of photonic bound states is correlated with the type of sublattice site a qubit is coupled to. Similar measurements when qubits are tuned to other frequencies near the edge of the MBG, or inside the upper bandgap (UBG), show the loss of directionality away from $\omega = \omega_0$ (App. E.6).

A remarkable consequence of the distinctive shape of bound states is direction-dependent photon-mediated interactions between qubits (Fig. 6.2d,e). Due to the site-dependent shapes of qubit-photon bound states, the interaction between qubits becomes substantial only when a qubit on sublattice A is on the left of the other qubit on sublattice B, i.e., $j > i$ for a qubit pair (Q_i^A, Q_j^B) . From the avoided crossing experiments centered at $\omega = \omega_0$, we extract the qubit-qubit coupling as a function of cell displacement $i - j$. An exponential fit of the data gives the localization length of $\xi = 1.7$ (in units of lattice constant), close to the estimated value from the circuit model of our system (see App. E.3). While theory predicts the coupling between qubits in the remaining combinations to be zero, we report that coupling of $|g_{ij}^{AA, BB}|/2\pi \lesssim 0.66$ MHz and $|g_{ij}^{AB}|/2\pi \lesssim 0.48$ MHz (for $i > j$) are observed, much smaller than the bound-state-induced coupling, e.g., $|g_{45}^{AB}|/2\pi = 32.9$ MHz. We attribute such spurious couplings to the unintended near-field interaction between qubits. Note that we find consistent coupling strength of qubit pairs dependent only on their relative displacement, not on the actual location in the array, suggesting that physics inside MBG remains intact with the introduced waveguide boundaries. In total, the avoided crossing and external linewidth experiments at $\omega = \omega_0$ provide strong evidence of the shape of qubit-photon bound states, compatible with the theoretical photon occupation illustrated in Fig. 6.2b.

Topology-dependent photon scattering

In the passband regime, i.e., when the qubit frequencies lie within the upper or lower passbands, the topology of the waveguide is imprinted on cooperative interaction between qubits and the single-photon scattering response of the system. The topology of the SSH model can be visualized by plotting the complex-valued momentum-space coupling $f(k)$ for k values in the first Brillouin zone (Fig. 6.3a). In the topological (trivial) phase, the contour of $f(k)$ encloses (excludes) the origin of the complex plane, resulting in the winding number of 1 (0) and the corresponding Zak phase of π (0) [260]. This is consistent with the earlier definition based on the sign of δ . It is known that for a regular waveguide with linear dispersion, the coherent exchange interaction J_{ij} and correlated decay Γ_{ij} between qubits at positions x_i and x_j along the waveguide take the forms $J_{ij} \propto \sin \varphi_{ij}$ and $\Gamma_{ij} \propto \cos \varphi_{ij}$ [116, 120], where $\varphi_{ij} = k|x_i - x_j|$ is the phase length. In the case of our topological waveguide, considering a pair of qubits coupled to A/B sublattice on i/j -th unit cell, this argument additionally collects the phase $\phi(k) \equiv \arg f(k)$ [55]. This is an important difference compared to the regular waveguide case, because the zeros of

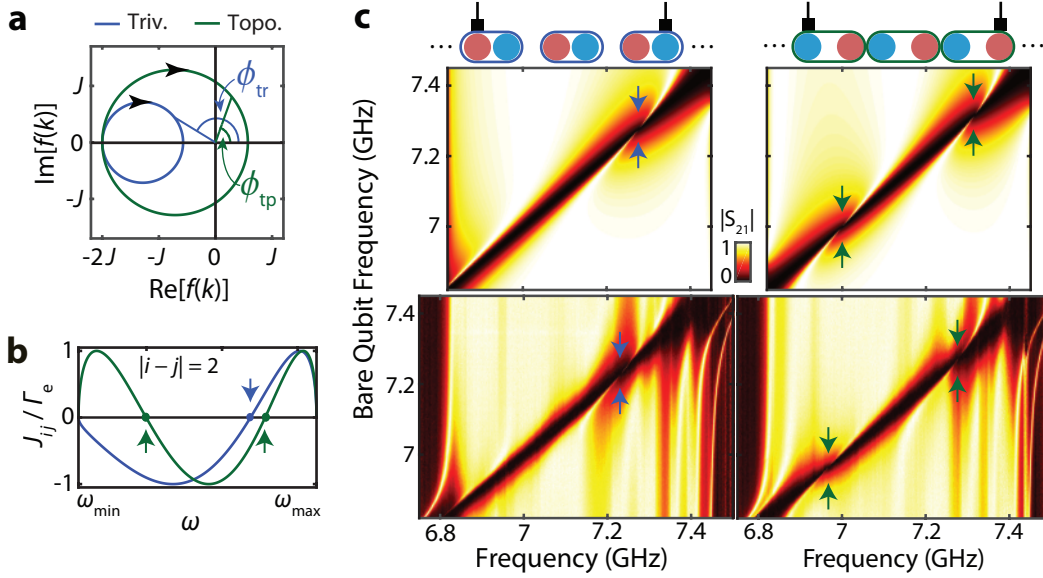


Figure 6.3: Probing band topology with qubits. (a) $f(k)$ in the complex plane for k values in the first Brillouin zone. ϕ_{tr} (ϕ_{tp}) is the phase angle of $f(k)$ for a trivial (topological) section of waveguide, which changes by 0 (π) radians as kd transitions from 0 to π (arc in upper plane following black arrowheads). (b) Coherent exchange interaction J_{ij} between a pair of coupled qubits as a function of frequency inside the passband, normalized to individual qubit decay rate Γ_e (only $kd \in [0, \pi)$ branch is plotted). Here, one qubit is coupled to the A sublattice of the i -th unit cell and the other qubit is coupled to the B sublattice of the j -th unit cell, where $|i - j| = 2$. Blue (green) curve corresponds to a trivial (topological) intermediate section of waveguide between qubits. The intercepts at $J_{ij} = 0$ (filled circles with arrows) correspond to points where perfect super-radiance occurs. (c) Waveguide transmission spectrum $|S_{21}|$ as a qubit pair are resonantly tuned across the UPB of Device I [left: (Q_2^A, Q_4^B) , right: (Q_2^B, Q_4^A)]. Top: schematic illustrating system configuration during the experiment, with left (right) system corresponding to an interacting qubit pair subtending a three-unit-cell section of waveguide in the trivial (topological) phase. Middle and Bottom: two-dimensional color intensity plots of $|S_{21}|$ from theory and experiment, respectively. Swirl patterns (highlighted by arrows) are observed in the vicinity of perfectly super-radiant points, whose number of occurrences differ by one between trivial and topological waveguide sections. The figure is adapted from Ref. [56].

equation

$$\varphi_{ij}(k) \equiv kd|i - j| - \phi(k) = 0 \pmod{\pi} \quad (6.2)$$

determine wavevectors (and corresponding frequencies) where perfect Dicke super-radiance [42] occurs. Due to the properties of $f(k)$ introduced above, for a fixed cell-distance $\Delta n \equiv |i - j| \geq 1$ between qubits there exists exactly $\Delta n - 1$ (Δn) frequency points inside the passband where perfect super-radiance occurs in the trivial (topological) phase. An example for the $\Delta n = 2$ case is shown in Fig. 6.3b. Note that although Eq. (6.2) is satisfied at the band-edge frequencies ω_{\min} and ω_{\max} ($kd = \{0, \pi\}$), they are excluded from the above counting due to breakdown of the Born-Markov approximation (see App. E.7).

To experimentally probe signatures of perfect super-radiance, we tune the frequency of a pair of qubits across the UPB of Device I while keeping the two qubits resonant with each other. We measure the waveguide transmission spectrum S_{21} during this tuning, keeping track of the lineshape of the two-qubit resonance as J_{ij} and Γ_{ij} varies over the tuning. Drastic changes in the waveguide transmission spectrum occur whenever the two-qubit resonance passes through the perfectly super-radiant points, resulting in a swirl pattern in $|S_{21}|$. Such patterns arise from the disappearance of the peak in transmission associated with interference between photons scattered by imperfect super- and sub-radiant states, resembling the electromagnetically-induced transparency in a V-type atomic level structure [263]. As an example, we discuss the cases with qubit pairs (Q_2^A, Q_4^B) and (Q_2^B, Q_5^A) , which are shown in Fig. 6.3c. Each qubit pair configuration encloses a three-unit-cell section of the waveguide; however for the (Q_2^A, Q_4^B) pair the waveguide section is in the trivial phase, whereas for (Q_2^A, Q_4^B) the waveguide section is in the topological phase. Both theory and measurement indicate that the qubit pair (Q_2^A, Q_4^B) has exactly one perfectly super-radiant frequency point in the UPB. For the other qubit pair (Q_2^B, Q_5^A) , with waveguide section in the topological phase, two such points occur (corresponding to $\Delta n = 2$). This observation highlights the fact that while the topological phase of the bulk in the SSH model is ambiguous, a finite section of the array can still be interpreted to have a definite topological phase. Apart from the unintended ripples near the band-edges, the observed lineshapes are in good qualitative agreement with the theoretical expectation in Ref. [55]. The frequency misalignment of swirl patterns between the theory and the experiment is due to the slight discrepancy between the realized circuit model and the ideal SSH model (see App. E.1 for details). Detailed description of the swirl pattern and similar measurement results for other qubit

combinations with varying Δn are reported in App. E.7.

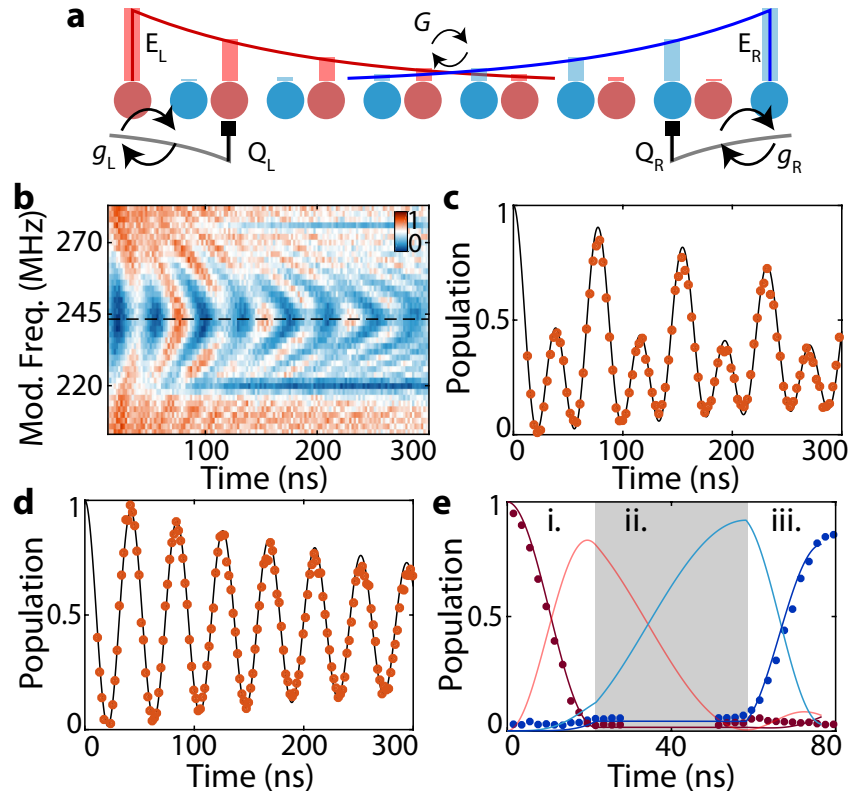


Figure 6.4: Qubit interaction with topological edge modes. (a) Schematic of Device II, consisting of 7 unit cells in the topological phase with qubits $Q_L = Q_i^\alpha$ and $Q_R = Q_j^\beta$ coupled at sites $(i, \alpha) = (2, A)$ and $(j, \beta) = (6, B)$, respectively. E_L and E_R are the left-localized and right-localized edge modes which interact with each other at rate G due to their overlap in the center of the finite waveguide. (b) Chevron-shaped oscillation of Q_L population arising from interaction with edge modes under variable frequency and duration of modulation pulse. The oscillation is nearly symmetric with respect to optimal modulation frequency 242.5 MHz, apart from additional features at (219, 275) MHz due to spurious interaction of unused sidebands with modes inside the passband. (c) Line-cut of panel b (indicated with a dashed line) at the optimal modulation frequency. A population oscillation involving two harmonics is observed due to coupling of E_L to E_R . (d) Vacuum Rabi oscillations between Q_L and E_L when Q_R is parked at the resonant frequency of edge modes to shift the frequency of E_R , during the process in panel (c). In panels (c) and (d) the filled orange circles (black solid lines) are the data from experiment (theory). (e) Population transfer from Q_L to Q_R composed of three consecutive swap transfers $Q_L \rightarrow E_L \rightarrow E_R \rightarrow Q_R$. The population of Q_L (Q_R) during the process is colored dark red (dark blue), with filled circles and solid lines showing the measured data and fit from theory, respectively. The light red (light blue) curve indicates the expected population in E_L (E_R) mode, calculated from theory. The figure is adapted from Ref. [56].

6.4 Quantum state transfer via topological edge states

Finally, to explore the physics associated with topological edge modes, we fabricated a second device, Device II, which realizes a closed quantum system with 7 unit cells in the topological phase (Fig. 6.4a). We denote the photonic sites in the array by (i, α) , where $i = 1-7$ is the cell index and $\alpha = A, B$ is the sublattice index. Due to reflection at the boundary, the passbands on this device appear as sets of discrete resonances. The system supports topological edge modes localized near the sites $(1, A)$ and $(7, B)$ at the boundary, labeled E_L and E_R . The edge modes are spatially distributed with exponentially attenuated tails directed toward the bulk. In a finite system, the non-vanishing overlap between the envelopes of edge states generates a coupling which depends on the localization length ξ and the system size L as $G \sim e^{-L/\xi}$. In Device II, two qubits denoted Q_L and Q_R are coupled to the topological waveguide at sites $(2, A)$ and $(6, B)$, respectively. Each qubit has a local drive line and a flux-bias line, which are connected to room-temperature electronics for control. The qubits are dispersively coupled to readout resonators, which are coupled to a coplanar waveguide for time-domain measurement. The edge mode E_L (E_R) has photon occupation on sublattice A (B), inducing interaction g_L (g_R) with Q_L (Q_R). Due to the directional properties discussed earlier, bound states arising from Q_L and Q_R have photonic envelopes facing away from each other inside the MBG, and hence have no direct coupling to each other. For additional details on Device II and qubit control, refer to App. E.8.

We probe the topological edge modes by utilizing the interaction with the qubits. While parking Q_L at frequency $f_q = 6.835$ GHz inside MBG, we initialize the qubit into its excited state by applying a microwave π -pulse to the local drive line. Then, the frequency of the qubit is parametrically modulated [77] such that the first-order sideband of the qubit transition frequency is nearly resonant with E_L . After a variable duration of the frequency modulation pulse, the state of the qubit is read out. From this measurement, we find a chevron-shaped oscillation of the qubit population in time centered at modulation frequency 242.5 MHz (Fig. 6.4b). We find the population oscillation at this modulation frequency to contain two harmonic components as shown in Fig. 6.4c, a general feature of a system consisting of three states with two exchange-type interactions g_1 and g_2 . In such cases, three single-excitation eigenstates exist at $0, \pm g$ with respect to the bare resonant frequency of the emitters ($g \equiv \sqrt{g_1^2 + g_2^2}$), and since the only possible spacing between the eigenstates in this case is g and $2g$, the dynamics of the qubit population exhibits two frequency components with a ratio of two. From fitting the Q_L population

oscillation data in Fig. 6.4c, the coupling between E_L and E_R is extracted to be $G/2\pi = 5.05$ MHz. Parking Q_R at the bare resonant frequency $\omega_E/2\pi = 6.601$ GHz of the edge modes, E_R strongly hybridizes with Q_R and is spectrally distributed at $\pm g_R$ with respect to the original frequency ($g_R/2\pi = 57.3$ MHz). As this splitting is much larger than the coupling of E_R to E_L , the interaction channel $E_L \leftrightarrow E_R$ is effectively suppressed and the vacuum Rabi oscillation only involving Q_L and E_L is recovered (Fig. 6.4d) by applying the above-mentioned pulse sequence on Q_L . The vacuum Rabi oscillation is a signature of strong coupling between the qubit and the edge state, a bosonic mode, as described by cavity QED [29]. A similar result was achieved by applying a simultaneous modulation pulse on Q_R to put its first-order sideband near-resonance with the bare edge modes (instead of parking it near resonance), which we call the *double-modulation* scheme. From the vacuum Rabi oscillation $Q_L \leftrightarrow E_L$ ($Q_R \leftrightarrow E_R$) using the double-modulation scheme, we find the effective qubit-edge mode coupling to be $\tilde{g}_L/2\pi = 23.8$ MHz ($\tilde{g}_R/2\pi = 22.5$ MHz).

The half-period of vacuum Rabi oscillation corresponds to an iSWAP gate between Q_L and E_L (or Q_R and E_R), which enables control over the edge modes with single-photon precision. As a demonstration of this tool, we perform remote population transfer between Q_L and Q_R through the non-local coupling of topological edge modes E_L and E_R . The qubit Q_L (Q_R) is parked at frequency 6.829 GHz (6.835 GHz) and prepared in its excited (ground) state. The transfer protocol, consisting of three steps, is implemented as follows: i) an iSWAP gate between Q_L and E_L is applied by utilizing the vacuum Rabi oscillation during the double-modulation scheme mentioned above, ii) the frequency modulation is turned off and population is exchanged from E_L to E_R using the interaction G , iii) another iSWAP gate between Q_R and E_R is applied to map the population from E_R to Q_R . The population of both qubits at any time within the transfer process is measured using multiplexed readout [264] (Fig. 6.4e). We find the final population in Q_R after the transfer process to be 87 %. Numerical simulations suggest that (App. E.8) the infidelity in preparing the initial excited state accounts for 1.6 % of the population decrease, the leakage to the unintended edge mode due to ever-present interaction G contributes 4.9 %, and the remaining 6.5 % is ascribed to the short coherence time of qubits away from the flux-insensitive point [$T_2^* = 344$ (539) ns for Q_L (Q_R) at working point].

We expect that a moderate improvement on the demonstrated population transfer protocol could be achieved by careful enhancement of the excited state preparation

and the iSWAP gates, i.e. optimizing the shapes of the control pulses [265–268]. The coherence-limited infidelity can be mitigated by utilizing a less flux-sensitive qubit design [269, 270] or by reducing the generic noise level of the experimental setup [271]. Further, incorporating tunable couplers [214] into the existing metamaterial architecture to control the localization length of edge states *in situ* will fully address the population leakage into unintended interaction channels, and more importantly, enable robust quantum state transfer over long distances [272]. Together with many-body protection to enhance the robustness of topological states [255], building blocks of quantum communication [26] under topological protection are also conceivable.

6.5 Discussion and outlook

Looking forward, we envision several research directions to be explored beyond the work presented here. First, the topology-dependent photon scattering in photonic bands that is imprinted in the cooperative interaction of qubits can lead to new ways of measuring topological invariants in photonic systems [273]. The directional and long-range photon-mediated interactions between qubits demonstrated in our work also opens avenues to synthesize non-trivial quantum many-body states of qubits, such as the double Néel state [55]. Even without technical advances in fabrication [274–276], a natural scale-up of the current system will allow for the construction of moderate to large-scale quantum many-body systems. Specifically, due to the on-chip wiring efficiency of a linear waveguide QED architecture, with realistic refinements involving placement of local control lines on qubits and compact readout resonators coupled to the tapered passband (intrinsically acting as Purcell filters [184]), we expect that a fully controlled quantum many-body system consisting of 100 qubits is realizable in the near future. In such systems, protocols for preparing and stabilizing [101, 255, 277] quantum many-body states could be utilized and tested. Additionally, the flexibility of superconducting metamaterial architectures [109, 153] can be further exploited to realize other novel types of topological photonic baths [46, 55, 259]. While the present work was limited to a one-dimensional system, the state-of-the-art technologies in superconducting quantum circuits [107] utilizing flip-chip methods [275, 276] will enable integration of qubits into two-dimensional metamaterial surfaces. It also remains to be explored whether topological models with broken time-reversal symmetry, an actively pursued approach in systems consisting of arrays of three-dimensional microwave cavities [253, 278], could be realized in compact chip-based architectures. Alto-

gether, our work sheds light on opportunities in superconducting circuits to explore quantum many-body physics originating from novel types of photon-mediated interactions in topological waveguide QED, and paves the way for creating synthetic quantum matter and performing quantum simulation [13, 82, 86, 93, 279].

*Chapter 7***AN INTERMEDIATE-SCALE QUANTUM PROCESSOR BASED
ON DISPERSIVE WAVEGUIDE QED**

The work discussed in the previous chapters laid the groundwork for realizing a scalable waveguide QED-based architecture for quantum simulation and computation. In particular, we have for the first time demonstrated coherent multi-qubit dynamics in waveguide QED in Chapter 4, developed and characterized a compact and extensible waveguide structure based on superconducting metamaterial in Chapter 5, and interfaced a large number of qubits with a metamaterial waveguide with limited control (only Z without XY and readout) and with spectroscopic characterization in Chapter 6. Integration of such building blocks of waveguide QED with state-of-the-art control tools developed for quantum information processing is predicted to enable new directions to perform quantum simulation of many-body physics and quantum computation. In this chapter, we introduce the culmination of our efforts, demonstrating our ongoing work on the construction of a scalable quantum processor with tunable-range waveguide-mediated connectivity, which involves ten superconducting qubits with full individual addressing and high-fidelity readout.

7.1 Introduction

Realizing a scalable architecture for quantum computation and simulation has been a central goal in the field of quantum information science, with numerous physical platforms, ranging from atom-based systems such as trapped ions and cold neutral atoms to solid-state systems such as superconducting qubits, quantum dots, and color centers in diamond, being actively investigated. While much of the attention was devoted to systems with only nearest-neighbor coupling between quantum emitters, particularly for the realization of surface code [65, 66], achieving a quantum processor with long-range connectivity remains an important subject. On the fundamental side, quantum many-body systems with high connectivity sheds new light on important topics in contemporary physics such as quantum thermalization [84], dynamics of quantum entanglement [86], and novel quantum phases of matter [15]. On the practical side, study of such long-range coupled systems can contribute to the realization of quantum algorithms and quantum error correcting codes which

harness non-local quantum gate operations [57].

Increasing the size of a system often contradicts with the requirement for maintaining a degree of connectivity that used to be present in a smaller-sized system. An example is the cavity-mediated coupling between qubits which enables all-to-all connectivity between qubits coupled to a common cavity [110–112]. There has been recent demonstrations of intermediate-scale superconducting quantum processors employing this principle, controlling about 20 qubits [105, 106], but it is evident that such scheme is not scalable owing to the breakdown of the single-mode picture [280], with the free-spectral range of cavity modes inversely proportional to the length scale of the cavity. An alternative approach is to utilize an intrinsically one-dimensional structure such as a waveguide [40], but operation in settings where emitters are nearly resonant to a continuum of waveguide modes is subjected to substantial spontaneous emission, requiring fine-tuned strategies to mitigate dissipation-induced loss of quantum information [108, 120, 124, 281].

An intermediate regime is to utilize quantum emitters whose transition frequencies are situated inside a bandgap of a photonic structure. As first predicted by Sajeev John and Jian Wang in 1990 [126], the quantum emitters in such a scenario are known to form emitter-photon bound states whose spontaneous emission to the photonic structure is forbidden. The photonic tails of the bound states have been shown to mediate tunable-range interactions between quantum emitters [127, 128], recently revisited in the context of quantum simulation of many-body physics [125]. While there has been pioneering demonstrations of atoms interfaced with engineered nanophotonic waveguides [44] to achieve this feat, systematic control over atom-photon bound states has been thwarted by technical difficulties associated with trapping of atoms near nanophotonic structures [134, 143]. Parallel efforts have been taken in superconducting circuits to implement this idea by coupling superconducting qubits to a microwave analog of photonic crystal [215], created with a impedance-modulated microwave transmission line, or a metamaterial composed of an array of deep sub-wavelength resonant elements, such as compact LC resonators [56, 109] or high-impedance resonators employing Josephson superinductance [282]. However, investigations of such platforms were so far restricted to cases involving only two qubits [199, 282] or a large number of qubits with limited control [56, 283], with the long-standing goal of realizing a fully controllable waveguide-based quantum processor involving many qubits still waiting to be explored.

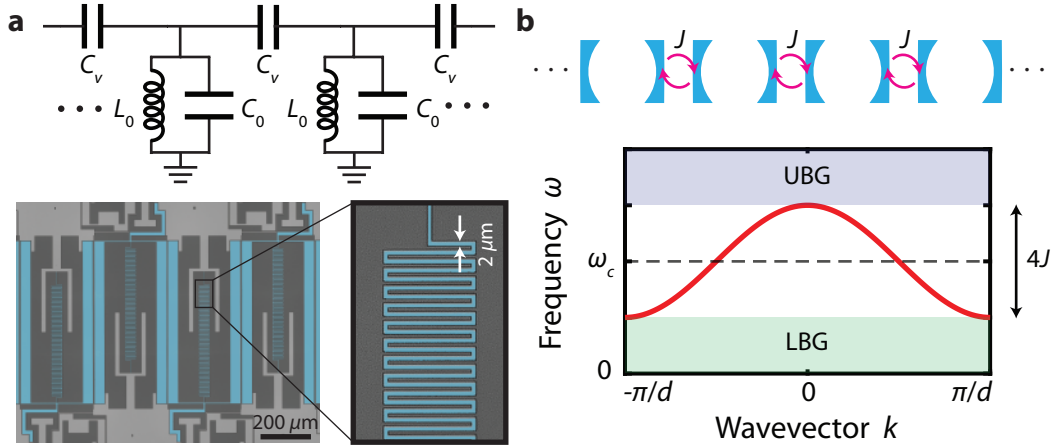


Figure 7.1: Metamaterial waveguide. **a**, The metamaterial waveguide consists of a one-dimensional array of LC resonators (parallel inductance L_0 and capacitance C_0 to the ground) capacitively coupled to nearest neighbors at capacitance C_v , whose electrical circuit model is illustrated on the top. The bottom panel shows the realization of this model with compact microwave resonators on chip, each consisting of a planar capacitor and a meander inductor with a $2\ \mu\text{m}$ pitch. **b**, A simple representation of the metamaterial waveguide in terms of an array of coupled cavities (resonant frequency ω_c) with nearest-neighbor tunneling rate J (top) and the corresponding dispersion relation assuming a lattice constant of d (bottom). Two bandgaps—upper bandgap (UBG) and lower bandgap (LBG)—and a transmission band at detunings $[-2J, 2J]$ with respect to the bare cavity frequency ω_c appears.

In this work, we demonstrate an intermediate-scale quantum processor based on an extensible photonic waveguide design, realized with superconducting qubits coupled to a compact, low-loss metamaterial waveguide on chip [56, 109, 153]. When the transition frequencies of qubits are tuned inside the band gap, the metamaterial waveguide acts as a bus for mediating tunable long-range coupling between distant qubits. In addition, the dressing of qubits with waveguide photons is shown to modify the spacing of energy levels, resulting in a tunable anharmonicity. The transmission band of the metamaterial waveguide is simultaneously utilized as a channel for rapid single-shot readout of qubits at a high fidelity without compromising the coherence time of qubits [184]. Finally, we explore quantum many-body dynamics associated with the long-range nature of coupling in this platform.

7.2 Metamaterial quantum processor

As a scalable photonic medium for inducing long-range interaction between qubits, we consider a metamaterial waveguide consisting of an array of lumped-element microwave resonators, illustrated in Fig. 7.1a. Each resonator forming the metamaterial can be described as a LC resonator of parallel inductance L_0 and capacitance

C_0 to the ground and is coupled to its nearest neighbors with capacitance C_v . To first order in the ratio of coupling capacitance to self capacitance, the metamaterial waveguide can be simply described as a tight-binding lattice of microwave cavities at a resonant frequency $\omega_c = 1/\sqrt{L_0(C_0 + 2C_v)}$ with a positive nearest-neighbor tunnel coupling $J = \omega_c C_v / [2(C_0 + 2C_v)]$ (Fig. 7.1b), whose Hamiltonian is written as

$$\hat{H}_{\text{wg}}/\hbar = \sum_n \left[\omega_c \hat{a}_n^\dagger \hat{a}_n + J(\hat{a}_n^\dagger \hat{a}_{n+1} + \hat{a}_{n+1}^\dagger \hat{a}_n) \right]. \quad (7.1)$$

Here, \hat{a}_n (\hat{a}_n^\dagger) is the annihilation (creation) operator of the cavity at the n th site of the metamaterial. In the momentum-space representation, this Hamiltonian is transformed into one with a set of uncoupled modes $\hat{H}_{\text{wg}} = \hbar \sum_k \omega_k \hat{a}_k^\dagger \hat{a}_k$ with a dispersion relation given by

$$\omega_k = \omega_c + 2J \cos(kd), \quad (7.2)$$

where k is the wavevector and d is the lattice constant of the metamaterial. Under this description, the transmission band lies at detunings $[-2J, 2J]$ with respect to the resonant frequency ω_c of the cavity. The photonic bandgap lying at frequencies lower (higher) than the transmission band is denoted as the lower (upper) bandgap. In practice, the spatially extended character of charge operators of the metamaterial canonically conjugate to the node fluxes [226] significantly alters the dispersion relation when the coupling capacitances are substantial, which is discussed in Refs. [56, 153].

Our quantum processor is realized by coupling ten transmon qubits [190] (labeled as Q_i , $i = 1-10$) to a common metamaterial waveguide consisting of 42 resonator sites with lattice constant $d = 292 \mu\text{m}$, as illustrated in Fig. 7.2. Each qubit, capacitively coupled to a resonator site of the metamaterial, is equipped with its own charge drive line and flux bias line for individual XY and Z controls, respectively. The metamaterial resonators are staggered to reduce stray near-field coupling between qubits coupled to the metamaterial waveguide. In addition, an additional compact LC resonator capacitively couples to each qubit as well as the metamaterial resonator at the corresponding site, allowing for dispersive readout of the qubit utilizing the transmission band of the metamaterial waveguide. Such readout resonators are designed to have resonant frequencies inside the transmission band of the metamaterial waveguide, whose sharp response in a finite-sized system owing to impedance mismatch at the boundary is mitigated by tapering sections. The

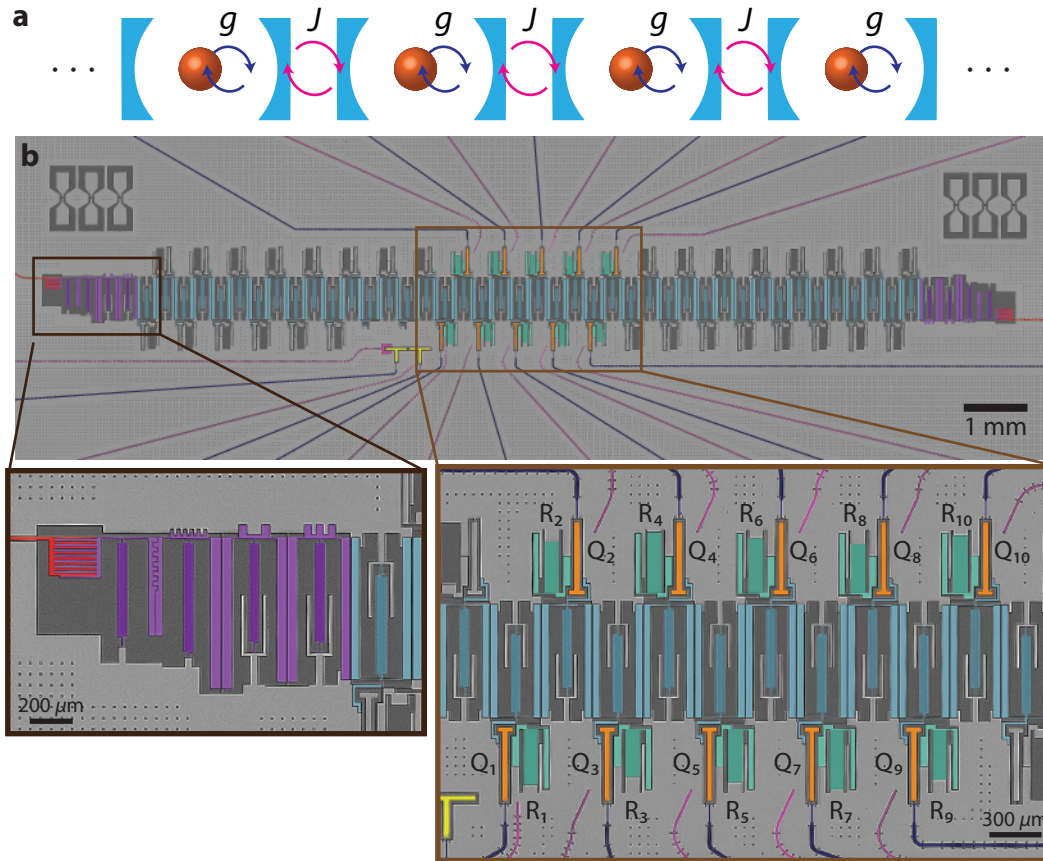


Figure 7.2: Description of the metamaterial quantum processor. **a**, A cartoon representing an array of cavities with atoms, with tunnel coupling J between photons of neighboring cavities and atom-photon coupling g inside each cavity. **b**, False-colored optical micrograph of the device, which realizes the scheme in panel **a** with superconducting circuits. The device consists of a metamaterial waveguide formed by an array of compact microwave resonators (light blue) to which superconducting transmon qubits (orange; labeled as Q_i) and readout resonators (green; labeled as R_i) are coupled ($i = 1-10$). The charge drive lines and flux bias lines for single-qubit manipulation are colored in dark blue and pink, respectively. The metamaterial waveguide transitions to the external input-output ports (red) at the boundary via engineered tapering sections (violet), each consisting of four specifically designed capacitively coupled compact microwave resonators. Two ancillary qubits, colored yellow, are beyond the scope of this work.

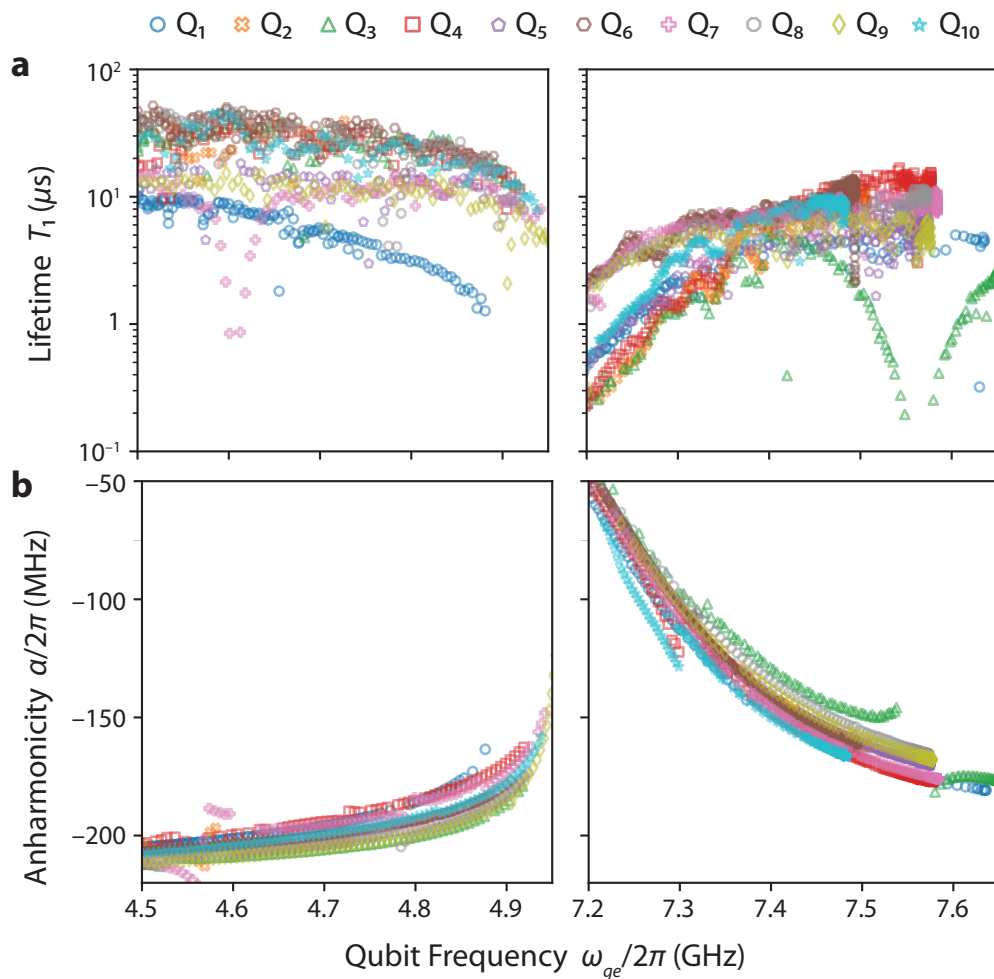


Figure 7.3: Single-qubit characterization. **a**, The lifetime T_1 of qubits plotted against the $|g\rangle-|e\rangle$ transition frequency ω_{ge} inside the lower (left panel) and the upper (right panel) bandgaps. **b**, The anharmonicity α of qubits plotted against the $|g\rangle-|e\rangle$ transition frequency ω_{ge} inside the lower (left panel) and the upper (right panel) bandgaps. Throughout the figure, the marker of each datapoint represents the qubit label, the meaning of which is summarized on the top.

tapering section consists of a set of four specifically designed resonators at each end of the metamaterial waveguide, prior to transition to coplanar waveguides with $Z_0 = 50 \Omega$ characteristic impedance connected to the input/output ports. Details on the fabrication of the device and the cryogenic setup is outlined in Chapter 3.

7.3 Single-qubit characterization

We begin the characterization of the metamaterial quantum processor by investigating the properties of each qubit dependent on the frequency tuning. We measure the lifetime T_1 of each qubit across both the lower and the upper bandgaps while the

transition frequencies of the remaining qubits are far-detuned to be situated inside the bandgap other than where the measured qubit lies in. The measurement result illustrated in Fig. 7.3a shows that the qubits are sufficiently protected from radiative decay deep inside the bandgap with a gradual reduction in lifetime as the transition frequency approaches the edges of the transmission band. The additional decay mechanism close to the band-edges is attributed to the overlap of long photonic tail of qubit-photon bound states with the external ports close to the band edge, which can be suppressed if a metamaterial long compared to the localization length of the bound states is used.

We also perform measurement of the anharmonicity $\alpha = \omega_{ef} - \omega_{ge}$ of qubit-photon bound states in the bandgap regime by performing spectroscopy conditioned on the qubit initialized in the first excited state $|e\rangle$ (Fig. 7.3b). Deep inside the lower bandgap near $\omega_{ge}/2\pi \approx 3.6$ GHz, we find a nearly constant value of anharmonicity $\alpha/2\pi \approx -220$ MHz of bare transmons, the magnitude of which is reduced by almost factor of two close to the lower band-edge (about 4.95 GHz) owing to the anomalous Lamb shift [129] of the $|g\rangle$ - $|e\rangle$ transition frequency ω_{ge} . Inside the upper bandgap, even stronger hybridization of $|e\rangle$ - $|f\rangle$ transition with the photonic modes inside the transmission band results in a change in anharmonicity sharper than inside the lower bandgap. Such modification of anharmonicity, as noted in Ref. [199], can be utilized as a knob for tuning the attractive interactions between photons on a transmon site, a unique feature of qubit-photon bound states. The variation of anharmonicity values between qubits is ascribed to the disorder in the fabrication.

7.4 Interaction between qubit-photon bound states

A notable property of the metamaterial waveguide is the interaction between qubit-photon bound states arising from the spatial overlap of photonic tails, which enables qubit-qubit connectivity beyond nearest neighbors. In the simplest description of the metamaterial waveguide in terms of coupled cavity array discussed in Eq. (7.1), it is known that the coupling J_{ij} between a pair of qubit-photon bound states associated with qubits at sites (i, j) of the metamaterial is given by [205]

$$J_{ij} = \frac{g_i g_j}{\sqrt{(\omega_c - \omega_b)^2 - 4J^2}} s_{ij} e^{-|i-j|/\xi} \quad (7.3)$$

where g_i is the coupling between the qubit and the cavity at the i th site, ω_b is the frequency of the qubit-photon bound state, and

$$\xi = \left[\operatorname{arccosh} \left(\frac{|\omega_c - \omega_b|}{2J} \right) \right]^{-1} \quad (7.4)$$

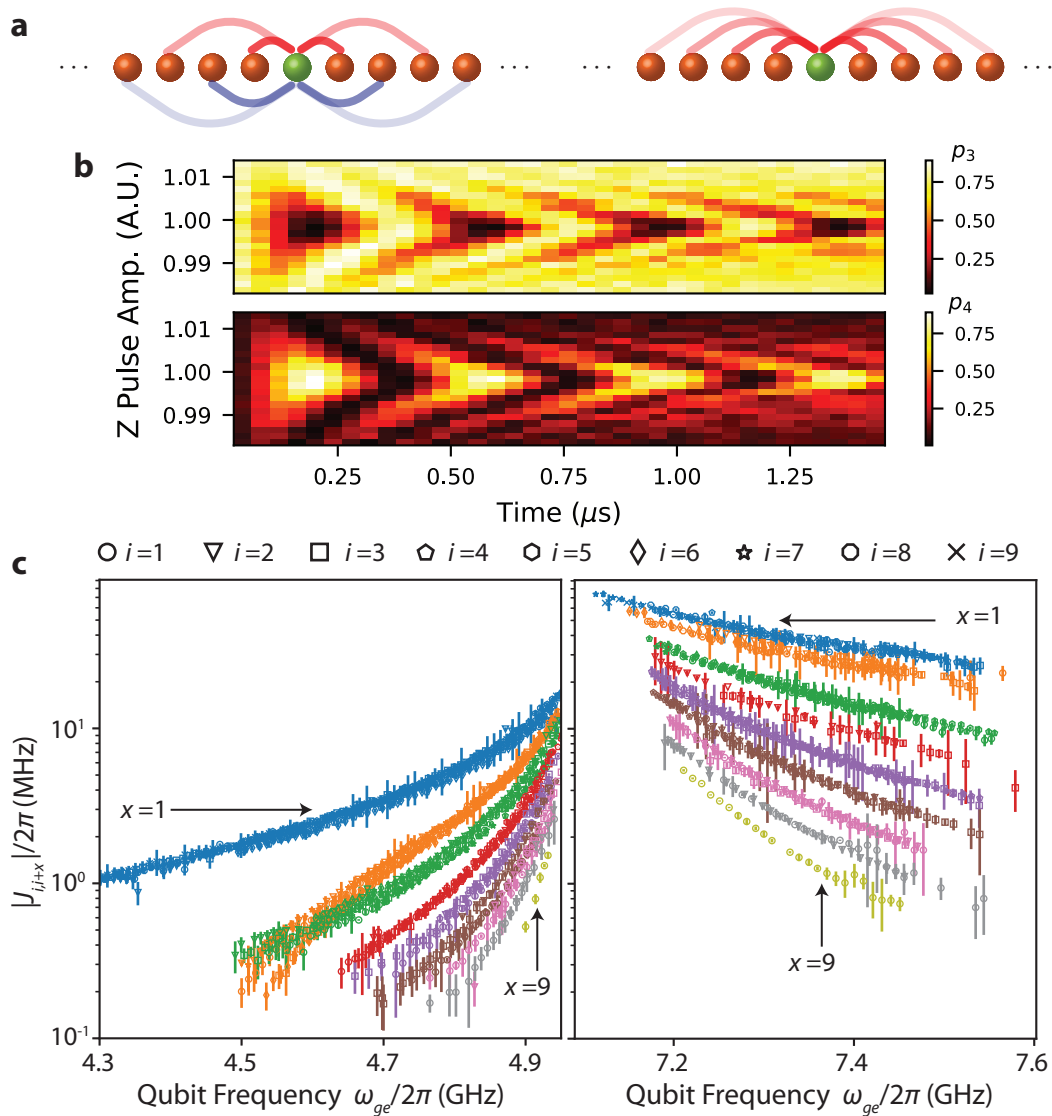


Figure 7.4: Qubit-qubit interactions. **a**, Cartoons illustrating the characteristics of long-range coupling between qubits in the metamaterial quantum processor. Left: inside the lower bandgap, the qubit-qubit coupling alternates between positive (red) and negative (blue) signs with magnitude decaying exponentially with the distance. Right: inside the upper bandgap, the sign of qubit-qubit coupling is positive (colored red) with magnitude decaying exponentially with the distance. **b**, Chevron pattern obtained from interaction of Q_3 and Q_4 , where Q_3 is initialized in the excited state and both Q_3 and Q_4 are dynamically tuned on resonance to 4.37 GHz. **c**, The magnitude of qubit-qubit interaction rate J_{ij} measured between qubit pair (Q_i, Q_j) at frequencies in the lower bandgap (left panel) and the upper bandgap (right panel). The colors of the datapoints indicate the distance $x = j - i$ between the pair of qubits (blue: $x = 1$, orange: $x = 2$, green: $x = 3$, red: $x = 4$, purple: $x = 5$, brown: $x = 6$, pink: $x = 7$, gray: $x = 8$, yellow: $x = 9$) and the shapes of marker represents the index of the first qubit Q_i of the pair, whose correspondence is summarized on the top of the panel.

is the localization length of the qubit-photon bound state. Here, the sign factor s_{ij} takes the value $s_{ij} = -(-1)^{i-j}$ ($s_{ij} = 1$) inside the lower (upper) bandgap, reflecting the wavevector $k = \pi/d$ ($k = 0$) at which the band-edge occurs (see Fig. 7.4a). In practice, the modification of dispersion relation discussed earlier also affects the exact form of the localization length ξ of qubit-photon bound states and their coupling J_{ij} to be modified from Eqs. (7.3) and (7.4), which can be numerically calculated.

We have characterized the strength of interaction between qubit-photon bound states in the time domain by utilizing a pulse sequence described as follows: we first prepare the qubit pair (i, j) in state $|e\rangle_i|g\rangle_j$ by applying a microwave π -pulse on Q_i , followed by crosstalk- and distortion-corrected [284] fast flux-bias pulses with a variable duration on both qubits to dynamically tune the qubits on resonance at the desired frequency, which induces vacuum Rabi oscillation between the chosen qubit pair. Here, the amplitude of the flux-bias pulse applied on one of the qubits is also swept to find an exact resonance condition. After the end of the flux-bias pulse, the qubits are returned to their original static frequencies and read out at a fixed time relative to the beginning of the sequence. Then, the magnitude of coupling rate $|J_{ij}|$ between the qubit pair is determined by fitting the two-dimensional Chevron pattern of qubit population plotted against the duration τ and the amplitude of the flux-bias pulse, an example of which is illustrated in Fig. 7.4b. We have repeated this experiment for all possible pairs of qubits in the system across a wide range of dynamically tuned frequencies close to the band-edges, summarized in Fig. 7.4c.

7.5 High-fidelity single-shot readout

The metamaterial waveguide in our quantum processor, having qubits operating inside the bandgaps and dispersive readout performed employing the transmission band, naturally satisfies the requirements for a Purcell filter [184, 285]. The excess spontaneous emission rate of a qubit caused by Purcell decay [114] through a readout resonator is known to be proportional to the ratio $r_P \equiv \text{Re}[Z_{\text{ext}}(\omega_q)]/\text{Re}[Z_{\text{ext}}(\omega_r)]$ associated with the external impedance $Z_{\text{ext}}(\omega)$ evaluated at the qubit frequency ω_q and at the readout resonator frequency ω_r [286]. Utilizing a Purcell filter based on periodic microwave structures, such as our metamaterial waveguide, will greatly suppress this ratio r_P as the Bloch impedance of a periodic structure becomes purely imaginary inside the bandgap while matching to the external 50Ω network inside the transmission band requires it to be purely real [180], resulting in a small number $r_P \ll 1$ arising only from parasitic intrinsic loss and finite-size effects. In such

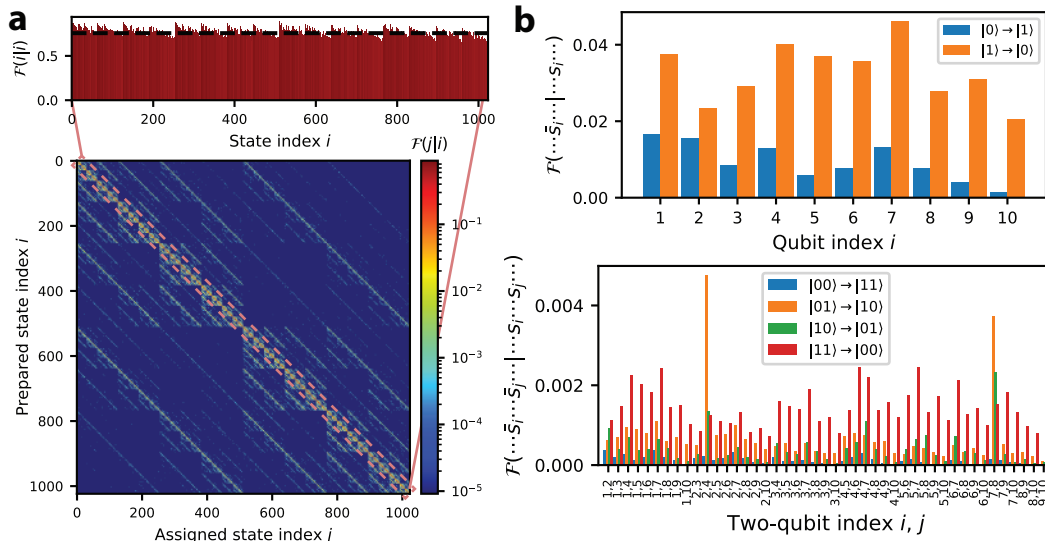


Figure 7.5: Multi-qubit readout characterization. **a**, Assignment probability matrix $\mathcal{F}(j|i)$ for each prepared multi-qubit basis state index i and the assigned multi-qubit basis state index j ($0 \leq i, j < 2^{10}$ are decimal representations of 10-bitstrings representing multi-qubit basis states), extracted from random preparation of multi-qubit basis states and measurement repeated for 10^6 counts. The inset shows the diagonal elements $\mathcal{F}(i|i)$ of the assignment probability matrix whose mean value 0.7566 (black dashed line) corresponds to the multi-qubit readout fidelity. **b**, Average of off-diagonal elements of the assignment probability matrix corresponding to each single-qubit and two-qubit error process. Top: single-qubit bit-flip error rate (average of assignment probability matrix elements corresponding to preparation of state s_i and assignment of state \bar{s}_i on qubit Q_i ; the states of remaining qubits are fixed) during the readout. It is observed that the single-qubit decay $|1\rangle \rightarrow |0\rangle$ (few percent on average) is the dominant contributor to the infidelity of the readout. Bottom: Two-qubit bit-flip error rate (average of assignment probability matrix elements corresponding to preparation of state s_i, s_j and assignment of state \bar{s}_i, \bar{s}_j on qubits Q_i, Q_j ; the states of remaining qubits are fixed) during the readout. The two-qubit error rates are an order of magnitude smaller than the single-qubit error rates.

a regime, the coupling between readout resonator and qubit as well as the decay rate κ of readout resonator can be made very large without compromising qubit coherence, potentially enabling an ultrafast qubit state measurement. From the design perspectives, this also allows us to perform resource-efficient without need for placing additional large-footprint elements on a chip for a rapid, high fidelity readout [185, 287].

From the experiment, we are able to find high single-qubit readout fidelity exceeding 98 % in most cases with only 100–200 ns long readout and integration with optimal weights [186, 288], on par with the state-of-the-art in the field [185]. While the naive approach of multiplexing the calibrated single-qubit readout pulses at different

frequencies was considered sufficient for long (about 1 μ s) multiplexed readout of few qubits, it was observed that this method is no longer valid for short (about 400 ns or shorter) multiplexed readout of all ten qubits in our system. This is ascribed to high overall readout power sent into the system, resulting in unexpected non-linear effects, the origin of which is yet to be confirmed. To overcome this, we have successfully developed a routine to simultaneously calibrate the set of frequencies and amplitudes of all ten readout signals based on linear discriminant analysis [186] for determination of readout fidelity and outlier counting to prevent measurement-induced state transitions [289]. An example of the multiplexed readout benchmark result after such calibration is illustrated in Fig. 7.5, where the fidelity of assignment of 2^{10} multi-qubit basis states of ten qubits is $\mathcal{F} = 75.66\%$, corresponding to about $\mathcal{F}_{1Q} \approx 97.25\%$ single-qubit readout fidelity. Our multiplexed readout is adversely affected by correlated multi-qubit state preparation error as well as readout crosstalk effects [287], which will be a subject of further investigations. Note that our method for processing readout signals for state discrimination is fully implemented in real time and therefore allows us to perform low-latency feedback operations based on the outcome of ten-qubit measurement. An example use of this real-time feedback is active reset where the state of all qubits is actively reset to the ground state based on the measured bitstring, allowing us to perform multi-qubit experiments at an ultrafast repetition rate exceeding 100 kHz.

7.6 Quantum many-body dynamics

Finally, as a demonstration of novel quantum many-body dynamics in our quantum processor, we induce quantum walk of two photons along the qubit-photon bound states inside the lower bandgap (Fig. 7.6), where the pair of qubits Q₅ and Q₆ located at the center of the array are initialized in the excited state at their idle frequencies after which a rapid simultaneous tuning of all qubits' transition frequencies to the desired interaction frequency takes place. After a variable interaction time, all the qubits return to their original idle frequencies and are simultaneously read out. The distribution of the bitstrings $|n_1 n_2 \cdots n_{10}\rangle$ measured after such quenched time evolution allows us to determine the population $p_i = \langle \hat{n}_i \rangle$ at each site i and the correlation matrix $C_{ij} = \langle \hat{n}_i \hat{n}_j \rangle$ for every pair (i, j) of sites $(i, j = 1-10)$. From the time evolution of population p_i shown in Fig. 7.6a, we find a gradual increase in the speed of propagation as the qubit-photon bound states are tuned closer to the band edge. Also, a more complicated interference pattern associated with long-range coupling is observed near the band edge, suggesting a rapid buildup of

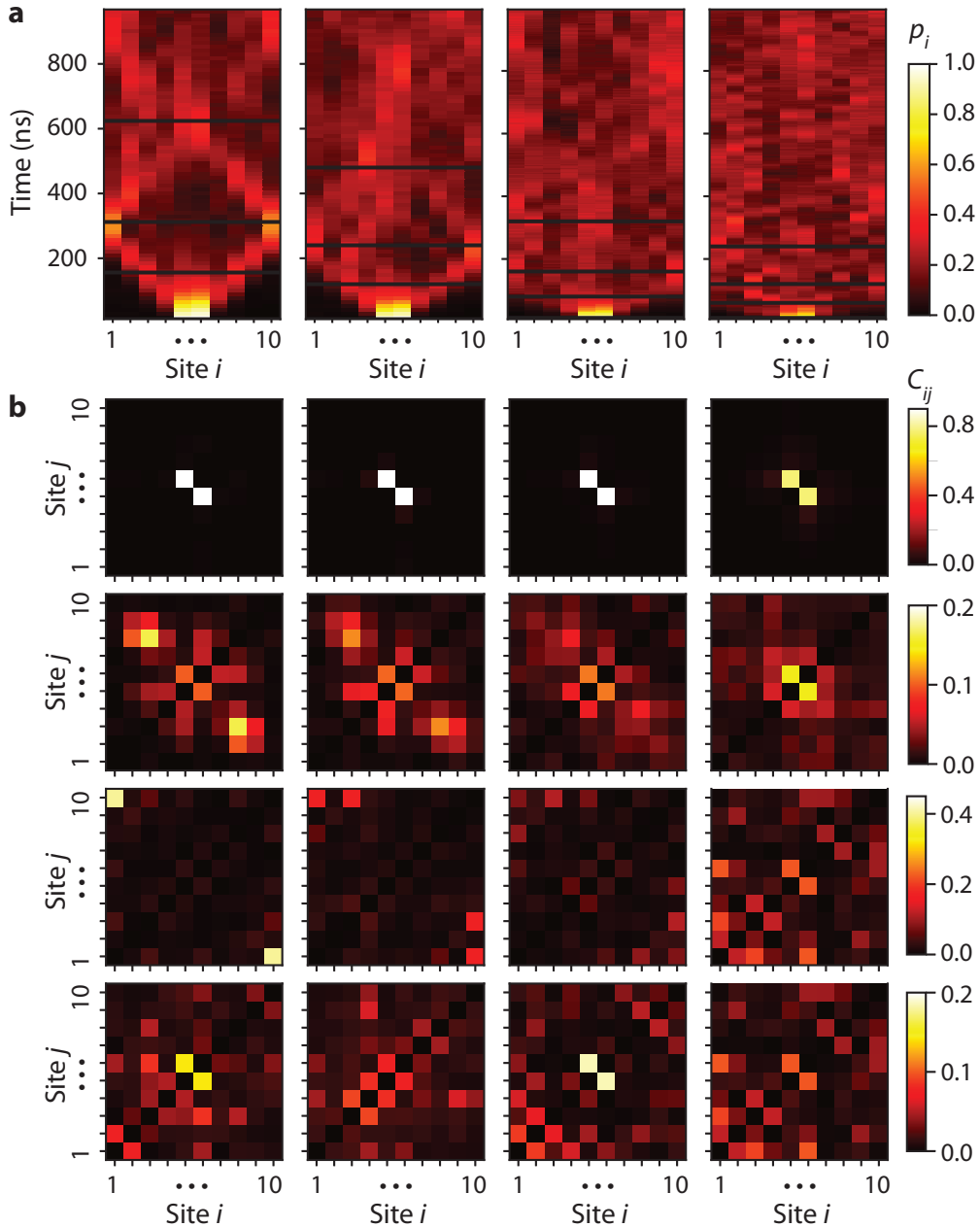


Figure 7.6: Quantum walk of two photons along qubit-photon bound states. **a**, Qubit population p_i plotted as a function of time during the quantum walk of two photons initialized at Q_5 and Q_6 . The subpanels correspond to quantum walks at interaction frequencies (4.50, 4.60, 4.71, 4.80)GHz from left to right. **b**, The particle-particle correlation matrix C_{ij} is plotted at a few time steps during the quantum walk illustrated in panel **a**. The subpanels on each column (corresponding to result from the interaction frequencies in panel **a**) shows the correlation matrix at the instances soon after initialization $t = 12$ ns, approximately halfway to the first propagation to the boundary $t = t_1/2$, approximately the first major reflection at the boundary $t = t_1$, and approximately the first major refocusing $t = 2t_1$, from top to bottom, which are indicated with black solid lines on the corresponding subpanel in panel **a**. Here, $t_1 = (312, 240, 160, 120)$ ns from left to right columns.

quantum entanglement that would have occurred at a much slower rate in the case of only nearest-neighbor coupling [100]. This is also observed in the pattern of the correlation matrix shown in Fig. 7.6b where the initially localized particle-particle correlation gets quickly delocalized with the presence of long-range coupling with refocusing quantum walkers becoming quickly invisible. Such long-range character of coupling gives rise to a non-integrable Hamiltonian in the two-excitation manifold, resulting in a chaotic quantum many-body evolution.

7.7 Discussion and outlook

The quantum processor demonstrated in our work naturally opens up novel opportunities to explore quantum many-body physics. An extension of our work will enable the study of emergent randomness from quantum many-body chaos [290, 291], which sheds new light on the understanding of quantum thermalization. Employing the capability to perform real-time measurement and feedforward operations at a low latency demonstrated in this work, a novel hybrid quantum-classical protocol for controlling quantum many-body states can be envisioned. While not scalable, qubit readout utilizing the transmission band of the metamaterial waveguide discussed in our work shows an interesting regime of Purcell filter, which can be harnessed to perform ultrafast dispersive readout at a high fidelity. With the addition of an individual filter between the metamaterial waveguide and each readout resonator, vanishingly small readout crosstalk can be achieved [287], where experimental studies of measurement-induced phase transition [292–295] are expected to be within reach [296]. On the practical hand, new ways of building up large-scale superconducting quantum processors can be conceived, which has been so far limited to nearest-neighbor connectivity in most cases [76, 297–299]. In particular, the integration of tunable coupler [300, 301] between qubits and metamaterial waveguide will enable high-fidelity metamaterial-mediated quantum gates, which will allow for experimental demonstrations of quantum algorithms and quantum error correction schemes requiring non-local quantum gate operations. Overall, our work opens up new avenues for quantum information processing in the noisy intermediate-scale quantum era [75].

OUTLOOK AND FUTURE DIRECTIONS

Our work described in the thesis, the experimental studies of waveguide QED in the platform of superconducting circuits, provides a unique ground for studying quantum many-body physics and quantum computation with long-range photon-mediated interactions between qubits. Below I will enumerate a few interesting potential directions beyond the work described in the thesis.

8.1 Opportunities for studying many-body physics

Compared to traditional atom-based systems, superconducting qubits are readily equipped with full individual local qubit control (XY and Z), quantum non-demolition measurement, and real-time feedback operation. Without need for trapping atoms, experiments with superconducting qubits can be performed at ultra-high repetition rates (up to ~ 1 MHz with active qubit reset [302–305]), offering new possibilities to study higher-order many-body effects that are often obscured by statistical fluctuations. Utilizing the advanced control and calibration techniques developed for building up practical quantum computers [76, 306], a novel set of tools for controlling and measuring quantum many-body systems could be envisioned. In the following, I outline few research directions for exploring quantum many-body physics with our quantum processor.

Extended Bose-Hubbard model

The Bose-Hubbard model [307, 308] describes the physics of interacting bosons subjected to a shallow lattice potential and was at the heart of pioneering quantum simulation experiments with cold atoms in optical lattice [87–89, 309–311]. Superconducting transmon qubits [190] are also often described as sites of the Bose-Hubbard model for photons due to their weak anharmonicity [101, 312, 313]. While most of the studies to date considered cases with inter-particle interactions on the same site and the range of hopping limited to only nearest-neighbor sites, investigating extended versions of the Bose-Hubbard model with longer-range interaction and hopping processes are expected to bring in new opportunities to study strongly-correlated quantum phases of matter [314, 315]. For example, inclusion of long-range interactions between particles is shown to enrich the phase diagram,

inducing Haldane insulator and density wave phases 1D [316] and supersolid phase with both superfluid and crystalline order in 2D [317]. Also, extended range of hopping is known to amplify long-range and higher-order quantum correlations e.g., by creating correlated triplon-hole-hole pairs in Mott insulators [318] and greatly influencing the phase boundary of Mott insulator-to-superfluid transition [319]. Our superconducting metamaterial quantum processor induces tunable long-range coupling between transmon qubits, naturally realizing an extended Bose-Hubbard model for photons. We envision experimental exploration of the canonical model in a new regime with an unprecedented level of control and with new methods for dissipative stabilizing quantum many-body states [101, 277].

Quantum information scrambling

Quantum information scrambling [320–323] refers to a general phenomenon where initially localized quantum information is spread across many-body quantum degrees of freedom, resulting in a complex entanglement structure which prohibits the recovery of originally encoded information with local measurements. This topic has been a subject of extensive theoretical studies [324–327] in the last few years. While there has been pioneering experimental efforts to measure out-of-time-ordered correlators [328, 329] and to probe quantum information scrambling [330, 331] in state-of-the-art quantum platforms, scrambling effects arising from a more generic scenario of thermalization in quantum many-body systems remain yet to be observed. Also, an interesting question here is whether we can retrieve the scrambled quantum information buried in multipartite quantum correlations by utilizing high level of local control over a closed quantum system. We are currently working on developing hybrid quantum-classical protocols to decode the scrambled quantum information from chaotic quantum many-body evolution by measurement and feed-forward. Our rapid high-fidelity multiplexed readout and the ability to perform low-latency ($< 1 \mu s$) feedback operations based on measurement outcomes of a subsystem will play a crucial role in realizing this scheme.

Measurement-induced phase transition

There has been recent theoretical studies of competition between the growth of entanglement in a quantum many-body system and local projective measurements [292–295]. It was shown that if the rate of randomly interspersed local projective measurement exceeds a certain threshold, the entanglement growth of the quantum many-body system is restricted to follow the area-law. Such transition from the

entangling phase (volume law) to the disentangling phase (area law) is called the measurement-induced phase transition. Experimentally probing the measurement-induced phase transition has been a formidable task as it requires ability to perform random mid-circuit readout of arbitrary subsets of qubits without fully collapsing the many-body wavefunction. A pioneering experiment conducted in a trapped ion quantum simulator overcame this challenge by exploiting entangling gates between system and ancilla qubits to defer the measurement until the end of the circuit [296]. However, this method limits the total number of measurements to the number of ancillae and therefore is only applicable to short time evolution and small system size. In superconducting circuits, it is known that the effect of measurement of one qubit on other unmeasured qubits is mild, only adding parasitic dephasing rates on the order of $\bar{\Gamma}/2\pi \sim 10^2$ kHz [287] during the on-time of readout pulses ($\tau_p \sim 10^2$ ns), and in principle can be avoided by careful design of feedlines and Purcell filters [184, 285, 287, 332] for readout resonators [231]. Employing the superconducting metamaterial waveguide as an efficient Purcell filter for readout, we look forward to probing full regimes of the measurement-induced phase transition including its criticality.

8.2 New directions for scaling up quantum processors

Scaling up quantum processors for conducting large-scale quantum computation and simulation experiments entails significant technical challenges. On one hand, realizing a large system often requires transition to a new scalable technology for constructing hardware and extensive engineering of electronics. On the other hand, achieving good systematic control over the large system involves serious efforts in software development. The state-of-the-art large-scale quantum experiments are being performed with ~ 60 qubits in superconducting circuits [76, 297, 298, 333], ~ 50 qubits in trapped ions [14, 69], and ~ 200 qubits in neutral atom quantum simulators [15, 16], all of which are expected to grow further in size over the next few years.

In Chapter 7, we have successfully developed hardware and software to systematically control ten superconducting qubits with full individual addressing and long-range coupling. With established and new methods for cryogenics [159], microwave packaging of device [152], and calibration [306], we expect to be able to run experiments on the scale of ~ 100 qubits in the near future. Specifically, leveraging the inherent 1D-scalability and long-range connectivity of the metamaterial quantum processor will be a key goal in this direction.

BIBLIOGRAPHY

- [1] M. Planck, “Zur theorie des gesetzes der energieverteilung im normalspektrum,” *Verhandl. Dtsch. Phys. Ges.* **2**, 237–245 (1900) (cit. on p. 1).
- [2] A. L. Schawlow and C. H. Townes, “Infrared and optical masers,” *Phys. Rev.* **112**, 1940–1949 (1958) [10.1103/PhysRev.112.1940](#) (cit. on p. 1).
- [3] T. H. Maiman, “Stimulated optical radiation in ruby,” *Nature* **187**, 493–494 (1960) [10.1038/187493a0](#) (cit. on p. 1).
- [4] E. Schrödinger, “Die gegenwärtige situation in der quantenmechanik,” *Naturwissenschaften* **23**, 807–812 (1935) [10.1007/BF01491891](#) (cit. on p. 1).
- [5] J. S. Bell, “On the Einstein Podolsky Rosen paradox,” *Physics Physique Fizika* **1**, 195–200 (1964) [10.1103/PhysicsPhysiqueFizika.1.195](#) (cit. on p. 1).
- [6] M. Berboucha, “IBM’s first commercial quantum computer,” *Forbes* (2017) (cit. on pp. 1, 30).
- [7] F. Lardinois, “Microsoft open-sources its quantum computing development tools,” *TechCrunch* (2019) (cit. on p. 1).
- [8] S. K. Moore and A. Nordrum, “Google’s quantum tech milestone excites scientists and spurs rivals,” *IEEE Spectrum* (2019) (cit. on p. 1).
- [9] J. Hsu, “Intel’s new path to quantum computing,” *IEEE Spectrum* (2018) (cit. on p. 1).
- [10] C. Q. Choi, “Amazon’s new quantum computer design relies on tiny Schrödinger’s cats,” *IEEE Spectrum* (2021) (cit. on p. 1).
- [11] J.-y. Choi, S. Hild, J. Zeiher, P. Schauß, A. Rubio-Abadal, T. Yefsah, V. Khemani, D. A. Huse, I. Bloch, and C. Gross, “Exploring the many-body localization transition in two dimensions,” *Science* **352**, 1547–1552 (2016) [10.1126/science.aaf8834](#) (cit. on p. 1).
- [12] M. Endres, H. Bernien, A. Keesling, H. Levine, E. R. Anschuetz, A. Krajenbrink, C. Senko, V. Vuletic, M. Greiner, and M. D. Lukin, “Atom-by-atom assembly of defect-free one-dimensional cold atom arrays,” *Science* **354**, 1024–1027 (2016) [10.1126/science.aah3752](#) (cit. on pp. 1, 9).
- [13] C. Gross and I. Bloch, “Quantum simulations with ultracold atoms in optical lattices,” *Science* **357**, 995–1001 (2017) [10.1126/science.aal3837](#) (cit. on pp. 1, 91).
- [14] J. Zhang, G. Pagano, P. W. Hess, A. Kyprianidis, P. Becker, H. Kaplan, A. V. Gorshkov, Z. -X. Gong, and C. Monroe, “Observation of a many-body dynamical phase transition with a 53-qubit quantum simulator,” *Nature* **551**, 601–604 (2017) [10.1038/nature24654](#) (cit. on pp. 1, 107).

- [15] S. Ebadi, T. T. Wang, H. Levine, A. Keesling, G. Semeghini, A. Omran, D. Bluvstein, R. Samajdar, H. Pichler, W. W. Ho, S. Choi, S. Sachdev, M. Greiner, V. Vuletić, and M. D. Lukin, “Quantum phases of matter on a 256-atom programmable quantum simulator,” *Nature* **595**, 227–232 (2021) [10.1038/s41586-021-03582-4](https://doi.org/10.1038/s41586-021-03582-4) (cit. on pp. 1, 9, 92, 107).
- [16] P. Scholl, M. Schuler, H. J. Williams, A. A. Eberharter, D. Barredo, K.-N. Schymik, V. Lienhard, L.-P. Henry, T. C. Lang, T. Lahaye, A. M. Läuchli, and A. Browaeys, “Quantum simulation of 2D antiferromagnets with hundreds of Rydberg atoms,” *Nature* **595**, 233–238 (2021) [10.1038/s41586-021-03585-1](https://doi.org/10.1038/s41586-021-03585-1) (cit. on pp. 1, 107).
- [17] J. D. Jackson, *Classical Electrodynamics*, 3rd ed. (John Wiley & Sons, 1999) (cit. on p. 2).
- [18] C. Cohen-Tannoudji, J. Dupont-Roc, and G. Grynberg, *Atom-Photon Interactions: Basic Process and Applications* (John Wiley & Sons, 1998), [10.1002/9783527617197](https://doi.org/10.1002/9783527617197) (cit. on p. 2).
- [19] H. J. Kimble, M. Dagenais, and L. Mandel, “Photon antibunching in resonance fluorescence,” *Phys. Rev. Lett.* **39**, 691–695 (1977) [10.1103/PhysRevLett.39.691](https://doi.org/10.1103/PhysRevLett.39.691) (cit. on p. 2).
- [20] M. Brune, F. Schmidt-Kaler, A. Maali, J. Dreyer, E. Hagley, J. M. Raimond, and S. Haroche, “Quantum Rabi oscillation: A direct test of field quantization in a cavity,” *Phys. Rev. Lett.* **76**, 1800–1803 (1996) [10.1103/PhysRevLett.76.1800](https://doi.org/10.1103/PhysRevLett.76.1800) (cit. on p. 2).
- [21] C. J. Foot, *Atomic Physics* (Oxford University Press, 2005) (cit. on pp. 2, 3).
- [22] G. Grynberg, A. Aspect, and C. Fabre, *Introduction to Quantum Optics: From the Semi-classical Approach to Quantized Light* (Cambridge University Press, 2010) (cit. on p. 2).
- [23] J. D. Hood, “Atom-light interactions in a photonic crystal waveguide,” PhD thesis (California Institute of Technology, 2017) (cit. on p. 2).
- [24] M. K. Tey, Z. Chen, S. A. Aljunid, B. Chng, F. Huber, G. Maslennikov, and C. Kurtsiefer, “Strong interaction between light and a single trapped atom without the need for a cavity,” *Nat. Phys.* **4**, 924–927 (2008) [10.1038/nphys1096](https://doi.org/10.1038/nphys1096) (cit. on pp. 3, 27).
- [25] F. Schmidt-Kaler, “Total surveillance,” *Nature* **446**, 275–276 (2007) [10.1038/446275a](https://doi.org/10.1038/446275a) (cit. on p. 3).
- [26] H. J. Kimble, “The quantum internet,” *Nature* **453**, 1023–1030 (2008) [10.1038/nature07127](https://doi.org/10.1038/nature07127) (cit. on pp. 3, 4, 13, 90).
- [27] A. Wallraff, D. I. Schuster, A. Blais, L. Frunzio, R. S. Huang, J. Majer, S. Kumar, S. M. Girvin, and R. J. Schoelkopf, “Strong coupling of a single photon to a superconducting qubit using circuit quantum electrodynamics,” *Nature* **431**, 162–167 (2004) [10.1038/nature02851](https://doi.org/10.1038/nature02851) (cit. on pp. 3, 66).

- [28] S. Haroche and D. Kleppner, “Cavity quantum electrodynamics,” *Phys. Today* **42**, 24–30 (1989) [10.1063/1.881201](#) (cit. on pp. 3, 12).
- [29] S. Haroche and J.-M. Raimond, *Exploring the Quantum: Atoms, Cavities, and Photons* (Oxford University Press, 2006) (cit. on pp. 3, 12, 78, 89).
- [30] E. T. Jaynes and F. W. Cummings, “Comparison of quantum and semiclassical radiation theories with application to the beam maser,” *Proc. IEEE* **51**, 89–109 (1963) [10.1109/PROC.1963.1664](#) (cit. on p. 3).
- [31] S. Haroche, “Nobel lecture: Controlling photons in a box and exploring the quantum to classical boundary,” *Rev. Mod. Phys.* **85**, 1083–1102 (2013) [10.1103/RevModPhys.85.1083](#) (cit. on p. 4).
- [32] H. J. Kimble, “Strong interactions of single atoms and photons in cavity QED,” *Phys. Scr.* **T76**, 127 (1998) [10.1238/physica.topical.076a00127](#) (cit. on p. 4).
- [33] G. Rempe, R. J. Thompson, H. J. Kimble, and R. Lalezari, “Measurement of ultralow losses in an optical interferometer,” *Opt. Lett.* **17**, 363–365 (1992) [10.1364/OL.17.000363](#) (cit. on p. 4).
- [34] T. Aoki, B. Dayan, E. Wilcut, W. P. Bowen, A. S. Parkins, T. J. Kippenberg, K. J. Vahala, and H. J. Kimble, “Observation of strong coupling between one atom and a monolithic microresonator,” *Nature* **443**, 671–674 (2006) [10.1038/nature05147](#) (cit. on p. 4).
- [35] A. Blais, R.-S. Huang, A. Wallraff, S. M. Girvin, and R. J. Schoelkopf, “Cavity quantum electrodynamics for superconducting electrical circuits: An architecture for quantum computation,” *Phys. Rev. A* **69**, 062320 (2004) [10.1103/PhysRevA.69.062320](#) (cit. on pp. 4, 66).
- [36] A. Blais, J. Gambetta, A. Wallraff, D. I. Schuster, S. M. Girvin, M. H. Devoret, and R. J. Schoelkopf, “Quantum-information processing with circuit quantum electrodynamics,” *Phys. Rev. A* **75**, 032329 (2007) [10.1103/PhysRevA.75.032329](#) (cit. on p. 4).
- [37] A. Blais, A. L. Grimsmo, S. M. Girvin, and A. Wallraff, “Circuit quantum electrodynamics,” *Rev. Mod. Phys.* **93**, 025005 (2021) [10.1103/RevModPhys.93.025005](#) (cit. on p. 4).
- [38] S. Haroche, M. Brune, and J. M. Raimond, “From cavity to circuit quantum electrodynamics,” *Nat. Phys.* **16**, 243–246 (2020) [10.1038/s41567-020-0812-1](#) (cit. on p. 4).
- [39] A. Reiserer and G. Rempe, “Cavity-based quantum networks with single atoms and optical photons,” *Rev. Mod. Phys.* **87**, 1379–1418 (2015) [10.1103/RevModPhys.87.1379](#) (cit. on p. 4).
- [40] D. Roy, C. M. Wilson, and O. Firstenberg, “Colloquium: Strongly interacting photons in one-dimensional continuum,” *Rev. Mod. Phys.* **89**, 021001 (2017) [10.1103/RevModPhys.89.021001](#) (cit. on pp. 4, 13, 47, 65, 78, 93).

- [41] K. Hammerer, A. S. Sørensen, and E. S. Polzik, “Quantum interface between light and atomic ensembles,” *Rev. Mod. Phys.* **82**, 1041–1093 (2010) [10.1103/RevModPhys.82.1041](https://doi.org/10.1103/RevModPhys.82.1041) (cit. on p. 4).
- [42] R. H. Dicke, “Coherence in spontaneous radiation processes,” *Phys. Rev.* **93**, 99–110 (1954) [10.1103/PhysRev.93.99](https://doi.org/10.1103/PhysRev.93.99) (cit. on pp. 4, 16, 46, 47, 86).
- [43] M. Gross and S. Haroche, “Superradiance: An essay on the theory of collective spontaneous emission,” *Phys. Rep.* **93**, 301–396 (1982) [https://doi.org/10.1016/0370-1573\(82\)90102-8](https://doi.org/10.1016/0370-1573(82)90102-8) (cit. on pp. 4, 16, 46).
- [44] D. E. Chang, J. S. Douglas, A. González-Tudela, C.-L. Hung, and H. J. Kimble, “Colloquium: Quantum matter built from nanoscopic lattices of atoms and photons,” *Rev. Mod. Phys.* **90**, 031002 (2018) [10.1103/RevModPhys.90.031002](https://doi.org/10.1103/RevModPhys.90.031002) (cit. on pp. 5, 13, 27, 78, 93).
- [45] A. S. Sheremet, M. I. Petrov, I. V. Iorsh, A. V. Poshakinskiy, and A. N. Poddubny, “Waveguide quantum electrodynamics: collective radiance and photon-photon correlations,” *arXiv:2103.06824* (2021) (cit. on pp. 5, 13).
- [46] P. Lodahl, S. Mahmoodian, S. Stobbe, A. Rauschenbeutel, P. Schneeweiss, J. Volz, H. Pichler, and P. Zoller, “Chiral quantum optics,” *Nature* **541**, 473–480 (2017) [10.1038/nature21037](https://doi.org/10.1038/nature21037) (cit. on pp. 5, 78, 90).
- [47] T. Ozawa, H. M. Price, A. Amo, N. Goldman, M. Hafezi, L. Lu, M. C. Rechtsman, D. Schuster, J. Simon, O. Zilberberg, and I. Carusotto, “Topological photonics,” *Rev. Mod. Phys.* **91**, 015006 (2019) [10.1103/RevModPhys.91.015006](https://doi.org/10.1103/RevModPhys.91.015006) (cit. on pp. 5, 77, 78, 80).
- [48] R. Mitsch, C. Sayrin, B. Albrecht, P. Schneeweiss, and A. Rauschenbeutel, “Quantum state-controlled directional spontaneous emission of photons into a nanophotonic waveguide,” *Nat. Commun.* **5**, 5713 (2014) [10.1038/ncomms6713](https://doi.org/10.1038/ncomms6713) (cit. on p. 5).
- [49] I. Shomroni, S. Rosenblum, Y. Lovsky, O. Bechler, G. Guendelman, and B. Dayan, “All-optical routing of single photons by a one-atom switch controlled by a single photon,” *Science* **345**, 903–906 (2014) [10.1126/science.1254699](https://doi.org/10.1126/science.1254699) (cit. on p. 5).
- [50] I. Söllner, S. Mahmoodian, S. L. Hansen, L. Midolo, A. Javadi, G. Kiršanskė, T. Pregnolato, H. El-Ella, E. H. Lee, J. D. Song, S. Stobbe, and P. Lodahl, “Deterministic photon-emitter coupling in chiral photonic circuits,” *Nat. Nanotechnol.* **10**, 775–778 (2015) [10.1038/nnano.2015.159](https://doi.org/10.1038/nnano.2015.159) (cit. on p. 5).
- [51] C. W. Gardiner, “Driving a quantum system with the output field from another driven quantum system,” *Phys. Rev. Lett.* **70**, 2269–2272 (1993) [10.1103/PhysRevLett.70.2269](https://doi.org/10.1103/PhysRevLett.70.2269) (cit. on p. 5).

- [52] K. Stannigel, P. Rabl, and P. Zoller, “Driven-dissipative preparation of entangled states in cascaded quantum-optical networks,” *New J. Phys.* **14**, 063014 (2012) [10.1088/1367-2630/14/6/063014](#) (cit. on p. 5).
- [53] L. W. Clark, N. Schine, C. Baum, N. Jia, and J. Simon, “Observation of Laughlin states made of light,” *Nature* **582**, 41–45 (2020) [10.1038/s41586-020-2318-5](#) (cit. on p. 5).
- [54] J. C. Owens, M. G. Panetta, B. Saxberg, G. Roberts, S. Chakram, R. Ma, A. Vrajitoarea, J. Simon, and D. Schuster, “Chiral cavity quantum electrodynamics,” [arXiv:2109.06033](#) (2021) (cit. on p. 5).
- [55] M. Bello, G. Platero, J. I. Cirac, and A. González-Tudela, “Unconventional quantum optics in topological waveguide QED,” *Sci. Adv.* **5**, eaaw0297 (2019) [10.1126/sciadv.aaw0297](#) (cit. on pp. 5, 78, 83, 84, 86, 90, 199, 206, 207).
- [56] E. Kim, X. Zhang, V. S. Ferreira, J. Banker, J. K. Iverson, A. Sipahigil, M. Bello, A. González-Tudela, M. Mirhosseini, and O. Painter, “Quantum electrodynamics in a topological waveguide,” *Phys. Rev. X* **11**, 011015 (2021) [10.1103/PhysRevX.11.011015](#), (cit. on pp. 5, 11, 32, 77, 79, 82, 85, 87, 93–95).
- [57] M. A. Nielsen and I. L. Chuang, *Quantum Computation and Quantum Information*, 2nd ed. (Cambridge University Press, 2010) (cit. on pp. 6, 93).
- [58] R. P. Feynman, “Simulating physics with computers,” *Int. J. Theor. Phys.* **21**, 467–488 (1982) [10.1007/BF02650179](#) (cit. on p. 6).
- [59] P. Shor, “Algorithms for quantum computation: discrete logarithms and factoring,” in *Proceedings 35th annual symposium on foundations of computer science* (1994), pp. 124–134, [10.1109/SFCS.1994.365700](#) (cit. on p. 6).
- [60] L. K. Grover, “A fast quantum mechanical algorithm for database search,” in *Proceedings of the twenty-eighth annual acm symposium on theory of computing, STOC '96* (1996), pp. 212–219, [10.1145/237814.237866](#) (cit. on p. 6).
- [61] R. Landauer, M. E. Welland, and J. K. Gimzewski, “Is quantum mechanics useful?” *Philos. Trans. R. Soc. A* **353**, 367–376 (1995) [10.1098/rsta.1995.0106](#) (cit. on p. 6).
- [62] P. W. Shor, “Scheme for reducing decoherence in quantum computer memory,” *Phys. Rev. A* **52**, R2493–R2496 (1995) [10.1103/PhysRevA.52.R2493](#) (cit. on p. 6).
- [63] A. M. Steane, “Error correcting codes in quantum theory,” *Phys. Rev. Lett.* **77**, 793–797 (1996) [10.1103/PhysRevLett.77.793](#) (cit. on p. 6).
- [64] D. Aharonov and M. Ben-Or, “Fault-tolerant quantum computation with constant error rate,” [arXiv:quant-ph/9906129](#) (1999) (cit. on p. 7).

- [65] A. G. Fowler, A. M. Stephens, and P. Groszkowski, “High-threshold universal quantum computation on the surface code,” *Phys. Rev. A* **80**, 052312 (2009) [10.1103/PhysRevA.80.052312](#) (cit. on pp. 7, 92).
- [66] A. G. Fowler, M. Mariantoni, J. M. Martinis, and A. N. Cleland, “Surface codes: Towards practical large-scale quantum computation,” *Phys. Rev. A* **86**, 032324 (2012) [10.1103/PhysRevA.86.032324](#) (cit. on pp. 7, 92).
- [67] S. B. Bravyi and A. Y. Kitaev, “Quantum codes on a lattice with boundary,” [arXiv:quant-ph/9811052](#) (1998) (cit. on p. 7).
- [68] V. V. Albert, K. Noh, K. Duivenvoorden, D. J. Young, R. T. Brierley, P. Reinhold, C. Vuillot, L. Li, C. Shen, S. M. Girvin, B. M. Terhal, and L. Jiang, “Performance and structure of single-mode bosonic codes,” *Phys. Rev. A* **97**, 032346 (2018) [10.1103/PhysRevA.97.032346](#) (cit. on p. 7).
- [69] A. Joshi, K. Noh, and Y. Y. Gao, “Quantum information processing with bosonic qubits in circuit QED,” *Quantum Sci. Technol.* **6**, 033001 (2021) [10.1088/2058-9565/abe989](#) (cit. on pp. 7, 107).
- [70] D. Gottesman, A. Kitaev, and J. Preskill, “Encoding a qubit in an oscillator,” *Phys. Rev. A* **64**, 012310 (2001) [10.1103/PhysRevA.64.012310](#) (cit. on p. 7).
- [71] Z. Leghtas, G. Kirchmair, B. Vlastakis, R. J. Schoelkopf, M. H. Devoret, and M. Mirrahimi, “Hardware-efficient autonomous quantum memory protection,” *Phys. Rev. Lett.* **111**, 120501 (2013) [10.1103/PhysRevLett.111.120501](#) (cit. on p. 7).
- [72] M. H. Michael, M. Silveri, R. T. Brierley, V. V. Albert, J. Salmilehto, L. Jiang, and S. M. Girvin, “New class of quantum error-correcting codes for a bosonic mode,” *Phys. Rev. X* **6**, 031006 (2016) [10.1103/PhysRevX.6.031006](#) (cit. on p. 7).
- [73] N. Ofek, A. Petrenko, R. Heeres, P. Reinhold, Z. Leghtas, B. Vlastakis, Y. Liu, L. Frunzio, S. M. Girvin, L. Jiang, M. Mirrahimi, M. H. Devoret, and R. J. Schoelkopf, “Extending the lifetime of a quantum bit with error correction in superconducting circuits,” *Nature* **536**, 441–445 (2016) [10.1038/nature18949](#) (cit. on p. 7).
- [74] M. H. Devoret and R. J. Schoelkopf, “Superconducting circuits for quantum information: An outlook,” *Science* **339**, 1169–1174 (2013) [10.1126/science.1231930](#) (cit. on p. 8).
- [75] J. Preskill, “Quantum computing in the NISQ era and beyond,” *Quantum* **2**, 79 (2018) [10.22331/q-2018-08-06-79](#) (cit. on pp. 8, 104).
- [76] F. Arute et al., “Quantum supremacy using a programmable superconducting processor,” *Nature* **574**, 505–510 (2019) [10.1038/s41586-019-1666-5](#) (cit. on pp. 9, 30, 104, 105, 107).

- [77] R. K. Naik, N. Leung, S. Chakram, P. Groszkowski, Y. Lu, N. Earnest, D. C. McKay, J. Koch, and D. I. Schuster, “Random access quantum information processors using multimode circuit quantum electrodynamics,” *Nat. Commun.* **8**, 1904 (2017) [10.1038/s41467-017-02046-6](https://doi.org/10.1038/s41467-017-02046-6) (cit. on pp. 9, 88).
- [78] S. Chakram, A. E. Oriani, R. K. Naik, A. V. Dixit, K. He, A. Agrawal, H. Kwon, and D. I. Schuster, “Seamless high- Q microwave cavities for multimode circuit quantum electrodynamics,” *Phys. Rev. Lett.* **127**, 107701 (2021) [10.1103/PhysRevLett.127.107701](https://doi.org/10.1103/PhysRevLett.127.107701) (cit. on p. 9).
- [79] Y. Y. Gao, B. J. Lester, K. S. Chou, L. Frunzio, M. H. Devoret, L. Jiang, S. M. Girvin, and R. J. Schoelkopf, “Entanglement of bosonic modes through an engineered exchange interaction,” *Nature* **566**, 509–512 (2019) (cit. on p. 9).
- [80] H. L. Stormer, D. C. Tsui, and A. C. Gossard, “The fractional quantum Hall effect,” *Rev. Mod. Phys.* **71**, S298–S305 (1999) [10.1103/RevModPhys.71.S298](https://doi.org/10.1103/RevModPhys.71.S298) (cit. on p. 9).
- [81] E. Dagotto, “Correlated electrons in high-temperature superconductors,” *Rev. Mod. Phys.* **66**, 763–840 (1994) [10.1103/RevModPhys.66.763](https://doi.org/10.1103/RevModPhys.66.763) (cit. on p. 9).
- [82] I. M. Georgescu, S. Ashhab, and F. Nori, “Quantum simulation,” *Rev. Mod. Phys.* **86**, 153–185 (2014) [10.1103/RevModPhys.86.153](https://doi.org/10.1103/RevModPhys.86.153) (cit. on pp. 9, 91).
- [83] E. Altman et al., “Quantum simulators: Architectures and opportunities,” *PRX Quantum* **2**, 017003 (2021) [10.1103/PRXQuantum.2.017003](https://doi.org/10.1103/PRXQuantum.2.017003) (cit. on p. 9).
- [84] E. Altman, “Many-body localization and quantum thermalization,” *Nat. Phys.* **14**, 979–983 (2018) [10.1038/s41567-018-0305-7](https://doi.org/10.1038/s41567-018-0305-7) (cit. on pp. 9, 92).
- [85] D. A. Abanin, E. Altman, I. Bloch, and M. Serbyn, “Colloquium: Many-body localization, thermalization, and entanglement,” *Rev. Mod. Phys.* **91**, 021001 (2019) [10.1103/RevModPhys.91.021001](https://doi.org/10.1103/RevModPhys.91.021001) (cit. on p. 9).
- [86] R. J. Lewis-Swan, A. Safavi-Naini, A. M. Kaufman, and A. M. Rey, “Dynamics of quantum information,” *Nat. Rev. Phys.* **1**, 627–634 (2019) [10.1038/s42254-019-0090-y](https://doi.org/10.1038/s42254-019-0090-y) (cit. on pp. 9, 91, 92).
- [87] I. Bloch, J. Dalibard, and W. Zwerger, “Many-body physics with ultracold gases,” *Rev. Mod. Phys.* **80**, 885–964 (2008) [10.1103/RevModPhys.80.885](https://doi.org/10.1103/RevModPhys.80.885) (cit. on pp. 9, 105).
- [88] W. S. Bakr, J. I. Gillen, A. Peng, S. Fölling, and M. Greiner, “A quantum gas microscope for detecting single atoms in a Hubbard-regime optical lattice,” *Nature* **462**, 74–77 (2009) [10.1038/nature08482](https://doi.org/10.1038/nature08482) (cit. on pp. 9, 105).

- [89] J. F. Sherson, C. Weitenberg, M. Endres, M. Cheneau, I. Bloch, and S. Kuhr, “Single-atom-resolved fluorescence imaging of an atomic Mott insulator,” *Nature* **467**, 68–72 (2010) [10.1038/nature09378](https://doi.org/10.1038/nature09378) (cit. on pp. 9, 105).
- [90] M. Endres, M. Cheneau, T. Fukuhara, C. Weitenberg, P. Schauß, C. Gross, L. Mazza, M. C. Bañuls, L. Pollet, I. Bloch, and S. Kuhr, “Observation of correlated particle-hole pairs and string order in low-dimensional Mott insulators,” *Science* **334**, 200–203 (2011) [10.1126/science.1209284](https://doi.org/10.1126/science.1209284) (cit. on p. 9).
- [91] P. M. Preiss, R. Ma, M. E. Tai, A. Lukin, M. Rispoli, P. Zupancic, Y. Lahini, R. Islam, and M. Greiner, “Strongly correlated quantum walks in optical lattices,” *Science* **347**, 1229–1233 (2015) [10.1126/science.1260364](https://doi.org/10.1126/science.1260364) (cit. on p. 9).
- [92] C. S. Chiu, G. Ji, A. Bohrdt, M. Xu, M. Knap, E. Demler, F. Grusdt, M. Greiner, and D. Greif, “String patterns in the doped Hubbard model,” *Science* **365**, 251–256 (2019) [10.1126/science.aav3587](https://doi.org/10.1126/science.aav3587) (cit. on p. 9).
- [93] R. Blatt and C. F. Roos, “Quantum simulations with trapped ions,” *Nat. Phys.* **8**, 277–284 (2012) [10.1038/nphys2252](https://doi.org/10.1038/nphys2252) (cit. on pp. 9, 91).
- [94] C. Monroe, W. C. Campbell, L.-M. Duan, Z.-X. Gong, A. V. Gorshkov, P. W. Hess, R. Islam, K. Kim, N. M. Linke, G. Pagano, P. Richerme, C. Senko, and N. Y. Yao, “Programmable quantum simulations of spin systems with trapped ions,” *Rev. Mod. Phys.* **93**, 025001 (2021) [10.1103/RevModPhys.93.025001](https://doi.org/10.1103/RevModPhys.93.025001) (cit. on p. 9).
- [95] P. Jurcevic, B. P. Lanyon, P. Hauke, C. Hempel, P. Zoller, R. Blatt, and C. F. Roos, “Quasiparticle engineering and entanglement propagation in a quantum many-body system,” *Nature* **511**, 202–205 (2014) [10.1038/nature13461](https://doi.org/10.1038/nature13461) (cit. on p. 9).
- [96] P. Jurcevic, H. Shen, P. Hauke, C. Maier, T. Brydges, C. Hempel, B. P. Lanyon, M. Heyl, R. Blatt, and C. F. Roos, “Direct observation of dynamical quantum phase transitions in an interacting many-body system,” *Phys. Rev. Lett.* **119**, 080501 (2017) [10.1103/PhysRevLett.119.080501](https://doi.org/10.1103/PhysRevLett.119.080501) (cit. on p. 9).
- [97] J. Zhang, P. W. Hess, A. Kyprianidis, P. Becker, A. Lee, J. Smith, G. Pagano, I. D. Potirniche, A. C. Potter, A. Vishwanath, N. Y. Yao, and C. Monroe, “Observation of a discrete time crystal,” *Nature* **543**, 217–220 (2017) [10.1038/nature21413](https://doi.org/10.1038/nature21413) (cit. on p. 9).
- [98] A. Kyprianidis, F. Machado, W. Morong, P. Becker, K. S. Collins, D. V. Else, L. Feng, P. W. Hess, C. Nayak, G. Pagano, N. Y. Yao, and C. Monroe, “Observation of a prethermal discrete time crystal,” *Science* **372**, 1192–1196 (2021) [10.1126/science.abg8102](https://doi.org/10.1126/science.abg8102) (cit. on p. 9).

- [99] Y. Ye et al., “Propagation and localization of collective excitations on a 24-qubit superconducting processor,” *Phys. Rev. Lett.* **123**, 050502 (2019) [10.1103/PhysRevLett.123.050502](https://doi.org/10.1103/PhysRevLett.123.050502) (cit. on p. 10).
- [100] Z. Yan, Y.-R. Zhang, M. Gong, Y. Wu, Y. Zheng, S. Li, C. Wang, F. Liang, J. Lin, Y. Xu, C. Guo, L. Sun, C.-Z. Peng, K. Xia, H. Deng, H. Rong, J. Q. You, F. Nori, H. Fan, X. Zhu, and J.-W. Pan, “Strongly correlated quantum walks with a 12-qubit superconducting processor,” *Science* **364**, 753–756 (2019) [10.1126/science.aaw1611](https://doi.org/10.1126/science.aaw1611) (cit. on pp. 10, 104).
- [101] R. Ma, B. Saxberg, C. Owens, N. Leung, Y. Lu, J. Simon, and D. I. Schuster, “A dissipatively stabilized Mott insulator of photons,” *Nature* **566**, 51–57 (2019) [10.1038/s41586-019-0897-9](https://doi.org/10.1038/s41586-019-0897-9) (cit. on pp. 10, 90, 105, 106).
- [102] J. Braumüller, A. H. Karamlou, Y. Yanay, B. Kannan, D. Kim, M. Kjaergaard, A. Melville, B. M. Niedzielski, Y. Sung, A. Vepsäläinen, R. Winik, J. L. Yoder, T. P. Orlando, S. Gustavsson, C. Tahan, and W. D. Oliver, “Probing quantum information propagation with out-of-time-ordered correlators,” *Nat. Phys.* **18**, 172–178 (2022) [10.1038/s41567-021-01430-w](https://doi.org/10.1038/s41567-021-01430-w) (cit. on p. 10).
- [103] X. Mi et al., “Information scrambling in quantum circuits,” *Science* **374**, 1479–1483 (2021) [10.1126/science.abg5029](https://doi.org/10.1126/science.abg5029) (cit. on p. 10).
- [104] K. Xu, J.-J. Chen, Y. Zeng, Y.-R. Zhang, C. Song, W. Liu, Q. Guo, P. Zhang, D. Xu, H. Deng, K. Huang, H. Wang, X. Zhu, D. Zheng, and H. Fan, “Emulating many-body localization with a superconducting quantum processor,” *Phys. Rev. Lett.* **120**, 050507 (2018) [10.1103/PhysRevLett.120.050507](https://doi.org/10.1103/PhysRevLett.120.050507) (cit. on p. 10).
- [105] K. Xu, Z.-H. Sun, W. Liu, Y.-R. Zhang, H. Li, H. Dong, W. Ren, P. Zhang, F. Nori, D. Zheng, H. Fan, and H. Wang, “Probing dynamical phase transitions with a superconducting quantum simulator,” *Sci. Adv.* **6**, eaba4935 (2020) [10.1126/sciadv.aba4935](https://doi.org/10.1126/sciadv.aba4935) (cit. on pp. 10, 93).
- [106] Q. Guo, C. Cheng, Z.-H. Sun, Z. Song, H. Li, Z. Wang, W. Ren, H. Dong, D. Zheng, Y.-R. Zhang, R. Mondaini, H. Fan, and H. Wang, “Observation of energy-resolved many-body localization,” *Nat. Phys.* **17**, 234–239 (2021) [10.1038/s41567-020-1035-1](https://doi.org/10.1038/s41567-020-1035-1) (cit. on pp. 10, 93).
- [107] P. Krantz, M. Kjaergaard, F. Yan, T. P. Orlando, S. Gustavsson, and W. D. Oliver, “A quantum engineer’s guide to superconducting qubits,” *Appl. Phys. Rev.* **6**, 021318 (2019) [10.1063/1.5089550](https://doi.org/10.1063/1.5089550) (cit. on pp. 11, 90).
- [108] M. Mirhosseini, E. Kim, X. Zhang, A. Sipahigil, P. B. Dieterle, A. J. Keller, A. Asenjo-Garcia, D. E. Chang, and O. Painter, “Cavity quantum electrodynamics with atom-like mirrors,” *Nature* **569**, 692–697 (2019) [10.1038/s41586-019-1196-1](https://doi.org/10.1038/s41586-019-1196-1), (cit. on pp. 11, 18, 28, 29, 32, 46, 48, 51–53, 55, 57, 93, 197).

- [109] M. Mirhosseini, E. Kim, V. S. Ferreira, M. Kalaei, A. Sipahigil, A. J. Keller, and O. Painter, “Superconducting metamaterials for waveguide quantum electrodynamics,” *Nat. Commun.* **9**, 3706 (2018) [10.1038/s41467-018-06142-z](#), (cit. on pp. 11, 15, 29, 32, 58, 65, 78, 81, 83, 90, 93, 94, 199).
- [110] S.-B. Zheng and G.-C. Guo, “Efficient scheme for two-atom entanglement and quantum information processing in cavity QED,” *Phys. Rev. Lett.* **85**, 2392–2395 (2000) [10.1103/PhysRevLett.85.2392](#) (cit. on pp. 12, 93).
- [111] S. Osnaghi, P. Bertet, A. Auffeves, P. Maioli, M. Brune, J. M. Raimond, and S. Haroche, “Coherent control of an atomic collision in a cavity,” *Phys. Rev. Lett.* **87**, 037902 (2001) [10.1103/PhysRevLett.87.037902](#) (cit. on pp. 12, 46, 93).
- [112] J. Majer, J. M. Chow, J. M. Gambetta, J. Koch, B. R. Johnson, J. A. Schreier, L. Frunzio, D. I. Schuster, A. A. Houck, A. Wallraff, A. Blais, M. H. Devoret, S. M. Girvin, and R. J. Schoelkopf, “Coupling superconducting qubits via a cavity bus,” *Nature* **449**, 443–447 (2007) [10.1038/nature06184](#) (cit. on pp. 12, 46, 93).
- [113] H. Pichler, S. Choi, P. Zoller, and M. D. Lukin, “Universal photonic quantum computation via time-delayed feedback,” *Proc. Natl. Acad. Sci. U.S.A.* **114**, 11362–11367 (2017) [10.1073/pnas.1711003114](#) (cit. on p. 13).
- [114] E. M. Purcell, “Spontaneous emission probabilities at radio frequencies,” *Phys. Rev.* **69**, 681 (1946) [10.1103/PhysRev.69.674.2](#) (cit. on pp. 13, 100).
- [115] D. E. Chang, A. S. Sørensen, E. A. Demler, and M. D. Lukin, “A single-photon transistor using nanoscale surface plasmons,” *Nat. Phys.* **3**, 807–812 (2007) [10.1038/nphys708](#) (cit. on pp. 13–15).
- [116] K. Lalumière, B. C. Sanders, A. F. van Loo, A. Fedorov, A. Wallraff, and A. Blais, “Input-output theory for waveguide QED with an ensemble of inhomogeneous atoms,” *Phys. Rev. A* **88**, 043806 (2013) [10.1103/PhysRevA.88.043806](#) (cit. on pp. 13, 16, 48, 84, 152, 156, 164, 206).
- [117] J. Combes, J. Kerckhoff, and M. Sarovar, “The SLH framework for modeling quantum input-output networks,” *Adv. Phys.: X* **2**, 784–888 (2017) [10.1080/23746149.2017.1343097](#) (cit. on p. 13).
- [118] J. T. Shen and S. Fan, “Coherent photon transport from spontaneous emission in one-dimensional waveguides,” *Opt. Lett.* **30**, 2001–2003 (2005) [10.1364/OL.30.002001](#) (cit. on pp. 14, 206).
- [119] J.-T. Shen and S. Fan, “Coherent single photon transport in a one-dimensional waveguide coupled with superconducting quantum bits,” *Phys. Rev. Lett.* **95**, 213001 (2005) [10.1103/PhysRevLett.95.213001](#) (cit. on pp. 14, 206).

- [120] D. E. Chang, L. Jiang, A. V. Gorshkov, and H. J. Kimble, “Cavity QED with atomic mirrors,” *New J. Phys.* **14**, 063003 (2012) [10.1088/1367-2630/14/6/063003](#) (cit. on pp. 15, 16, 18, 46–49, 84, 93).
- [121] J.-T. Shen and S. Fan, “Strongly correlated two-photon transport in a one-dimensional waveguide coupled to a two-level system,” *Phys. Rev. Lett.* **98**, 153003 (2007) [10.1103/PhysRevLett.98.153003](#) (cit. on p. 15).
- [122] J.-T. Shen and S. Fan, “Strongly correlated multiparticle transport in one dimension through a quantum impurity,” *Phys. Rev. A* **76**, 062709 (2007) [10.1103/PhysRevA.76.062709](#) (cit. on p. 15).
- [123] V. Paulisch, H. J. Kimble, and A. González-Tudela, “Universal quantum computation in waveguide QED using decoherence free subspaces,” *New J. Phys.* **18**, 043041 (2016) [10.1088/1367-2630/18/4/043041](#) (cit. on pp. 18, 58, 161).
- [124] A. Frisk Kockum, “Quantum optics with giant atoms—the first five years,” in *International Symposium on Mathematics, Quantum Theory, and Cryptography*, edited by T. Takagi, M. Wakayama, K. Tanaka, N. Kunihiro, K. Kimoto, and Y. Ikematsu (2021), pp. 125–146, [10.1007/978-981-15-5191-8_12](#) (cit. on pp. 20, 93).
- [125] J. S. Douglas, H. Habibian, C.-L. Hung, A. V. Gorshkov, H. J. Kimble, and D. E. Chang, “Quantum many-body models with cold atoms coupled to photonic crystals,” *Nat. Photonics* **9**, 326–331 (2015) [10.1038/nphoton.2015.57](#) (cit. on pp. 20, 21, 65, 71, 76, 78, 93).
- [126] S. John and J. Wang, “Quantum electrodynamics near a photonic band gap: Photon bound states and dressed atoms,” *Phys. Rev. Lett.* **64**, 2418–2421 (1990) [10.1103/physrevlett.64.2418](#) (cit. on pp. 22, 65, 83, 93).
- [127] S. John, “Localization of light,” *Phys. Today* **44**, 32–40 (1991) [10.1063/1.881300](#) (cit. on pp. 22, 93).
- [128] G. Kurizki, “Two-atom resonant radiative coupling in photonic band structures,” *Phys. Rev. A* **42**, 2915–2924 (1990) [10.1103/physreva.42.2915](#) (cit. on pp. 25, 83, 93).
- [129] S. John and J. Wang, “Quantum optics of localized light in a photonic band gap,” *Phys. Rev. B* **43**, 12772–12789 (1991) [10.1103/PhysRevB.43.12772](#) (cit. on pp. 25, 73, 98).
- [130] T. Nieddu, V. Gokhroo, and S. N. Chormaic, “Optical nanofibres and neutral atoms,” *J. Opt.* **18**, 053001 (2016) [10.1088/2040-8978/18/5/053001](#) (cit. on p. 27).
- [131] K. P. Nayak, M. Sadgrove, R. Yalla, F. L. Kien, and K. Hakuta, “Nanofiber quantum photonics,” *J. Opt.* **20**, 073001 (2018) [10.1088/2040-8986/aac35e](#) (cit. on p. 27).

- [132] P. Lodahl, S. Mahmoodian, and S. Stobbe, “Interfacing single photons and single quantum dots with photonic nanostructures,” *Rev. Mod. Phys.* **87**, 347–400 (2015) [10.1103/RevModPhys.87.347](https://doi.org/10.1103/RevModPhys.87.347) (cit. on pp. 27–29, 47, 65, 78).
- [133] P. Ball, “Strong light reflection from few atoms,” *Physics* **9**, 109 (2016) [10.1103/physics.9.109](https://doi.org/10.1103/physics.9.109) (cit. on p. 28).
- [134] X. Luan, J.-B. Béguin, A. P. Burgers, Z. Qin, S.-P. Yu, and H. J. Kimble, “The integration of photonic crystal waveguides with atom arrays in optical tweezers,” *Adv. Quantum Technol.* **3**, 2000008 (2020) <https://doi.org/10.1002/qute.202000008> (cit. on pp. 28, 29, 93).
- [135] A. Rosario Hamann, C. Müller, M. Jerger, M. Zanner, J. Combes, M. Pletyukhov, M. Weides, T. M. Stace, and A. Fedorov, “Nonreciprocity realized with quantum nonlinearity,” *Phys. Rev. Lett.* **121**, 123601 (2018) [10.1103/PhysRevLett.121.123601](https://doi.org/10.1103/PhysRevLett.121.123601) (cit. on pp. 28, 29, 58).
- [136] A. S. Prasad, J. Hinney, S. Mahmoodian, K. Hammerer, S. Rind, P. Schneeweiss, A. S. Sørensen, J. Volz, and A. Rauschenbeutel, “Correlating photons using the collective nonlinear response of atoms weakly coupled to an optical mode,” *Nat. Photonics* **14**, 719–722 (2020) [10.1038/s41566-020-0692-z](https://doi.org/10.1038/s41566-020-0692-z) (cit. on p. 28).
- [137] A. Goban, C.-L. Hung, J. D. Hood, S.-P. Yu, J. A. Muniz, O. Painter, and H. J. Kimble, “Superradiance for atoms trapped along a photonic crystal waveguide,” *Phys. Rev. Lett.* **115**, 063601 (2015) [10.1103/PhysRevLett.115.063601](https://doi.org/10.1103/PhysRevLett.115.063601) (cit. on pp. 28, 29, 65).
- [138] S. Kumar and S. I. Bozhevolnyi, “Single photon emitters coupled to plasmonic waveguides: A review,” *Adv. Quantum Technol.* **4**, 2100057 (2021) <https://doi.org/10.1002/qute.202100057> (cit. on pp. 28, 29).
- [139] K. P. Nayak, P. N. Melentiev, M. Morinaga, F. L. Kien, V. I. Balykin, and K. Hakuta, “Optical nanofiber as an efficient tool for manipulating and probing atomic fluorescence,” *Opt. Express* **15**, 5431–5438 (2007) [10.1364/OE.15.005431](https://doi.org/10.1364/OE.15.005431) (cit. on p. 28).
- [140] E. Vetsch, D. Reitz, G. Sagué, R. Schmidt, S. T. Dawkins, and A. Rauschenbeutel, “Optical interface created by laser-cooled atoms trapped in the evanescent field surrounding an optical nanofiber,” *Phys. Rev. Lett.* **104**, 203603 (2010) [10.1103/PhysRevLett.104.203603](https://doi.org/10.1103/PhysRevLett.104.203603) (cit. on pp. 28, 65).
- [141] A. Goban, C. -L. Hung, S. -P. Yu, J. D. Hood, J. A. Muniz, J. H. Lee, M. J. Martin, A. C. McClung, K. S. Choi, D. E. Chang, O. Painter, and H. J. Kimble, “Atom–light interactions in photonic crystals,” *Nat. Commun.* **5**, 3808 (2014) [10.1038/ncomms4808](https://doi.org/10.1038/ncomms4808) (cit. on p. 29).
- [142] J. D. Hood, A. Goban, A. Asenjo-Garcia, M. Lu, S.-P. Yu, D. E. Chang, and H. J. Kimble, “Atom–atom interactions around the band edge of a photonic

- crystal waveguide,” *Proc. Natl. Acad. Sci. U.S.A.* **113**, 10507–10512 (2016) [10.1073/pnas.1603788113](#) (cit. on pp. 29, 47, 65).
- [143] A. P. Burgers, L. S. Peng, J. A. Muniz, A. C. McClung, M. J. Martin, and H. J. Kimble, “Clocked atom delivery to a photonic crystal waveguide,” *Proc. Natl. Acad. Sci. U.S.A.* **116**, 456–465 (2019) [10.1073/pnas.1817249115](#) (cit. on pp. 29, 93).
- [144] M. Antezza, L. P. Pitaevskii, and S. Stringari, “Effect of the Casimir-Polder force on the collective oscillations of a trapped Bose-Einstein condensate,” *Phys. Rev. A* **70**, 053619 (2004) [10.1103/PhysRevA.70.053619](#) (cit. on p. 29).
- [145] R. Uppu, L. Midolo, X. Zhou, J. Carolan, and P. Lodahl, “Quantum-dot-based deterministic photon–emitter interfaces for scalable photonic quantum technology,” *Nat. Nanotechnol.* **16**, 1308–1317 (2021) [10.1038/s41565-021-00965-6](#) (cit. on p. 29).
- [146] O. Astafiev, A. M. Zagoskin, A. A. Abdumalikov, Y. A. Pashkin, T. Yamamoto, K. Inomata, Y. Nakamura, and J. S. Tsai, “Resonance fluorescence of a single artificial atom,” *Science* **327**, 840–843 (2010) [10.1126/science.1181918](#) (cit. on pp. 29, 50, 152).
- [147] A. F. van Loo, A. Fedorov, K. Lalumière, B. C. Sanders, A. Blais, and A. Wallraff, “Photon-mediated interactions between distant artificial atoms,” *Science* **342**, 1494–1496 (2013) [10.1126/science.1244324](#) (cit. on pp. 29, 47, 206).
- [148] M. Zanner, T. Orell, C. M. F. Schneider, R. Albert, S. Oleschko, M. L. Juan, M. Silveri, and G. Kirchmair, “Coherent control of a symmetry-engineered multi-qubit dark state in waveguide quantum electrodynamics,” [arXiv:2106.05623](#) (2021) (cit. on p. 29).
- [149] G. J. Dolan, “Offset masks for lift-off photoprocessing,” *Appl. Phys. Lett.* **31**, 337–339 (1977) [10.1063/1.89690](#) (cit. on p. 31).
- [150] A. Dunsworth, A. Megrant, C. Quintana, Z. Chen, R. Barends, B. Burkett, B. Foxen, Y. Chen, B. Chiaro, A. Fowler, R. Graff, E. Jeffrey, J. Kelly, E. Lucero, J. Y. Mutus, M. Neeley, C. Neill, P. Roushan, D. Sank, A. Vainsencher, J. Wenner, T. C. White, and J. M. Martinis, “Characterization and reduction of capacitive loss induced by sub-micron Josephson junction fabrication in superconducting qubits,” *Appl. Phys. Lett.* **111**, 022601 (2017) [10.1063/1.4993577](#) (cit. on pp. 31, 148).
- [151] M. J. Rooks, E. Kratschmer, R. Viswanathan, J. Katine, R. E. Fontana, and S. A. MacDonald, “Low stress development of poly(methylmethacrylate) for high aspect ratio structures,” *J. Vac. Sci. Technol. B* **20**, 2937–2941 (2002) [10.1116/1.1524971](#) (cit. on pp. 31, 143).

- [152] S. Huang, B. Lienhard, G. Calusine, A. Vepsäläinen, J. Braumüller, D. K. Kim, A. J. Melville, B. M. Niedzielski, J. L. Yoder, B. Kannan, T. P. Orlando, S. Gustavsson, and W. D. Oliver, “Microwave package design for superconducting quantum processors,” *PRX Quantum* **2**, 020306 (2021) [10.1103/PRXQuantum.2.020306](https://doi.org/10.1103/PRXQuantum.2.020306) (cit. on pp. 32, 107).
- [153] V. S. Ferreira, J. Banker, A. Sipahigil, M. H. Matheny, A. J. Keller, E. Kim, M. Mirhosseini, and O. Painter, “Collapse and revival of an artificial atom coupled to a structured photonic reservoir,” *Phys. Rev. X* **11**, 041043 (2021) [10.1103/PhysRevX.11.041043](https://doi.org/10.1103/PhysRevX.11.041043), (cit. on pp. 32, 78, 81, 90, 94, 95, 191, 199, 201).
- [154] R. N. Simons, *Coplanar Waveguide Circuits, Components, and Systems* (John Wiley & Sons, 2001), [10.1002/0471224758](https://doi.org/10.1002/0471224758) (cit. on p. 33).
- [155] R. Stephens, “The thermal properties of sample addenda used in $T < 1$ K specific heat measurements: 1 – Specific heat and thermal conductivity of General Electric 7031 varnish,” *Cryogenics* **15**, 420–422 (1975) [https://doi.org/10.1016/0011-2275\(75\)90012-0](https://doi.org/10.1016/0011-2275(75)90012-0) (cit. on p. 35).
- [156] L. Salerno, P. Kittel, and A. Spivak, “Thermal conductance of pressed metallic contacts augmented with indium foil or Apiezon grease at liquid helium temperatures,” *Cryogenics* **34**, 649–654 (1994) [https://doi.org/10.1016/0011-2275\(94\)90142-2](https://doi.org/10.1016/0011-2275(94)90142-2) (cit. on p. 35).
- [157] J.-H. Yeh, J. LeFebvre, S. Premaratne, F. C. Wellstood, and B. S. Palmer, “Microwave attenuators for use with quantum devices below 100 mK,” *J. Appl. Phys.* **121**, 224501 (2017) [10.1063/1.4984894](https://doi.org/10.1063/1.4984894) (cit. on pp. 35, 36, 58, 63, 154, 200, 210).
- [158] J.-H. Yeh, Y. Huang, R. Zhang, S. Premaratne, J. LeFebvre, F. C. Wellstood, and B. S. Palmer, “Hot electron heatsinks for microwave attenuators below 100 mK,” *Appl. Phys. Lett.* **114**, 152602 (2019) [10.1063/1.5097369](https://doi.org/10.1063/1.5097369) (cit. on p. 35).
- [159] S. Krinner, S. Storz, P. Kurpiers, P. Magnard, J. Heinsoo, R. Keller, J. Lütolf, C. Eichler, and A. Wallraff, “Engineering cryogenic setups for 100-qubit scale superconducting circuit systems,” *EPJ Quantum Technol.* **6**, 2 (2019) [10.1140/epjqt/s40507-019-0072-0](https://doi.org/10.1140/epjqt/s40507-019-0072-0) (cit. on pp. 35, 107).
- [160] Z. Wang, S. Shankar, Z. Mineev, P. Campagne-Ibarcq, A. Narla, and M. Devoret, “Cavity attenuators for superconducting qubits,” *Phys. Rev. Applied* **11**, 014031 (2019) [10.1103/PhysRevApplied.11.014031](https://doi.org/10.1103/PhysRevApplied.11.014031) (cit. on p. 35).
- [161] M. L. Roukes, M. R. Freeman, R. S. Germain, R. C. Richardson, and M. B. Ketchen, “Hot electrons and energy transport in metals at millikelvin temperatures,” *Phys. Rev. Lett.* **55**, 422–425 (1985) [10.1103/PhysRevLett.55.422](https://doi.org/10.1103/PhysRevLett.55.422) (cit. on p. 36).

- [162] F. C. Wellstood, C. Urbina, and J. Clarke, “Hot-electron effects in metals,” *Phys. Rev. B* **49**, 5942–5955 (1994) [10.1103/PhysRevB.49.5942](#) (cit. on p. 36).
- [163] X. Y. Jin, A. Kamal, A. P. Sears, T. Gudmundsen, D. Hover, J. Miloshi, R. Slattery, F. Yan, J. Yoder, T. P. Orlando, S. Gustavsson, and W. D. Oliver, “Thermal and residual excited-state population in a 3D transmon qubit,” *Phys. Rev. Lett.* **114**, 240501 (2015) [10.1103/PhysRevLett.114.240501](#) (cit. on p. 36).
- [164] A. Kulikov, R. Navarathna, and A. Fedorov, “Measuring effective temperatures of qubits using correlations,” *Phys. Rev. Lett.* **124**, 240501 (2020) [10.1103/PhysRevLett.124.240501](#) (cit. on p. 36).
- [165] A. A. Clerk and D. W. Utami, “Using a qubit to measure photon-number statistics of a driven thermal oscillator,” *Phys. Rev. A* **75**, 042302 (2007) [10.1103/PhysRevA.75.042302](#) (cit. on p. 36).
- [166] C. Rigetti, J. M. Gambetta, S. Poletto, B. L. T. Plourde, J. M. Chow, A. D. Córcoles, J. A. Smolin, S. T. Merkel, J. R. Rozen, G. A. Keefe, M. B. Rothwell, M. B. Ketchen, and M. Steffen, “Superconducting qubit in a waveguide cavity with a coherence time approaching 0.1 ms,” *Phys. Rev. B* **86**, 100506 (2012) [10.1103/PhysRevB.86.100506](#) (cit. on p. 36).
- [167] F. Pobell, *Matter and Methods at Low Temperature* (Springer, 2007) (cit. on p. 36).
- [168] G. Ventura and L. Risegari, *The Art of Cryogenics: Low-Temperature Experimental Techniques* (Elsevier, 2008) (cit. on p. 36).
- [169] J. Aumentado, “Superconducting parametric amplifiers: the state of the art in Josephson parametric amplifiers,” *IEEE Microw. Mag.* **21**, 45–59 (2020) [10.1109/MMM.2020.2993476](#) (cit. on p. 37).
- [170] C. Macklin, K. O’Brien, D. Hover, M. E. Schwartz, V. Bolkhovskiy, X. Zhang, W. D. Oliver, and I. Siddiqi, “A near-quantum-limited Josephson traveling-wave parametric amplifier,” *Science* **350**, 307–310 (2015) [10.1126/science.aaa8525](#) (cit. on pp. 37, 66).
- [171] M. Esposito, A. Ranadive, L. Planat, and N. Roch, “Perspective on traveling wave microwave parametric amplifiers,” *Appl. Phys. Lett.* **119**, 120501 (2021) [10.1063/5.0064892](#) (cit. on p. 37).
- [172] R. Barends, J. Wenner, M. Lenander, Y. Chen, R. C. Bialczak, J. Kelly, E. Lucero, P. O’Malley, M. Mariantoni, D. Sank, H. Wang, T. C. White, Y. Yin, J. Zhao, A. N. Cleland, J. M. Martinis, and J. J. A. Baselmans, “Minimizing quasiparticle generation from stray infrared light in superconducting quantum circuits,” *Appl. Phys. Lett.* **99**, 113507 (2011) [10.1063/1.3638063](#) (cit. on p. 38).

- [173] A. D. Córcoles, J. M. Chow, J. M. Gambetta, C. Rigetti, J. R. Rozen, G. A. Keefe, M. Beth Rothwell, M. B. Ketchen, and M. Steffen, “Protecting superconducting qubits from radiation,” *Appl. Phys. Lett.* **99**, 181906 (2011) [10.1063/1.3658630](#) (cit. on p. 38).
- [174] D. F. Santavicca and D. E. Prober, “Impedance-matched low-pass stripline filters,” *Meas. Sci. Technol.* **19**, 087001 (2008) [10.1088/0957-0233/19/8/087001](#) (cit. on p. 38).
- [175] D. H. Slichter, O. Naaman, and I. Siddiqi, “Millikelvin thermal and electrical performance of lossy transmission line filters,” *Appl. Phys. Lett.* **94**, 192508 (2009) [10.1063/1.3133362](#) (cit. on p. 38).
- [176] M. Fang, “Development of Hardware for Scaling Up Superconducting Qubits and Simulation of Quantum Chaos,” Bachelor thesis (UC Santa Barbara, 2015) (cit. on p. 38).
- [177] T. Klaassen, J. Blok, J. Hovenier, G. Jakob, D. Rosenthal, and K. Wildeman, “Absorbing coatings and diffuse reflectors for the Herschel platform sub-millimeter spectrometers HIFI and PACS,” in *Proceedings, IEEE Tenth International Conference on Terahertz Electronics* (2002), pp. 32–35, [10.1109/THZ.2002.1037582](#) (cit. on p. 38).
- [178] S. W. Jolin, R. Borgani, M. O. Tholén, D. Forchheimer, and D. B. Haviland, “Calibration of mixer amplitude and phase imbalance in superconducting circuits,” *Rev. Sci. Instrum.* **91**, 124707 (2020) [10.1063/5.0025836](#) (cit. on p. 40).
- [179] E. Rubiola, “Tutorial on the double balanced mixer,” [arXiv:physics/0608211](#) (2006) (cit. on p. 40).
- [180] D. M. Pozar, *Microwave Engineering*, 4th ed. (John Wiley & Sons, 2012) (cit. on pp. 40, 66, 70, 100, 170).
- [181] F. Marki and C. Marki, *Mixer Basics Primer: A Tutorial for RF & Microwave Mixers*, available online at https://www.markimicrowave.com/assets/appnotes/mixer_basics_primer.pdf, 2010 (cit. on p. 40).
- [182] D. Jorgesen, *IQ, Image Reject & Single Sideband Mixer Primer*, available online at https://www.markimicrowave.com/assets/appnotes/IQ_IR_SSB_Mixer_Primer.pdf, 2018 (cit. on p. 40).
- [183] S. Simbierowicz, V. Y. Monarkha, S. Singh, N. Messaoudi, P. Krantz, and R. E. Lake, “Microwave calibration of qubit drive line components at millikelvin temperatures,” [arXiv:2112.05152](#) (2021) (cit. on p. 41).
- [184] E. Jeffrey, D. Sank, J. Y. Mutus, T. C. White, J. Kelly, R. Barends, Y. Chen, Z. Chen, B. Chiaro, A. Dunsworth, A. Megrant, P. J. J. O’Malley, C. Neill, P. Roushan, A. Vainsencher, J. Wenner, A. N. Cleland, and J. M. Martinis, “Fast accurate state measurement with superconducting qubits,” *Phys. Rev.*

- Lett. **112**, 190504 (2014) [10.1103/physrevlett.112.190504](https://doi.org/10.1103/physrevlett.112.190504) (cit. on pp. 45, 90, 94, 100, 107).
- [185] T. Walter, P. Kurpiers, S. Gasparinetti, P. Magnard, A. Potočnik, Y. Salathé, M. Pechal, M. Mondal, M. Oppliger, C. Eichler, and A. Wallraff, “Rapid high-fidelity single-shot dispersive readout of superconducting qubits,” *Phys. Rev. Applied* **7**, 054020 (2017) [10.1103/PhysRevApplied.7.054020](https://doi.org/10.1103/PhysRevApplied.7.054020) (cit. on pp. 45, 101).
- [186] E. Magesan, J. M. Gambetta, A. D. Córcoles, and J. M. Chow, “Machine learning for discriminating quantum measurement trajectories and improving readout,” *Phys. Rev. Lett.* **114**, 200501 (2015) [10.1103/PhysRevLett.114.200501](https://doi.org/10.1103/PhysRevLett.114.200501) (cit. on pp. 45, 101, 102).
- [187] E. M. Purcell, H. C. Torrey, and R. V. Pound, “Resonance absorption by nuclear magnetic moments in a solid,” *Phys. Rev.* **69**, 37–38 (1946) [10.1103/PhysRev.69.37](https://doi.org/10.1103/PhysRev.69.37) (cit. on p. 46).
- [188] R. Röhlberger, K. Schlage, B. Sahoo, S. Couet, and R. Ruffer, “Collective Lamb shift in single-photon superradiance,” *Science* **328**, 1248–1251 (2010) [10.1126/science.1187770](https://doi.org/10.1126/science.1187770) (cit. on p. 46).
- [189] M. O. Scully, “Collective Lamb shift in single photon Dicke superradiance,” *Phys. Rev. Lett.* **102**, 143601 (2009) [10.1103/PhysRevLett.102.143601](https://doi.org/10.1103/PhysRevLett.102.143601) (cit. on p. 46).
- [190] J. Koch, M. Y. Terri, J. Gambetta, A. A. Houck, D. I. Schuster, J. Majer, A. Blais, M. H. Devoret, S. M. Girvin, and R. J. Schoelkopf, “Charge-insensitive qubit design derived from the Cooper pair box,” *Phys. Rev. A* **76**, 042319 (2007) [10.1103/PhysRevA.76.042319](https://doi.org/10.1103/PhysRevA.76.042319) (cit. on pp. 46, 66, 71, 72, 75, 78, 81, 95, 105, 162).
- [191] A. Albrecht, L. Henriot, A. Asenjo-Garcia, P. B. Dieterle, O. Painter, and D. E. Chang, “Subradiant states of quantum bits coupled to a one-dimensional waveguide,” *New J. Phys.* **21**, 025003 (2019) [10.1088/1367-2630/ab0134](https://doi.org/10.1088/1367-2630/ab0134) (cit. on pp. 46, 47, 58).
- [192] T. Ramos, H. Pichler, A. J. Daley, and P. Zoller, “Quantum spin dimers from chiral dissipation in cold-atom chains,” *Phys. Rev. Lett.* **113**, 237203 (2014) [10.1103/PhysRevLett.113.237203](https://doi.org/10.1103/PhysRevLett.113.237203) (cit. on pp. 46, 47, 58).
- [193] S. Mahmoodian, M. Čepulkovskis, S. Das, P. Lodahl, K. Hammerer, and A. S. Sørensen, “Strongly correlated photon transport in waveguide quantum electrodynamics with weakly coupled emitters,” *Phys. Rev. Lett.* **121**, 143601 (2018) [10.1103/PhysRevLett.121.143601](https://doi.org/10.1103/PhysRevLett.121.143601) (cit. on pp. 46, 47, 58).
- [194] A. González-Tudela, V. Paulisch, D. E. Chang, H. J. Kimble, and J. I. Cirac, “Deterministic generation of arbitrary photonic states assisted by dissipation,” *Phys. Rev. Lett.* **115**, 163603 (2015) [10.1103/PhysRevLett.115.163603](https://doi.org/10.1103/PhysRevLett.115.163603) (cit. on pp. 46, 47, 58).

- [195] X. Gu, A. F. Kockum, A. Miranowicz, Y.-x. Liu, and F. Nori, “Microwave photonics with superconducting quantum circuits,” *Phys. Rep.* **718**, 1–102 (2017) [10.1016/j.physrep.2017.10.002](#) (cit. on pp. 47, 65, 66, 78).
- [196] D. Dzsoţjan, A. S. Sørensen, and M. Fleischhauer, “Quantum emitters coupled to surface plasmons of a nanowire: A Green’s function approach,” *Phys. Rev. B* **82**, 075427 (2010) [10.1103/PhysRevB.82.075427](#) (cit. on p. 47).
- [197] A. Asenjo-Garcia, J. D. Hood, D. E. Chang, and H. J. Kimble, “Atom-light interactions in quasi-one-dimensional nanostructures: A Green’s-function perspective,” *Phys. Rev. A* **95**, 033818 (2017) [10.1103/PhysRevA.95.033818](#) (cit. on p. 47).
- [198] A. F. Kockum, G. Johansson, and F. Nori, “Decoherence-free interaction between giant atoms in waveguide quantum electrodynamics,” *Phys. Rev. Lett.* **120**, 140404 (2018) [10.1103/PhysRevLett.120.140404](#) (cit. on p. 47).
- [199] N. M. Sundaresan, R. Lundgren, G. Zhu, A. V. Gorshkov, and A. A. Houck, “Interacting qubit-photon bound states with superconducting circuits,” *Phys. Rev. X* **9**, 011021 (2019) [10.1103/PhysRevX.9.011021](#) (cit. on pp. 47, 76, 78, 93, 98).
- [200] R. J. Cook and H. J. Kimble, “Possibility of direct observation of quantum jumps,” *Phys. Rev. Lett.* **54**, 1023–1026 (1985) [10.1103/PhysRevLett.54.1023](#) (cit. on p. 56).
- [201] N. T. Bronn, V. P. Adiga, S. B. Olivadese, X. Wu, J. M. Chow, and D. P. Pappas, “High coherence plane breaking packaging for superconducting qubits,” *Quantum Sci. Technol.* **3**, 024007 (2018) [10.1088/2058-9565/aaa645](#) (cit. on p. 58).
- [202] X. Chen, Z.-C. Gu, Z.-X. Liu, and X.-G. Wen, “Symmetry protected topological orders and the group cohomology of their symmetry group,” *Phys. Rev. B* **87**, 155114 (2013) [10.1103/physrevb.87.155114](#) (cit. on pp. 61, 77).
- [203] M.-D. Wu, S.-M. Deng, R.-B. Wu, and P. Hsu, “Full-wave characterization of the mode conversion in a coplanar waveguide right-angled bend,” *IEEE Trans. Microw. Theory Technol.* **43**, 2532–2538 (1995) [10.1109/22.473174](#) (cit. on p. 61).
- [204] P. Yao, C. Van Vlack, A. Reza, M. Patterson, M. M. Dignam, and S. Hughes, “Ultrahigh Purcell factors and Lamb shifts in slow-light metamaterial waveguides,” *Phys. Rev. B* **80**, 195106 (2009) [10.1103/PhysRevB.80.195106](#) (cit. on p. 65).
- [205] G. Calajó, F. Ciccarello, D. Chang, and P. Rabl, “Atom-field dressed states in slow-light waveguide QED,” *Phys. Rev. A* **93**, 033833 (2016) [10.1103/PhysRevA.93.033833](#) (cit. on pp. 65, 76, 98, 206).

- [206] V. P. Bykov, “Spontaneous emission from a medium with a band spectrum,” *Sov. J. Quantum Electron.* **4**, 861–871 (1975) [10.1070/qe1975v004n07abeh009654](#) (cit. on p. 65).
- [207] A. Kofman, G. Kurizki, and B. Sherman, “Spontaneous and induced atomic decay in photonic band structures,” *J. Mod. Opt.* **41**, 353–384 (1994) [10.1080/09500349414550381](#) (cit. on pp. 65, 73).
- [208] E. Munro, L. C. Kwek, and D. E. Chang, “Optical properties of an atomic ensemble coupled to a band edge of a photonic crystal waveguide,” *New Journal of Physics* **19**, 083018 (2017) [10.1088/1367-2630/aa7fad](#) (cit. on p. 65).
- [209] E. Shahmoon, P. Grišins, H. P. Stimming, I. Mazets, and G. Kurizki, “Highly nonlocal optical nonlinearities in atoms trapped near a waveguide,” *Optica* **3**, 725–733 (2016) [10.1364/OPTICA.3.000725](#) (cit. on p. 65).
- [210] J. S. Douglas, T. Caneva, and D. E. Chang, “Photon molecules in atomic gases trapped near photonic crystal waveguides,” *Phys. Rev. X* **6**, 031017 (2016) [10.1103/PhysRevX.6.031017](#) (cit. on pp. 65, 76).
- [211] S.-P. Yu, J. D. Hood, J. A. Muniz, M. J. Martin, R. Norte, C.-L. Hung, S. M. Meenehan, J. D. Cohen, O. Painter, and H. J. Kimble, “Nanowire photonic crystal waveguides for single-atom trapping and strong light-matter interactions,” *Appl. Phys. Lett.* **104**, 111103 (2014) [10.1063/1.4868975](#) (cit. on p. 65).
- [212] A. Javadi, I. Söllner, M. Arcari, S. L. Hansen, L. Midolo, S. Mahmoodian, G. Kiršanskė, T. Pregnolato, E. H. Lee, J. D. Song, S. Stobbe, and P. Lodahl, “Single-photon non-linear optics with a quantum dot in a waveguide,” *Nat. Commun.* **6**, 8655 (2015) [10.1038/ncomms9655](#) (cit. on p. 65).
- [213] M. K. Bhaskar, D. D. Sukachev, A. Sipahigil, R. E. Evans, M. J. Burek, C. T. Nguyen, L. J. Rogers, P. Siyushev, M. H. Metsch, H. Park, F. Jelezko, M. Lončar, and M. D. Lukin, “Quantum nonlinear optics with a germanium-vacancy color center in a nanoscale diamond waveguide,” *Phys. Rev. Lett.* **118**, 223603 (2017) [10.1103/PhysRevLett.118.223603](#) (cit. on p. 65).
- [214] Y. Chen, C. Neill, P. Roushan, N. Leung, M. Fang, R. Barends, J. Kelly, B. Campbell, Z. Chen, B. Chiaro, A. Dunsworth, E. Jeffrey, A. Megrant, J. Y. Mutus, P. J. J. O’Malley, C. M. Quintana, D. Sank, A. Vainsencher, J. Wenner, T. C. White, M. R. Geller, A. N. Cleland, and J. M. Martinis, “Qubit architecture with high coherence and fast tunable coupling,” *Phys. Rev. Lett.* **113**, 220502 (2014) [10.1103/physrevlett.113.220502](#) (cit. on pp. 66, 90).
- [215] Y. Liu and A. A. Houck, “Quantum electrodynamics near a photonic bandgap,” *Nat. Phys.* **13**, 48–52 (2016) [10.1038/nphys3834](#) (cit. on pp. 66, 78, 83, 93).

- [216] D. R. Smith, W. J. Padilla, D. C. Vier, S. C. Nemat-Nasser, and S. Schultz, “Composite medium with simultaneously negative permeability and permittivity,” *Phys. Rev. Lett.* **84**, 4184–4187 (2000) [10.1103/PhysRevLett.84.4184](#) (cit. on p. 66).
- [217] C. Caloz and T. Itoh, *Electromagnetic Metamaterials: Transmission Line Theory and Microwave Applications* (John Wiley & Sons, 2006) (cit. on p. 66).
- [218] T. Koschny, C. M. Soukoulis, and M. Wegener, “Metamaterials in microwaves, optics, mechanics, thermodynamics, and transport,” *J. Opt.* **19**, 084005 (2017) [10.1088/2040-8986/aa7288](#) (cit. on p. 66).
- [219] A. Alù and N. Engheta, “Enabling a new degree of wave control with metamaterials: a personal perspective,” *J. Opt.* **19**, 084008 (2017) [10.1088/2040-8986/aa7790](#) (cit. on p. 66).
- [220] H.-T. Chen, A. J. Taylor, and N. Yu, “A review of metasurfaces: physics and applications,” *Rep. Prog. Phys.* **79**, 076401 (2016) [10.1088/0034-4885/79/7/076401](#) (cit. on p. 66).
- [221] A. L. Rakhmanov, A. M. Zagoskin, S. Savel’ev, and F. Nori, “Quantum metamaterials: Electromagnetic waves in a Josephson qubit line,” *Phys. Rev. B* **77**, 144507 (2008) [10.1103/PhysRevB.77.144507](#) (cit. on p. 66).
- [222] M. Göppl, A. Fragner, M. Baur, R. Bianchetti, S. Filipp, J. M. Fink, P. J. Leek, G. Puebla, L. Steffen, and A. Wallraff, “Coplanar waveguide resonators for circuit quantum electrodynamics,” *J. Appl. Phys.* **104**, 113904 (2008) [10.1063/1.3010859](#) (cit. on pp. 66, 70).
- [223] T. C. White, J. Y. Mutus, I.-C. Hoi, R. Barends, B. Campbell, Y. Chen, Z. Chen, B. Chiaro, A. Dunsworth, E. Jeffrey, J. Kelly, A. Megrant, C. Neill, P. J. J. O’Malley, P. Roushan, D. Sank, A. Vainsencher, J. Wenner, S. Chaudhuri, J. Gao, and J. M. Martinis, “Traveling wave parametric amplifier with Josephson junctions using minimal resonator phase matching,” *Appl. Phys. Lett.* **106**, 242601 (2015) [10.1063/1.4922348](#) (cit. on p. 66).
- [224] D. C. McKay, R. Naik, P. Reinhold, L. S. Bishop, and D. I. Schuster, “High-contrast qubit interactions using multimode cavity QED,” *Phys. Rev. Lett.* **114**, 080501 (2015) [10.1103/PhysRevLett.114.080501](#) (cit. on p. 66).
- [225] J. C. Hernández-Herrejón, F. M. Izrailev, and L. Tessieri, “Anomalous localization in the aperiodic Kronig–Penney model,” *J. Phys. A: Math. Theor.* **43**, 425004 (2010) [10.1088/1751-8113/43/42/425004](#) (cit. on pp. 68, 176).
- [226] M. H. Devoret, “Quantum fluctuations in electrical circuits,” in *Proceedings of the Les Houches Summer School, Session LXIII*, edited by S. Reynaud, E. Giacobino, and J. Zinn-Justin (Elsevier Science B. V., New York, 1997) (cit. on pp. 69, 95, 165).

- [227] J. Zhou, M. Lancaster, and F. Huang, “Superconducting microstrip filters using compact resonators with double-spiral inductors and interdigital capacitors,” in *IEEE MTT-S International Microwave Symposium Digest*, 2003, Vol. 3 (2003), 1889–1892 vol.3, [10.1109/MWSYM.2003.1210526](#) (cit. on p. 70).
- [228] D. L. Underwood, W. E. Shanks, J. Koch, and A. A. Houck, “Low-disorder microwave cavity lattices for quantum simulation with photons,” *Phys. Rev. A* **86**, 023837 (2012) [10.1103/PhysRevA.86.023837](#) (cit. on pp. 70, 175).
- [229] D. S. Wiersma, P. Bartolini, A. Lagendijk, and R. Righini, “Localization of light in a disordered medium,” *Nature* **390**, 671–673 (1997) [10.1038/37757](#) (cit. on p. 71).
- [230] A. J. Keller, P. B. Dieterle, M. Fang, B. Berger, J. M. Fink, and O. Painter, “Al transmon qubits on silicon-on-insulator for quantum device integration,” *Applied Physics Letters* **111**, 042603 (2017) [10.1063/1.4994661](#) (cit. on p. 71).
- [231] A. Wallraff, D. I. Schuster, A. Blais, L. Frunzio, J. Majer, M. H. Devoret, S. M. Girvin, and R. J. Schoelkopf, “Approaching unit visibility for control of a superconducting qubit with dispersive readout,” *Phys. Rev. Lett.* **95**, 060501 (2005) [10.1103/PhysRevLett.95.060501](#) (cit. on pp. 73, 107).
- [232] G. Nikoghosyan and M. Fleischhauer, “Photon-number selective group delay in cavity induced transparency,” *Phys. Rev. Lett.* **105**, 013601 (2010) [10.1103/PhysRevLett.105.013601](#) (cit. on p. 76).
- [233] A. Albrecht, T. Caneva, and D. E. Chang, “Changing optical band structure with single photons,” *New J. Phys.* **19**, 115002 (2017) [10.1088/1367-2630/aa83ea](#) (cit. on p. 76).
- [234] K. Inomata, Z. Lin, K. Koshino, W. D. Oliver, J.-S. Tsai, T. Yamamoto, and Y. Nakamura, “Single microwave-photon detector using an artificial Λ -type three-level system,” *Nat. Commun.* **7**, 12303 (2016) [10.1038/ncomms12303](#) (cit. on p. 76).
- [235] J.-C. Besse, S. Gasparinetti, M. C. Collodo, T. Walter, P. Kurpiers, M. Pechal, C. Eichler, and A. Wallraff, “Single-shot quantum nondemolition detection of individual itinerant microwave photons,” *Phys. Rev. X* **8**, 021003 (2018) [10.1103/PhysRevX.8.021003](#) (cit. on p. 76).
- [236] A. D. Greentree, C. Tahan, J. H. Cole, and L. C. L. Hollenberg, “Quantum phase transitions of light,” *Nat. Phys.* **2**, 856–861 (2006) [10.1038/nphys466](#) (cit. on p. 76).
- [237] M. J. Hartmann, F. G. S. L. Brandão, and M. B. Plenio, “Strongly interacting polaritons in coupled arrays of cavities,” *Nat. Phys.* **2**, 849–855 (2006) [10.1038/nphys462](#) (cit. on p. 76).

- [238] A. A. Houck, H. E. Türeci, and J. Koch, “On-chip quantum simulation with superconducting circuits,” *Nat. Phys.* **8**, 292–299 (2012) [10.1038/nphys2251](#) (cit. on p. 76).
- [239] C. Noh and D. G. Angelakis, “Quantum simulations and many-body physics with light,” *Rep. Prog. Phys.* **80**, 016401 (2016) [10.1088/0034-4885/80/1/016401](#) (cit. on p. 76).
- [240] F. D. M. Haldane and S. Raghu, “Possible realization of directional optical waveguides in photonic crystals with broken time-reversal symmetry,” *Phys. Rev. Lett.* **100**, 013904 (2008) [10.1103/PhysRevLett.100.013904](#) (cit. on p. 77).
- [241] L. Lu, J. D. Joannopoulos, and M. Soljačić, “Topological photonics,” *Nat. Photonics* **8**, 821–829 (2014) [10.1038/nphoton.2014.248](#) (cit. on pp. 77, 78).
- [242] K. von Klitzing, “The quantized Hall effect,” *Rev. Mod. Phys.* **58**, 519–531 (1986) [10.1103/RevModPhys.58.519](#) (cit. on p. 77).
- [243] M. Z. Hasan and C. L. Kane, “Colloquium: Topological insulators,” *Rev. Mod. Phys.* **82**, 3045–3067 (2010) [10.1103/revmodphys.82.3045](#) (cit. on p. 77).
- [244] D. Smirnova, D. Leykam, Y. Chong, and Y. Kivshar, “Nonlinear topological photonics,” *Appl. Phys. Rev.* **7**, 021306 (2020) [10.1063/1.5142397](#) (cit. on p. 77).
- [245] W. P. Su, J. R. Schrieffer, and A. J. Heeger, “Solitons in polyacetylene,” *Phys. Rev. Lett.* **42**, 1698–1701 (1979) [10.1103/physrevlett.42.1698](#) (cit. on pp. 77, 183).
- [246] J. K. Asbóth, L. Oroszlány, and A. Pályi, *A Short Course on Topological Insulators*, Lecture Notes in Physics (Springer, 2016), [10.1007/978-3-319-25607-8](#) (cit. on pp. 77, 80, 193).
- [247] P. St-Jean, V. Goblot, E. Galopin, A. Lemaître, T. Ozawa, L. Le Gratiet, I. Sagnes, J. Bloch, and A. Amo, “Lasing in topological edge states of a one-dimensional lattice,” *Nat. Photonics* **11**, 651–656 (2017) [10.1038/s41566-017-0006-2](#) (cit. on p. 78).
- [248] H. Zhao, P. Miao, M. H. Teimourpour, S. Malzard, R. El-Ganainy, H. Schomerus, and L. Feng, “Topological hybrid silicon microlasers,” *Nat. Commun.* **9**, 981 (2018) [10.1038/s41467-018-03434-2](#) (cit. on p. 78).
- [249] Y. Ota, R. Katsumi, K. Watanabe, S. Iwamoto, and Y. Arakawa, “Topological photonic crystal nanocavity laser,” *Commun. Phys.* **1**, 86 (2018) [10.1038/s42005-018-0083-7](#) (cit. on p. 78).
- [250] S. Kruk, A. Poddubny, D. Smirnova, L. Wang, A. Slobozhanyuk, A. Shorokhov, I. Kravchenko, B. Luther-Davies, and Y. Kivshar, “Nonlinear light genera-

- tion in topological nanostructures,” *Nat. Nanotechnol.* **14**, 126–130 (2019) [10.1038/s41565-018-0324-7](https://doi.org/10.1038/s41565-018-0324-7) (cit. on p. 78).
- [251] I. Carusotto and C. Ciuti, “Quantum fluids of light,” *Rev. Mod. Phys.* **85**, 299 (2013) [10.1103/RevModPhys.85.299](https://doi.org/10.1103/RevModPhys.85.299) (cit. on p. 78).
- [252] P. Roushan, C. Neill, A. Megrant, Y. Chen, R. Babbush, R. Barends, B. Campbell, Z. Chen, B. Chiaro, A. Dunsworth, A. Fowler, E. Jeffrey, J. Kelly, E. Lucero, J. Mutus, P. J. J. O’Malley, M. Neeley, C. Quintana, D. Sank, A. Vainsencher, J. Wenner, T. White, E. Kapit, H. Neven, and J. Martinis, “Chiral ground-state currents of interacting photons in a synthetic magnetic field,” *Nat. Phys.* **13**, 146 (2017) [10.1038/nphys3930](https://doi.org/10.1038/nphys3930) (cit. on p. 78).
- [253] B. M. Anderson, R. Ma, C. Owens, D. I. Schuster, and J. Simon, “Engineering topological many-body materials in microwave cavity arrays,” *Phys. Rev. X* **6**, 041043 (2016) [10.1103/physrevx.6.041043](https://doi.org/10.1103/physrevx.6.041043) (cit. on pp. 78, 90).
- [254] W. Cai, J. Han, F. Mei, Y. Xu, Y. Ma, X. Li, H. Wang, Y. Song, Z.-Y. Xue, Z.-q. Yin, et al., “Observation of topological magnon insulator states in a superconducting circuit,” *Phys. Rev. Lett.* **123**, 080501 (2019) [10.1103/PhysRevLett.123.080501](https://doi.org/10.1103/PhysRevLett.123.080501) (cit. on p. 78).
- [255] S. de Léséleuc, V. Lienhard, P. Scholl, D. Barredo, S. Weber, N. Lang, H. P. Büchler, T. Lahaye, and A. Browaeys, “Observation of a symmetry-protected topological phase of interacting bosons with Rydberg atoms,” *Science* **365**, 775–780 (2019) [10.1126/science.aav9105](https://doi.org/10.1126/science.aav9105) (cit. on pp. 78, 90).
- [256] T. Shi, Y.-H. Wu, A. González-Tudela, and J. I. Cirac, “Effective many-body Hamiltonians of qubit-photon bound states,” *New J. Phys.* **20**, 105005 (2018) [10.1088/1367-2630/aae4a9](https://doi.org/10.1088/1367-2630/aae4a9) (cit. on p. 78).
- [257] C.-L. Hung, A. González-Tudela, J. I. Cirac, and H. J. Kimble, “Quantum spin dynamics with pairwise-tunable, long-range interactions,” *Proc. Natl. Acad. Sci. U.S.A* **113**, E4946–E4955 (2016) [10.1073/pnas.1603777113](https://doi.org/10.1073/pnas.1603777113) (cit. on p. 78).
- [258] S. Barik, A. Karasahin, C. Flower, T. Cai, H. Miyake, W. DeGottardi, M. Hafezi, and E. Waks, “A topological quantum optics interface,” *Science* **359**, 666–668 (2018) [10.1126/science.aaq0327](https://doi.org/10.1126/science.aaq0327) (cit. on p. 78).
- [259] I. García-Elcano, A. González-Tudela, and J. Bravo-Abad, “Tunable and robust long-range coherent interactions between quantum emitters mediated by Weyl bound states,” *Phys. Rev. Lett.* **125**, 163602 (2020) [10.1103/PhysRevLett.125.163602](https://doi.org/10.1103/PhysRevLett.125.163602) (cit. on pp. 78, 90).
- [260] J. Zak, “Berry’s phase for energy bands in solids,” *Phys. Rev. Lett.* **62**, 2747–2750 (1989) [10.1103/physrevlett.62.2747](https://doi.org/10.1103/physrevlett.62.2747) (cit. on pp. 81, 84, 187).
- [261] M. Biondi, S. Schmidt, G. Blatter, and H. E. Türeci, “Self-protected polariton states in photonic quantum metamaterials,” *Phys. Rev. A* **89**, 025801 (2014) [10.1103/physreva.89.025801](https://doi.org/10.1103/physreva.89.025801) (cit. on p. 83).

- [262] M. S. Khalil, M. J. A. Stoutimore, F. C. Wellstood, and K. D. Osborn, “An analysis method for asymmetric resonator transmission applied to superconducting devices,” *J. Appl. Phys.* **111**, 054510 (2012) [10.1063/1.3692073](#) (cit. on p. 83).
- [263] D. Witthaut and A. S. Sorensen, “Photon scattering by a three-level emitter in a one-dimensional waveguide,” *New J. Phys.* **12**, 043052 (2010) [10.1088/1367-2630/12/4/043052](#) (cit. on pp. 86, 206).
- [264] Y. Chen, D. Sank, P. O’Malley, T. White, R. Barends, B. Chiaro, J. Kelly, E. Lucero, M. Mariantoni, A. Megrant, C. Neill, A. Vainsencher, J. Wenner, Y. Yin, A. N. Cleland, and J. M. Martinis, “Multiplexed dispersive readout of superconducting phase qubits,” *Appl. Phys. Lett.* **101**, 182601 (2012) [10.1063/1.4764940](#) (cit. on p. 89).
- [265] N. Khaneja, T. Reiss, C. Kehlet, T. Schulte-Herbrüggen, and S. J. Glaser, “Optimal control of coupled spin dynamics: design of NMR pulse sequences by gradient ascent algorithms,” *J. Magn. Reson.* **172**, 296–305 (2005) [10.1016/j.jmr.2004.11.004](#) (cit. on p. 90).
- [266] F. Motzoi, J. M. Gambetta, P. Rebentrost, and F. K. Wilhelm, “Simple pulses for elimination of leakage in weakly nonlinear qubits,” *Phys. Rev. Lett.* **103**, 110501 (2009) [10.1103/physrevlett.103.110501](#) (cit. on p. 90).
- [267] N. Didier, E. A. Sete, J. Combes, and M. P. d. Silva, “AC flux sweet spots in parametrically-modulated superconducting qubits,” *Phys. Rev. Appl.* **12**, 054015 (2018) [10.1103/physrevapplied.12.054015](#) (cit. on p. 90).
- [268] S. S. Hong, A. T. Papageorge, P. Sivarajah, G. Crossman, N. Didier, A. M. Polloreno, E. A. Sete, S. W. Turkowski, M. P. d. Silva, and B. R. Johnson, “Demonstration of a parametrically activated entangling gate protected from flux noise,” *Phys. Rev. A* **101**, 012302 (2020) [10.1103/physreva.101.012302](#) (cit. on p. 90).
- [269] E. A. Sete, M. J. Reagor, N. Didier, and C. T. Rigetti, “Charge- and flux-insensitive tunable superconducting qubit,” *Phys. Rev. Appl.* **8**, 024004 (2017) [10.1103/PhysRevApplied.8.024004](#) (cit. on p. 90).
- [270] M. D. Hutchings, J. B. Hertzberg, Y. Liu, N. T. Bronn, G. A. Keefe, M. Brink, J. M. Chow, and B. L. T. Plourde, “Tunable superconducting qubits with flux-independent coherence,” *Phys. Rev. Appl.* **8**, 044003 (2017) [10.1103/physrevapplied.8.044003](#) (cit. on p. 90).
- [271] H. W. Ott, *Electromagnetic Compatibility Engineering* (John Wiley & Sons, 2009), [10.1002/9780470508510](#) (cit. on p. 90).
- [272] N. Lang and H. P. Büchler, “Topological networks for quantum communication between distant qubits,” *npj Quantum Inf.* **3**, 47 (2017) [10.1038/s41534-017-0047-x](#) (cit. on p. 90).

- [273] D. T. Tran, A. Dauphin, A. G. Grushin, P. Zoller, and N. Goldman, “Probing topology by “heating”: Quantized circular dichroism in ultracold atoms,” *Sci. Adv.* **3**, e1701207 (2017) [10.1126/sciadv.1701207](https://doi.org/10.1126/sciadv.1701207) (cit. on p. 90).
- [274] A. Dunsworth, R. Barends, Y. Chen, Z. Chen, B. Chiaro, A. Fowler, B. Foxen, E. Jeffrey, J. Kelly, P. V. Klimov, E. Lucero, J. Y. Mutus, M. Neeley, C. Neill, C. Quintana, P. Roushan, D. Sank, A. Vainsencher, J. Wenner, T. C. White, H. Neven, J. M. Martinis, and A. Megrant, “A method for building low loss multi-layer wiring for superconducting microwave devices,” *Appl. Phys. Lett.* **112**, 063502 (2018) [10.1063/1.5014033](https://doi.org/10.1063/1.5014033) (cit. on p. 90).
- [275] D. Rosenberg, D. Kim, R. Das, D. Yost, S. Gustavsson, D. Hover, P. Krantz, A. Melville, L. Racz, G. O. Samach, S. J. Weber, F. Yan, J. Yoder, A. J. Kerman, and W. D. Oliver, “3D integrated superconducting qubits,” *npj Quantum Inf.* **3**, 42 (2017) [10.1038/s41534-017-0044-0](https://doi.org/10.1038/s41534-017-0044-0) (cit. on p. 90).
- [276] B. Foxen, J. Y. Mutus, E. Lucero, R. Graff, A. Megrant, Y. Chen, C. Quintana, B. Burkett, J. Kelly, E. Jeffrey, Y. Yang, A. Yu, K. Arya, R. Barends, Z. Chen, B. Chiaro, A. Dunsworth, A. Fowler, C. Gidney, M. Giustina, T. Huang, P. Klimov, M. Neeley, C. Neill, P. Roushan, D. Sank, A. Vainsencher, J. Wenner, T. C. White, and J. M. Martinis, “Qubit compatible superconducting interconnects,” *Quantum Sci. Technol.* **3**, 014005 (2017) [10.1088/2058-9565/aa94fc](https://doi.org/10.1088/2058-9565/aa94fc) (cit. on p. 90).
- [277] R. Ma, C. Owens, A. Houck, D. I. Schuster, and J. Simon, “Autonomous stabilizer for incompressible photon fluids and solids,” *Phys. Rev. A* **95**, 043811 (2017) [10.1103/physreva.95.043811](https://doi.org/10.1103/physreva.95.043811) (cit. on pp. 90, 106).
- [278] C. Owens, A. LaChapelle, B. Saxberg, B. M. Anderson, R. Ma, J. Simon, and D. I. Schuster, “Quarter-flux hofstadter lattice in a qubit-compatible microwave cavity array,” *Phys. Rev. A* **97**, 013818 (2018) [10.1103/physreva.97.013818](https://doi.org/10.1103/physreva.97.013818) (cit. on p. 90).
- [279] I. Carusotto, A. A. Houck, A. J. Kollár, P. Roushan, D. I. Schuster, and J. Simon, “Photonic materials in circuit quantum electrodynamics,” *Nat. Phys.* **16**, 268–279 (2020) [10.1038/s41567-020-0815-y](https://doi.org/10.1038/s41567-020-0815-y) (cit. on p. 91).
- [280] Y. P. Zhong, H. -S. Chang, K. J. Satzinger, M. -H. Chou, A. Bienfait, C. R. Conner, É. Dumur, J. Grebel, G. A. Peairs, R. G. Povey, D. I. Schuster, and A. N. Cleland, “Violating Bell’s inequality with remotely connected superconducting qubits,” *Nat. Phys.* **15**, 741–744 (2019) [10.1038/s41567-019-0507-7](https://doi.org/10.1038/s41567-019-0507-7) (cit. on p. 93).
- [281] B. Kannan, M. J. Ruckriegel, D. L. Campbell, A. Frisk Kockum, J. Braumüller, D. K. Kim, M. Kjaergaard, P. Krantz, A. Melville, B. M. Niedzielski, A. Vepsäläinen, R. Winik, J. L. Yoder, F. Nori, T. P. Orlando, S. Gustavsson, and W. D. Oliver, “Waveguide quantum electrodynamics with superconducting artificial giant atoms,” *Nature* **583**, 775–779 (2020) [10.1038/s41586-020-2529-9](https://doi.org/10.1038/s41586-020-2529-9) (cit. on p. 93).

- [282] M. Scigliuzzo, G. Calajó, F. Ciccarello, D. P. Lozano, A. Bengtsson, P. Scarlino, A. Wallraff, D. Chang, P. Delsing, and S. Gasparinetti, “Extensible quantum simulation architecture based on atom-photon bound states in an array of high-impedance resonators,” arXiv:2107.06852 (2021) (cit. on p. 93).
- [283] M. Fitzpatrick, N. M. Sundaresan, A. C. Y. Li, J. Koch, and A. A. Houck, “Observation of a dissipative phase transition in a one-dimensional circuit QED lattice,” *Phys. Rev. X* **7**, 011016 (2017) [10.1103/PhysRevX.7.011016](#) (cit. on p. 93).
- [284] M. A. Rol, L. Ciorciaro, F. K. Malinowski, B. M. Tarasinski, R. E. Sagastizabal, C. C. Bultink, Y. Salathe, N. Haandbaek, J. Sedivy, and L. DiCarlo, “Time-domain characterization and correction of on-chip distortion of control pulses in a quantum processor,” *Appl. Phys. Lett.* **116**, 054001 (2020) [10.1063/1.5133894](#) (cit. on p. 100).
- [285] M. D. Reed, B. R. Johnson, A. A. Houck, L. DiCarlo, J. M. Chow, D. I. Schuster, L. Frunzio, and R. J. Schoelkopf, “Fast reset and suppressing spontaneous emission of a superconducting qubit,” *Appl. Phys. Lett.* **96**, 203110 (2010) [10.1063/1.3435463](#) (cit. on pp. 100, 107).
- [286] A. Y. Cleland, M. Pechal, P.-J. C. Stas, C. J. Sarabalis, E. A. Wollack, and A. H. Safavi-Naeini, “Mechanical Purcell filters for microwave quantum machines,” *Appl. Phys. Lett.* **115**, 263504 (2019) [10.1063/1.5111151](#) (cit. on p. 100).
- [287] J. Heinsoo, C. K. Andersen, A. Remm, S. Krinner, T. Walter, Y. Salathé, S. Gasparinetti, J.-C. Besse, A. Potočnik, A. Wallraff, and C. Eichler, “Rapid high-fidelity multiplexed readout of superconducting qubits,” *Phys. Rev. Applied* **10**, 034040 (2018) [10.1103/PhysRevApplied.10.034040](#) (cit. on pp. 101, 102, 104, 107).
- [288] C. A. Ryan, B. R. Johnson, J. M. Gambetta, J. M. Chow, M. P. da Silva, O. E. Dial, and T. A. Ohki, “Tomography via correlation of noisy measurement records,” *Phys. Rev. A* **91**, 022118 (2015) [10.1103/PhysRevA.91.022118](#) (cit. on p. 101).
- [289] D. Sank, Z. Chen, M. Khezri, J. Kelly, R. Barends, B. Campbell, Y. Chen, B. Chiaro, A. Dunsworth, A. Fowler, E. Jeffrey, E. Lucero, A. Megrant, J. Mutus, M. Neeley, C. Neill, P. J. J. O’Malley, C. Quintana, P. Roushan, A. Vainsencher, T. White, J. Wenner, A. N. Korotkov, and J. M. Martinis, “Measurement-induced state transitions in a superconducting qubit: Beyond the rotating wave approximation,” *Phys. Rev. Lett.* **117**, 190503 (2016) [10.1103/PhysRevLett.117.190503](#) (cit. on p. 102).
- [290] J. S. Cotler, D. K. Mark, H.-Y. Huang, F. Hernandez, J. Choi, A. L. Shaw, M. Endres, and S. Choi, “Emergent quantum state designs from individual many-body wavefunctions,” arXiv:2103.03536 (2021) (cit. on p. 104).

- [291] J. Choi, A. L. Shaw, I. S. Madjarov, X. Xie, J. P. Covey, J. S. Cotler, D. K. Mark, H.-Y. Huang, A. Kale, H. Pichler, F. G. S. L. Brandão, S. Choi, and M. Endres, “Emergent randomness and benchmarking from many-body quantum chaos,” arXiv:2103.03535 (2021) (cit. on p. 104).
- [292] Y. Li, X. Chen, and M. P. A. Fisher, “Quantum Zeno effect and the many-body entanglement transition,” *Phys. Rev. B* **98**, 205136 (2018) [10.1103/PhysRevB.98.205136](#) (cit. on pp. 104, 106).
- [293] S. Choi, Y. Bao, X.-L. Qi, and E. Altman, “Quantum error correction in scrambling dynamics and measurement-induced phase transition,” *Phys. Rev. Lett.* **125**, 030505 (2020) [10.1103/PhysRevLett.125.030505](#) (cit. on pp. 104, 106).
- [294] M. J. Gullans and D. A. Huse, “Dynamical purification phase transition induced by quantum measurements,” *Phys. Rev. X* **10**, 041020 (2020) [10.1103/PhysRevX.10.041020](#) (cit. on pp. 104, 106).
- [295] B. Skinner, J. Ruhman, and A. Nahum, “Measurement-induced phase transitions in the dynamics of entanglement,” *Phys. Rev. X* **9**, 031009 (2019) [10.1103/PhysRevX.9.031009](#) (cit. on pp. 104, 106).
- [296] C. Noel, P. Niroula, D. Zhu, A. Risinger, L. Egan, D. Biswas, M. Cetina, A. V. Gorshkov, M. J. Gullans, D. A. Huse, and C. Monroe, “Observation of measurement-induced quantum phases in a trapped-ion quantum computer,” arXiv:2106.05881 (2021) (cit. on pp. 104, 107).
- [297] Y. Wu et al., “Strong quantum computational advantage using a superconducting quantum processor,” *Phys. Rev. Lett.* **127**, 180501 (2021) [10.1103/PhysRevLett.127.180501](#) (cit. on pp. 104, 107).
- [298] M. Gong et al., “Quantum walks on a programmable two-dimensional 62-qubit superconducting processor,” *Science* **372**, 948–952 (2021) [10.1126/science.abg7812](#) (cit. on pp. 104, 107).
- [299] S. Krinner, N. Lacroix, A. Remm, A. D. Paolo, E. Genois, C. Leroux, C. Hellings, S. Lazar, F. Swiadek, J. Herrmann, G. J. Norris, C. K. Andersen, M. Müller, A. Blais, C. Eichler, and A. Wallraff, “Realizing repeated quantum error correction in a distance-three surface code,” arXiv:2112.03708 (2021) (cit. on p. 104).
- [300] F. Yan, P. Krantz, Y. Sung, M. Kjaergaard, D. L. Campbell, T. P. Orlando, S. Gustavsson, and W. D. Oliver, “Tunable coupling scheme for implementing high-fidelity two-qubit gates,” *Phys. Rev. Applied* **10**, 054062 (2018) [10.1103/PhysRevApplied.10.054062](#) (cit. on p. 104).
- [301] Y. Sung, L. Ding, J. Braumüller, A. Vepsäläinen, B. Kannan, M. Kjaergaard, A. Greene, G. O. Samach, C. McNally, D. Kim, A. Melville, B. M. Niedzielski, M. E. Schwartz, J. L. Yoder, T. P. Orlando, S. Gustavsson, and W. D. Oliver, “Realization of high-fidelity CZ and ZZ-free iSWAP gates with a

- tunable coupler,” *Phys. Rev. X* **11**, 021058 (2021) [10.1103/PhysRevX.11.021058](#) (cit. on p. 104).
- [302] D. Ristè, C. C. Bultink, K. W. Lehnert, and L. DiCarlo, “Feedback control of a solid-state qubit using high-fidelity projective measurement,” *Phys. Rev. Lett.* **109**, 240502 (2012) [10.1103/PhysRevLett.109.240502](#) (cit. on p. 105).
- [303] Y. Salathé, P. Kurpiers, T. Karg, C. Lang, C. K. Andersen, A. Akin, S. Krinner, C. Eichler, and A. Wallraff, “Low-latency digital signal processing for feedback and feedforward in quantum computing and communication,” *Phys. Rev. Applied* **9**, 034011 (2018) [10.1103/PhysRevApplied.9.034011](#) (cit. on p. 105).
- [304] P. Magnard, P. Kurpiers, B. Royer, T. Walter, J.-C. Besse, S. Gasparinetti, M. Pechal, J. Heinsoo, S. Storz, A. Blais, and A. Wallraff, “Fast and unconditional all-microwave reset of a superconducting qubit,” *Phys. Rev. Lett.* **121**, 060502 (2018) [10.1103/PhysRevLett.121.060502](#) (cit. on p. 105).
- [305] M. McEwen et al., “Removing leakage-induced correlated errors in superconducting quantum error correction,” *Nat. Commun.* **12**, 1761 (2021) [10.1038/s41467-021-21982-y](#) (cit. on p. 105).
- [306] J. Kelly, P. O’Malley, M. Neeley, H. Neven, and J. M. Martinis, “Physical qubit calibration on a directed acyclic graph,” [arXiv:1803.03226](#) (2018) (cit. on pp. 105, 107).
- [307] M. P. A. Fisher, P. B. Weichman, G. Grinstein, and D. S. Fisher, “Boson localization and the superfluid-insulator transition,” *Phys. Rev. B* **40**, 546–570 (1989) [10.1103/PhysRevB.40.546](#) (cit. on p. 105).
- [308] D. Jaksch, C. Bruder, J. I. Cirac, C. W. Gardiner, and P. Zoller, “Cold bosonic atoms in optical lattices,” *Phys. Rev. Lett.* **81**, 3108–3111 (1998) [10.1103/PhysRevLett.81.3108](#) (cit. on p. 105).
- [309] M. Greiner, O. Mandel, T. Esslinger, T. W. Hänsch, and I. Bloch, “Quantum phase transition from a superfluid to a Mott insulator in a gas of ultracold atoms,” *Nature* **415**, 39–44 (2002) [10.1038/415039a](#) (cit. on p. 105).
- [310] W. S. Bakr, A. Peng, M. E. Tai, R. Ma, J. Simon, J. I. Gillen, S. Fölling, L. Pollet, and M. Greiner, “Probing the superfluid-to-Mott insulator transition at the single-atom level,” *Science* **329**, 547–550 (2010) [10.1126/science.1192368](#) (cit. on p. 105).
- [311] I. Bloch, J. Dalibard, and S. Nascimbène, “Quantum simulations with ultracold quantum gases,” *Nat. Phys.* **8**, 267–276 (2012) [10.1038/nphys2259](#) (cit. on p. 105).
- [312] S. Hacohe-Gourgy, V. V. Ramasesh, C. De Grandi, I. Siddiqi, and S. M. Girvin, “Cooling and autonomous feedback in a Bose-Hubbard chain with

- attractive interactions,” *Phys. Rev. Lett.* **115**, 240501 (2015) [10.1103/PhysRevLett.115.240501](#) (cit. on p. 105).
- [313] T. Orell, A. A. Michailidis, M. Serbyn, and M. Silveri, “Probing the many-body localization phase transition with superconducting circuits,” *Phys. Rev. B* **100**, 134504 (2019) [10.1103/PhysRevB.100.134504](#) (cit. on p. 105).
- [314] O. Dutta, M. Gajda, P. Hauke, M. Lewenstein, D.-S. Lühmann, B. A. Malomed, T. Sowiński, and J. Zakrzewski, “Non-standard Hubbard models in optical lattices: a review,” *Rep. Prog. Phys.* **78**, 066001 (2015) [10.1088/0034-4885/78/6/066001](#) (cit. on p. 105).
- [315] R. Landig, L. Hruby, N. Dogra, M. Landini, R. Mottl, T. Donner, and T. Esslinger, “Quantum phases from competing short- and long-range interactions in an optical lattice,” *Nature* **532**, 476–479 (2016) [10.1038/nature17409](#) (cit. on p. 105).
- [316] D. Rossini and R. Fazio, “Phase diagram of the extended Bose–Hubbard model,” *New J. Phys.* **14**, 065012 (2012) [10.1088/1367-2630/14/6/065012](#) (cit. on p. 106).
- [317] A. van Otterlo, K.-H. Wagenblast, R. Baltin, C. Bruder, R. Fazio, and G. Schön, “Quantum phase transitions of interacting bosons and the supersolid phase,” *Phys. Rev. B* **52**, 16176–16186 (1995) [10.1103/PhysRevB.52.16176](#) (cit. on p. 106).
- [318] W. S. Bakr, “Microscopic Studies of Quantum Phase Transitions in Optical Lattices,” PhD thesis (Harvard University, 2011) (cit. on p. 106).
- [319] M. Ferraretto and L. Salasnich, “Effects of long-range hopping in the Bose-Hubbard model,” *Phys. Rev. A* **99**, 013618 (2019) [10.1103/PhysRevA.99.013618](#) (cit. on p. 106).
- [320] P. Hayden and J. Preskill, “Black holes as mirrors: quantum information in random subsystems,” *J. High Energy Phys.* **2007**, 120–120 (2007) [10.1088/1126-6708/2007/09/120](#) (cit. on p. 106).
- [321] Y. Sekino and L. Susskind, “Fast scramblers,” *J. High Energy Phys.* **2008**, 065–065 (2008) [10.1088/1126-6708/2008/10/065](#) (cit. on p. 106).
- [322] S. H. Shenker and D. Stanford, “Black holes and the butterfly effect,” *J. High Energy Phys.* **2014**, 67 (2014) [10.1007/JHEP03\(2014\)067](#) (cit. on p. 106).
- [323] P. Hosur, X.-L. Qi, D. A. Roberts, and B. Yoshida, “Chaos in quantum channels,” *J. High Energy Phys.* **2016**, 4 (2016) [10.1007/JHEP02\(2016\)004](#) (cit. on p. 106).
- [324] B. Swingle, G. Bentsen, M. Schleier-Smith, and P. Hayden, “Measuring the scrambling of quantum information,” *Phys. Rev. A* **94**, 040302 (2016) [10.1103/PhysRevA.94.040302](#) (cit. on p. 106).

- [325] N. Yunger Halpern, “Jarzynski-like equality for the out-of-time-ordered correlator,” *Phys. Rev. A* **95**, 012120 (2017) [10.1103/PhysRevA.95.012120](https://doi.org/10.1103/PhysRevA.95.012120) (cit. on p. 106).
- [326] B. Yoshida and N. Y. Yao, “Disentangling scrambling and decoherence via quantum teleportation,” *Phys. Rev. X* **9**, 011006 (2019) [10.1103/PhysRevX.9.011006](https://doi.org/10.1103/PhysRevX.9.011006) (cit. on p. 106).
- [327] B. Vermersch, A. Elben, L. M. Sieberer, N. Y. Yao, and P. Zoller, “Probing scrambling using statistical correlations between randomized measurements,” *Phys. Rev. X* **9**, 021061 (2019) [10.1103/PhysRevX.9.021061](https://doi.org/10.1103/PhysRevX.9.021061) (cit. on p. 106).
- [328] M. Gärttner, J. G. Bohnet, A. Safavi-Naini, M. L. Wall, J. J. Bollinger, and A. M. Rey, “Measuring out-of-time-order correlations and multiple quantum spectra in a trapped-ion quantum magnet,” *Nat. Phys.* **13**, 781–786 (2017) [10.1038/nphys4119](https://doi.org/10.1038/nphys4119) (cit. on p. 106).
- [329] J. Li, R. Fan, H. Wang, B. Ye, B. Zeng, H. Zhai, X. Peng, and J. Du, “Measuring out-of-time-order correlators on a nuclear magnetic resonance quantum simulator,” *Phys. Rev. X* **7**, 031011 (2017) [10.1103/PhysRevX.7.031011](https://doi.org/10.1103/PhysRevX.7.031011) (cit. on p. 106).
- [330] K. A. Landsman, C. Figgatt, T. Schuster, N. M. Linke, B. Yoshida, N. Y. Yao, and C. Monroe, “Verified quantum information scrambling,” *Nature* **567**, 61–65 (2019) [10.1038/s41586-019-0952-6](https://doi.org/10.1038/s41586-019-0952-6) (cit. on p. 106).
- [331] M. S. Blok, V. V. Ramasesh, T. Schuster, K. O’Brien, J. M. Kreikebaum, D. Dahlen, A. Morvan, B. Yoshida, N. Y. Yao, and I. Siddiqi, “Quantum information scrambling on a superconducting qutrit processor,” *Phys. Rev. X* **11**, 021010 (2021) [10.1103/PhysRevX.11.021010](https://doi.org/10.1103/PhysRevX.11.021010) (cit. on p. 106).
- [332] A. A. Houck, J. A. Schreier, B. R. Johnson, J. M. Chow, J. Koch, J. M. Gambetta, D. I. Schuster, L. Frunzio, M. H. Devoret, S. M. Girvin, and R. J. Schoelkopf, “Controlling the spontaneous emission of a superconducting transmon qubit,” *Phys. Rev. Lett.* **101**, 080502 (2008) [10.1103/PhysRevLett.101.080502](https://doi.org/10.1103/PhysRevLett.101.080502) (cit. on p. 107).
- [333] IBM Quantum, <https://quantum-computing.ibm.com/>, 2021 (cit. on p. 107).
- [334] L. J. Zeng, S. Nik, T. Greibe, P. Krantz, C. M. Wilson, P. Delsing, and E. Olsson, “Direct observation of the thickness distribution of ultra thin AlO_x barriers in $\text{Al}/\text{AlO}_x/\text{Al}$ Josephson junctions,” *J. Phys. D: Appl. Phys.* **48**, 395308 (2015) [10.1088/0022-3727/48/39/395308](https://doi.org/10.1088/0022-3727/48/39/395308) (cit. on p. 147).
- [335] J. D. Teufel, “Superconducting Tunnel Junctions as Direct Detectors for Submillimeter Astronomy,” PhD thesis (Yale University, 2008) (cit. on p. 148).
- [336] C. Gardiner and P. Zoller, *Quantum Noise*, 3rd ed. (Springer, 2004) (cit. on pp. 151, 160).

- [337] B. Peropadre, J. Lindkvist, I.-C. Hoi, C. M. Wilson, J. J. Garcia-Ripoll, P. Delsing, and G. Johansson, “Scattering of coherent states on a single artificial atom,” *New J. Phys.* **15**, 035009 (2013) [10.1088/1367-2630/15/3/035009](#) (cit. on p. 152).
- [338] J. Johansson, P. Nation, and F. Nori, “QuTiP: An open-source python framework for the dynamics of open quantum systems,” *Comput. Phys. Commun.* **183**, 1760–1772 (2012) [10.1016/J.CPC.2012.02.021](#) (cit. on pp. 158, 210).
- [339] J. Johansson, P. Nation, and F. Nori, “QuTiP 2: A Python framework for the dynamics of open quantum systems,” *Comput. Phys. Commun.* **184**, 1234–1240 (2013) [10.1016/J.CPC.2012.11.019](#) (cit. on pp. 158, 210).
- [340] L.-M. Duan and G.-C. Guo, “Reducing spatially correlated noise and decoherence with quantum error correcting codes,” [arXiv:quant-ph/9811058](#) (1998) (cit. on p. 160).
- [341] J. M. Martinis, S. Nam, J. Aumentado, K. Lang, and C. Urbina, “Decoherence of a superconducting qubit due to bias noise,” *Phys. Rev. B* **67**, 094510 (2003) [10.1103/PhysRevB.67.094510](#) (cit. on p. 162).
- [342] G. Ithier, E. Collin, P. Joyez, P. J. Meeson, D. Vion, D. Esteve, F. Chiarello, A. Shnirman, Y. Makhlin, J. Schrieffer, and G. Schön, “Decoherence in a superconducting quantum bit circuit,” *Phys. Rev. B* **72**, 134519 (2005) [10.1103/PhysRevB.72.134519](#) (cit. on p. 162).
- [343] B. Karyapudi and J.-S. Hong, “Coplanar waveguide periodic structures with resonant elements and their application in microwave filters,” in *Ieee mtt-s international microwave symposium digest, 2003, Vol. 3* (2003), 1619–1622 vol.3, [10.1109/MWSYM.2003.1210448](#) (cit. on p. 169).
- [344] K. O’Brien, C. Macklin, I. Siddiqi, and X. Zhang, “Resonant phase matching of Josephson junction traveling wave parametric amplifiers,” *Phys. Rev. Lett.* **113**, 157001 (2014) [10.1103/PhysRevLett.113.157001](#) (cit. on p. 169).
- [345] P. B. Dieterle, M. Kalaei, J. M. Fink, and O. Painter, “Superconducting cavity electromechanics on a silicon-on-insulator platform,” *Phys. Rev. Applied* **6**, 014013 (2016) [10.1103/PhysRevApplied.6.014013](#) (cit. on p. 175).
- [346] J. Gao, “The Physics of Superconducting Microwave Resonators,” PhD thesis (California Institute of Technology, 2008) (cit. on p. 175).
- [347] V. Dossetti-Romero, F. Izrailev, and A. Krokhin, “Transport properties of 1D tight-binding disordered models: the Hamiltonian map approach,” *Phys. E Low-dimens. Syst. Nanostruct.* **25**, 13–22 (2004) [10.1016/j.physe.2004.05.007](#) (cit. on p. 176).
- [348] F. M. Izrailev, T. Kottos, and G. P. Tsironis, “Hamiltonian map approach to resonant states in paired correlated binary alloys,” *Phys. Rev. B* **52**, 3274–3279 (1995) [10.1103/PhysRevB.52.3274](#) (cit. on p. 176).

- [349] N. A. Melosh, A. Boukai, F. Diana, B. Gerardot, A. Badolato, P. M. Petroff, and J. R. Heath, “Ultrahigh-density nanowire lattices and circuits,” *Science* **300**, 112–115 (2003) [10.1126/science.1081940](#) (cit. on p. 182).
- [350] N. Samkharadze, A. Bruno, P. Scarlino, G. Zheng, D. P. DiVincenzo, L. DiCarlo, and L. M. K. Vandersypen, “High-kinetic-inductance superconducting nanowire resonators for circuit QED in a magnetic field,” *Phys. Rev. Applied* **5**, 044004 (2016) [10.1103/PhysRevApplied.5.044004](#) (cit. on p. 182).
- [351] T. Goren, K. Plekhanov, F. Appas, and K. L. Hur, “Topological Zak phase in strongly coupled LC circuits,” *Phys. Rev. B* **97**, 041106 (2018) [10.1103/physrevb.97.041106](#) (cit. on p. 190).
- [352] A. F. Kockum, A. Miranowicz, S. D. Liberato, S. Savasta, and F. Nori, “Ultrastrong coupling between light and matter,” *Nat. Rev. Phys.* **1**, 19–40 (2019) [10.1038/s42254-018-0006-2](#) (cit. on p. 191).
- [353] B. Pérez-González, M. Bello, Á. Gómez-León, and G. Platero, *SSH model with long-range hoppings: topology, driving and disorder*, 2018 (cit. on p. 193).
- [354] S. Longhi, “Probing one-dimensional topological phases in waveguide lattices with broken chiral symmetry,” *Opt. Lett.* **43**, 4639–4642 (2018) [10.1364/OL.43.004639](#) (cit. on p. 193).
- [355] D. T. Sank, “Fast, accurate state measurement in superconducting qubits,” PhD thesis (UC Santa Barbara, 2014) (cit. on p. 199).
- [356] *iFilter™ Module, AWR Design Environment*, <https://www.awr.com/software/options/ifilter> (cit. on p. 201).

*Appendix A***FABRICATION DETAILS**

In this appendix, I provide details on the fabrication steps of the quantum devices used in the thesis.

A.1 Cleaning the chip tray and glass beakers

- Cleaning the tray

Before placing cleaned chips inside the tray, rinse it with IPA and blow dry with N₂. Note: Acetone attacks the tray (made of polyethylene) and should not be used for cleaning it. It is advised to keep your tray away from fume hood to avoid contamination of the tray. Moreover, you need to be cautious about putting a wet chip on the tray since any remaining acetone on the chip might dissolve the tray, and the chip may adhere to it.

- Cleaning glass beakers

Before using each beaker, rinse it with the solvent you would need to keep. i.e., rinse TCE beaker with TCE, ACE beaker with ACE, and IPA beaker with IPA.

A.2 Chip cleaning

The chip cleaning is the first thing you need to do after you take a chip from a diced wafer, and this consists of three rinse steps (TCE-ACE-IPA) and blow dry.

1. Trichloroethylene (TCE) rinse: > 5 min (usually 15 min) at 80°C.

Trichloroethylene is an effective solvent for a variety of organic materials and we use warm TCE at the very first step of chip cleaning. Warning: TCE is toxic and you should try not to inhale the air above it by keeping yourself outside the fume hood. Also, try to cover the beaker with Al foil when carrying TCE in it, so that you can avoid smelling it.

2. Acetone (ACE) rinse: 5 min at room temperature.

Spray the chip with acetone while transferring the chip from TCE bath to minimize solvent mixing. Sonicate for 5 minutes at half-maximum power and maximum frequency setting of the sonicator.

3. Isopropyl alcohol (IPA) rinse: 3 min at room temperature.
Spray the chip with IPA while transferring the chip from acetone to minimize solvent mixing. Sonicate for 3 minutes at half-maximum power and maximum frequency setting of the sonicator.
4. Blow dry with N₂ gun.
Hold the chip tightly on top of a sheet of Texwipe with a tweezer and use the other hand to blow dry.

A.3 Pre-spin/bake or pre-evaporation cleaning

The following steps must be done immediately before spin/baking resist or evaporating Al, to clean the surface of the chip.

1. Oxygen plasma ashing:
5 minutes of conditioning run followed by the main run typically of 2 minutes. The duration of main run can be varied depending of the level of ashing you want. For the fabrication of Josephson junctions or airbridges, we do 20 seconds of light oxygen plasma since it eats away resist and can widen dimensions significantly.
2. Hydrofluoric acid (HF) cleaning:
We perform two kinds of HF cleaning in our fabrication depending on the processing step.
 - Wet HF (BOE; Buffered Oxide Etch):
We perform wet HF cleaning prior to spinning and baking the resist or before electron-beam evaporation as long as there is no aluminum deposited on the chip. Extra precautions have to be taken in this step as exposure to HF can be lethal. The process consists of the following steps:
 - i. Swivel the chip inside buffered oxide etchant for 15 seconds.
 - ii. Rinse the chip for 10 seconds in the first DI water bath.
 - iii. Rinse the chip for 10 seconds in the second DI water bath.
 - iv. Careful blow-dry with a nitrogen gun.
 - Vapor HF:
If wet HF cleaning is not possible (wet HF attacks aluminum on chip), we use SPTS uEtch in the Painter lab cleanroom to perform selective etching

of oxides. A simple HF flash process exposes the chip to anhydrous HF vapor to remove native oxides and create hydrogen-terminated silicon surface.

A.4 Spin & bake

After chip cleaning, the chip is placed on the spinner and coated with a resist just enough to cover the top surface of the chip (without overflowing), followed by spinning at a calibrated rate. The chip is also baked on top of a hot plate either before or after spinning the resist. We use the following recipes for spin and bake:

- ZEP520A resist for marker, ground plane, and bandage layers: spin at 3 krpm with 1.5 krpm/s ramp rate, bake at 180 °C
We first prebake the chip for 3 minutes. Then, we spin ZEP520A resist followed by a 3-minute bake.
- Bilayer resist for Josephson junction layer: spin at 2.2 krpm with 1.5 krpm/s ramp rate, bake at 170 °C
We first prebake the chip for 3 minutes. Then, we spin copolymer MMA(8.5)MAA EL11 resist followed by a 3-minute bake. The chip is then spun with 950 PMMA A4 resist and baked for another 3 minutes.
- Trilayer resist for airbridge layer: spin at 4 krpm with 1.5 krpm/s ramp rate, bake at 170 °C
We first prebake the chip for 3 minutes. Then, we spin 950 PMMA A9 resist (this resist is very viscous and it is recommended to use a positive-displacement pipette for dropping this resist on the chip), followed by baking for 3 minutes. After this, we spin copolymer MMA(8.5)MAA EL11 resist and bake at the same condition as before. Finally, the chip is again spun with 950 PMMA A9 resist and baked with the identical settings as before.

A.5 Electron-beam lithography

After spinning and baking the resist, electron-beam lithography is performed with Raith EBPG 5200 in Kavli Nanoscience Institute (KNI) to write patterns. We use various set of beam current, aperture, and dose settings depending on the resist and the pattern that is written, which are summarized below.

- Marker layer (ZEP520A resist):
Beam current: 10 nA, Aperture: 300 μm , Dose: 210–245 $\mu\text{C}/\text{cm}^2$

- Ground plane layer (ZEP520A resist):
Beam current: 1 nA for planar coils and capacitors and 100 nA for ground plane, Aperture: 300 μm , Dose: 210–245 $\mu\text{C}/\text{cm}^2$
- Josephson junction layer (bilayer resist):
Beam current: 1 nA, Aperture: 300 μm , Dose: 939 $\mu\text{C}/\text{cm}^2$
To reduce disorder, we have used smaller beam current and aperture settings in later experiments to perform beamwriting with small spot size:
Beam current: 180 pA, Aperture: 200 μm , Dose: 990 $\mu\text{C}/\text{cm}^2$
- Airbridge layer (trilayer resist):
Beam current: 4nA, Aperture: 300 μm , Dose: 480 $\mu\text{C}/\text{cm}^2$

For details on the general workflow of electron-beam lithography, refer to the EBPG manual.

A.6 Development

After writing patterns with electron-beam lithography, we perform development depending on the type of the resist used in the spin and bake process introduced in Sec. A.4, outlined as follows:

- ZEP520A resist for marker, ground plane, and bandage layers:
We develop the chip in ZED-N50 developer for 2 minutes and 30 seconds, followed by rinsing in methyl isobutyl ketone (MIBK) for 30 seconds and a gentle blow-dry with a nitrogen gun.
- Bilayer resist for Josephson junction layer:
We use a cold development procedure for developing patterns written on the bilayer resists. This process is extremely temperature-sensitive (higher temperature makes the development faster) and requires special attention to

¹Note that neither IPA nor water alone cannot dissolve electron-beam exposed resist, yet the mixture of them acts as a cosolvent can develop the resist. The mechanism is uncertain, but it has been suggested that the presence of highly polar water molecules modify the alcohol molecule, improving the solvent action of IPA [151].

²The temperature controller setup consists of a thermoelectric cooling plate that is thermally anchored to a container with a bath of water, whose temperature is kept equilibrated by using an electric stirrer operating at 500 rpm. The temperature of the water bath is monitored using a digital thermometer. The beakers containing the developer and the rinsing solvent stay inside this water bath throughout all the development stages.

the temperature of the developer and the duration of development. During the preparation stage, a beaker containing a mixture of IPA and DI water in a volume ratio of 3:1, used as a developer for this resist¹, and another beaker containing IPA are covered with aluminum foil and cooled down to 10.0 °C for at least an hour by using a custom-designed temperature controller setup². Once the developer and the rinsing solvent are cold, we develop the chip in the developer for 90 seconds, quickly transfer the chip to the cold IPA bath and rinse for 10 seconds, followed by an immediate blow dry with a nitrogen gun.

- Trilayer resist for airbridge layer:

For the development of airbridge patterns on the trilayer resist written with grayscale electron-beam lithography, we use the same procedure as the bilayer resist but in a less stringent room-temperature setting. First, the chip is developed in 3:1 IPA:water developer for about 2 minutes. Then the chip is rinsed in IPA for 10 seconds, followed by blow-dry with nitrogen. We inspect the chip with an optical microscope to check the progress. We repeat these steps of development (with shorter duration)-rinsing-blow drying-inspection until we find that the resist is fully developed. After this, we perform 2 hours of resist reflow at 105 °C.

A.7 Evaporation

We use the electron-beam evaporator Plassys MEB550S in the Painter lab cleanroom for thin-film deposition of metals on chip. The evaporator consists of a loadlock with a tiltable and rotatable stage on which samples are loaded and a chamber where pre-loaded materials are melted with electron beam and evaporated. We use titanium (Ti) as an absorbent to reduce oxygen and water vapor, conditioning the loadlock before evaporating other metals. Aluminum (Al) is used for fabrication of superconducting resonators and qubits and niobium (Nb) is used for fabrication of alignment markers. The critical pressures for running a process is 10^{-6} mbar for loadlock and 10^{-7} mbar for chamber. We use the following recipes for electron-beam evaporation:

- Marker layer:

Pump out time is not important for this process. It is good to run the process when the pressures are lower than the critical values.

- i. Evaporation of Ti at a rate of 0.15 nm/s for 3 minutes.

ii. Evaporation of 150 nm of Nb at a rate of 0.4 nm/s.

- Ground plane layer:

It is good to pump out the loadlock for at least 4 hours after loading the samples.

i. Evaporation of Ti at a rate of 0.2 nm/s rate for 3 minutes.

ii. Evaporation of 120 nm of Al at a rate of 1 nm/s.

iii. Exposure to static O₂ at a pressure of 10 mbar for 2 minutes.

- Josephson junction layer:

It is necessary to pump out for at least 12 hours after loading the samples for best reproducibility.

i. Evaporation of Ti at a rate of 0.2 nm/s rate for 3 minutes.

ii. Evaporation of 60 nm of Al at a rate of 1 nm/s with a tilt and rotation of (60°, 90°).

iii. Exposure to static O₂ at a pressure of 5 mbar for 20 minutes.

iv. Evaporation of 120 nm of Al at 1 nm/s rate with a tilt and rotation of (20°, 180°).

v. Exposure to static O₂ at a pressure of 10 mbar for 2 minutes.

- Bandage layer:

i. Ar ion milling at voltage and current (400 V, 21 mA) for 6 minutes.

ii. Evaporation of Ti at a rate of 0.2 nm/s for 3 minutes.

iii. Evaporation of 200 nm of Al at a rate of 1 nm/s.

iv. Exposure to static O₂ at a pressure of 10 mbar for 2 minutes.

A.8 Liftoff

The liftoff after the electron-beam evaporation is performed by first placing the chip inside a bath of N-methyl-2-pyrrolidone (NMP) heated to 150 °C. If niobium were evaporated on the chip, the niobium deposited on regions outside the desired pattern immediately detaches from the chip upon touching the hot NMP bath and we shoot bubbles of air to strip off the remaining pieces of metal by using a pipette. If aluminum were evaporated on chip, we leave the chips in the hot NMP bath for at least 2 hours, followed by sonication or pipetting to aid the liftoff process. Then, the

chip is moved to another clean heated bath of NMP and left for another hour or more (depending on the quality of the first liftoff), followed by sonication or pipetting. After this, we sonicate the chips in a bath of acetone for 5 minutes, followed by 3-minute sonication in IPA and blow drying with a nitrogen gun. When suspended structures such as airbridges are fabricated on chip, one needs to be careful about the choice of parameters for sonication.

Appendix B

DESIGNING JOSEPHSON JUNCTIONS FOR TRANSMON QUBITS

In this note, I describe considerations for designing Josephson junctions for transmon qubits and getting the frequencies of fabricated qubits (or “sweet spot” frequencies for frequency-tunable qubits) close to the design values.

B.1 Basics

The frequency ω_q of transmon qubits are determined by two factors, the charging energy $E_C = e^2/(2C_\Sigma)$ and the Josephson energy E_J , and is written as

$$\hbar\omega_q = \sqrt{8E_J E_C} - E_C.$$

Here, the effective capacitance C_Σ is a sum of capacitance contributions that couples to the qubit node, including the capacitance C_J of the Josephson junction. Normally, the contributions other than the junction capacitance $C_\Sigma - C_J$ are thought to be accurately estimated by using EM simulators such as Sonnet. It is important to note that the anharmonicity of transmon qubit is given by $\alpha = -E_C/\hbar$, which can be directly measured in the experiment by either a high-power spectroscopy that drives two-photon excitation or a frequency sweep of XY drive conditioned on the first excitation (by sending π -pulse at frequency resonant to first transition $|g\rangle \rightarrow |e\rangle$). Together with the sweet spot frequencies $\omega_{q,\max}$ measured in the experiment, one can fully determine the Josephson energies of fabricated junctions of qubits. This allows us to test the accuracy of the design.

B.2 Design

In the design of qubits, both the Josephson energy E_J and junction capacitance C_J depends on the area and oxide properties of Josephson junctions and hence determining the properties of Josephson junctions are crucial to accurate design of the experiments.

Josephson capacitance C_J

Assuming the Josephson junction is a parallel plate capacitor, with aluminum oxide (typical relative permittivity $\epsilon_r = 10$ for Al_2O_3) as a dielectric and distance $d = 1.8$ nm [334], the junction capacitance per area (C_J/A_J) is calculated as

$$\frac{C_J}{A_J} = \frac{\epsilon_0 \epsilon_r}{d} \approx 0.049 \text{ F/m}^2 = 49 \text{ fF}/\mu\text{m}^2$$

This is very close to the value quoted in page 62 of John Teufel's thesis [335] from Prof. Robert Schoelkopf's lab, although their junction fabrication process is not necessarily identical to ours. Professor John Martinis lab's typical value is reported to be $C_J/A_J = 4 \text{ fF}/(300 \text{ nm})^2 = 44.4 \text{ fF}/\mu\text{m}^2$ (see Supplementary Information of Ref. [150]).

Assuming $C_J/A_J = 50 \text{ fF}/\mu\text{m}^2$, for a typical junction area of $A_J = 0.232 \mu\text{m}^2$, the capacitance arising from Josephson junctions is $C_J = 11.6 \text{ fF}$ which can account for $> 10 \%$ of effective qubit capacitance C_Σ . After taking into account this factor, the charging energy of transmon qubits we fabricated in the lab were consistently measured to be close to the design values.

Josephson energy E_J

For E_J/A_J , we find values fluctuating roughly by 10% , somewhere in the $E_J/A_J = 125\text{--}132 \text{ GHz}/\mu\text{m}^2$ range when the areas taken into account were determined by high-resolution imaging with Nova 200/600 scanning electron microscope in KNI. It is believed that this number is sensitive to conditions in the e-beam evaporation chamber, changing after material refills.

B.3 Fabrication of test junctions

Accurate fabrication of superconducting qubits is a challenging task due to the fact that a lot of factors can play roles in the fabrication of Josephson junctions, the size of which is only few hundred nanometers. For example, about 30 nm error in each dimension of Josephson junctions from design values can result in about 1 GHz error in qubit frequency, which can make certain experiments infeasible. Prior to fabrication of the device for experiments, we perform a few rounds of test fabrication to accurately calibrate the area of Josephson junctions, which is crucial to accurate prediction of qubit frequencies. We fabricate a test device consisting of an array of Josephson junctions with a single-layer processing step for Josephson junctions discussed in Appendix A. The junctions in the array have CAD dimensions swept in both X and Y directions with a step of about $5\text{--}10 \text{ nm}$ with enough repetitions and have designs identical to the ones that will be used for qubits in the experiment. Once fabricated, the Josephson junctions in the test devices are imaged with a scanning electron microscope from which a set of CAD dimensions expected to realize the

desired fabricated dimensions can be determined. This process is repeated until we get a fabricated junction dimensions close enough to the design values (within about 10 nm).

B.4 Imaging

Obtaining a scanning electron micrograph of good quality with calibrated dimensions is crucial to achieving accurate determination of junction area A_J . Here, I describe important tips for using Nova 200/600 SEM in KNI to image Josephson junctions in a consistent fashion.

For imaging of Josephson junctions for dimension extraction, the scanning electron micrographs are acquired with the following settings (developed with the help of former KNI staff Dr. Matthew Hunt):

- High Voltage (HV): 10.00 kV
- Beam Current: 130 pA
- Working distance (WD): sample located at the eucentric height (reproducible WD based only on chamber geometry, not on lens parameters)
- Horizontal Field Width (HFW): 1.00um
- Detector: through-the-lens detector (TLD) in the immersion mode, which achieves ultra-high sub-10 nm resolution.
- Dwell time: 10 μ s
- If not in hurry, the sample is mounted to the stage with NIST-traceable standard specimen¹, which can be used to calibrate the dimensions measured in the SEM more accurately (Nova is reported to be off by $\sim 1-2\%$, which is within the specification of the system).
- Save the images in .tif format, which saves all the configurations used for imaging in the metadata.

An example of the image taken with these settings is illustrated in Fig. B.1a, in which we can observe clear boundary of a Josephson junction accurate to within about few nanometers.

¹Available from Ted Pella, Inc. https://www.tedpella.com/calibration_html/CDMS-Critical_Dimension_Magnification_Standards.htm

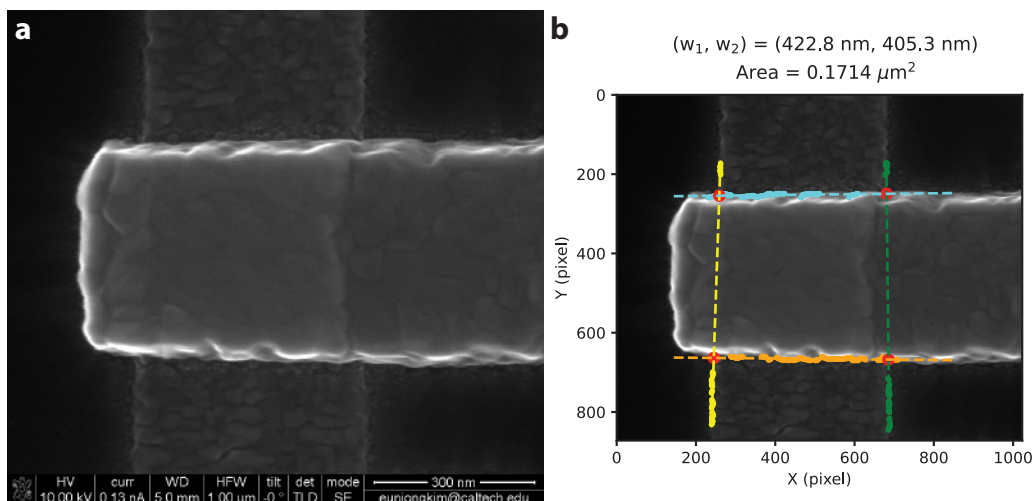


Figure B.1: Scanning electron micrograph of a Josephson junction. **a**, An image of a Josephson junction taken with Nova 200 scanning electron microscope following the settings in Sec. B.4. **b**, Determination of dimensions of the Josephson junction in panel **a** with image processing.

Note that images taken with Hitachi S4300 SEM in Painter lab cleanroom didn't have enough resolution to accurately determine the critical dimensions of Josephson junctions. Also, the dimension calibration in the Hitachi S4300 SEM seems to be unreliable for accuracy within about 40 nm, which can often be larger than 10 % of dimensions of Josephson junctions. A careful set of calibrations must be implemented to be able to use Hitachi S4300 SEM for Josephson junction calibration.

B.5 Determination of critical dimensions

The critical dimensions of Josephson junctions can be obtained by employing built-in softwares for scanning electron microscopes to draw lines on the image and extract the corresponding dimensions. This manual process, however, can easily add errors on the order of 10 nm which is larger than the resolution of the image. For a fast and reliable determination of critical dimensions of Josephson junctions, I have developed an imaging processing routine to detect the boundary of Josephson junctions from an image and calculate the area. Thus routine involves the use of Sobel filter for edge detection and fitting of points into lines. An example of the result from this process is illustrated in Fig. B.1b.

Appendix C

SUPPLEMENTARY INFORMATION FOR CHAPTER 4

C.1 Spectroscopic measurement of individual qubits

The master equation of a qubit in a thermal bath at temperature T , driven by a classical field is given by $\dot{\hat{\rho}} = -i[\hat{H}/\hbar, \hat{\rho}] + \mathcal{L}[\hat{\rho}]$, where the Hamiltonian \hat{H} and the Liouvillian \mathcal{L} is written as [336]

$$\hat{H}/\hbar = -\frac{\omega_p - \omega_q}{2} \hat{\sigma}_z + \frac{\Omega_p}{2} \hat{\sigma}_x, \quad (\text{C.1})$$

$$\mathcal{L}[\hat{\rho}] = (\bar{n}_{\text{th}} + 1)\Gamma_1 \mathcal{D}[\hat{\sigma}_-]\hat{\rho} + \bar{n}_{\text{th}}\Gamma_1 \mathcal{D}[\hat{\sigma}_+]\hat{\rho} + \frac{\Gamma_\varphi}{2} \mathcal{D}[\hat{\sigma}_z]\hat{\rho}. \quad (\text{C.2})$$

Here, ω_p (ω_q) is the frequency of the drive (qubit), Ω_p is the Rabi frequency of the drive, $\bar{n}_{\text{th}} = 1/(e^{\hbar\omega_q/k_B T} - 1)$ is the thermal occupation of photons in the bath, Γ_1 and Γ_φ are relaxation rate and pure dephasing rates of the qubit, respectively. The superoperator

$$\mathcal{D}[\hat{A}]\hat{\rho} = \hat{A}\hat{\rho}\hat{A}^\dagger - \frac{1}{2}\{\hat{A}^\dagger\hat{A}, \hat{\rho}\} \quad (\text{C.3})$$

denotes the Lindblad dissipator. The master equation can be rewritten in terms of density matrix elements $\rho_{a,b} \equiv \langle a|\hat{\rho}|b\rangle$ as

$$\dot{\rho}_{e,e} = \frac{i\Omega_p}{2}(\rho_{e,g} - \rho_{g,e}) - (\bar{n}_{\text{th}} + 1)\Gamma_1\rho_{e,e} + \bar{n}_{\text{th}}\Gamma_1\rho_{g,g} \quad (\text{C.4})$$

$$\dot{\rho}_{e,g} = \left[i(\omega_p - \omega_q) - \frac{(2\bar{n}_{\text{th}} + 1)\Gamma_1 + 2\Gamma_\varphi}{2} \right] \rho_{e,g} + \frac{i\Omega_p}{2}(\rho_{e,e} - \rho_{g,g}) \quad (\text{C.5})$$

$$\dot{\rho}_{g,e} = \dot{\rho}_{e,g}^*; \quad \dot{\rho}_{g,g} = -\dot{\rho}_{e,e} \quad (\text{C.6})$$

With $\rho_{e,e} + \rho_{g,g} = 1$, the steady-state solution ($\dot{\hat{\rho}} = 0$) to the master equation can be expressed as

$$\rho_{e,e}^{\text{ss}} = \frac{\bar{n}_{\text{th}}}{2\bar{n}_{\text{th}} + 1} \frac{1 + (\delta\omega/\Gamma_2^{\text{th}})^2}{1 + (\delta\omega/\Gamma_2^{\text{th}})^2 + \Omega_p^2/(\Gamma_1^{\text{th}}\Gamma_2^{\text{th}})} + \frac{1}{2} \frac{\Omega_p^2/(\Gamma_1^{\text{th}}\Gamma_2^{\text{th}})}{1 + (\delta\omega/\Gamma_2^{\text{th}})^2 + \Omega_p^2/(\Gamma_1^{\text{th}}\Gamma_2^{\text{th}})}, \quad (\text{C.7})$$

$$\rho_{e,g}^{\text{ss}} = -i \frac{\Omega_p}{2\Gamma_2^{\text{th}}(2\bar{n}_{\text{th}} + 1)} \frac{1 + i\delta\omega/\Gamma_2^{\text{th}}}{1 + (\delta\omega/\Gamma_2^{\text{th}})^2 + \Omega_p^2/(\Gamma_1^{\text{th}}\Gamma_2^{\text{th}})}, \quad (\text{C.8})$$

where $\delta\omega = \omega_p - \omega_q$ is the detuning of the drive from qubit frequency, $\Gamma_1^{\text{th}} = (2\bar{n}_{\text{th}} + 1)\Gamma_1$ and $\Gamma_2^{\text{th}} = \Gamma_1^{\text{th}}/2 + \Gamma_\varphi$ are the thermally enhanced decay rate and dephasing rate of the qubit.

Now, let us consider the case where a qubit is coupled to the waveguide with decay rate of Γ_{1D} . If we send in a probe field \hat{a}_{in} from left to right along the waveguide, the right-propagating output field \hat{a}_{out} after interaction with the qubit is written as [116]

$$\hat{a}_{out} = \hat{a}_{in} + \sqrt{\frac{\Gamma_{1D}}{2}} \hat{\sigma}_-.$$

The probe field creates a classical drive on the qubit with the rate of $\Omega_p/2 = -i\langle\hat{a}_{in}\rangle\sqrt{\Gamma_{1D}/2}$. With the steady-state solution of master equation (C.8) the transmission amplitude $t = \langle\hat{a}_{out}\rangle/\langle\hat{a}_{in}\rangle$ can be written as

$$t(\delta\omega) = 1 - \frac{\Gamma_{1D}}{2\Gamma_2^{\text{th}}(2\bar{n}_{\text{th}} + 1)} \frac{1 + i\delta\omega/\Gamma_2^{\text{th}}}{1 + (\delta\omega/\Gamma_2^{\text{th}})^2 + \Omega_p^2/(\Gamma_1\Gamma_2^{\text{th}})}. \quad (\text{C.9})$$

At zero temperature ($\bar{n}_{\text{th}} = 0$) Eq. (C.9) reduces to [146, 337]

$$t(\delta\omega) = 1 - \frac{\Gamma_{1D}}{2\Gamma_2} \frac{1 + i\delta\omega/\Gamma_2}{1 + (\delta\omega/\Gamma_2)^2 + \Omega_p^2/(\Gamma_1\Gamma_2)}. \quad (\text{C.10})$$

Here, $\Gamma_2 = \Gamma_\varphi + \Gamma_1/2$ is the dephasing rate of the qubit in the absence of thermal occupancy. In the following, we define the parasitic decoherence rate of the qubit as $\Gamma' = 2\Gamma_2 - \Gamma_{1D} = \Gamma_{\text{loss}} + 2\Gamma_\varphi$, where Γ_{loss} denotes the decay rate of qubit induced by channels other than the waveguide. Examples of Γ_{loss} in superconducting qubits include dielectric loss, decay into slotline mode, and loss from coupling to two-level system (TLS) defects.

Effect of saturation

To discuss the effect of saturation on the extinction in transmission, we start with the zero temperature case of Eq. (C.10). We introduce the saturation parameter $s \equiv \Omega_p^2/\Gamma_1\Gamma_2$ to rewrite the on-resonance transmittivity as

$$t(0) = 1 - \frac{\Gamma_{1D}}{2\Gamma_2} \frac{1}{1+s} \approx 1 - \frac{\Gamma_{1D}}{2\Gamma_2} (1-s) = \left(1 + s \frac{\Gamma_{1D}}{\Gamma'}\right) \left(\frac{\Gamma'}{\Gamma' + \Gamma_{1D}}\right), \quad (\text{C.11})$$

where the low-power assumption $s \ll 1$ has been made in the last step. For the extinction to get negligible effect from saturation, the power-dependent part in Eq. (C.11) should be small compared to the power-independent part. This is equivalent to $s < \Gamma'/\Gamma_{1D}$. Using the relation

$$\Omega_p = \sqrt{\frac{2\Gamma_{1D}P_p}{\hbar\omega_q}}$$

between the driven Rabi frequency and the power P_p of the probe and assuming $\Gamma' \ll \Gamma_{1D}$, this reduces to

$$P_p \lesssim \frac{\hbar\omega_q\Gamma'}{4}. \quad (\text{C.12})$$

In the experiment, the probe power used to resolve the extinction was -150 dBm (10^{-18} W), which gives a limit to the observable Γ' due to our coherent drive of $\Gamma'/2\pi \approx 150$ kHz.

Effect of thermal occupation

To take into account the effect of thermal occupancy, we take the limit where the saturation is very small ($\Omega_p \approx 0$). On resonance, the transmission amplitude is expressed as

$$t(0) = 1 - \frac{\Gamma_{1D}}{[(2\bar{n}_{\text{th}} + 1)\Gamma_1 + 2\Gamma_\varphi](2\bar{n}_{\text{th}} + 1)} \approx 1 - \frac{\Gamma_{1D}}{2\Gamma_2} + \frac{(\Gamma_1 + \Gamma_\varphi)\Gamma_{1D}}{\Gamma_2^2}\bar{n}_{\text{th}}, \quad (\text{C.13})$$

where we have assumed the thermal occupation is very small, $\bar{n}_{\text{th}} \ll 1$. In the limit where Γ_{1D} is dominating spurious loss and pure dephasing rates ($\Gamma_2 \approx \Gamma_{1D}/2$), this reduces to

$$t(0) \approx t(0)|_{T=0} + 4\bar{n}_{\text{th}} \quad (\text{C.14})$$

and hence the thermal contribution dominates the transmission amplitude unless $\bar{n}_{\text{th}} < \Gamma'/4\Gamma_{1D}$.

Using this relation, we can estimate the upper bound on the temperature of the environment based on our measurement of extinction. We have measured the

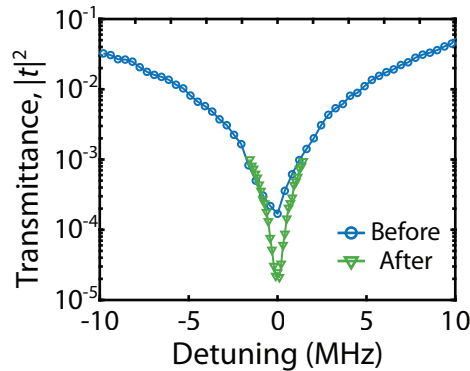


Figure C.1: Effect of thermal occupancy on extinction. The transmittance of Q_1 is measured at the flux-insensitive point before and after installation of customized microwave attenuator. We observe an order-of-magnitude enhancement in extinction after the installation, indicating a better thermalization of input signals to the chip.

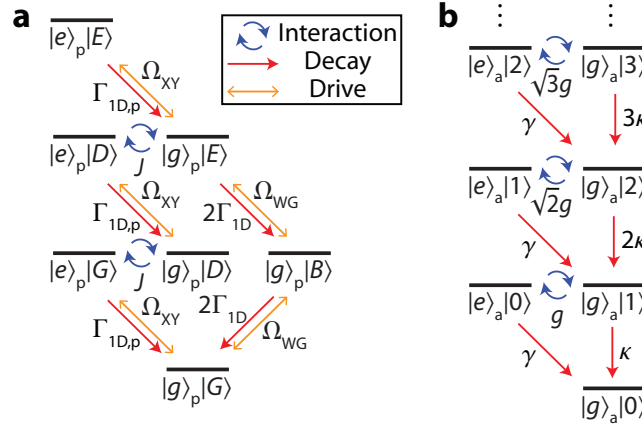


Figure C.2: Level structure of the atomic cavity and linear cavity. **a**, Level structure of the three-qubit system of probe qubit and atomic cavity. $\Gamma_{1D,p}$ and $2\Gamma_{1D}$ denotes the decay rates into the waveguide channel, Ω_{XY} is the local drive on the probe qubit, and Ω_{WG} is the drive from the waveguide. The coupling strength J is the same for the first excitation and second excitation levels, **b**, Level structure of an atom coupled to a linear cavity. $|e\rangle_a$ ($|g\rangle_a$) denotes the excited state (ground state) of the atom, while $|n\rangle$ is the n -photon Fock state of the cavity field. g is the coupling, γ is the decay rate of the atom, and κ is the photon loss rate of the cavity.

transmittance of Q_1 at its maximum frequency (Figure C.1) before and after installing a thin-film microwave attenuator, which is customized for proper thermalization of the input signals sent into the waveguide with the mixing chamber plate of the dilution refrigerator [157]. The minimum transmittance was measured to be $|t|^2 \approx 1.7 \times 10^{-4}$ (2.1×10^{-5}) before (after) installation of the attenuator, corresponding to the upper bound on thermal photon number of $\bar{n}_{th} \lesssim 3.3 \times 10^{-3}$ (1.1×10^{-3}). With the attenuator, this corresponds to temperature of 43 mK, close to the temperature values reported in Ref. [157].

C.2 Detailed modeling of the atomic cavity

In this section, we analyze the atomic cavity discussed in the Chapter 4 in more detail, taking into account its higher excitation levels. The atomic cavity is formed by two identical *mirror* qubits [frequency ω_q , decay rate Γ_{1D} (Γ') to waveguide (spurious loss) channel placed at $\lambda/2$ distance along the waveguide (Figure 1a). From the $\lambda/2$ spacing, the correlated decay of the two qubits is maximized to $-\Gamma_{1D}$, while the exchange interaction is zero. This results in formation of dark state $|D\rangle$ and bright state $|B\rangle$

$$|D\rangle = \frac{|eg\rangle + |ge\rangle}{\sqrt{2}}, \quad |B\rangle = \frac{|eg\rangle - |ge\rangle}{\sqrt{2}}, \quad (\text{C.15})$$

which are single-excitation states of two qubits with suppressed and enhanced waveguide decay rates $\Gamma_{1D,D} = 0$, $\Gamma_{1D,B} = 2\Gamma_{1D}$ to the waveguide. Here, g (e) denotes the ground (excited) state of each qubit. Other than the ground state $|G\rangle \equiv |gg\rangle$, there also exists a second excited state $|E\rangle \equiv |ee\rangle$ of two qubits, completing $2^2 = 4$ eigenstates in the Hilbert space of two qubits. We can alternatively define $|D\rangle$ and $|B\rangle$ in terms of collective annihilation operators

$$\hat{S}_D = \frac{1}{\sqrt{2}} \left(\hat{\sigma}_-^{(1)} + \hat{\sigma}_-^{(2)} \right), \quad \hat{S}_B = \frac{1}{\sqrt{2}} \left(\hat{\sigma}_-^{(1)} - \hat{\sigma}_-^{(2)} \right) \quad (\text{C.16})$$

as $|D\rangle = \hat{S}_D^\dagger |G\rangle$ and $|B\rangle = \hat{S}_B^\dagger |G\rangle$. Here, $\hat{\sigma}_-^{(i)}$ de-excites the state of i -th mirror qubit. Note that the doubly-excited state $|E\rangle$ can be obtained by successive application of either \hat{S}_D^\dagger or \hat{S}_B^\dagger twice on the ground state $|G\rangle$.

The interaction of qubits with the field in the waveguide is written in the form of $\hat{H}_{\text{WG}} \propto (\hat{S}_B + \hat{S}_B^\dagger)$, and hence the state transfer via classical drive on the waveguide can be achieved only between states of non-vanishing transition dipole $\langle f | \hat{S}_B | i \rangle$. In the present case, only $|G\rangle \leftrightarrow |B\rangle$ and $|B\rangle \leftrightarrow |E\rangle$ transitions are available via the waveguide with the same transition dipole. This implies that the waveguide decay rate of $|E\rangle$ is equal to that of $|B\rangle$, $\Gamma_{1D,E} = 2\Gamma_{1D}$.

To investigate the level structure of the dark state, which is not accessible via the waveguide channel, we introduce an ancilla *probe* qubit [frequency ω_q , decay rate $\Gamma_{1D,p}$ (Γ'_p) to waveguide (loss) channel] at the center of mirror qubits. The probe qubit is separated by $\lambda/4$ from mirror qubits, maximizing the exchange interaction to $\sqrt{\Gamma_{1D,p}\Gamma_{1D}}/2$ with zero correlated decay. This creates an interaction of excited state of probe qubit to the dark state of mirror qubits $|e\rangle_p |G\rangle \leftrightarrow |g\rangle_p |D\rangle$, while the bright state remains decoupled from this dynamics.

The master equation of the three-qubit system reads $\dot{\hat{\rho}} = -i[\hat{H}/\hbar, \hat{\rho}] + \mathcal{L}[\hat{\rho}]$, where the Hamiltonian \hat{H} and the Liouvillian \mathcal{L} are given by

$$\hat{H} = \hbar J \left[\hat{\sigma}_-^{(p)} \hat{S}_D^\dagger + \hat{\sigma}_+^{(p)} \hat{S}_D \right] \quad (\text{C.17})$$

$$\mathcal{L}[\hat{\rho}] = (\Gamma_{1D,p} + \Gamma'_p) \mathcal{D}[\hat{\sigma}_-^{(p)}] \hat{\rho} + (2\Gamma_{1D} + \Gamma') \mathcal{D}[\hat{S}_B] \hat{\rho} + \Gamma' \mathcal{D}[\hat{S}_D] \hat{\rho} \quad (\text{C.18})$$

Here, $\hat{\sigma}_\pm^{(p)}$ are the Pauli operators for the probe qubit, $2J = \sqrt{2\Gamma_{1D,p}\Gamma_{1D}}$ is the interaction between probe qubit and dark state, and $\mathcal{D}[\cdot]$ is the Lindblad dissipator defined in Eq. (C.3). The full level structure of the $2^3 = 8$ states of three qubits and the rates in the system are summarized in Fig. C.2a. Note that the effective (non-Hermitian) Hamiltonian \hat{H}_{eff} in Eq. (4.2) can be obtained from absorbing part of the Liouvillian in Eq. (C.18) excluding terms associated with quantum jumps.

To reach the dark state of the atomic cavity, we first apply a local gate $|g\rangle_p|G\rangle \rightarrow |e\rangle_p|G\rangle$ on the probe qubit (Ω_{XY} in Fig. C.2a) to prepare the state in the first-excitation manifold. Then, the Rabi oscillation $|e\rangle_p|G\rangle \leftrightarrow |g\rangle_p|D\rangle$ takes place with the rate of J . We can identify $g = J$, $\gamma = \Gamma_{1D,p} + \Gamma'_p$, $\kappa = \Gamma'$ in analogy to cavity QED (Fig. 4.1a and Fig. C.2b) and calculate cooperativity as

$$C = \frac{(2J)^2}{\Gamma_{1,p}\Gamma_{1,D}} = \frac{2\Gamma_{1D,p}\Gamma_{1D}}{(\Gamma_{1D,p} + \Gamma'_p)\Gamma'} \approx \frac{2\Gamma_{1D}}{\Gamma'},$$

when the spurious loss rate Γ' is small. A high cooperativity can be achieved in this case due to collective suppression of radiation in atomic cavity and cooperative enhancement in the interaction, scaling linearly with the Purcell factor $P_{1D} = \Gamma_{1D}/\Gamma'$. Thus, we can successfully map the population from the excited state of probe qubit to dark state of mirror qubits with the interaction time of $(2J/\pi)^{-1}$.

Going further, we attempt to reach the second-excited state $|E\rangle = (\hat{S}_D^\dagger)^2|G\rangle$ of atomic cavity. After the state preparation of $|g\rangle_p|D\rangle$ mentioned above, we apply another local gate $|g\rangle_p|D\rangle \rightarrow |e\rangle_p|D\rangle$ on the probe qubit and prepare the state in the second-excitation manifold. In this case, the second excited states $|e\rangle_p|D\rangle \leftrightarrow |g\rangle_p|E\rangle$ have interaction strength J , same as the first excitation, while the $|E\rangle$ state becomes highly radiative to waveguide channel. The cooperativity C is calculated as

$$C = \frac{(2J)^2}{\Gamma_{1,p}\Gamma_{1,E}} = \frac{2\Gamma_{1D,p}\Gamma_{1D}}{(\Gamma_{1D,p} + \Gamma'_p)(2\Gamma_{1D} + \Gamma')} < 1,$$

which is always smaller than unity. Therefore, the state $|g\rangle_p|E\rangle$ is only virtually populated and the interaction maps the population in $|e\rangle_p|D\rangle$ to $|g\rangle_p|B\rangle$ with the rate of $(2J)^2/(2\Gamma_{1D}) = \Gamma_{1D,p}$. This process competes with radiative decay (at a rate of $\Gamma_{1D,p}$) of probe qubit $|e\rangle_p|D\rangle \rightarrow |g\rangle_p|D\rangle$ followed by the Rabi oscillation in the first-excitation manifold, giving rise to damped Rabi oscillation in Fig. 4.5e.

Effect of phase length mismatch

Deviation of phase length between mirror qubits from $\lambda/2$ along the waveguide can act as a non-ideal contribution in the dynamics of atomic cavity. The waveguide decay rate of dark state can be written as $\Gamma_{1D,D} = \Gamma_{1D}(1 - |\cos \phi|)$, where $\phi = k_{1D}d$ is the phase separation between mirror qubits [116]. Here, k_{1D} is the wavenumber and d is the distance between mirror qubits.

We consider the case where the phase mismatch $\Delta\phi = \phi - \pi$ of mirror qubits is small. The decay rate of the dark state scales as $\Gamma_{1D,D} \approx \Gamma_{1D}(\Delta\phi)^2/2$ only adding

a small contribution to the decay rate of dark state. Based on the decay rate of dark states from time-domain measurement in Table C.2, we estimate the upper bound on the phase mismatch $\Delta\phi/\pi$ to be 5% for type I and 3.5% for type II.

Effect of asymmetry in Γ_{1D}

So far we have assumed that the waveguide decay rate Γ_{1D} of mirror qubits are identical and neglected the asymmetry. If the waveguide decay rates of mirror qubits are given by $\Gamma_{1D,1} \neq \Gamma_{1D,2}$, the dark state and bright state are redefined as

$$|D\rangle = \frac{\sqrt{\Gamma_{1D,2}}|eg\rangle + \sqrt{\Gamma_{1D,1}}|ge\rangle}{\sqrt{\Gamma_{1D,1} + \Gamma_{1D,2}}}, \quad |B\rangle = \frac{\sqrt{\Gamma_{1D,1}}|eg\rangle - \sqrt{\Gamma_{1D,2}}|ge\rangle}{\sqrt{\Gamma_{1D,1} + \Gamma_{1D,2}}}, \quad (C.19)$$

with collectively suppressed and enhanced waveguide decay rates of $\Gamma_{1D,D} = 0$, $\Gamma_{1D,B} = \Gamma_{1D,1} + \Gamma_{1D,2}$, remaining fully dark and fully bright even in the presence of asymmetry. We also generalize Eq. (C.16) as

$$\hat{S}_D = \frac{\sqrt{\Gamma_{1D,2}}\hat{\sigma}_-^{(1)} + \sqrt{\Gamma_{1D,1}}\hat{\sigma}_-^{(2)}}{\sqrt{\Gamma_{1D,1} + \Gamma_{1D,2}}}, \quad \hat{S}_B = \frac{\sqrt{\Gamma_{1D,1}}\hat{\sigma}_-^{(1)} - \sqrt{\Gamma_{1D,2}}\hat{\sigma}_-^{(2)}}{\sqrt{\Gamma_{1D,1} + \Gamma_{1D,2}}}. \quad (C.20)$$

With this basis, the Hamiltonian can be written as

$$\hat{H} = \hbar J_D \left(\hat{\sigma}_-^{(p)} \hat{S}_D^\dagger + \hat{\sigma}_+^{(p)} \hat{S}_D \right) + \hbar J_B \left(\hat{\sigma}_-^{(p)} \hat{S}_B^\dagger + \hat{\sigma}_+^{(p)} \hat{S}_B \right), \quad (C.21)$$

where

$$J_D = \frac{\sqrt{\Gamma_{1D,p}\Gamma_{1D,1}\Gamma_{1D,2}}}{\sqrt{\Gamma_{1D,1} + \Gamma_{1D,2}}}, \quad J_B = \frac{\sqrt{\Gamma_{1D,p}}(\Gamma_{1D,1} - \Gamma_{1D,2})}{2\sqrt{\Gamma_{1D,1} + \Gamma_{1D,2}}}.$$

Thus, the probe qubit interacts with both the dark state and bright state with the ratio of $J_D : J_B = 2\sqrt{\Gamma_{1D,1}\Gamma_{1D,2}} : (\Gamma_{1D,1} - \Gamma_{1D,2})$, and thus for a small asymmetry in the waveguide decay rate, the coupling to the dark state dominates the dynamics. In addition, we note that the bright state superradiantly decays to the waveguide, and it follows that coupling of probe qubit to the bright state manifest only as contribution of

$$\frac{(2J_B)^2}{\Gamma_{1D,1} + \Gamma_{1D,2}} = \Gamma_{1D,p} \left(\frac{\Gamma_{1D,1} - \Gamma_{1D,2}}{\Gamma_{1D,1} + \Gamma_{1D,2}} \right)^2$$

to the probe qubit decay rate into spurious loss channel. In our experiment, the maximum asymmetry $d = \frac{|\Gamma_{1D,1} - \Gamma_{1D,2}|}{\Gamma_{1D,1} + \Gamma_{1D,2}}$ in waveguide decay rate between qubits is 0.14 (0.03) for type I (type II) from Table C.1, and this affects the decay rate of probe qubit by at most $\sim 2\%$.

Fitting of Rabi oscillation curves

The Rabi oscillation curves in Fig. 4.4 and Fig. 4.6d are modeled using a numerical master equation solver [338, 339]. The qubit parameters used for fitting the Rabi oscillation curves are summarized in Table C.1. For all the qubits, Γ_{1D} was found from spectroscopy. In addition, we have done a time-domain population decay measurement on the probe qubit to find the total decay rate of $\Gamma_1/2\pi = 1.1946$ MHz (95% confidence interval [1.1644, 1.2263] MHz, measured at 6.55 GHz). Using the value of $\Gamma_{1D}/2\pi = 1.1881$ MHz (95% confidence interval [1.1550, 1.2211] MHz, measured at 6.6 GHz) from spectroscopy, we find the spurious population decay rate $\Gamma_{\text{loss}}/2\pi = \Gamma_1/2\pi - \Gamma_{1D}/2\pi = 6.5$ kHz (with uncertainty of 45.3 kHz) for the probe qubit. The value of spurious population decay rate is assumed to be identical for all the qubits in the experiment. Note that the decaying rate of the envelope in the Rabi oscillation curve is primarily set by the waveguide decay rate of the probe qubit $\Gamma_{1D,p}$, and the large relative uncertainty in Γ_{loss} does not substantially affect the fit curve.

The dephasing rate of the probe qubit is derived from time-domain population decay and Ramsey sequence measurements $\Gamma_\varphi = \Gamma_2 - \Gamma_1/2$. In the case of the mirror qubits, the table shows effective single qubit parameters inferred from measurements of the dark state lifetime. We calculate single mirror qubit dephasing rates that theoretically yield the corresponding measured collective value. Assuming an uncorrelated Markovian dephasing for the mirror qubits forming the cavity we find $\Gamma_{\varphi,m} = \Gamma_{\varphi,D}$ (See Sec. C.3). Similarly, the waveguide decay rate of the mirror qubits is found from the spectroscopy of the bright collective state as $\Gamma_{1D,m} = \Gamma_{1D,B}/2$. The detuning between probe qubit and the atomic cavity (Δ) is treated as the only free parameter in our model. The value of Δ sets the visibility and frequency of the Rabi oscillation, and is found from the the fitting algorithm.

C.3 Lifetime (T_1) and coherence time (T_2^*) of dark state

The dark state of mirror qubits belongs to the decoherence-free subspace in the system due to its collectively suppressed radiation to the waveguide channel. However, there exists non-ideal channels that each qubit is coupled to, and such channels contribute to the finite lifetime (T_1) and coherence time (T_2^*) of the dark state (See Table C.2). In the experiment, we have measured the decoherence rate $\Gamma_{2,D}$ of the dark state to be always larger than the decay rate $\Gamma_{1,D}$, which cannot be explained by simple Markovian model of two qubits subject to their own independent noise. We discuss possible scenarios that can give rise to this situation of $\Gamma_{2,D} > \Gamma_{1,D}$, with

Type	Qubits involved	$\Gamma_{1D,p}/2\pi$ (MHz)	$\Gamma_{1D,m}/2\pi$ (MHz)	$\Gamma_{\varphi,p}/2\pi$ (kHz)	$\Gamma_{\varphi,m}/2\pi$ (kHz)	$\Delta/2\pi$ (MHz)
I	Q ₂ , Q ₆	1.19	13.4	191	210	1.0
II	Q ₁ , Q ₇	0.87	96.7	332	581	5.9
Dark compound	Q ₂ Q ₃ , Q ₅ Q ₆	1.19	4.3	191	146	0.9
Bright compound	Q ₂ Q ₃ , Q ₅ Q ₆	1.19	20.2	191	253	1.4

Table C.1: Parameters used for fitting Rabi oscillation curves. The first and second row are the data for 2-qubit dark states, the third and fourth row are the data for 4-qubit dark states made of compound mirrors. Here, $\Gamma_{1D,p}$ ($\Gamma_{1D,m}$) is the waveguide decay rate and $\Gamma_{\varphi,p}$ ($\Gamma_{\varphi,m}$) is the pure dephasing rate of probe (mirror) qubit, Δ is the detuning between probe qubit and mirror qubits used for fitting the data.

distinction of the Markovian and non-Markovian noise contributions.

There are two major channels that can affect the coherence of the dark state. First, coupling of a qubit to dissipative channels other than the waveguide can give rise to additional decay rate $\Gamma_{\text{loss}} = \Gamma_1 - \Gamma_{1D}$ (so-called non-radiative decay rate). This type of decoherence is uncorrelated between qubits and is well understood in terms of the Lindblad form of master equation, whose contribution to lifetime and coherence time of dark state is similar as in individual qubit case. Another type of contribution that severely affects the dark state coherence arises from fluctuations in qubit frequency, which manifest as pure dephasing rate Γ_{φ} in the individual qubit case. This can affect the decoherence of the dark state in two ways: (i) By accumulating a relative phase between different qubit states, this act as a channel to map the dark state into the bright state with short lifetime, and hence contributes to loss of population in

Type	Qubits involved	$\Gamma_{1,D}/2\pi$ (kHz)	$\Gamma_{2,D}/2\pi$ (kHz)
I	Q ₂ , Q ₆	210	366
II	Q ₁ , Q ₇	581	838
Dark compound	Q ₂ Q ₃ , Q ₅ Q ₆	146	215
Bright compound	Q ₂ Q ₃ , Q ₅ Q ₆	253	376

Table C.2: Decay rate and decoherence rate of dark states. The first and second row are the data for 2-qubit dark states, the third and fourth row are the data for 4-qubit dark states made of compound mirrors. Here, $\Gamma_{1,D}$ ($\Gamma_{2,D}$) is the decay (decoherence) rate of the dark state.

the dark state; (ii) fluctuations in qubit frequency also induces the frequency jitter of the dark state and therefore contributes to the dephasing of dark state.

In the following, we model the aforementioned contributions to the decoherence of dark state. Let us consider two qubits separated by $\lambda/2$ along the waveguide on resonance, in the presence of fluctuations $\tilde{\Delta}_j(t)$ in the qubit frequency. The master equation can be written as $\dot{\hat{\rho}} = -i[\hat{H}/\hbar, \hat{\rho}] + \mathcal{L}[\hat{\rho}]$, where the Hamiltonian \hat{H} and the Liouvillian \mathcal{L} are given by

$$\hat{H}(t) = \hbar \sum_{j=1,2} \tilde{\Delta}_j(t) \hat{\sigma}_+^{(j)} \hat{\sigma}_-^{(j)}, \quad (\text{C.22})$$

$$\mathcal{L}[\hat{\rho}] = \sum_{j,k=1,2} [(-1)^{j-k} \Gamma_{\text{ID}} + \delta_{jk} \Gamma_{\text{loss}}] \left(\hat{\sigma}_-^{(j)} \hat{\rho} \hat{\sigma}_+^{(k)} - \frac{1}{2} \{ \hat{\sigma}_+^{(k)} \hat{\sigma}_-^{(j)}, \hat{\rho} \} \right). \quad (\text{C.23})$$

Here, Γ_{ID} (Γ_{loss}) is the decay rate of qubits into waveguide (spurious loss) channel. Note that we have assumed the magnitude of fluctuation $\tilde{\Delta}_j(t)$ in qubit frequency is small and neglected its effect on exchange interaction and correlated decay. We investigate two scenarios in the following subsections depending on the correlation of noise that gives rise to qubit frequency fluctuations.

Markovian noise

If the frequency fluctuations of the individual qubits satisfy the conditions for Born and Markov approximations, i.e. the noise is weakly coupled to the qubit and has short correlation time, the frequency jitter can be described in terms of the standard Lindblad form of dephasing [336].

More generally, we also consider the correlation between frequency jitter of different qubits. Such contribution can arise when different qubits are coupled to a single fluctuating noise source. For instance, if two qubits in a system couple to a magnetic field $B_0 + \tilde{B}(t)$ that is global to the chip with $D_j \equiv \partial \tilde{\Delta}_j / \partial \tilde{B}$, the correlation between detuning of different qubits follows correlation of the fluctuations in magnetic field, giving $\langle \tilde{\Delta}_1(t) \tilde{\Delta}_2(t + \tau) \rangle = D_1 D_2 \langle \tilde{B}(t) \tilde{B}(t + \tau) \rangle \neq 0$. The Liouvillian associated with dephasing can be written as [340]

$$\mathcal{L}_{\varphi,jk}[\hat{\rho}] = \frac{\Gamma_{\varphi,jk}}{2} \left(\hat{\sigma}_z^{(j)} \hat{\rho} \hat{\sigma}_z^{(k)} - \frac{1}{2} \{ \hat{\sigma}_z^{(k)} \hat{\sigma}_z^{(j)}, \hat{\rho} \} \right), \quad (\text{C.24})$$

where the dephasing rate $\Gamma_{\varphi,jk}$ between qubit j and qubit k ($j = k$ denotes individual qubit dephasing and $j \neq k$ is the correlated dephasing) is given by

$$\Gamma_{\varphi,jk} \equiv \frac{1}{2} \int_{-\infty}^{+\infty} d\tau \langle \tilde{\Delta}_j(0) \tilde{\Delta}_k(\tau) \rangle. \quad (\text{C.25})$$

Here, the average $\langle \cdot \rangle$ is taken over an ensemble of fluctuators in the environment. Note that the correlated dephasing rate $\Gamma_{\varphi,jk}$ can be either positive or negative depending on the sign of noise correlation, while the individual pure dephasing rate $\Gamma_{\varphi,jj}$ is always positive.

After we incorporate the frequency jitter as the dephasing contributions to the Liouvillian, the master equation takes the form

$$\begin{aligned} \dot{\hat{\rho}} = \sum_{j,k=1,2} \left\{ \left[(-1)^{j-k} \Gamma_{1D} + \delta_{jk} \Gamma_{\text{loss}} \right] \left(\hat{\sigma}_-^{(j)} \hat{\rho} \hat{\sigma}_+^{(k)} - \frac{1}{2} \{ \hat{\sigma}_+^{(k)} \hat{\sigma}_-^{(j)}, \hat{\rho} \} \right) \right. \\ \left. + \frac{\Gamma_{\varphi,jk}}{2} \left(\hat{\sigma}_z^{(j)} \hat{\rho} \hat{\sigma}_z^{(k)} - \frac{1}{2} \{ \hat{\sigma}_z^{(k)} \hat{\sigma}_z^{(j)}, \hat{\rho} \} \right) \right\}, \end{aligned} \quad (\text{C.26})$$

We diagonalize the correlated decay part of the Liouvillian describe the two-qubit system in terms of bright and dark states defined in Eq. (C.15). From now on, we assume the pure dephasing rate and the correlated dephasing rate are identical for the two qubits, and write $\Gamma_{\varphi} \equiv \Gamma_{\varphi,11} = \Gamma_{\varphi,22}$, $\Gamma_{\varphi,c} \equiv \Gamma_{\varphi,12} = \Gamma_{\varphi,21}$. For qubits with a large Purcell factor ($\Gamma_{1D} \gg \Gamma_{\varphi}, |\Gamma_{\varphi,c}|, \Gamma_{\text{loss}}$), we can assume that the superradiant states $|B\rangle$ and $|E\rangle$ are only virtually populated [123] and neglect the density matrix elements associated with $|B\rangle$ and $|E\rangle$. Rewriting Eq. (C.26) in the basis of $\{|G\rangle, |B\rangle, |D\rangle, |E\rangle\}$, the dynamics related to dark state can be expressed as $\dot{\rho}_{D,D} \approx -\Gamma_{1,D} \rho_{D,D}$ and $\dot{\rho}_{D,G} \approx -\Gamma_{2,D} \rho_{D,G}$, where

$$\Gamma_{1,D} = \Gamma_{\text{loss}} + \Gamma_{\varphi} - \Gamma_{\varphi,c}, \quad \Gamma_{2,D} = \frac{\Gamma_{\text{loss}}}{2} + \Gamma_{\varphi}. \quad (\text{C.27})$$

Note that if the correlated dephasing rate $\Gamma_{\varphi,c}$ is zero, $\Gamma_{1,D}$ is always larger than $\Gamma_{2,D}$, which is in contradiction to our measurement result.

We estimate the decay rate into non-ideal channels to be $\Gamma_{\text{loss}}/2\pi = 6.5$ kHz from the difference in Γ_1 and Γ_{1D} of the probe qubit, and assume Γ_{loss} to be similar for all the qubits. Applying Eq. (C.27) to measured values of $\Gamma_{2,D}$ listed in Table C.2, we expect that the pure dephasing of the individual qubit is the dominant decay and decoherence source for the dark state. In addition, we compare the decay rate $\Gamma_{1,D}$ and decoherence rate $\Gamma_{2,D}$ of dark states in the Markovian noise model and infer that the correlated dephasing rate $\Gamma_{\varphi,c}$ is positive and is around a third of the individual dephasing rate Γ_{φ} for all types of mirror qubits.

Non-Markovian noise

In a realistic experimental setup, there also exists non-Markovian noise sources contributing to the dephasing of the qubits, e.g. $1/f$ -noise or quasi-static noise

[190, 341, 342]. In such cases, the frequency jitter cannot be simply put into the Lindblad form as described above. In this subsection, we consider how the individual qubit dephasing induced by non-Markovian noise influences the decoherence of dark state. As shown below, we find that a non-Markovian noise source can lead to a shorter coherence time to lifetime ratio for the dark states, in a similar fashion to correlated dephasing. However, we find that the functional form of the visibility of Ramsey fringes is not necessarily an exponential for a non-Markovian noise source.

We start from the master equation introduced in Eqs. (C.22)-(C.23) can be written in terms of the basis of $\{|G\rangle, |B\rangle, |D\rangle, |E\rangle\}$,

$$\dot{\hat{\rho}} = -\frac{i}{\hbar}[\hat{H}, \hat{\rho}] + (2\Gamma_{1D} + \Gamma_{\text{loss}}) \mathcal{D}[\hat{S}_B]\hat{\rho} + \Gamma_{\text{loss}}\mathcal{D}[\hat{S}_D]\hat{\rho}, \quad (\text{C.28})$$

where the Hamiltonian is written using the common frequency jitter $\tilde{\Delta}_c(t) \equiv [\tilde{\Delta}_1(t) + \tilde{\Delta}_2(t)]/2$ and differential frequency jitter $\tilde{\Delta}_d(t) \equiv [\tilde{\Delta}_1(t) - \tilde{\Delta}_2(t)]/2$

$$\hat{H}(t)/\hbar = \tilde{\Delta}_c(t) (2|E\rangle\langle E| + |D\rangle\langle D| + |B\rangle\langle B|) + \tilde{\Delta}_d(t) (|B\rangle\langle D| + |D\rangle\langle B|). \quad (\text{C.29})$$

Here, \hat{S}_B and \hat{S}_D are defined in Eq. (C.16). From the Hamiltonian in Eq. (C.29), we see that the common part of frequency fluctuation $\tilde{\Delta}_c(t)$ results in the frequency jitter of the dark state while the differential part of frequency fluctuation $\tilde{\Delta}_d(t)$ drives the transition between $|D\rangle$ and $|B\rangle$, which acts as a decay channel for the dark state.

For uncorrelated low-frequency noise on the two qubits, the decoherence rate is approximately the standard deviation of the common frequency jitter $\sqrt{\langle \tilde{\Delta}_c(t)^2 \rangle}$. The decay rate in this model can be found by modeling the bright state as a cavity in the Purcell regime, and calculate the damping rate of the dark state using the Purcell factor as $\langle 4\tilde{\Delta}_d(t)^2 / \Gamma_B \rangle$. As evident, in this model the dark state's population decay rate is strongly suppressed by the large damping rate of bright state Γ_B , while the dark state's coherence time can be sharply reduced due to dephasing.

C.4 Shelving

We consider the case of two identical mirror qubits of frequency ω_q , separated by distance $\lambda/2$ along the waveguide. In addition to free evolution of qubits, we include a coherent probe signal from the waveguide in the analysis. In the absence of pure dephasing ($\Gamma_\varphi = 0$) and thermal occupancy ($\bar{n}_{\text{th}} = 0$), the master equation in the rotating frame of the probe signal takes the same form as Eq. (C.28), where the Hamiltonian containing the drive from the probe signal is written as

$$\hat{H}/\hbar = \sum_{\mu=B,D} \left[-\delta\omega \hat{S}_\mu^\dagger \hat{S}_\mu + \frac{\Omega_\mu}{2} (\hat{S}_\mu + \hat{S}_\mu^\dagger) \right], \quad (\text{C.30})$$

where \hat{S}_B and \hat{S}_D are defined in Eq. (C.16), $\delta\omega = \omega_p - \omega_q$ is the detuning of the probe signal from the mirror qubit frequency, Ω_μ is the corresponding driven Rabi frequency. Note that due to the symmetry of the excitations with respect to the waveguide, we see that $\Omega_D = 0$ and $\Omega_B = \sqrt{2}\Omega_1$, where Ω_1 is the Rabi frequency of one of the mirror qubits from the probe signal along the waveguide.

Let us consider the limit where the Purcell factor $P_{1D} = \Gamma_{1D}/\Gamma'$ of qubits is much larger than unity (equivalent to $\Gamma_D = \Gamma' \ll \Gamma_B = 2\Gamma_{1D} + \Gamma'$) and the drive applied to the qubits is weak $\Omega_B \ll \Gamma_B$. Then, we can effectively remove some of the density matrix elements¹,

$$\rho_{E,E}, \rho_{B,E}, \rho_{E,B}, \rho_{G,E}, \rho_{E,G} \approx 0$$

and restrict the analysis to ones involved with three levels $\{|G\rangle, |D\rangle, |B\rangle\}$. In addition, the dark state $|D\rangle$ is effectively decoupled from $|G\rangle$ and $|B\rangle$, acting as a metastable state. Therefore, we only consider the following set of the master equation:

$$\dot{\rho}_{B,B} \approx -\Gamma_B \rho_{B,B} + \frac{i\Omega_B}{2}(\rho_{B,G} - \rho_{G,B}) \quad (\text{C.31})$$

$$\dot{\rho}_{B,G} \approx \left(i\delta\omega - \frac{\Gamma_B}{2}\right)\rho_{B,G} + \frac{i\Omega_B}{2}(\rho_{B,B} - \rho_{G,G}) \quad (\text{C.32})$$

$$\dot{\rho}_{G,G} \approx -\dot{\rho}_{B,B}; \quad \dot{\rho}_{G,B} = \dot{\rho}_{B,G}^* \quad (\text{C.33})$$

¹From the master equation, the time-evolution of part of the density matrix elements are approximately written as

$$\begin{aligned} \dot{\rho}_{E,E} &= -(\Gamma_B + \Gamma_D)\rho_{E,E} + \frac{i\Omega_B}{2}(\rho_{B,E} - \rho_{E,B}), \\ \dot{\rho}_{E,B} &= \left[i\delta\omega - \left(\Gamma_B + \frac{\Gamma_D}{2}\right)\right]\rho_{E,B} + \frac{i\Omega_B}{2}(\rho_{B,B} - \rho_{E,E} + \rho_{E,G}), \\ \dot{\rho}_{E,G} &= \left(2i\delta\omega - \frac{\Gamma_B + \Gamma_D}{2}\right)\rho_{E,G} + \frac{i\Omega_B}{2}(\rho_{B,G} + \rho_{E,B}), \\ \dot{\rho}_{E,B} &= \dot{\rho}_{B,E}^*; \quad \dot{\rho}_{E,G} = \dot{\rho}_{G,E}^*. \end{aligned}$$

In the steady state, it can be shown that

$$\begin{aligned} \rho_{E,E} &\sim \mathcal{O}(x^2)\rho_{B,B} + \mathcal{O}(x^3)(\rho_{B,G} - \rho_{G,B}) \\ \rho_{B,E} &\sim \mathcal{O}(x)\rho_{B,B} + \mathcal{O}(x^2)\rho_{G,B} \\ \rho_{G,E} &\sim \mathcal{O}(x^2)\rho_{B,B} + \mathcal{O}(x)\rho_{G,B} \end{aligned}$$

to leading order in $x \equiv \Omega_B/\Gamma_B < 1$, and hence we can neglect the contributions from $\rho_{E,E}$, $\rho_{B,E}$, $\rho_{E,B}$, $\rho_{G,E}$, $\rho_{E,G}$ from the analysis in the weak driving limit. The probe power we have used in the experiment corresponds to $x \sim 0.15$, which makes this approximation valid.

Using the normalization of total population $\rho_{G,G} + \rho_{D,D} + \rho_{B,B} \approx 1$ with Eqs. (C.31)-(C.33), we obtain the approximate steady-state solution

$$\langle \hat{S}_B \rangle \approx \rho_{B,G} \approx -\frac{i\Omega_B(1 - \rho_{D,D})}{\Gamma_B - 2i\delta\omega}. \quad (\text{C.34})$$

The input-output relation [116] is given as

$$\hat{a}_{\text{out}} = \hat{a}_{\text{in}} + \sqrt{\frac{\Gamma_{1D}}{2}}\hat{\sigma}_-^{(1)} - \sqrt{\frac{\Gamma_{1D}}{2}}\hat{\sigma}_-^{(2)} = \hat{a}_{\text{in}} + \sqrt{\Gamma_{1D}}\hat{S}_B, \quad (\text{C.35})$$

where \hat{a}_{in} is the input field operator and \hat{a}_{out} is the operator for output field propagating in the same direction as the input field (here, the input field is assumed to be incident from only one direction). The transmission amplitude is calculated as

$$t = \frac{\langle \hat{a}_{\text{out}} \rangle}{\langle \hat{a}_{\text{in}} \rangle} = 1 - \frac{(1 - \rho_{D,D})\Gamma_{1D}}{-i\delta\omega + \Gamma_B/2} \quad (\text{C.36})$$

where the relation $\Omega_1/2 = -i\langle \hat{a}_{\text{in}} \rangle\sqrt{\Gamma_{1D}/2}$ has been used.

In the measurement, we use the state transfer protocol to transfer part of the ground state population into the dark state. Following this, we drive the $|G\rangle \leftrightarrow |B\rangle$ transition by sending a weak coherent pulse with a duration 260 ns into the waveguide, and recording the transmission spectrum. As a comparison, we also measure the transmission spectrum when the mirror qubits are in the ground state, which corresponds to having $\rho_{D,D} = 0$. The transmittance in the two cases (Figure 3d) are fitted with identical parameters for Γ_{1D} and Γ_B . The dark state population $\rho_{D,D}$ following the iSWAP gate is extracted from the data as 0.58, which is lower than the value (0.68) found from the Rabi oscillation peaks (Fig. 4.4). The lower value of the dark state population can be understood considering the finite lifetime of dark state (757 ns), which leads to a partial population decay during the measurement time (the single-shot measurement time is set by the duration of the input pulse). It should be noted that the input pulse has a transform-limited bandwidth of ~ 3.8 MHz, which results in frequency averaging of the spectral response over this bandwidth. For this reason, the on-resonance transmission extinction measured in the pulsed scheme is lower than the value found from continuous wave (CW) measurement (Fig. 4.2).

SUPPLEMENTARY INFORMATION FOR CHAPTER 5

D.1 Band structure analysis**Quantization of a periodic resonator-loaded waveguide**

We consider the case of a waveguide that is periodically loaded with microwave resonators. Figure D.1 depicts a unit cell for this configuration. The Lagrangian for this system can be written as [226]

$$L = \sum_n \left[\frac{1}{2} C_0 (\dot{\Phi}_n^a)^2 - \frac{(\Phi_n^a - \Phi_{n-1}^a)^2}{2L_0} + \frac{1}{2} C_r (\dot{\Phi}_n^b)^2 + \frac{1}{2} C_g (\Phi_n^a - \Phi_n^b)^2 - \frac{(\Phi_n^b)^2}{2L_r} \right]. \quad (\text{D.1})$$

In order to find solutions in form of traveling waves, it is easier to work with the Fourier transform of node fluxes. We use the following convention for defining the (discrete) Fourier transformation

$$\Phi_\kappa^{a,b} = \frac{1}{\sqrt{M}} \sum_{n=-N}^N e^{-i2\pi(\kappa/M)n} \Phi_n^{a,b}, \quad (\text{D.2})$$

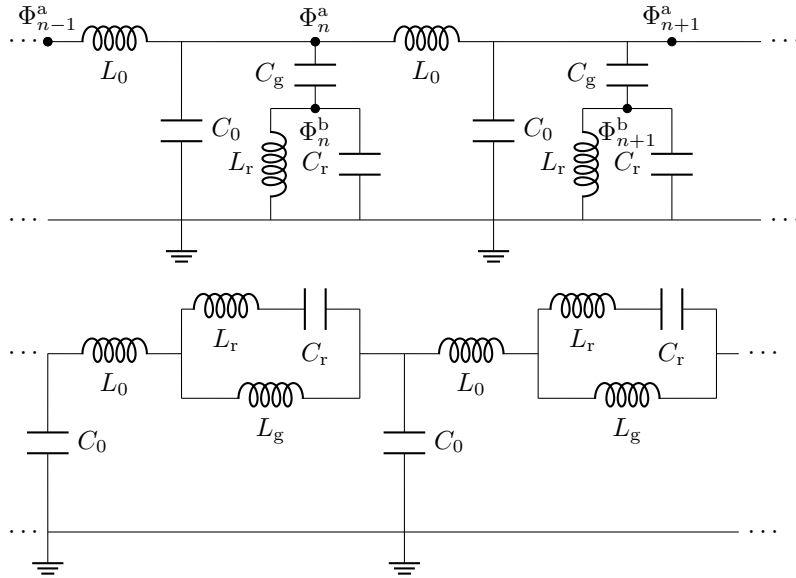


Figure D.1: Circuit diagram of metamaterial waveguide. The waveguide can be made from periodic arrays of transmission line sections loaded with capacitively coupled resonators (top), or inductively loaded resonators (bottom).

where $M = 2N + 1$ is the total number of periods in the waveguide. Using the Fourier relation we find the Lagrangian in k -space as

$$L = \sum_{\kappa} \left[\frac{1}{2} (C_0 + C_g) |\dot{\Phi}_{\kappa}^a|^2 - \left| 1 - e^{-i2\pi(\kappa/M)} \right|^2 \frac{|\Phi_{\kappa}^a|^2}{2L_0} + \frac{1}{2} (C_g + C_r) |\dot{\Phi}_{\kappa}^b|^2 - \frac{|\Phi_{\kappa}^b|^2}{2L_r} - C_g \frac{\dot{\Phi}_{\kappa}^b \dot{\Phi}_{-\kappa}^a + \dot{\Phi}_{-\kappa}^b \dot{\Phi}_{\kappa}^a}{2} \right].$$

To proceed further, we need to find the canonical node charges which are defined as $Q_{\kappa}^{a,b} = \frac{\partial L}{\partial \dot{\Phi}_{\kappa}^{a,b}}$, and subsequently derive the Hamiltonian of the system by using a Legendre transformation. Doing so we find

$$H = \sum_{\kappa} \left[\frac{Q_{\kappa}^a Q_{-\kappa}^a}{2C'_0} + \left| 1 - e^{-i2\pi(\kappa/M)} \right|^2 \frac{\Phi_{\kappa}^a \Phi_{-\kappa}^a}{2L_0} + \frac{Q_{\kappa}^b Q_{-\kappa}^b}{2C'_r} + \frac{\Phi_{\kappa}^b \Phi_{-\kappa}^b}{2L_r} + \frac{Q_{\kappa}^a Q_{-\kappa}^b + Q_{-\kappa}^a Q_{\kappa}^b}{2C'_g} \right].$$

Here, we have defined the following quantities

$$C'_0 = \frac{C_g C_r + C_g C_0 + C_0 C_r}{C_g + C_r}, \quad C'_r = \frac{C_g C_r + C_g C_0 + C_0 C_r}{C_g + C_0}, \quad C'_g = \frac{C_g C_r + C_g C_0 + C_0 C_r}{C_g}.$$

The canonical commutation relation $[\Phi_{\kappa}^i, Q_{-\kappa'}^j] = i\hbar \delta_{i,j} \delta_{\kappa,\kappa'}$ allows us to define the following annihilation operators as a function of charge and flux operators

$$\hat{a}_{\kappa} = \sqrt{\frac{C'_0 \Omega_k}{2\hbar}} \left(\Phi_{\kappa}^a + \frac{i}{C'_0 \Omega_k} Q_{\kappa}^a \right), \quad \hat{b}_{\kappa} = \sqrt{\frac{C'_r \omega_0}{2\hbar}} \left(\Phi_{\kappa}^b + \frac{i}{C'_r \omega_0} Q_{\kappa}^b \right). \quad (D.3)$$

Here, we have defined the resonance frequency for each mode as

$$\Omega_k = \sqrt{\frac{4\sin^2(kd/2)}{L_0 C'_0}}, \quad \omega_0 = \frac{1}{\sqrt{L_r C'_r}}, \quad (D.4)$$

where $k = 2\pi\kappa/(Md)$ is the wavenumber. It is evident that Ω_k has the expected dispersion relation of a discrete periodic transmission line and ω_0 is the resonance frequency of the loaded microwave resonators. Using the above definitions for $\hat{a}_{\kappa}, \hat{b}_{\kappa}$

$$\hat{H} = \frac{\hbar}{2} \sum_{\kappa} \left[\Omega_k \left(\hat{a}_{\kappa}^{\dagger} \hat{a}_{\kappa} + \hat{a}_{-\kappa} \hat{a}_{-\kappa}^{\dagger} \right) + \omega_0 \left(\hat{b}_{\kappa}^{\dagger} \hat{b}_{\kappa} + \hat{b}_{-\kappa} \hat{b}_{-\kappa}^{\dagger} \right) - g_k \left(\hat{b}_{-\kappa} - \hat{b}_{\kappa}^{\dagger} \right) \left(\hat{a}_{\kappa} - \hat{a}_{-\kappa}^{\dagger} \right) - g_k \left(\hat{a}_{\kappa}^{\dagger} - \hat{a}_{-\kappa} \right) \left(\hat{b}_{-\kappa}^{\dagger} - \hat{b}_{\kappa} \right) \right], \quad (D.5)$$

along with the coupling coefficient

$$g_k = \frac{\sqrt{C'_0 C'_r}}{2C'_g} \sqrt{\omega_0 \Omega_k} = \frac{C_g \sqrt{\omega_0 \Omega_k}}{2\sqrt{(C_0 + C_g)(C_r + C_g)}}. \quad (D.6)$$

An alternative structure for coupling microwave resonators is depicted in the bottom panel of Fig. D.1. In this geometry, the coupling is controlled by the inductive element L_g . Repeating the analysis above for this case, we find

$$\Omega_k = \sqrt{\frac{4\sin^2(kd/2)}{C_0 L'_0}}, \quad \omega_0 = \frac{1}{\sqrt{C_r L'_r}}, \quad g_k = \frac{\sqrt{L'_0 L'_r}}{2L'_g} \sqrt{\omega_0 \Omega_k}. \quad (\text{D.7})$$

We have defined the modified inductance values as

$$L'_0 = \frac{L_g L_r + L_g L_0 + L_0 L_r}{L_g + L_r}, \quad L'_r = \frac{L_g L_r + L_g L_0 + L_0 L_r}{L_g + L_0}, \quad L'_g = \frac{L_g L_r + L_g L_0 + L_0 L_r}{L_g}.$$

Band structure calculation with RWA

Using the rotating wave approximation, the Hamiltonian in Eq. (D.5) can be simplified to

$$\hat{H} = \hbar \sum_k \left[\Omega_k \hat{a}_k^\dagger \hat{a}_k + \omega_0 \hat{b}_k^\dagger \hat{b}_k + g_k \left(\hat{b}_k^\dagger \hat{a}_k + \hat{a}_k^\dagger \hat{b}_k \right) \right]. \quad (\text{D.8})$$

Note that this approximation is applicable only when the coupling is sufficiently weak, $g_k \ll \min(\omega_0, \Omega_k)$, and the detuning is sufficiently small $|\omega_0 - \Omega_k| \ll (\omega_0 + \Omega_k)$. Assuming Ω_k and ω_0 are of the same order, this condition is satisfied when $C_g \ll 2\sqrt{(C_0 C_r)}$.

The simplified Hamiltonian can be written in the compact form

$$\hat{H} = \hbar \sum_k \mathbf{x}_k^\dagger \mathbf{H}_k \mathbf{x}_k, \quad (\text{D.9})$$

where

$$\mathbf{H}_k = \begin{bmatrix} \Omega_k & g_k \\ g_k & \omega_0 \end{bmatrix}, \quad \mathbf{x}_k = \begin{bmatrix} \hat{a}_k \\ \hat{b}_k \end{bmatrix}. \quad (\text{D.10})$$

We desire to transform the Hamiltonian to a diagonalized form

$$\tilde{\mathbf{H}}_k = \begin{bmatrix} \omega_{+,k} & 0 \\ 0 & \omega_{-,k} \end{bmatrix}. \quad (\text{D.11})$$

It is straightforward to use the eigenvalue decomposition to find $\omega_{\pm,k}$ as

$$\omega_{\pm,k} = \frac{1}{2} \left[(\Omega_k + \omega_0) \pm \sqrt{(\Omega_k - \omega_0)^2 + 4g_k^2} \right], \quad (\text{D.12})$$

along with the corresponding eigenstates $|\pm, k\rangle = \hat{\alpha}_{\pm,k}|0\rangle$, where

$$\hat{\alpha}_{\pm,k} = \frac{(\omega_{\pm,k} - \omega_0)}{\sqrt{(\omega_{\pm,k} - \omega_0)^2 + g_k^2}} \hat{a}_k + \frac{g_k}{\sqrt{(\omega_{\pm,k} - \omega_0)^2 + g_k^2}} \hat{b}_k. \quad (\text{D.13})$$

Band structure calculation beyond RWA

The exact Hamiltonian in Eq. (D.5) can be written in the compact form

$$\hat{H} = \frac{\hbar}{2} \sum_k \mathbf{x}_k^\dagger \mathbf{H}_k \mathbf{x}_k, \quad (\text{D.14})$$

where

$$\mathbf{H}_k = \begin{bmatrix} \Omega_k & 0 & g_k & -g_k \\ 0 & \Omega_k & -g_k & g_k \\ g_k & -g_k & \omega_0 & 0 \\ -g_k & g_k & 0 & \omega_0 \end{bmatrix}, \quad \mathbf{x}_k = \begin{bmatrix} \hat{a}_k \\ \hat{a}_{-k}^\dagger \\ \hat{b}_k \\ \hat{b}_{-k}^\dagger \end{bmatrix}. \quad (\text{D.15})$$

To find the eigenstates of the system, we can use a linear transform to map the state vector $\tilde{\mathbf{x}}_k = \mathbf{S}_k \mathbf{x}_k$ such that $\mathbf{x}_k^\dagger \mathbf{H}_k \mathbf{x}_k = \tilde{\mathbf{x}}_k^\dagger \tilde{\mathbf{H}}_k \tilde{\mathbf{x}}_k$ with the transformed diagonal Hamiltonian matrix

$$\tilde{\mathbf{H}}_k = \begin{bmatrix} \omega_{+,k} & 0 & 0 & 0 \\ 0 & \omega_{+,k} & 0 & 0 \\ 0 & 0 & \omega_{-,k} & 0 \\ 0 & 0 & 0 & \omega_{-,k} \end{bmatrix} \quad (\text{D.16})$$

In order to preserve the canonical commutation relations, the matrix \mathbf{S}_k has to be symplectic, i.e. $\mathbf{J} = \mathbf{S}_k \mathbf{J} \mathbf{S}_k^\dagger$, with the matrix $\mathbf{J} = \text{diag}(1, -1, 1, -1)$. A linear transformation (such as \mathbf{S}_k) that diagonalizes a set of quadratically coupled boson fields while preserving their canonical commutation relations is often referred to as a Bogoliubov-Valatin transformation. While it is generally difficult to find the transform matrix \mathbf{S}_k , it is easy to find the eigenvalues of the diagonalized Hamiltonian by exploiting some of the properties of \mathbf{S}_k . Note that since $\mathbf{J} = \mathbf{S}_k \mathbf{J} \mathbf{S}_k^\dagger$, the matrices $\mathbf{J} \tilde{\mathbf{H}}_k$ and $\mathbf{J} \mathbf{H}_k$ share the same set of eigenvalues. The eigenvalues of $\mathbf{J} \tilde{\mathbf{H}}_k$ are the two frequencies $\omega_{\pm,k}$, and thus we have

$$\omega_{\pm,k}^2 = \frac{1}{2} \left[\left(\Omega_k^2 + \omega_0^2 \right) \pm \sqrt{\left(\Omega_k^2 - \omega_0^2 \right)^2 + 16\omega_0 \Omega_k g_k^2} \right]. \quad (\text{D.17})$$

Circuit theory derivation of the band structure

Consider the pair of equations that describe the propagation of a monochromatic electromagnetic wave of the form $v(x, t) = V(x) e^{-ikx} e^{i\omega t}$ (along with the corresponding current relation) inside a transmission line

$$\frac{d}{dx} V(x) = -Z(\omega) I(x), \quad \frac{d}{dx} I(x) = -Y(\omega) V(x). \quad (\text{D.18})$$

Here, $Z(\omega)$ and $Y(\omega)$ are frequency dependent impedance and admittance functions that model the linear response of the series and parallel portions of a transmission line with length d . It is straightforward to check that the solutions to these equation satisfy $k(\omega) = n\omega/c = \sqrt{-Z(\omega)Y(\omega)}/d$. For a loss-less waveguide and in the absence of dispersion we have $Z(\omega) = i\omega L_0$ and $Y(\omega) = i\omega C_0$, and thus we find the familiar dispersion relation $k(\omega) = \omega\sqrt{L_0 C_0}/d$. Nevertheless, the pair of equations above remain valid for arbitrary impedance and admittance functions $Z(\omega)$ and $Y(\omega)$, provided that the dimension of the model circuit remains much smaller than the wavelength under consideration. In this model, a real and negative quantity for the product ZY results in an imaginary wavenumber and subsequently creates a stop band in the dispersion relation. This situation can be achieved by periodically loading a transmission line with an array of resonators [343, 344]. Assuming a unit length of d we find

$$k^2 = \left(\frac{\omega}{c}\right)^2 n^2 \left[1 + \frac{2c\gamma_e}{nd} \frac{1}{\omega_0^2 - \omega^2} \right]. \quad (\text{D.19})$$

Here, ω_0 is the resonance frequency, and γ_e is the external coupling decay rate of an individual resonator in the array. For moderate values of gap-midgap ratio (Δ/ω_m), the frequency gap can be found as

$$\Delta = \frac{c}{nd} \left(\frac{\gamma_e}{\omega_0} \right), \quad (\text{D.20})$$

and $\omega_m = \omega_0 + \Delta/2$. We have defined the gap as the range of frequencies where the wavenumber is imaginary.

Although a microwave resonator can be realized by using a two-element LC-circuit, the three-element circuits in Fig. D.1 provide an additional degree of freedom which enables setting the coupling γ_e independent of the resonance frequency ω_0 . Using circuit theory, it is straightforward to show

$$\omega_0 = \frac{1}{\sqrt{L_r(C_r + C_g)}}, \quad \gamma_e = \frac{Z_0}{2L_r} \left(\frac{C_g}{C_r + C_g} \right)^2. \quad (\text{D.21})$$

Here, Z_0 is the characteristic impedance of the unloaded waveguide. It is easy to check that for small values of C_g/C_r , the resonance frequency is only a weak function of C_g . As a result, it is possible to adjust the coupling rate γ_e by setting the capacitor C_g while keeping the resonance frequency almost constant. Fig. D.1 also depicts an alternative strategy for coupling microwave resonators to the waveguide. In this design, the inductive element L_g is used to set the coupling in a ‘‘current

divider" geometry. We provide experimental results for implementation of bandgap waveguide based on both designs in the next section.

While the "continuum" model described above provides a heuristic explanation for formation of bandgap in a waveguide loaded with resonators, its results remains valid as far as $k \ll 2\pi/d$. To avoid this approximation, we can use the transfer matrix method to find the exact dispersion relation for a system with discrete periodic symmetry [180]. In this case, Equation (D.19) is modified to

$$\cos(kd) = 1 - \left(\frac{\omega}{c}\right)^2 \frac{n^2 d^2}{2} - \frac{nd\gamma_e}{c} \frac{\omega^2}{\omega_0^2 - \omega^2}. \quad (\text{D.22})$$

Note that this relation still requires d to be much smaller than the wavelength of the unloaded waveguide $\lambda = 2\pi c/(n\omega)$.

Dispersion and group index near the band-edges

Equation (D.17) can be reversed to find the wavenumber k as a function of frequency. Assuming, a linear dispersion relation of the form $k = n\Omega_k/c$ for the bare waveguide we find

$$k = \frac{n\omega}{c} \sqrt{\frac{\omega^2 - \omega_{c+}^2}{\omega^2 - \omega_{c-}^2}}. \quad (\text{D.23})$$

Here, $\omega_{c+} = \omega_0$ and $\omega_{c-} = \omega_0 \sqrt{1 - 4g_k^2/(\Omega_k \omega_0)}$ are the upper and lower cut-off frequencies, respectively. The quantity $g_k^2/(\Omega_k \omega_0)$ is a unit-less parameter quantifying the size of the bandgap and is independent of the wavenumber k .

The dispersion relation can be written in simpler forms by expanding the wavenumber in the vicinity of the two band-edges

$$k = \begin{cases} \frac{n\omega_{c-}}{c} \sqrt{\frac{\Delta}{-\delta_-}} & \text{for } \omega \approx \omega_{c-}, \\ \frac{n\omega_{c+}}{c} \sqrt{\frac{\delta_+}{\Delta}} & \text{for } \omega \approx \omega_{c+}. \end{cases} \quad (\text{D.24})$$

Here, $\Delta = \omega_{c+} - \omega_{c-}$ is the frequency span of the bandgap and $\delta_{\pm} = \omega - \omega_{c\pm}$ are the detunings from the band-edges.

The form of the dispersion relation Eq. (D.17) suggests that the maxima of the group index happens near the band-edges. Having the wavenumber, we can evaluate the group velocity $v_g = \partial\omega/\partial k$ and find the group index $n_g = c/v_g$ as

$$n_g = \begin{cases} \frac{n\omega_{c-}\sqrt{\Delta}}{\sqrt{-4(\delta_- - i\gamma_i)^3}} & \text{for } \omega \approx \omega_{c-}, \\ \frac{n\omega_{c+}}{\sqrt{4\Delta(\delta_+ - i\gamma_i)}} & \text{for } \omega \approx \omega_{c+}. \end{cases} \quad (\text{D.25})$$

Note that we have replaced δ_{\pm} with $\delta_{\pm} - i\gamma_i$ to account for finite internal quality factor of the resonators in the structure.

Coupling a Josephson junction qubit to a metamaterial waveguide

We consider the coupling of a Josephson junction qubit to the metamaterial waveguide. Assuming rotating wave approximation (valid for weak coupling $f_k \ll \omega_k, \omega_q$), the Hamiltonian of this system can be written as

$$\hat{H} = \hbar \sum_k \left[\omega_k \hat{a}_k^\dagger \hat{a}_k + \frac{\omega_q}{2} \hat{\sigma}_z + f_k \left(\hat{a}_k^\dagger \hat{\sigma}^- + \hat{a}_k \hat{\sigma}^+ \right) \right] \quad (\text{D.26})$$

Here f_k is the coupling factor of the qubit to the waveguide photons, and $\omega_k = \omega_{\pm,k}$, where the plus or minus sign is chosen such that the qubit frequency ω_q lies within the band. Without loss of generality, we assume f_k to be a real number. The Heisenberg equations of motions for the qubit and the photon operators can be written as

$$\frac{\partial}{\partial t} \hat{a}_k = -i\omega_k \hat{a}_k - i f_k \hat{\sigma}^- \quad (\text{D.27})$$

$$\frac{\partial}{\partial t} \hat{\sigma}^- = -i\omega_q \hat{\sigma}^- - i \sum_k f_k \hat{a}_k \quad (\text{D.28})$$

The equation for \hat{a}_k can be formally integrated and substituted in the equation for $\hat{\sigma}^-$ to find

$$\begin{aligned} \frac{\partial}{\partial t} \hat{\sigma}^- &= -i\omega_q \hat{\sigma}^- - i \sum_k f_k e^{-i\omega_k(t-t_0)} \hat{a}_k(t_0) \\ &\quad - \sum_k f_k^2 \int_{t_0}^t e^{-i(\omega_k)(t-\tau)} \hat{\sigma}^-(\tau) d\tau. \end{aligned} \quad (\text{D.29})$$

We now use the Markov approximation to write $\hat{\sigma}^-(\tau) \approx \hat{\sigma}^-(t) e^{-i(\omega_q)(\tau-t)}$, and thus

$$\begin{aligned} \frac{\partial}{\partial t} \hat{\sigma}^- &= -i\omega_q \hat{\sigma}^- - i \sum_k f_k e^{-i\omega_k(t-t_0)} \hat{a}_k(t_0) \\ &\quad - \sum_k f_k^2 \left(\int_{t_0}^t e^{-i(\omega_k - \omega_q)(t-\tau)} d\tau \right) \hat{\sigma}^-(t). \end{aligned} \quad (\text{D.30})$$

Considering the generic equation of motion for a linearly decaying qubit, $(\partial/\partial t)\hat{\sigma}^- = -i\omega_q \hat{\sigma}^- - (\gamma/2)\hat{\sigma}^-$, we can identify real part of the last term in the equation above as the decay rate due to radiation of the qubit into the waveguide. We can extend the integral's bound to approximately evaluate this term as $\gamma \approx 2\pi \sum_k f_k^2 \delta(\omega_k - \omega_q)$.

Band	Frequency (GHz)	$g/2\pi$ (MHz)	$Q_e (\times 10^3)$	$Q_i (\times 10^3)$
Lower	4.2131	15.3	49.47	74.99
Lower	4.6012	19.74	35.09	76.25
Lower	4.7395	18.14	43.58	75
Lower	4.8044	16.53	94.17	75.59
Lower	4.8373	14.03	152.06	73.77
Lower	4.856	9.73	455.8	76.47
Lower	4.8654	4.48	2100	72
Upper	6.6768	39.44	15.74	68.06
Upper	7.309	58.06	12.02	70.44

Table D.1: Measured resonance parameters for metamaterial waveguide. The values are measured for the waveguide of Figs. 5.2-5.4. The resonances are measured in reflection from the input 50- Ω CPW port. The qubit-resonance coupling, g , is inferred from the anti-crossing observed as the qubit is tuned through each waveguide resonance.

Assuming the coupling rate f_k is a smooth function of the k -vector, we can evaluate this some in the continuum limit as

$$\begin{aligned} \gamma &= 2\pi \sum_k f_k^2 \delta(\omega_k - \omega_q) \approx Md \int dk f_k^2 \delta(\omega_k - \omega_q) \\ &= L \int d\omega \left(\frac{\partial k}{\partial \omega} \right) f_k^2 \delta(\omega_k - \omega_q) = \frac{L}{c} f(\omega_q)^2 n_g(\omega_q). \end{aligned}$$

It is evident that reducing the group velocity increases the radiation decay rate of the qubit. A similar analysis can be applied to find the decay rate of a linear cavity with resonance frequency of ω_0 (i.e. a harmonic oscillator) that has been coupled to the waveguide with coupling constant $g(\omega)$. In this case we find

$$\gamma = \frac{L}{c} g(\omega_0)^2 n_g(\omega_0), \quad Q_e = \omega_0/\gamma = \frac{\omega_0 c}{L} \frac{1}{g(\omega_0)^2 n_g(\omega_0)}.$$

D.2 Characterization and modeling of the metamaterial waveguide

Several competing effects in the design of the metamaterial waveguide influence its utility within a waveguide QED setting. We desire a compact waveguide unit cell to reduce the required real estate in a chip-scale platform. This should be combined with a large bandgap to provide more spectral bandwidth and tighter localization of photon bound states. We also require efficient qubit-waveguide coupling. These attributes allow for denser integration of qubits both in space and frequency, enabling larger-scale and more complex quantum circuits. They can be obtained in a single metamaterial design provided both the resonator elements and the waveguide sections are of high impedance, and that the waveguide section has

large inductance. The logic for this is as follows. The bandgap of the metamaterial waveguide scales roughly with the product of the coupling capacitance, the zero-point voltage of the resonator, and the zero-point voltage of the waveguide section, $\Delta \propto C_k V_{\text{zpf}}^{\text{CPW}} V_{\text{zpf}}^{\text{res}}$. The zero-point voltage fluctuations scale with the impedance. Additionally, a large bandgap requires that the inductance of the waveguide section be large so that the resonant frequency of the bare waveguide section at the X -point ($kd = \pi/a$) is not too far detuned from that of the bare resonators, $\Omega_{k=\pi/da} = (L_0 C_0')^{-1/2} \sim \omega_r$.

We obtain a large resonator impedance by using spiral inductors made from narrow cross-section wires of long coil length, with the impedance of the resonator roughly scaling as the inverse of the square root of the coil width (w), $Z_{\text{res}} \sim 1/\sqrt{w}$. The impedance of the CPW line can be set by adjusting the ratio of the center conductor width to the physical gap between center conductor and the ground plane (smaller ratio yields higher impedance). In order to also realize a large inductance at the same time, without dramatically increasing the length of the waveguide section, we meander the center conductor of the waveguide section to give it more effective path length and larger inductance. In the devices presented in this work the period of the metamaterial waveguide is $350 \mu\text{m}$, with the length of the waveguide section corresponding to $210 \mu\text{m}$ of this length. The wire width of the CPW center conductor (resonator coil) was chosen conservatively to be $5 \mu\text{m}$ ($1 \mu\text{m}$) to limit the potential disorder arising from fluctuations in the kinetic inductance due to wire width inhomogeneity.

Estimates of the resulting lumped element parameters obtained from fits to the measured transmission data of the fabricated metamaterial waveguide in Fig. 5.1 are: $C_r = 345 \text{ fF}$, $L_r = 1.43 \text{ nH}$, $C_g = 389 \text{ fF}$, $C_0 = 50.5 \text{ fF}$, $L_0 = 0.7885 \text{ nH}$. These values are very close to the design values. From the measured widths of the waveguide resonances in the transmission bands, we find a good fit to the loss in the waveguide by assuming a resistance $R_r = 8 \times 10^{-4} \Omega$ in series with L_r and a resistance $R_0 = 4 \times 10^{-4} \Omega$ in series with L_0 . For the metamaterial waveguide coupled to the qubit of Figs. 5.2-5.4 we used a slightly different design, with estimated lumped-element parameters equal to: $C_r = 240 \text{ fF}$, $L_r = 2.10 \text{ nH}$, $R_r = 1.1 \times 10^{-3} \Omega$, $C_g = 252 \text{ fF}$, $C_0 = 52.0 \text{ fF}$, $L_0 = 1.19 \text{ nH}$, $R_0 = 6 \times 10^{-4} \Omega$. Here, the fit parameters were inferred from the frequencies and linewidths of the lower and upper band resonances (within the 4-8 GHz circulator bandwidth of our set-up), measured in reflection from the input $50\text{-}\Omega$ CPW port. The read-out of the

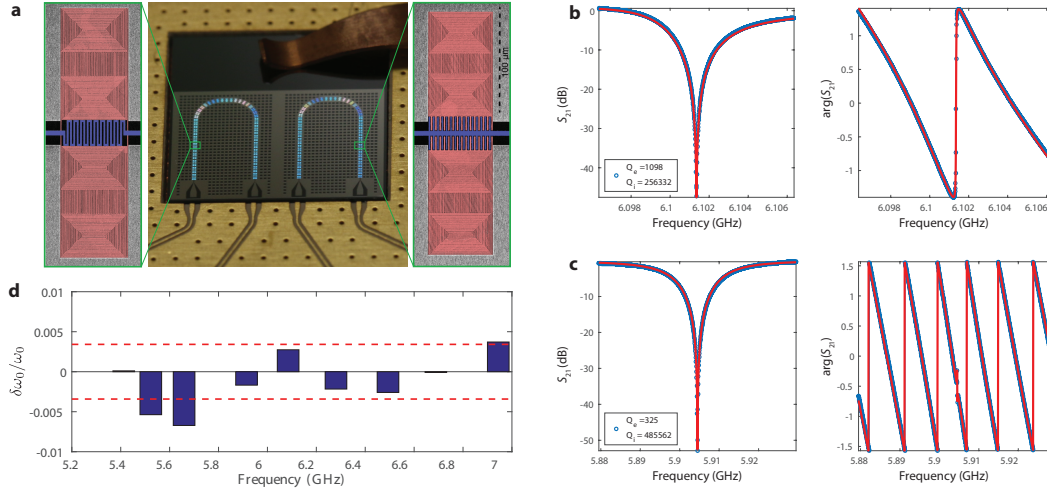


Figure D.2: Characterization of lumped element resonators **a**, Optical and scanning electron micrographs of microwave resonator array chip. Middle: optical image of the chip with two arrays of coupled resonators on a 1×1 cm silicon chip. Left and Right: SEM image (false-color) of the fabricated inductively (left) and capacitively (right) coupled microwave resonator pairs. The resonator region is colored red and the waveguide central conductor is colored blue. **b-c**, Amplitude and phase response of two capacitively-coupled microwave resonator pairs measured at the fridge temperature $T_f \approx 7$ mK. The legends show the intrinsic ($Q_i = \omega_0/\gamma_i$) and extrinsic ($Q_e = \omega_0/\gamma_e$) quality factors extracted from a Fano line shape fit. **d**, Difference between the measured and the expected design value of the resonance frequencies for 9 resonators with similar geometries and wire widths of 500 nm. The dashed lines mark the standard deviation of the frequency difference, which is equivalent to a normalized value of $\sigma = 0.3\%$.

qubit state has been performed using one of the two upper band modes ($f = 6.67$ GHz, and $f = 7.3$ GHz), depending on the frequency of the qubit at each flux bias point. The measured resonance parameters, along with their coupling (g) to the qubit, are tabulated in Table D.1. The qubit-to-waveguide coupling was designed and simulated to be given by a coupling capacitance of $C_g = 4.8$ fF. In all our circuit model fits this coupling capacitance was fixed at the design value, and not needed as a fitting parameter.

D.3 Characterization of lumped-element microwave resonators

We have achieved a characteristic size of $\lambda_0/150$ ($130 \mu\text{m} \times 76 \mu\text{m}$ for $\omega_0/2\pi \approx 6$ GHz) and $\lambda_0/76$ ($155 \mu\text{m} \times 92 \mu\text{m}$ for $\omega_0/2\pi \approx 10$ GHz), using a wire width of 500 nm and $1 \mu\text{m}$, respectively.

Figure D.2 shows the typical amplitude and phase of measured for a waveguide coupled to a pair of identical resonators. Microwave spectroscopy of the fabricated resonators is performed in a dilution refrigerator cooled-down to a temperature of

$T_f \approx 7$ mK. The input microwave is launched onto the chip via a 50- Ω CPW. The output microwave signal is subsequently amplified and analyzed using a network analyzer (for more details regarding the measurement setup, refer to Ref. [345]). We have extracted the intrinsic and extrinsic decay rates of the cavity by fitting the transmission data to a Fano line shape of the form

$$S_{21}(\omega) = 1 - \frac{\gamma_e e^{i\phi_0}}{\gamma_i + \gamma_e + 2i(\omega - \omega_0)}. \quad (\text{D.31})$$

Here γ_e and γ_i are the extrinsic and intrinsic decay rates of the resonator, respectively. The phase ϕ_0 is a parameter that sets the asymmetry of the Fano line shape [346]. The data demonstrates that it is possible to adjust the external coupling to the resonator in a wide range without much degradation in the internal quality factor (it is straightforward to convert the extrinsic quality factor Q_e to the coupling constants g_k used in our theoretical analysis above). We have compared the measured resonance frequency with the resonance frequency found from numerical simulations in Fig. D.2d. We find that the measured resonance frequencies are in agreement with the simulated values, with a multiplicative scaling factor of 0.85. Using this scale factor, we have measured a random variation 0.3% in the resonance frequency. It has been previously suggested that the shift in the resonance frequency and its statistical variation can be attributed to the kinetic inductance of the free charge carriers in the superconductor, and the variations can be mitigated by increasing the wire width [228].

D.4 Disorder and Anderson localization

Propagation of electron waves in a one dimensional quasi-periodic potential is described by

$$\left[-\frac{\partial^2}{\partial x^2} + \sum_n (U + U_n) \delta(x - an) \right] \psi_q(x) = q^2 \psi_q(x). \quad (\text{D.32})$$

Here, q is the quasi momentum and U_n is the random variable that models compositional disorder at position $x = na$. Disorder leads to localization of waves with a characteristic length defined as

$$\ell^{-1} = \lim_{N \rightarrow \infty} \left\langle \frac{1}{N} \sum_{n=0}^{N-1} \ln \left| \frac{\psi_{n+1}}{\psi_n} \right| \right\rangle. \quad (\text{D.33})$$

Here, the brackets represent averaging over different realization of the disorder, whereas the summation accounts for spatial/temporal averaging for traveling waves.

For this model, previous authors have found the localization length to be [225, 347, 348]

$$\frac{\ell}{d} = \frac{2\Gamma(1/6)}{6^{1/3}\sqrt{\pi}}\sigma^{-2/3} \approx 3.45\sigma^{-2/3}. \quad (\text{D.34})$$

In this model $\sigma^2 = \langle U_n^2 \rangle \sin^2(q_0 a)/q_0^2$ is a parameter that quantifies the strength of disorder, and q_0 is the value of quasi-momentum at the band-edge.

Now, we consider the propagation of current waves in a one dimensional waveguide that has been periodically loaded with resonators (a similar analysis can be applied to the voltage waves for the case of inductively coupled resonators). Starting from Eq. (D.19), it is straightforward to find

$$\frac{\partial^2 I(x)}{\partial x^2} + I(x) \left(\frac{\omega}{c}\right)^2 n^2 \left[1 + \sum_n \frac{d\Delta \delta(x - an)}{\omega_{0,n} - \omega + i\gamma_i} \right] = 0. \quad (\text{D.35})$$

By comparing this equation with the Schrodinger equation for the Kronig-Penny model Eq. (D.32) we find

$$q^2 \rightarrow \left(\frac{\omega}{c}\right)^2 n^2, \quad U + U_n \rightarrow -\left(\frac{\omega}{c}\right)^2 n^2 \left[\frac{d\Delta}{\omega_{0,n} - \omega + i\gamma_i} \right]. \quad (\text{D.36})$$

For small variation in resonance frequencies, $\delta\omega_0$, we can expand the resonance potential term to find

$$U_n = -\left(\frac{\omega_0}{c}\right)^2 n^2 \frac{\partial}{\partial \omega_{0,n}} \left(\frac{d\Delta}{\omega_{0,n} - \omega + i\gamma_i} \right) \delta\omega_0 \quad (\text{D.37})$$

By evaluating the expression for U_n and substituting it in the relation above for σ^2 , we find

$$\sigma_{\text{low}}^2 = \left(\frac{\gamma_e}{\gamma_i}\right)^4 \left(\frac{\delta\omega_0}{\Delta}\right)^2, \quad \sigma_{\text{high}}^2 = \left(\frac{\gamma_e}{\Delta}\right)^4 \left(\frac{\delta\omega_0}{\Delta}\right)^2. \quad (\text{D.38})$$

The analysis above gives us ℓ_{dis} . In addition to disorder, absorption loss in the meta-material waveguide components (specifically the resonators) leads to an exponential extinction of the wave's amplitude. An effective localization length incorporating absorption loss, ℓ_{loss} , can be found by solving for the complex band structure and setting $\ell_{\text{loss}} = 1/\text{Im}(k)$. For propagation of a classical wave through the waveguide both loss and disorder contribute to exponential extinction of the wave with a total localization length of

$$\frac{1}{\ell_{\text{total}}} = \frac{1}{\ell_{\text{dis}}} + \frac{1}{\ell_{\text{loss}}}. \quad (\text{D.39})$$

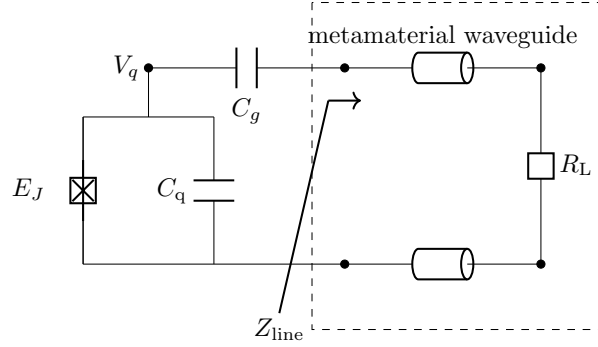


Figure D.3: Circuit diagram for a transmon qubit coupled to a metamaterial waveguide. The resistive termination is used to model radiation into the 50Ω coplanar waveguide.

Two important points should be made here. First, ℓ_{loss} as defined is purely an absorption loss effect only outside any photonic bandgap region. Inside a photonic bandgap the periodic loading of the waveguide gives rise to an imaginary k -vector as well. As such, ℓ_{loss} inside the gap will contain both periodic loading effects and absorption loss effects. Second, the exponential localization of the photonic wavefunction caused by the periodic loading of the waveguide and the localization caused by structural disorder are coherent (unitary) effects. On the contrary, the exponential attenuation of a traveling wavepacket due to the loss in the resonators is a dissipative effect. When considering photon-mediated interactions between qubits, these two effects for the most part need to be addressed separately. In this context, the value of ℓ_{total} as a single parameter is limited to primarily estimating the spatial extent over which strong coherent interactions can be obtained.

D.5 Qubit frequency shift and lifetime

Circuit theory modeling

The qubit frequency shift can be derived from circuit theory by modeling the qubit as a linear resonator. Consider the circuit diagram in Fig. D.3. The load impedance seen from the qubit port can be written as

$$Z_L(\omega) = \frac{1}{i\omega C_g} + Z_{\text{line}}(\omega), \quad (\text{D.40})$$

and

$$Y_L(\omega) = \frac{i\omega C_g}{1 + Z_{\text{line}}(\omega)i\omega C_g}. \quad (\text{D.41})$$

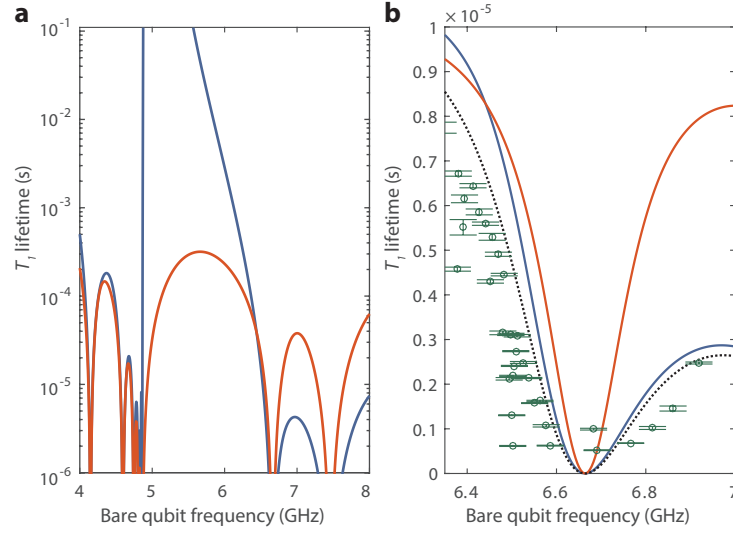


Figure D.4: Qubit lifetime as a function of resonance frequency. **a**, Simulated qubit lifetime set by radiation into the output CPW port (blue), and structural loss in the waveguide (red). **b**, Comparison of the experimental results (open circles) with the simulated qubit lifetime (solid and dashed lines) near the first resonance dip in the upper transmission band. The lifetime set by radiation into the output port and structural loss in the waveguide are shown as blue and red solid lines, respectively. Both of these contributions have been adjusted to include a frequency independent intrinsic qubit life time of $10.86 \mu\text{s}$. The black dashed line shows the theoretical qubit excited state lifetime including all contributions.

For weak coupling, the decay rate can be found using the real part of the load impedance as

$$\kappa \approx \omega_q^2 L_J \text{Re} [Y_L(\omega_q)]. \quad (\text{D.42})$$

Here, ω_q is the resonance frequency of the qubit. Similarly, the shift in qubit frequency is found as

$$\Delta\omega_q \approx -\frac{\omega_q^2 L_J}{2} \text{Im} [Y_L(\omega_q)]. \quad (\text{D.43})$$

For a transmon qubit, we have the following relation that approximate its behavior in the linear regime

$$L_J = \frac{\left(\frac{\Phi_0}{2\pi}\right)^2}{E_J}, \quad \omega_q = \frac{1}{\sqrt{L_J C_q}}. \quad (\text{D.44})$$

We first use the simplified continuum model to find the input impedance Z_{line}

$$Z_{\text{line}}(\omega) = Z_B(\omega) \frac{R_L + Z_B(\omega) \tanh \{\text{Im}[k(\omega)]x\}}{Z_B(\omega) + R_L \tanh \{\text{Im}[k(\omega)]x\}}. \quad (\text{D.45})$$

Here, $\text{Im}[k(\omega)]$ is the attenuation constant (we are assuming $\text{Re}[k(\omega)] = 0$, i.e. valid when the value of ω is within the bandgap), $Z_B(\omega)$ is the Bloch impedance of the periodic structure, and x is the length of the waveguide. Assuming $\text{Im}[k(\omega)]x \gg 1$, this expression can be simplified as

$$\begin{aligned} Z_{\text{line}}(\omega) &\approx Z_B(\omega) + \frac{4R_L|Z_B(\omega)|^2}{R_L^2 + |Z_B(\omega)|^2} e^{-2\text{Im}[k(\omega)]x} \\ &\approx Z_B(\omega) + 4R_L e^{-2\text{Im}[k(\omega)]x}. \end{aligned} \quad (\text{D.46})$$

Note that we have assumed $R_L \ll |Z_B(\omega)|$ to make the last approximation. For weak coupling, the qubit coupling capacitance, C_g , should be chosen such that the magnitude of impedance $Z_g = 1/(i\omega C_g)$ is much larger than $|Z_{\text{line}}(\omega)|$. In this situation, we use Eq. (D.43) and Eq. (D.46) to find

$$\begin{aligned} \frac{\Delta\omega_q}{\omega_q} &= -\frac{1}{2}(L_J\omega_q)(C_g\omega_q) - \frac{1}{2}(L_J\omega_q)(C_g\omega_q)^2 \text{Im}[Z_B(\omega_q)] \\ &= -\frac{C_g}{2C_q} - \frac{C_g}{2C_q} \text{Im}[Z_B(\omega_q)] C_g\omega_q. \end{aligned} \quad (\text{D.47})$$

Note that the first term in the frequency shift is merely caused by addition of the coupling capacitor to the overall qubit capacitance.

We find the qubit's decay rate caused by radiation into the output port by substituting Eq. (D.46) in Eq. (D.42)

$$\kappa_{\text{rad}} = \frac{4\omega_q^2 C_g^2}{C_q} R_L e^{-2\text{Im}[k(\omega)]x}. \quad (\text{D.48})$$

Subsequently, the lifetime of the qubit can be written as

$$T_{1,\text{extrad}} = \frac{C_q}{4\omega_q^2 C_g^2 R_L} e^{2x/\ell(\omega_q)}, \quad (\text{D.49})$$

where $\ell(\omega) = 1/\text{Im}[k(\omega)]$ is the localization length in the bandgap. We note that the analysis from circuit theory is only valid for weak qubit-waveguide coupling rates, where the Markov approximation can be applied. In the strong coupling regime, the qubit frequency and lifetime can be found by numerically finding the zeros of the circuit's admittance function $Y(\omega) = Y_L(\omega) + Y_q(\omega)$, where $Y_q(\omega) = i\omega_q C_q + 1/(i\omega_q L_J)$.

Effect of structural loss in the waveguide on the qubit lifetime

Equation (D.48) gives the decay rate of qubit's excited state caused by radiation into the output CPW port. In addition to this radiative component, the loss in the

waveguide also contributes to the decay rate of the qubit excited state. The effect of loss in the waveguide can be modeled as the (incoherent) sum of contributions to the decay rate from the individual resonances in the transmission bands of the waveguide:

$$\kappa_{\text{loss}} = \sum_m \frac{g_m^2 \kappa_{i,m}}{2g_m^2 + |\kappa_{i,m} - i(\omega_q - \omega_{0,m})|^2}. \quad (\text{D.50})$$

Here, m denotes the index of each waveguide resonance, g_m is the coupling rate of the qubit to the waveguide resonance, and $\kappa_{i,m}$ is the intrinsic decay rate for each waveguide resonance. The parameters ω_q and $\omega_{0,m}$ denote the fundamental transition frequency of the qubit and the resonance frequency of the waveguide mode, respectively. For a finite waveguide made from 9 unit cells we expect a total of 18 resonances, with half of them distributed in the lower frequency transmission band and half of them distributed in the upper transmission band. Table D.1 presents the measured $\omega_{0,m}$, $Q_{i,m} = \omega_{0,m}/\kappa_{i,m}$, and g_m parameters for the 9 resonances closest to the waveguide bandgap that are observable in the frequency band of the circulators used in our experiment. The total lifetime of the qubit excited state can be determined from $T_1 = 1/(\kappa_{\text{rad}} + \kappa_{\text{loss}} + \kappa_i)$, where κ_i represents a third decay channel for the qubit corresponding to coupling to all other degrees of freedom (two-level systems, etc.). From a fit to the measured qubit T_1 data deep in the bandgap we find an intrinsic lifetime of $\kappa_i^{-1} = 10.86 \mu\text{s}$.

To identify regions of frequency space where the qubit lifetime is limited by output port radiation, and therefore may tell us about the finite extent of the photon wavepacket coupled to the qubit, we plot in Fig. D.4a the estimated loss and output radiation contributions to the qubit lifetime as a function of frequency in and around the waveguide bandgap for our experiment. It is evident the internal waveguide loss contribution is the dominant factor deep in the band gap and near the lower transmission band-edge, where the localization length of the photon wavepacket coupled to the qubit is much smaller than the finite length of the waveguide. On the contrary, the radiation into the output CPW port is the dominant factor near the upper band-edge frequency in the band gap and inside the upper transmission band, where the localization length becomes comparable and larger than the finite length of the waveguide. A zoomed-in plot around the upper band-edge frequency of the measured qubit excited state lifetime along with the different estimated components of the qubit decay are shown in Fig. D.4b. The asymmetric profile of the measured lifetime near the first resonance in the upper transmission band is a clear sign of

the radiation into the output port, where the shorter lifetime for frequencies above the resonance frequency can be attributed to coherent (constructive) interference from multiple waveguide resonances. These subtle features help differentiate single mode and incoherent multi-mode cavity-QED effects, from true waveguide-QED effects in which multi-mode interference leads to radiative dynamics governed by a localized photon wavepacket.

D.6 Group delay and the qubit lifetime profile

Equation (D.49) demonstrates the relation between the qubit lifetime and the localization length. Moving the qubit frequency beyond the gap, results in a drastic increase in the localization length and subsequently reduces the qubit lifetime. The normalized slope of the lifetime profile in the vicinity of the band-edge can be written as

$$\left| \frac{1}{T_{1,\text{rad}}} \frac{\partial T_{1,\text{rad}}}{\partial \omega} \right| = \left| x \frac{\partial \text{Im}(k)}{\partial \omega} \right| = |x \text{Im}(n_g)/c|. \quad (\text{D.51})$$

We now evaluate Eq. (D.25) to find the group index at the upper and lower band-edges $\delta_{\pm} = 0$

$$|\text{Re}(n_g)| = |\text{Im}(n_g)| = \begin{cases} n\omega_{c-} \sqrt{\frac{\Delta}{8\gamma_i^3}} & \text{for } \omega = \omega_{c-}, \\ n\omega_{c+} \frac{1}{\sqrt{8\Delta\gamma_i}} & \text{for } \omega = \omega_{c+}. \end{cases} \quad (\text{D.52})$$

Consequently, we can write the normalized slope of the lifetime profile at the band-edge as

$$\left(\frac{1}{T_{1,\text{rad}}} \left| \frac{\partial T_{1,\text{rad}}}{\partial \omega} \right| \right) \Bigg|_{\omega=\omega_{c\pm}} = |x \text{Im}[n_g(\omega_{c\pm})]/c| = |x \text{Re}[n_g(\omega_{c\pm})]/c| = \tau_{\text{delay}}. \quad (\text{D.53})$$

This result has a simple description: the normalized slope of the lifetime profile at the band-edge is equal to the (maximum) group delay.

D.7 Scaling the waveguide length

Scaling the length of the waveguide to the extreme limits requires dealing with a number of technical challenges. Below, we outline a number of these challenges and possible strategies for addressing them. A systematic study of these challenges and efficient strategies for overcoming them will be the subject of a future study.

Resonator size: The size of lumped-element resonators is ultimately limited by the fabrication considerations for thin-film aluminum nano-wires. A pitch size of

60 nm can be achieved in these structures by using electron beam lithography for patterning the wires [349]. Assuming a quarter-wave resonator geometry, and a wire-to-airgap ratio of unity, we find the characteristic size for the resonator as $d = \sqrt{(60 \text{ nm} \times \lambda/4)}$. Using $\lambda = 2 \text{ cm}$ for a 6 GHz resonator (on Si substrate), we have $d = \lambda/1100$. An alternative strategy for miniaturizing the resonators is to use kinetic inductance of disordered superconductors [350].

We emphasize that using smaller resonators requires a careful study of disorder in the resonance frequency, and possible strategies for reducing it.

Bandgap size: The lumped-element nature of the components in our device allows for achieving a larger bandgap-to-midgap ratio by simply increasing the coupling capacitor, C_g , and reducing the internal capacitance, C_r . Ultimately, however, the gap size will be limited by the minimum value of C_r which is itself set by the parasitic capacitance of the inductor in the resonator (L_r). Considering the numerical values of these quantities listed in the Sec. D.2, we anticipate that a two-fold increase in the bandgap-to-midgap is feasible.

Parasitic modes: The placement of the qubit with respect to the metamaterial waveguide in our device relies on the symmetry of the waveguide modes to eliminate coupling to the parasitic modes of the structure. Alternatively, Aluminum air bridges can be implemented in the coplanar waveguide (CPW) sections of our device in order to suppress the slot-line modes of the waveguide. Suppressing the slot-line modes allows for realizing a more flexible geometry where multiple qubits can be capacitively coupled to resonators along the waveguide.

Making turns with the metamaterial waveguide: Effective use of chip's area requires the ability to make $90^\circ/180^\circ$ turns along the path for long waveguides. In our device, turns can be implemented by modifying the CPW sections between the cavities. To this end, the meandered coplanar waveguide between the cavities can be unwrapped to realize turns with a radius of curvature $50\text{--}200 \mu\text{m}$. The resulting asymmetry and local frequency shift caused by the bend can be compensated by numerical modeling of these effects and making proper adjustments to the neighboring resonators.

Appendix E

SUPPLEMENTARY INFORMATION FOR CHAPTER 6

E.1 Modeling of the topological waveguide

In this section we provide a theoretical description of the topological waveguide discussed in Chapter 6, an analog to the Su-Schrieffer-Heeger model [245]. An approximate form of the physically realized waveguide is given by an array of coupled LC resonators, a unit cell of which is illustrated in Fig. E.1. Each unit cell of the topological waveguide has two sites A and B whose intra- and inter-cell coupling capacitance (mutual inductance) are given by C_v (M_v) and C_w (M_w). We denote the flux variable of each node as $\Phi_n^\alpha(t) \equiv \int_{-\infty}^t dt' V_n^\alpha(t')$ and the current going through each inductor as i_n^α ($\alpha = \{A, B\}$). The Lagrangian in position space reads

$$\mathcal{L} = \sum_n \left\{ \frac{C_v}{2} (\dot{\Phi}_n^B - \dot{\Phi}_n^A)^2 + \frac{C_w}{2} (\dot{\Phi}_{n+1}^A - \dot{\Phi}_n^B)^2 + \frac{C_0}{2} \left[(\dot{\Phi}_n^A)^2 + (\dot{\Phi}_n^B)^2 \right] - \frac{L_0}{2} \left[(i_n^A)^2 + (i_n^B)^2 \right] - M_v i_n^A i_n^B - M_w i_n^B i_{n+1}^A \right\}. \quad (\text{E.1})$$

The node flux variables are written in terms of current through the inductors as

$$\Phi_n^A = L_0 i_n^A + M_v i_n^B + M_w i_{n-1}^B, \quad \Phi_n^B = L_0 i_n^B + M_v i_n^A + M_w i_{n+1}^A. \quad (\text{E.2})$$

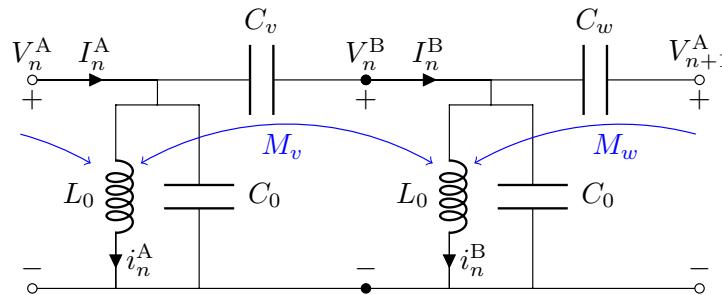


Figure E.1: Modeling of the topological waveguide. LC resonators of inductance L_0 and capacitance C_0 are coupled with alternating coupling capacitance C_v , C_w and mutual inductance M_v , M_w . The voltage and current at each resonator node A (B) are denoted as V_n^A , I_n^A (V_n^B , I_n^B).

Considering the discrete translational symmetry in our system, we can rewrite the variables in terms of Fourier components as

$$\Phi_n^\alpha = \frac{1}{\sqrt{N}} \sum_k e^{inkd} \Phi_k^\alpha, \quad i_n^\alpha = \frac{1}{\sqrt{N}} \sum_k e^{inkd} i_k^\alpha, \quad (\text{E.3})$$

where $\alpha = \text{A, B}$, N is the number of unit cells, and $k = \frac{2\pi m}{Nd}$ ($m = -N/2, \dots, N/2-1$) are points in the first Brillouin zone. Equation (E.2) is written as

$$\sum_{k'} e^{ink'd} \Phi_{k'}^\text{A} = \sum_{k'} e^{ink'd} \left(L_0 i_{k'}^\text{A} + M_v i_{k'}^\text{B} + e^{-ik'd} M_w i_{k'}^\text{B} \right)$$

under this transform. Multiplying the above equation with e^{-inkd} and summing over all n , we get a linear relation between Φ_k^α and i_k^α :

$$\begin{pmatrix} \Phi_k^\text{A} \\ \Phi_k^\text{B} \end{pmatrix} = \begin{pmatrix} L_0 & M_v + M_w e^{-ikd} \\ M_v + M_w e^{ikd} & L_0 \end{pmatrix} \begin{pmatrix} i_k^\text{A} \\ i_k^\text{B} \end{pmatrix}.$$

By calculating the inverse of this relation, the Lagrangian of the system (E.1) can be rewritten in k -space as

$$\begin{aligned} \mathcal{L} = \sum_k \left[\frac{C_0 + C_v + C_w}{2} \left(\dot{\Phi}_{-k}^\text{A} \dot{\Phi}_k^\text{A} + \dot{\Phi}_{-k}^\text{B} \dot{\Phi}_k^\text{B} \right) - C_g(k) \dot{\Phi}_{-k}^\text{A} \dot{\Phi}_k^\text{B} \right. \\ \left. - \frac{\frac{L_0}{2} (\Phi_{-k}^\text{A} \Phi_k^\text{A} + \Phi_{-k}^\text{B} \Phi_k^\text{B}) - M_g(k) \Phi_{-k}^\text{A} \Phi_k^\text{B}}{L_0^2 - M_g(-k)M_g(k)} \right] \end{aligned} \quad (\text{E.4})$$

where $C_g(k) \equiv C_v + C_w e^{-ikd}$ and $M_g(k) \equiv M_v + M_w e^{-ikd}$. The node charge variables $Q_k^\alpha \equiv \partial \mathcal{L} / \partial \dot{\Phi}_k^\alpha$ canonically conjugate to node flux Φ_k^α are

$$\begin{pmatrix} Q_k^\text{A} \\ Q_k^\text{B} \end{pmatrix} = \begin{pmatrix} C_0 + C_v + C_w & -C_g(-k) \\ -C_g(k) & C_0 + C_v + C_w \end{pmatrix} \begin{pmatrix} \dot{\Phi}_{-k}^\text{A} \\ \dot{\Phi}_{-k}^\text{B} \end{pmatrix}.$$

Note that due to the Fourier transform implemented on flux variables, the canonical charge in momentum space is related to that in real space by

$$Q_n^\alpha = \frac{\partial \mathcal{L}}{\partial \dot{\Phi}_n^\alpha} = \sum_k \frac{\partial \mathcal{L}}{\partial \dot{\Phi}_k^\alpha} \frac{\partial \dot{\Phi}_k^\alpha}{\partial \dot{\Phi}_n^\alpha} = \frac{1}{\sqrt{N}} \sum_k e^{-inkd} Q_k^\alpha,$$

which is in the opposite sense of regular Fourier transform in Eq. (E.3). Also, due to the Fourier-transform properties, the constraint that Φ_n^α and Q_n^α are real reduces to $(\Phi_k^\alpha)^* = \Phi_{-k}^\alpha$ and $(Q_k^\alpha)^* = Q_{-k}^\alpha$. Applying the Legendre transformation

$H = \sum_{k,\alpha} Q_k^\alpha \dot{\Phi}_k^\alpha - \mathcal{L}$, the Hamiltonian takes the form

$$H = \sum_k \left[\frac{C_\Sigma(Q_{-k}^A Q_k^A + Q_{-k}^B Q_k^B) + C_g(-k)Q_{-k}^A Q_k^B + C_g(k)Q_{-k}^B Q_k^A}{2C_d^2(k)} + \frac{L_0(\Phi_{-k}^A \Phi_k^A + \Phi_{-k}^B \Phi_k^B) - M_g(k)\Phi_{-k}^A \Phi_k^B - M_g(-k)\Phi_{-k}^B \Phi_k^A}{2L_d^2(k)} \right],$$

where

$$C_\Sigma \equiv C_0 + C_v + C_w, \quad C_d^2(k) \equiv C_\Sigma^2 - C_g(-k)C_g(k), \quad L_d^2(k) \equiv L_0^2 - M_g(-k)M_g(k).$$

Note that $C_d^2(k)$ and $L_d^2(k)$ are real and even function in k . We impose the canonical commutation relation between real-space conjugate variables $[\hat{\Phi}_n^\alpha, \hat{Q}_{n'}^\beta] = i\hbar\delta_{\alpha,\beta}\delta_{n,n'}$ to promote the flux and charge variables to quantum operators. This reduces to $[\hat{\Phi}_k^\alpha, \hat{Q}_{k'}^\beta] = i\hbar\delta_{\alpha,\beta}\delta_{k,k'}$ in the momentum space [Note that due to the Fourier transform, $(\hat{\Phi}_k^\alpha)^\dagger = \hat{\Phi}_{-k}^\alpha$ and $(\hat{Q}_k^\alpha)^\dagger = \hat{Q}_{-k}^\alpha$, meaning flux and charge operators in momentum space are *non-Hermitian* since the Hermitian conjugate flips the sign of k]. The Hamiltonian can be written as a sum $\hat{H} = \hat{H}_0 + \hat{V}$, where the ‘‘uncoupled’’ part \hat{H}_0 and coupling terms \hat{V} are written as

$$\hat{H}_0 = \sum_{k,\alpha} \left[\frac{\hat{Q}_{-k}^\alpha \hat{Q}_k^\alpha}{2C_0^{\text{eff}}(k)} + \frac{\hat{\Phi}_{-k}^\alpha \hat{\Phi}_k^\alpha}{2L_0^{\text{eff}}(k)} \right], \quad \hat{V} = \sum_k \left[\frac{\hat{Q}_{-k}^A \hat{Q}_k^B}{2C_g^{\text{eff}}(k)} + \frac{\hat{\Phi}_{-k}^A \hat{\Phi}_k^B}{2L_g^{\text{eff}}(k)} + \text{H.c.} \right], \quad (\text{E.5})$$

with the effective self-capacitance $C_0^{\text{eff}}(k)$, self-inductance $L_0^{\text{eff}}(k)$, coupling capacitance $C_g^{\text{eff}}(k)$, and coupling inductance $L_g^{\text{eff}}(k)$ given by

$$C_0^{\text{eff}}(k) = \frac{C_d^2(k)}{C_\Sigma}, \quad L_0^{\text{eff}}(k) = \frac{L_d^2(k)}{L_0}, \quad C_g^{\text{eff}}(k) = \frac{C_d^2(k)}{C_g(-k)}, \quad L_g^{\text{eff}}(k) = -\frac{L_d^2(k)}{M_g(k)}. \quad (\text{E.6})$$

The diagonal part \hat{H}_0 of the Hamiltonian can be written in a second-quantized form by introducing annihilation operators \hat{a}_k and \hat{b}_k , which are operators of the Bloch waves on A and B sublattice, respectively:

$$\hat{a}_k \equiv \frac{1}{\sqrt{2\hbar}} \left[\frac{\hat{\Phi}_k^A}{\sqrt{Z_0^{\text{eff}}(k)}} + i\sqrt{Z_0^{\text{eff}}(k)}\hat{Q}_{-k}^A \right], \quad \hat{b}_k \equiv \frac{1}{\sqrt{2\hbar}} \left[\frac{\hat{\Phi}_k^B}{\sqrt{Z_0^{\text{eff}}(k)}} + i\sqrt{Z_0^{\text{eff}}(k)}\hat{Q}_{-k}^B \right].$$

Here, $Z_0^{\text{eff}}(k) \equiv \sqrt{L_0^{\text{eff}}(k)/C_0^{\text{eff}}(k)}$ is the effective impedance of the oscillator at wavevector k . Unlike the Fourier transform notation, for bosonic modes \hat{a}_k and \hat{b}_k , we use the notation $(\hat{a}_k)^\dagger \equiv \hat{a}_k^\dagger$ and $(\hat{b}_k)^\dagger \equiv \hat{b}_k^\dagger$. Under this definition, the

commutation relation is rewritten as $[\hat{a}_k, \hat{a}_{k'}^\dagger] = [\hat{b}_k, \hat{b}_{k'}^\dagger] = \delta_{k,k'}$. Note that the flux and charge operators are written in terms of mode operators as

$$\begin{aligned}\hat{\Phi}_k^A &= \sqrt{\frac{\hbar Z_0^{\text{eff}}(k)}{2}} (\hat{a}_k + \hat{a}_{-k}^\dagger), & \hat{Q}_k^A &= \frac{1}{i} \sqrt{\frac{\hbar}{2Z_0^{\text{eff}}(k)}} (\hat{a}_{-k} - \hat{a}_k^\dagger), \\ \hat{\Phi}_k^B &= \sqrt{\frac{\hbar Z_0^{\text{eff}}(k)}{2}} (\hat{b}_k + \hat{b}_{-k}^\dagger), & \hat{Q}_k^B &= \frac{1}{i} \sqrt{\frac{\hbar}{2Z_0^{\text{eff}}(k)}} (\hat{b}_{-k} - \hat{b}_k^\dagger).\end{aligned}$$

The uncoupled Hamiltonian is written as

$$\hat{H}_0 = \sum_k \frac{\hbar \omega_0(k)}{2} (\hat{a}_k^\dagger \hat{a}_k + \hat{a}_{-k} \hat{a}_{-k}^\dagger + \hat{b}_k^\dagger \hat{b}_k + \hat{b}_{-k} \hat{b}_{-k}^\dagger), \quad (\text{E.7})$$

where the ‘‘uncoupled’’ oscillator frequency is given by $\omega_0(k) \equiv [L_0^{\text{eff}}(k)C_0^{\text{eff}}(k)]^{-1/2}$, which ranges between values

$$\begin{aligned}\omega_0(k=0) &= \sqrt{\frac{L_0 C_\Sigma}{[L_0^2 - (M_v + M_w)^2][C_\Sigma^2 - (C_v + C_w)^2]}} \\ \omega_0\left(k = \frac{\pi}{d}\right) &= \sqrt{\frac{L_0 C_\Sigma}{(L_0^2 - |M_v - M_w|^2)(C_\Sigma^2 - |C_v - C_w|^2)}}.\end{aligned}$$

The coupling Hamiltonian \hat{V} is rewritten as

$$\begin{aligned}\hat{V} &= - \sum_k \left[\frac{\hbar g_C(k)}{2} (\hat{a}_{-k} \hat{b}_k - \hat{a}_{-k} \hat{b}_{-k}^\dagger - \hat{a}_k^\dagger \hat{b}_k + \hat{a}_k^\dagger \hat{b}_{-k}^\dagger) \right. \\ &\quad \left. + \frac{\hbar g_L(k)}{2} (\hat{a}_{-k} \hat{b}_k + \hat{a}_{-k} \hat{b}_{-k}^\dagger + \hat{a}_k^\dagger \hat{b}_k + \hat{a}_k^\dagger \hat{b}_{-k}^\dagger) + \text{H.c.} \right], \quad (\text{E.8})\end{aligned}$$

where the capacitive coupling $g_C(k)$ and inductive coupling $g_L(k)$ are simply written as

$$g_C(k) = \frac{\omega_0(k)C_g(k)}{2C_\Sigma}, \quad g_L(k) = \frac{\omega_0(k)M_g(k)}{2L_0}, \quad (\text{E.9})$$

respectively. Note that $g_C^*(k) = g_C(-k)$ and $g_L^*(k) = g_L(-k)$. In the following, we discuss the diagonalization of this Hamiltonian to explain the dispersion relation and band topology.

Band structure within the rotating-wave approximation

We first consider the band structure of the system within the rotating-wave approximation (RWA), where we discard the counter-rotating terms $\hat{a}\hat{b}$ and $\hat{a}^\dagger\hat{b}^\dagger$ in the

Hamiltonian. This assumption is known to be valid when the strength of the couplings $|g_L(k)|$, $|g_C(k)|$ are small compared to the uncoupled oscillator frequency $\omega_0(k)$. Under this approximation, the Hamiltonian in Eqs. (E.7)-(E.8) reduces to a simple form $\hat{H} = \hbar \sum_k (\hat{\mathbf{v}}_k)^\dagger \mathbf{h}(k) \hat{\mathbf{v}}_k$, where the single-particle kernel of the Hamiltonian is,

$$\mathbf{h}(k) = \begin{pmatrix} \omega_0(k) & f(k) \\ f^*(k) & \omega_0(k) \end{pmatrix}. \quad (\text{E.10})$$

Here, $\hat{\mathbf{v}}_k = (\hat{a}_k, \hat{b}_k)^T$ is the vector of annihilation operators at wavevector k and $f(k) \equiv g_C(k) - g_L(k)$. In this case, the Hamiltonian is diagonalized to the form

$$\hat{H} = \hbar \sum_k \left[\omega_+(k) \hat{a}_{+,k}^\dagger \hat{a}_{+,k} + \omega_-(k) \hat{a}_{-,k}^\dagger \hat{a}_{-,k} \right], \quad (\text{E.11})$$

where two bands $\omega_\pm(k) = \omega_0(k) \pm |f(k)|$ symmetric with respect to $\omega_0(k)$ at each wavevector k appear [here, note that $\hat{a}_{\pm,k}^\dagger \equiv (\hat{a}_{\pm,k})^\dagger$]. The supermodes $\hat{a}_{\pm,k}$ are written as $\hat{a}_{\pm,k} = [\pm e^{-i\phi(k)} \hat{a}_k + \hat{b}_k] / \sqrt{2}$, where $\phi(k) \equiv \arg f(k)$ is the phase of coupling term. The Bloch states in the single-excitation bands are written as

$$|\psi_{k,\pm}\rangle = \hat{a}_{\pm,k}^\dagger |0\rangle = \frac{1}{\sqrt{2}} \left(\pm e^{i\phi(k)} |1_k, 0_k\rangle + |0_k, 1_k\rangle \right),$$

where $|n_k, n'_k\rangle$ denotes a state with n (n') photons in mode \hat{a}_k (\hat{b}_k).

As discussed below in App. E.2, the kernel of the Hamiltonian in Eq. (E.10) has an inversion symmetry in the sublattice unit cell which is known to result in bands with quantized Zak phase [260]. In our system the Zak phase of the two bands are evaluated as

$$\mathcal{Z} = i \oint_{\text{B.Z.}} dk \frac{1}{\sqrt{2}} \begin{pmatrix} \pm e^{-i\phi(k)} & 1 \end{pmatrix} \frac{\partial}{\partial k} \left[\frac{1}{\sqrt{2}} \begin{pmatrix} \pm e^{i\phi(k)} \\ 1 \end{pmatrix} \right] = -\frac{1}{2} \oint_{\text{B.Z.}} dk \frac{\partial \phi(k)}{\partial k}.$$

The Zak phase of photonic bands is determined by the behavior of $f(k)$ in the complex plane. If the contour of $f(k)$ for k values in the first Brillouin zone excludes (encloses) the origin, the Zak phase is given by $\mathcal{Z} = 0$ ($\mathcal{Z} = \pi$) corresponding to the trivial (topological) phase.

Band structure beyond the rotating-wave approximation

Considering all the terms in the Hamiltonian in Eqs. (E.7)-(E.8), the Hamiltonian can be written in a compact form $\hat{H} = \frac{\hbar}{2} \sum_k (\hat{\mathbf{v}}_k)^\dagger \mathbb{h}(k) \hat{\mathbf{v}}_k$ with a vector composed

of mode operators $\hat{\mathbf{v}}_k = (\hat{a}_k, \hat{b}_k, \hat{a}_{-k}^\dagger, \hat{b}_{-k}^\dagger)^T$ and

$$\mathbb{h}(k) = \begin{pmatrix} \omega_0(k) & f(k) & 0 & g(k) \\ f^*(k) & \omega_0(k) & g^*(k) & 0 \\ 0 & g(k) & \omega_0(k) & f(k) \\ g^*(k) & 0 & f^*(k) & \omega_0(k) \end{pmatrix} = \omega_0(k) \begin{pmatrix} 1 & \frac{c_k - l_k}{2} & 0 & \frac{-c_k - l_k}{2} \\ \frac{c_k^* - l_k^*}{2} & 1 & \frac{-c_k^* - l_k^*}{2} & 0 \\ 0 & \frac{-c_k - l_k}{2} & 1 & \frac{c_k - l_k}{2} \\ \frac{-c_k^* - l_k^*}{2} & 0 & \frac{c_k^* - l_k^*}{2} & 1 \end{pmatrix}, \quad (\text{E.12})$$

where $f(k) \equiv g_C(k) - g_L(k)$ as before and $g(k) \equiv -g_C(k) - g_L(k)$. Here, $l_k \equiv M_g(k)/L_0$ and $c_k \equiv C_g(k)/C_\Sigma$ are inductive and capacitive coupling normalized to frequency. The dispersion relation can be found by diagonalizing the kernel of the Hamiltonian in Eq. (E.12) with the Bogoliubov transformation

$$\hat{\mathbf{w}}_k = \mathbf{S}_k \hat{\mathbf{v}}_k, \quad \mathbf{S}_k = \begin{pmatrix} \mathbf{U}_k & \mathbf{V}_{-k}^* \\ \mathbf{V}_k & \mathbf{U}_{-k}^* \end{pmatrix} \quad (\text{E.13})$$

where $\hat{\mathbf{w}}_k \equiv (\hat{a}_{+,k}, \hat{a}_{-,k}, \hat{a}_{+,-k}^\dagger, \hat{a}_{-,-k}^\dagger)^T$ is the vector composed of supermode operators and $\mathbf{U}_k, \mathbf{V}_k$ are 2×2 matrices forming blocks in the transformation \mathbf{S}_k . We want to find \mathbf{S}_k such that $(\hat{\mathbf{v}}_k)^\dagger \mathbb{h}(k) \hat{\mathbf{v}}_k = (\hat{\mathbf{w}}_k)^\dagger \tilde{\mathbb{h}}(k) \hat{\mathbf{w}}_k$, where $\tilde{\mathbb{h}}(k)$ is diagonal. To preserve the commutation relations, the matrix \mathbf{S}_k has to be symplectic, satisfying $\mathbf{J} = \mathbf{S}_k \mathbf{J} (\mathbf{S}_k)^\dagger$, with $\mathbf{J} = \text{diag}(1, 1, -1, -1)$. Due to this symplecticity, it can be shown that the matrices $\mathbf{J} \mathbb{h}(k)$ and $\mathbf{J} \tilde{\mathbb{h}}(k)$ are similar under transformation \mathbf{S}_k . Thus, finding the eigenvalues and eigenvectors of the coefficient matrix

$$\mathfrak{m}(k) \equiv \frac{\mathbf{J} \mathbb{h}(k)}{\omega_0(k)} = \begin{pmatrix} 1 & \frac{c_k - l_k}{2} & 0 & \frac{-c_k - l_k}{2} \\ \frac{c_k^* - l_k^*}{2} & 1 & \frac{-c_k^* - l_k^*}{2} & 0 \\ 0 & \frac{c_k + l_k}{2} & -1 & \frac{-c_k + l_k}{2} \\ \frac{c_k^* + l_k^*}{2} & 0 & \frac{-c_k^* + l_k^*}{2} & -1 \end{pmatrix} \quad (\text{E.14})$$

is sufficient to obtain the dispersion relation and supermodes of the system. The eigenvalues of matrix $\mathfrak{m}(k)$ are evaluated as

$$\pm \sqrt{1 - \frac{l_k c_k^* + l_k^* c_k}{2}} \pm \sqrt{\left(1 - \frac{l_k c_k^* + l_k^* c_k}{2}\right)^2 - (1 - |l_k|^2)(1 - |c_k|^2)}$$

and hence the dispersion relation of the system taking into account all terms in Hamiltonian (E.12) is

$$\tilde{\omega}_\pm(k) = \tilde{\omega}_0(k) \sqrt{1 \pm \sqrt{1 - \frac{[L_0^2 - M_g(-k)M_g(k)][C_\Sigma^2 - C_g(-k)C_g(k)]}{\{L_0 C_\Sigma - \frac{1}{2}[M_g(-k)C_g(k) + C_g(-k)M_g(k)]\}^2}}} \quad (\text{E.15})$$

where

$$\tilde{\omega}_0(k) \equiv \omega_0(k) \sqrt{1 - \frac{M_g(k)C_g(-k) + M_g(-k)C_g(k)}{2L_0C_\Sigma}}.$$

The two passbands range over frequencies $[\omega_+^{\min}, \omega_+^{\max}]$ and $[\omega_-^{\min}, \omega_-^{\max}]$, where the band-edge frequencies are written as

$$\omega_+^{\min} = \frac{1}{\sqrt{[L_0 + p_2(M_v - M_w)][C_\Sigma - p_2(C_v - C_w)]}}, \quad (\text{E.16a})$$

$$\omega_+^{\max} = \frac{1}{\sqrt{[L_0 + p_1(M_v + M_w)][C_\Sigma - p_1(C_v + C_w)]}}, \quad (\text{E.16b})$$

$$\omega_-^{\min} = \frac{1}{\sqrt{[L_0 - p_1(M_v + M_w)][C_\Sigma + p_1(C_v + C_w)]}}, \quad (\text{E.16c})$$

$$\omega_-^{\max} = \frac{1}{\sqrt{[L_0 - p_2(M_v - M_w)][C_\Sigma + p_2(C_v - C_w)]}}. \quad (\text{E.16d})$$

Here, $p_1 \equiv \text{sgn}[L_0(C_v + C_w) - C_\Sigma(M_v + M_w)]$ and $p_2 \equiv \text{sgn}[L_0(C_v - C_w) - C_\Sigma(M_v - M_w)]$ are sign factors. In principle, the eigenvectors of the matrix $\mathfrak{m}(k)$ in Eq. (E.14) can be analytically calculated to find the transformation \mathbf{S}_k of the original modes to supermodes $\hat{a}_{\pm,k}$. For the sake of brevity, we perform the calculation in the limit of vanishing mutual inductance ($M_v = M_w = 0$), where the matrix $\mathfrak{m}(k)$ reduces to

$$\mathfrak{m}_C(k) \equiv \begin{pmatrix} 1 & c_k/2 & 0 & -c_k/2 \\ c_k^*/2 & 1 & -c_k^*/2 & 0 \\ 0 & c_k/2 & -1 & -c_k/2 \\ c_k^*/2 & 0 & -c_k^*/2 & -1 \end{pmatrix}. \quad (\text{E.17})$$

In this case, the block matrices $\mathbf{U}_k, \mathbf{V}_k$ in the transformation in Eq. (E.13) are written as

$$\mathbf{U}_k = \frac{1}{2\sqrt{2}} \begin{pmatrix} e^{-i\phi(k)}x_{+,k} & x_{+,k} \\ -e^{-i\phi(k)}x_{-,k} & x_{-,k} \end{pmatrix}, \quad \mathbf{V}_k = \frac{1}{2\sqrt{2}} \begin{pmatrix} e^{-i\phi(k)}y_{+,k} & y_{+,k} \\ -e^{-i\phi(k)}y_{-,k} & y_{-,k} \end{pmatrix},$$

where $x_{\pm,k} = \sqrt[4]{1 \pm |c_k|} + \frac{1}{\sqrt[4]{1 \pm |c_k|}}$, $y_{\pm,k} = \sqrt[4]{1 \pm |c_k|} - \frac{1}{\sqrt[4]{1 \pm |c_k|}}$, and $\phi(k) = \arg c_k$.

Note that the constants are normalized by relation $x_{\pm,k}^2 - y_{\pm,k}^2 = 4$.

The knowledge of the transformation \mathbf{S}_k allows us to evaluate the Zak phase of photonic bands. In the Bogoliubov transformation, the Zak phase can be evaluated

as [351]

$$\begin{aligned}\mathcal{Z} &= i \oint_{\text{B.Z.}} dk \frac{1}{2\sqrt{2}} \begin{pmatrix} \pm e^{-i\phi(k)} x_{\pm,k} & x_{\pm,k} & \pm e^{-i\phi(k)} y_{\pm,k} & y_{\pm,k} \end{pmatrix} \cdot \mathbf{J} \cdot \frac{\partial}{\partial k} \left[\frac{1}{2\sqrt{2}} \begin{pmatrix} \pm e^{i\phi(k)} x_{\pm,k} \\ x_{\pm,k} \\ \pm e^{i\phi(k)} y_{\pm,k} \\ y_{\pm,k} \end{pmatrix} \right] \\ &= i \oint_{\text{B.Z.}} dk \frac{1}{8} \left[i \frac{\partial \phi(k)}{\partial k} (x_{\pm,k}^2 - y_{\pm,k}^2) + \frac{\partial}{\partial k} (x_{\pm,k}^2 - y_{\pm,k}^2) \right] = -\frac{1}{2} \oint_{\text{B.Z.}} dk \frac{\partial \phi(k)}{\partial k},\end{aligned}$$

identical to the expression within the RWA. Again, the Zak phase of photonic bands is determined by the winding of $f(k)$ around the origin in complex plane, leading to $\mathcal{Z} = 0$ in the trivial phase and $\mathcal{Z} = \pi$ in the topological phase.

Extraction of circuit parameters and the breakdown of the circuit model

As discussed in Fig. 6.1d, the parameters in the circuit model of the topological waveguide is found by fitting the waveguide transmission spectrum of the test structures. We find that two lowest-frequency modes inside the lower passband fail to be captured according to our model with capacitively and inductively coupled LC resonators. We believe that this is due to the broad range of frequencies (about 1.5 GHz) covered in the spectrum compared to the bare resonator frequency ~ 6.6 GHz and the distributed nature of the coupling, which can cause our simple model based on frequency-independent lumped elements (inductor, capacitor, and mutual inductance) to break down. Such deviation is also observed in the fitting of waveguide transmission data of Device I (Fig. E.7).

E.2 Mapping of the system to the SSH model and discussion on robustness of edge modes

Mapping of the topological waveguide to the SSH model

We discuss how the physical model of topological waveguide in App. E.1 could be mapped to the photonic SSH model, whose Hamiltonian is given as Eq. (6.1). Throughout this section, we consider the realistic circuit parameters extracted from fitting of test structures given in Fig. 6.1: resonator inductance and resonator capacitance, $L_0 = 1.9$ nH and $C_0 = 253$ fF, and coupling capacitance and parasitic mutual inductance, $(C_v, C_w) = (33, 17)$ fF and $(M_v, M_w) = (-38, -32)$ pH in the trivial phase (the values are interchanged in the topological phase).

To most directly and simply link the Hamiltonian described in Eqs. (E.7)-(E.8) to the SSH model, here we impose a few approximations. First, the counter-rotating terms in the Hamiltonian are discarded such that only photon-number-conserving terms

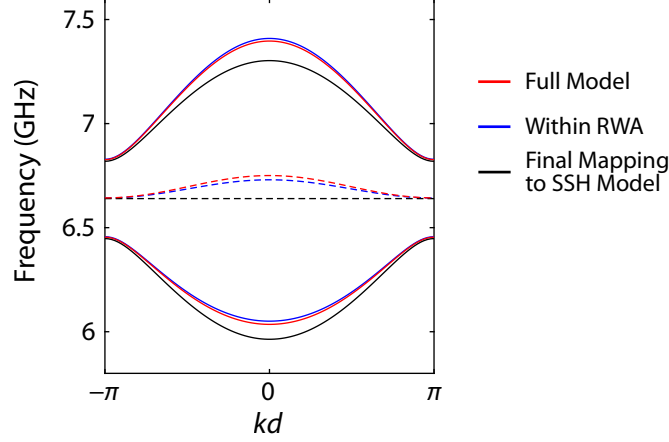


Figure E.2: Band structure of the realized topological waveguide under various assumptions discussed in App. E.2. The solid lines show the dispersion relation in the upper (lower) passband, $\omega_{\pm}(k)$: full model without any assumptions (red), model within RWA (blue), and the final mapping to SSH model (black) in the weak coupling limit. The dashed lines indicate the uncoupled resonator frequency $\omega_0(k)$ under corresponding assumptions.

are left. To achieve this, the RWA is applied to reduce the kernel of the Hamiltonian into one involving a 2×2 matrix as in Eq. (E.10). Such an assumption is known to be valid when the coupling terms in the Hamiltonian are much smaller than the frequency scale of the uncoupled Hamiltonian \hat{H}_0 [352]. According to the coupling terms derived in Eq. (E.9), this is a valid approximation given that

$$\left| \frac{g_C(k)}{\omega_0(k)} \right| \leq \frac{|C_v + C_w|}{2C_\Sigma} \approx 0.083, \quad \left| \frac{g_L(k)}{\omega_0(k)} \right| \leq \frac{|M_v| + |M_w|}{2L_0} \approx 0.018.$$

and the RWA affects the dispersion relation by less than 0.3 % in frequency.

Also different than in the original SSH Hamiltonian, are the k -dependent diagonal elements $\omega_0(k)$ of the single-particle kernel of the Hamiltonian for the circuit model. This k -dependence can be understood as arising from the coupling between resonators beyond nearest-neighbor pairs, which is inherent in the canonical quantization of capacitively coupled LC resonator array (due to circuit topology) as discussed in Ref. [153]. The variation in $\omega_0(k)$ can be effectively suppressed in the limit of $C_v, C_w \ll C_\Sigma$ and $M_v, M_w \ll L_0$ as derived in Eq. (E.6). We note that while our coupling capacitances are small compared to C_Σ ($C_v/C_\Sigma \approx 0.109$, $C_w/C_\Sigma \approx 0.056$ in the trivial phase), we find that they are sufficient to cause the $\omega_0(k)$ to vary by ~ 1.2 % in the first Brillouin zone. Considering this limit of small coupling capacitance and mutual inductance, the effective capacitance and inductance of (E.6) become quantities independent of k , $C_0^{\text{eff}}(k) \approx C_\Sigma$, $L_0^{\text{eff}}(k) \approx L_0$, and

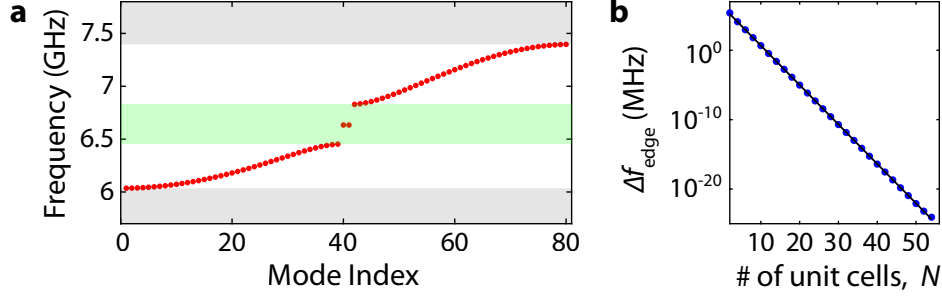


Figure E.3: Eigenspectrum of the finite-sized topological circuit. **a**, Resonant frequencies of a finite system with $N = 40$ unit cells, calculated from eigenmodes of Eq. (E.19). The bandgap regions calculated from dispersion relation are shaded in gray (green) for upper and lower bandgaps (middle bandgap). The two data points inside the middle bandgap (mode indices 40 and 41) correspond to edge modes. **b**, Frequency splitting Δf_{edge} of edge modes with no disorder in the system are plotted against the number of unit cells N . The black solid curve indicates exponential fit to the edge mode splitting, with decay constant of $\xi = 1.76$.

the kernel of the Hamiltonian under RWA reduces to

$$\mathbf{h}(k) = \begin{pmatrix} \omega_0 & f(k) \\ f^*(k) & \omega_0 \end{pmatrix}.$$

Here,

$$\omega_0 = \frac{1}{\sqrt{L_0 C_\Sigma}}, \quad f(k) = \frac{\omega_0}{2} \left[\left(\frac{C_v}{C_\Sigma} - \frac{M_v}{L_0} \right) + \left(\frac{C_w}{C_\Sigma} - \frac{M_w}{L_0} \right) e^{-ikd} \right].$$

This is equivalent to the photonic SSH Hamiltonian in Eq. (6.1) under redefinition of gauge which transforms operators as $(\hat{a}_k, \hat{b}_k) \rightarrow (\hat{a}_k, -\hat{b}_k)$. Here, we can identify the parameters J and δ as

$$J = \frac{\omega_0}{4} \left(\frac{C_v + C_w}{C_\Sigma} - \frac{M_v + M_w}{L_0} \right), \quad \delta = \frac{L_0(C_v - C_w) - C_\Sigma(M_v - M_w)}{L_0(C_v + C_w) - C_\Sigma(M_v + M_w)}, \quad (\text{E.18})$$

where $J(1 \pm \delta)$ is defined as intra-cell and inter-cell coupling, respectively. The dispersion relations under different stages of approximations mentioned above are plotted in Fig. E.2, where we find a clear deviation of our system from the original SSH model due to the k -dependent reference frequency.

Robustness of edge modes under perturbation in circuit parameters

While we have linked our system to the SSH Hamiltonian in Eq. (6.1), we find that our system fails to strictly satisfy chiral symmetry $C\mathbf{h}(k)C^{-1} = -\mathbf{h}(k)$ ($C = \hat{\sigma}_z$ is the chiral symmetry operator in the sublattice space). This is due to the k -dependent

diagonal $\omega_0(k)$ terms in $\mathbf{h}(k)$, resulting from the non-local nature of the quantized charge and nodal flux in the circuit model which results in next-nearest-neighbor coupling terms between sublattices of the same type. Despite this, an inversion symmetry, $\mathcal{I}\mathbf{h}(k)\mathcal{I}^{-1} = \mathbf{h}(-k)$ ($\mathcal{I} = \hat{\sigma}_x$ in the sublattice space), still holds for the circuit model. This ensures the quantization of the Zak phase (\mathcal{Z}) and the existence of an invariant band winding number ($\nu = \mathcal{Z}/\pi$) for perturbations that maintain the inversion symmetry. However, as shown in Refs. [353, 354], the inversion symmetry does not protect the edge states for highly delocalized coupling along the dimer resonator chain, and the correspondence between winding number and the number of localized edge states at the boundary of a finite section of waveguide is not guaranteed.

For weak breaking of the chiral symmetry (i.e., beyond nearest-neighbor coupling much smaller than nearest neighbor coupling) the correspondence between winding number and the number of pairs of gapped edge states is preserved, with winding number $\nu = 0$ in the trivial phase ($\delta > 0$) and $\nu = 1$ in the topological ($\delta < 0$) phase. Beyond just the existence of the edge states and their locality at the boundaries, chiral symmetry is special in that it pins the edge mode frequencies at the center of the middle bandgap (ω_0). Chiral symmetry is maintained in the presence of disorder in the coupling between the different sublattice types along the chain, providing stability to the frequency of the edge modes. In order to study the robustness of the edge mode frequencies in our circuit model, we perform a simulation over different types of disorder realizations in the circuit illustrated in Fig. E.1. As the original SSH Hamiltonian with chiral symmetry gives rise to topological edge states which are robust against the disorder in coupling, not in on-site energies [246], it is natural to consider disorder in circuit elements that induce coupling between resonators: C_v, C_w, M_v, M_w .

The classical equations of motion of a circuit consisting of N unit cells is written as

$$\begin{aligned} V_n^A &= L_0 \frac{di_n^A}{dt} + M_v^{(n)} \frac{di_n^B}{dt} + M_w^{(n)} \frac{di_{n-1}^B}{dt}, & i_n^A &= -C_{\Sigma,A}^{(n)} \frac{dV_n^A}{dt} + C_v^{(n)} \frac{dV_n^B}{dt} + C_w^{(n-1)} \frac{dV_{n-1}^B}{dt}, \\ V_n^B &= L_0 \frac{di_n^B}{dt} + M_w^{(n)} \frac{di_{n+1}^A}{dt} + M_v^{(n)} \frac{di_n^A}{dt}, & i_n^B &= -C_{\Sigma,B}^{(n)} \frac{dV_n^B}{dt} + C_v^{(n)} \frac{dV_n^A}{dt} + C_w^{(n)} \frac{dV_{n+1}^A}{dt}, \end{aligned}$$

where the superscripts indicate index of cell of each circuit element and

$$C_{\Sigma,A}^{(n)} = C_0 + C_v^{(n)} + C_w^{(n-1)}, \quad C_{\Sigma,B}^{(n)} = C_0 + C_v^{(n)} + C_w^{(n)}.$$

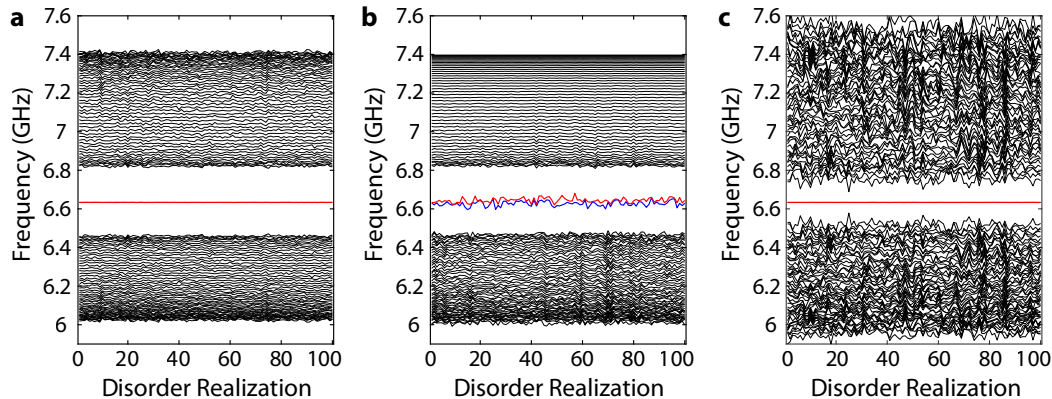


Figure E.4: Eigenfrequencies of the system under 100 disorder realizations in coupling elements. Each disorder realization is achieved by uniformly sampling the parameters within fraction $\pm r$ of the original value. **a**, Disorder in mutual inductance M_v and M_w between neighboring resonators with the strength $r = 0.5$. **b**, Disorder in coupling capacitance C_v and C_w between neighboring resonators with the strength $r = 0.1$. **c**, The same disorder as panel **b** with $r = 0.5$, while keeping the bare self-capacitance C_Σ of each resonator fixed (correlated disorder between coupling capacitances and resonator C_0).

under 100 independent realizations, where we find the frequencies of the edge modes to be stable, while frequencies of modes in the passbands fluctuate to a much larger extent. This suggests that the frequencies of edge modes have some sort of added robustness against disorder in the mutual inductance between neighboring resonators despite the fact that our circuit model does not satisfy chiral symmetry. The reduction in sensitivity results from the fact that the effective self-inductance $L_0^{\text{eff}}(k)$ of the resonators, which influences the on-site resonator frequency, depends on the mutual inductances only to second-order in small parameter ($M_{v,w}/L_0$). It is this second-order fluctuation in the resonator frequencies, causing shifts in the diagonal elements of the Hamiltonian, which results in fluctuations in the edge mode frequencies. The direct fluctuation in the mutual inductance couplings themselves, corresponding to off-diagonal Hamiltonian elements, do not cause the edge modes to fluctuate due to chiral symmetry protection (the off-diagonal part of the kernel of the Hamiltonian is chiral symmetric).

Disorder in coupling capacitance C_v and C_w are also investigated using a similar model, where the values of $C_v^{(n)}$, $C_w^{(n)}$ are allowed to vary by a fraction $\pm r$ of the original values (uniformly sampled), while the remaining circuit parameters are kept constant. From Fig. E.4b we observe severe fluctuations in the frequencies of the edge modes even under a mild disorder level of $r = 0.1$. This is due to the fact that the coupling capacitance C_v and C_w contribute to the effective self-

	Q ₁ ^A	Q ₁ ^B	Q ₂ ^A	Q ₂ ^B	Q ₃ ^A	Q ₃ ^B	Q ₄ ^A	Q ₄ ^B	Q ₅ ^A	Q ₅ ^B	Q ₆ ^A	Q ₆ ^B	Q ₇ ^A	Q ₇ ^B
$\Gamma'/2\pi$ (kHz)	326	150	247	105 ^a	268	183	221	224	193	263	206	333	88	347

^a Measured in a separate cooldown

Table E.1: Qubit coherence in the middle bandgap. The parasitic decoherence rate Γ' of qubits on Device I at 6.621 GHz inside the MBG. The data for Q₂^B was taken in a separate cooldown due to coupling to a two-level system defect.

capacitance of each resonator $C_0^{\text{eff}}(k)$ to first-order in small parameter ($C_{v,w}/C_0$), thus directly breaking chiral symmetry and causing the edge modes to fluctuate. An interesting observation in Fig. E.4b is the stability of frequencies of modes in the upper passband with respect to disorder in C_v and C_w . This can be explained by noting the expressions for band-edge frequencies in Eqs. (E.16a)-(E.16d), where the dependence on coupling capacitance gets weaker close to the upper band-edge frequency $\omega_+^{\text{max}} = 1/\sqrt{(L_0 + M_v + M_w)C_0}$ of the upper passband.

Finally, we consider a special type of disorder where we keep the bare self-capacitance C_Σ of each resonator fixed. Although unrealistic, we allow C_v and C_w to fluctuate and compensate for the disorder in C_Σ by subtracting the deviation in C_v and C_w from C_0 . This suppresses the lowest-order resonator frequency fluctuations, and hence helps stabilize the edge mode frequencies even under strong disorder $r = 0.5$, as illustrated in Fig. E.4c. While being an unrealistic model for disorder in our physical system, this observation sheds light on the fact that the circuit must be carefully designed to take advantage of the topological protection. It should also be noted that in all of the above examples, the standard deviation in the edge mode frequencies scale linearly to lowest order with the standard deviation of the disorder in the inter- and intra-cell coupling circuit elements (only the pre-coefficient changes). Exponential suppression of edge mode fluctuations due to disorder in the coupling elements as afforded by the SSH model with chiral symmetry would require a redesign of the circuit to eliminate the next-nearest-neighbor coupling present in the current circuit layout.

E.3 Device I characterization and Experimental setup

In this section, we provide a detailed description of elements on Device I, where the directional qubit-photon bound state and passband topology experiments are performed. The optical micrograph of Device I is shown in Fig. E.5.

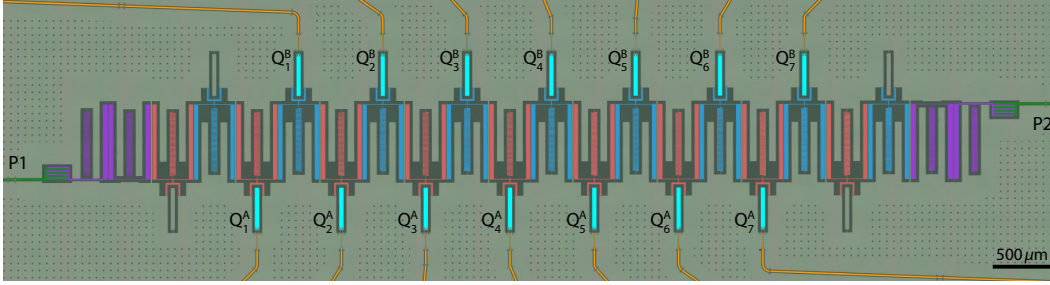


Figure E.5: Optical micrograph of Device I (false-colored). The device consists of a topological waveguide with 9 unit cells (resonators corresponding to A/B sublattice colored red/blue) in the trivial phase, where the intra-cell coupling is larger than the inter-cell coupling. Qubits (cyan, labeled Q_j^α where $i=1-7$ and $\alpha=A,B$) are coupled to every site of the seven inner unit cells of the topological waveguide, each connected to on-chip flux-bias lines (orange) for individual frequency control. At the boundary of the topological waveguide are tapering sections (purple), which provide impedance matching to the external waveguides (green) at upper bandgap frequencies. P1 (P2) denotes port 1 (port 2) of the device.

Qubits

All 14 qubits on Device I are designed to be nominally identical with asymmetric Josephson junctions (JJs) on superconducting quantum interference device (SQUID) loop to reduce the sensitivity to flux noise away from maximum and minimum frequencies, referred to as “sweet spots”. The sweet spots of all qubits lie deep inside the upper and lower bandgaps, where the coupling of qubits to external ports are small due to strong localization. This makes it challenging to access the qubits with direct spectroscopic methods near the sweet spots. Alternatively, a strong drive tone near resonance with a given qubit frequency was sent into the waveguide to excite the qubit, and a passband mode dispersively coupled to the qubit is simultaneously monitored with a second probe tone. With this method, the lower (upper) sweet spot of Q_1^A is found to be at 5.22 GHz (8.38 GHz), and the anharmonicity near the upper sweet spot is measured to be 297 MHz (effective qubit capacitance of $C_q = 65$ fF). The Josephson energies of two JJs of Q_1^A are extracted to be $(E_{J1}, E_{J2})/h = (21.85, 9.26)$ GHz giving the junction asymmetry of $d = \frac{E_{J1} - E_{J2}}{E_{J1} + E_{J2}} = 0.405$.

The coherence of qubits is characterized using spectroscopy inside the middle bandgap (MBG). Here, the parasitic decoherence rate is defined as $\Gamma' \equiv 2\Gamma_2 - \kappa_{e,1} - \kappa_{e,2}$, where $2\Gamma_2$ is the total linewidth of qubit, and $\kappa_{e,1}$ ($\kappa_{e,2}$) is the external coupling rate to port 1 (2) (see Supplementary Note 1 of Ref. [108] for a detailed discussion). Here, Γ' contains contributions from both qubit decay to spurious channels other than the desired external waveguide as well as pure dephasing. Table E.1 shows the

parasitic decoherence rate of all 14 qubits at 6.621 GHz extracted from spectroscopic measurement at a power at least 5 dB below the single-photon level (defined as $\hbar\omega\kappa_{e,p}$ with $p = 1, 2$) from both ports.

Utilizing the dispersive coupling between the qubit and a resonator mode in the passband, we have also performed time-domain characterization of qubits. The measurement on Q_4^B at 6.605 GHz in the MBG gives $T_1 = 1.23 \mu\text{s}$ and $T_2^* = 783 \text{ ns}$ corresponding to $\Gamma'/2\pi = 281.3 \text{ kHz}$, consistent with the result from spectroscopy in Table E.1. At the upper sweet spot, Q_4^B was hard to access due to the small coupling to external ports arising from short localization length and a large physical distance from the external ports. Instead, Q_1^B is characterized to be $T_1 = 9.197 \mu\text{s}$ and $T_2^* = 11.57 \mu\text{s}$ at its upper sweet spot (8.569 GHz).

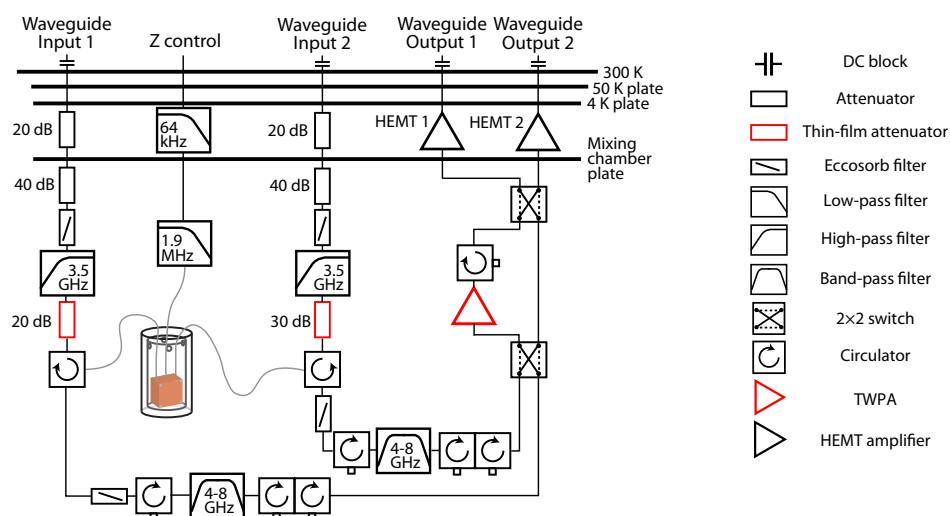


Figure E.6: Schematic of the measurement setup inside the dilution refrigerator for Device I. The meaning of each symbol in the schematic on the left is enumerated on the right. The level of attenuation of each attenuator is indicated with number next to the symbol. The cutoff frequencies of each filter is specified with numbers inside the symbol. Small squares attached to circulator symbols indicate port termination with $Z_0 = 50 \Omega$, allowing us to use the 3-port circulator as a 2-port isolator. The input pump line for TWPA is not shown in the diagram for simplicity.

Metamaterial waveguide and coupling to qubits

As shown in Fig. E.5, the metamaterial waveguide consists of a SSH array in the trivial configuration and tapering sections at the boundary (the design of tapering sections is discussed in App. E.4). The array contains 18 identical LC resonators, whose design is slightly different from the one in test structures shown in Fig. 6.1b. Namely, the “claw” used to couple qubits to resonators on each site is extended to

generate a larger coupling capacitance of $C_g = 5.6$ fF and the resonator capacitance to ground was reduced accordingly to maintain the designed reference frequency. On resonator sites where no qubit is present, an island with shape identical to that of a qubit was patterned and shorted to ground plane in order to mimic the self-capacitance contribution from a qubit to the resonator. The fitting of the whole structure to the waveguide transmission spectrum results in a set of circuit parameters similar yet slightly different from ones of the test structures quoted in Fig. 6.1: $(C_v, C_w) = (35, 19.2)$ fF, $(M_v, M_w) = (-38, -32)$ pH, $C_0 = 250$ fF, $L_0 = 1.9$ nH. Here, the definition of C_0 includes contributions from coupling capacitance between qubit and resonator, but excludes the contribution to the resonator self-capacitance from the coupling capacitances C_v, C_w between resonators in the array. With these parameters we calculate the corresponding parameters in the SSH model to be $J/2\pi = 356$ MHz and $\delta = 0.256$ following Eq. (E.18), resulting in the localization length $\xi = [\ln(\frac{1+\delta}{1-\delta})]^{-1} = 1.91$ at the reference frequency. From the measured avoided crossing $g_{45}^{AB}/2\pi = 32.9$ MHz between qubit-photon bound states facing toward each other on nearest-neighboring sites together with J and δ , we infer the qubit coupling to each resonator site to be $g = \sqrt{g_{45}^{AB} J(1 + \delta)} = 2\pi \times 121.3$ MHz [55], close to the value

$$\frac{C_g}{2\sqrt{C_q C_\Sigma}} \omega_0 = 2\pi \times 132 \text{ MHz}$$

expected from designed coupling capacitance [355]. Note that we find an inconsistent set of values $J/2\pi = 368$ MHz and $\delta = 0.282$ (with $\xi = 1.73$ and $g/2\pi = 124.6$ MHz accordingly) from calculation based on the difference in observed band-edge frequencies, where the frequency difference between the highest frequency in the UPB and the lowest frequency in the LPB equals $4J$ and the size of the MBG equals $4J|\delta|$. The inconsistency indicates the deviation of our system from the proposed circuit model (see App. E.1 for discussion), which accounts for the difference between theoretical curves and the experimental data in Fig. 6.1d and left sub-panel of Fig. 6.2c. The values of J , δ and g from the band-edge frequencies are used to generate the theoretical curves in Fig. 6.3 as well as in Fig. E.11. The intrinsic quality factor of one of the normal modes (resonant frequency 6.158 GHz) of the metamaterial waveguide was measured to be $Q_i = 9.8 \times 10^4$ at power below the single-photon level, similar to typical values reported in Refs. [109, 153].

Experimental setup

The measurement setup inside the dilution refrigerator is illustrated in Fig. E.6. All the 14 qubits on Device I are DC-biased with individual flux-bias (Z control) lines,

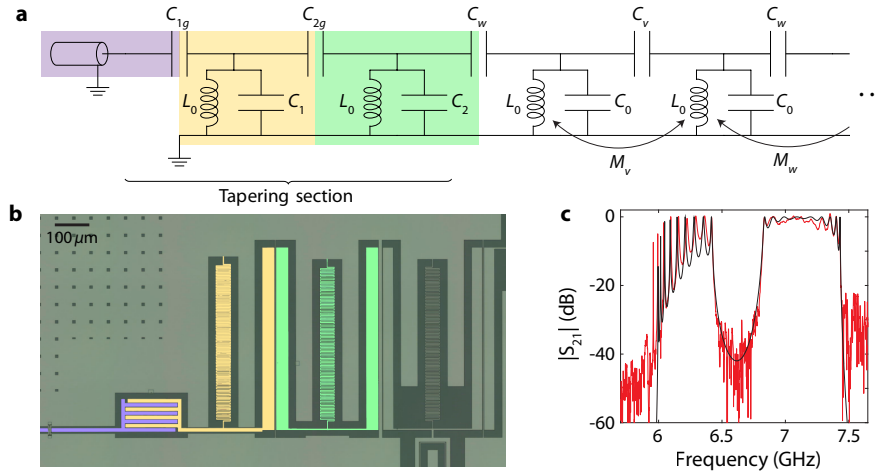


Figure E.7: Tapering section of Device I. **a**, The circuit diagram of the tapering section connecting a coplanar waveguide to the topological waveguide. The coplanar waveguide, first tapering resonator, and second tapering resonator are shaded in purple, yellow, and green, respectively. **b**, Optical micrograph (false colored) of the tapering section on Device I. The tapering section is colored in the same manner as the corresponding components in panel **a**. **c**, Red: measured waveguide transmission spectrum $|S_{21}|$ for Device I. Black: fit to the data with parameters $(C_v, C_w) = (35, 19.2)$ fF, $(M_v, M_w) = (-38, -32)$ pH, $(C_{1g}, C_{2g}) = (141, 35)$ fF, $(C_1, C_2) = (128.2, 230)$ fF, $C_0 = 250$ fF, $L_0 = 1.9$ nH.

filtered by a 64 kHz low-pass filter at the 4K plate and a 1.9 MHz low-pass filter at the mixing chamber plate. The Waveguide Input 1 (2) passes through a series of attenuators and filters including a 20 dB (30 dB) thin-film attenuator developed in B. Palmer's group [157]. It connects via a circulator to port 1 (2) of Device I, which is enclosed in two layers of magnetic shielding. The output signals from Device I are routed by the same circulator to the output lines containing a series of circulators and filters. The pair of 2×2 switches in the amplification chain allows us to choose the branch to be further amplified in the first stage by a traveling-wave parametric amplifier (TWPA) from MIT Lincoln Laboratories. Both of the output lines are amplified by an individual high electron mobility transistor (HEMT) at the 4K plate, followed by room-temperature amplifiers at 300 K. All four S-parameters S_{ij} ($i, j \in \{1, 2\}$) involving port 1 and 2 on Device I can be measured with this setup by choosing one of the waveguide input ports and one of the waveguide output ports, e.g. S_{11} can be measured by sending the input signal into Waveguide Input 1 and collecting the output signal from Waveguide Output 2 with both 2×2 switches in the cross (\times) configuration.

E.4 Tapering sections on Device I

The finite system size of metamaterial waveguide gives rise to sharp resonances inside the passband associated with reflection at the boundary (Fig. 6.1d). Also, the decay rate of qubits to external ports inside the middle bandgap (MBG) is small, making the spectroscopic measurement of qubits inside the MBG hard to achieve. In order to reduce ripples in transmission spectrum inside the upper passband and increase the decay rates of qubits to external ports comparable to their intrinsic contributions inside the middle bandgap, we added two resonators at each end of the metamaterial waveguide in Device I as tapering section.

Similar to the procedure described in Appendix C of Ref. [153], the idea is to increase the coupling capacitance gradually across the two resonators while keeping the resonator frequency the same as other resonators by changing the self capacitance as well. However, unlike the simple case of an array of LC resonators with uniform coupling capacitance, the SSH waveguide consists of alternating coupling capacitance between neighboring resonators and two separate passbands form as a result. In this particular work, the passband experiments are designed to take place at the upper passband frequencies and hence we have slightly modified the resonant frequencies of tapering resonators to perform impedance-matching inside the upper passband. The circuit diagram shown in Fig. E.7a was used to model the tapering section in our system. While designing of tapering sections involves empirical trials, microwave filter design software, e.g. iFilter module in AWR Microwave Office [356], can be used to aid the choice of circuit parameters and optimization method.

Figure E.7b shows the optical micrograph of a tapering section on Device I. The circuit parameters are extracted by fitting the normalized waveguide transmission spectrum (S_{21}) data from measurement with theoretical circuit models. We find a good agreement in the frequency of normal modes and the level of ripples between the theoretical model and the experiment as illustrated in Fig. E.7c. The level of ripples in the transmission spectrum of the entire upper passband is about 8 dB and decreases to below 2 dB near the center of the band, allowing us to probe the cooperative interaction between qubits at these frequencies.

E.5 Directional shape of qubit-photon bound state

In this section, we provide detailed explanations on the directional shape of qubit-photon bound states discussed in Chapter 6. As an example, we consider a system

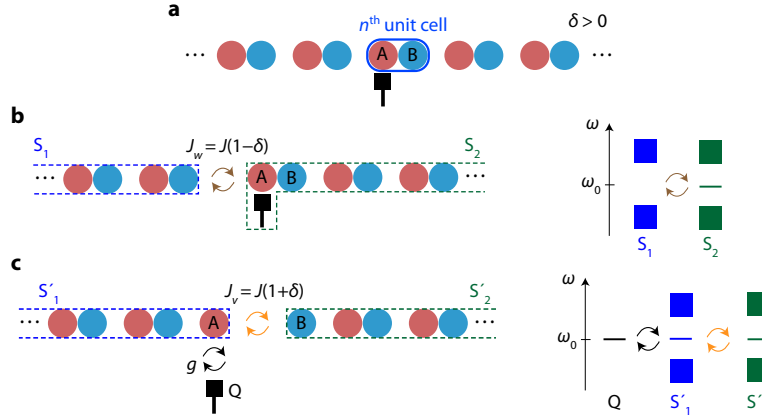


Figure E.8: Understanding the directionality of qubit-photon bound states. **a**, Schematic of the full system consisting of an infinite SSH waveguide with a qubit coupled to the A sublattice of the n -th unit cell and tuned to frequency ω_0 in the center of the MBG. Here we make the unit cell choice in which the waveguide is in the trivial phase ($\delta > 0$). **b**, Division of system in panel **a** into two subsystems S_1 and S_2 in Description I. **c** Division of system in panel **a** into three subsystems [qubit (Q), S'_1 , S'_2] in Description II. For panels **b** and **c**, the left side shows the schematic of the division into subsystems and the right side illustrates the mode spectrum of the subsystems and the coupling between them.

consisting of a topological waveguide in the trivial phase and a qubit coupled to the A sublattice of the n -th unit cell (Fig. E.8a). Our descriptions are based on partitioning the system into subsystems under two alternative pictures (Fig. E.8b,c), where the array is divided on the left (Description I) or the right (Description II) of the site (n, A) where the qubit is coupled to.

Description I

We divide the array into two parts by breaking the inter-cell coupling $J_w = J(1 - \delta)$ that exists on the left of the site (n, A) where the qubit is coupled to, i.e., between sites ($n - 1, B$) and (n, A). The system is described in terms of two subsystems S_1 and S_2 as shown in Fig. E.8b. The subsystem S_1 is a semi-infinite array in the trivial phase extended from the ($n - 1$)-th unit cell to the left and the subsystem S_2 comprising a qubit and a semi-infinite array in the trivial phase extended from the n -th unit cell to the right. The coupling between the two subsystems is interpreted to take place at a boundary site with coupling strength J_w . When the qubit frequency is resonant to the reference frequency ω_0 , the subsystem S_2 can be viewed as a semi-infinite array in the topological phase, where the qubit effectively acts as an edge site. Here, the resulting topological edge mode of subsystem S_2 is the qubit-photon bound state, with photon occupation mostly on the qubit itself and on every B site with a decaying envelope. Coupling of subsystem S_2 to S_1 only has a minor effect

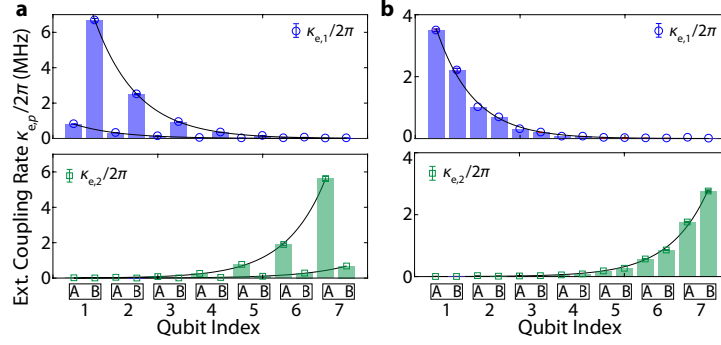


Figure E.9: External coupling rate of qubit-photon bound states away from the reference frequency. **a**, Upper (Lower) plots: external coupling rate of the qubit-photon bound states to port 1 (2) at 6.72 GHz in the middle bandgap. Exponential fit (black curve) on the data gives the localization length of $\xi = 2$. **b**, Upper (Lower) plots: external coupling rate of the qubit-photon bound states to port 1 (2) at 7.485 GHz in the upper bandgap. Exponential fit (black curve) on the data gives the localization length of $\xi = 1.8$. The localization lengths are represented in units of lattice constant. For all panels, the error bars show 95% confidence interval and are removed on data points whose error is smaller than the marker size.

on the edge mode of S_2 as the modes in subsystem S_1 are concentrated at passband frequencies, far-detuned from $\omega = \omega_0$. Also, the presence of an edge state of S_2 at $\omega = \omega_0$ cannot induce an additional occupation on S_1 by this coupling in a way that resembles an edge state since the edge mode of S_2 does not occupy sites on the A sublattice. The passband modes S_1 and S_2 near-resonantly couple to each other, whose net effect is redistribution of modes within the passband frequencies. Therefore, the qubit-photon bound state can be viewed as a topological edge mode for subsystem S_2 which is unperturbed by coupling to subsystem S_1 . The directionality and photon occupation distribution along the resonator chain of the qubit-photon bound state can be naturally explained according to this picture.

Description II

In this alternate description, we divide the array into two parts by breaking the intra-cell coupling $J_v = J(1 + \delta)$ that exists on the right of the site (n, A) where the qubit is coupled to, i.e., between sites (n, A) and (n, B) . We consider the division of the system into three parts: the qubit, subsystem S'_1 , and subsystem S'_2 as illustrated in Fig. E.8c. Here, the subsystem S'_1 (S'_2) is a semi-infinite array in the topological phase extended to the left (right), where the last site hosting the topological edge mode E'_1 (E'_2) at $\omega = \omega_0$ is the A (B) sublattice of the n -th unit cell. The subsystem S'_1 is coupled to both the qubit and the subsystem S'_2 with coupling

strength g and $J_v = J(1 + \delta)$, respectively. Similar to Description I, the result of coupling between subsystem modes inside the passband is the reorganization of modes without significant change in the spectrum inside the middle bandgap. On the other hand, modes of the subsystems at $\omega = \omega_0$ (qubit, E'_1 , and E'_2) can be viewed as emitters coupled in a linear chain configuration, whose eigenfrequencies and corresponding eigenstates in the single-excitation manifold are given by

$$\tilde{\omega}_{\pm} = \omega_0 \pm \sqrt{\tilde{g}^2 + \tilde{J}_v^2}, \quad |\psi_{\pm}\rangle = \frac{1}{\sqrt{2}} \left(\frac{\tilde{g}}{\sqrt{\tilde{g}^2 + \tilde{J}_v^2}} |100\rangle \pm |010\rangle + \frac{\tilde{J}_v}{\sqrt{\tilde{g}^2 + \tilde{J}_v^2}} |001\rangle \right),$$

and

$$\tilde{\omega}_0 = \omega_0, \quad |\psi_0\rangle = \frac{1}{\sqrt{\tilde{g}^2 + \tilde{J}_v^2}} (\tilde{J}_v |100\rangle - \tilde{g} |001\rangle),$$

where $|n_1 n_2 n_3\rangle$ denotes a state with (n_1, n_2, n_3) photons in the (qubit, E'_1 , E'_2), respectively. Here, \tilde{g} (\tilde{J}_v) is the coupling between edge mode E'_1 and the qubit (edge mode E'_2), diluted from g (J_v) due to the admixture of photonic occupation on sites other than the boundary in the edge modes. Note that in the limit of short localization length, we recover $\tilde{g} \approx g$ and $\tilde{J}_v \approx J_v$. Among the three single-excitation eigenstates, the states $|\psi_{\pm}\rangle$ lie at frequencies of approximately $\omega_0 \pm J$, and are absorbed into the passbands. The only remaining state inside the middle bandgap is the state $|\psi_0\rangle$, existing exactly at $\omega = \omega_0$, which is an anti-symmetric superposition of qubit excited state and the single-photon state of E'_2 , whose photonic envelope is directed to the right with occupation on every B site. This accounts for the directional qubit-photon bound state emerging in this scenario.

E.6 Coupling of qubit-photon bound states to external ports at different frequencies

As noted in Chapter 6 (Fig. 6.2), the perfect directionality of the qubit-photon bound states is achieved only at the reference frequency ω_0 inside the middle bandgap. In this section, we discuss the breakdown of the observed perfect directionality when qubits are tuned to different frequencies inside the middle bandgap by showing the behavior of the external coupling $\kappa_{e,p}$ ($p = 1, 2$) to the ports.

Inside the middle bandgap, detuned from the reference frequency

Figure E.9a shows the external coupling rate of qubits to the ports at 6.72 GHz, a frequency in the middle bandgap close to band-edge. The alternating behavior of external coupling rate is still observed, but with a smaller contrast than in Fig. 6.2 of Chapter 6. The dependence of external linewidth on qubit index still exhibits the

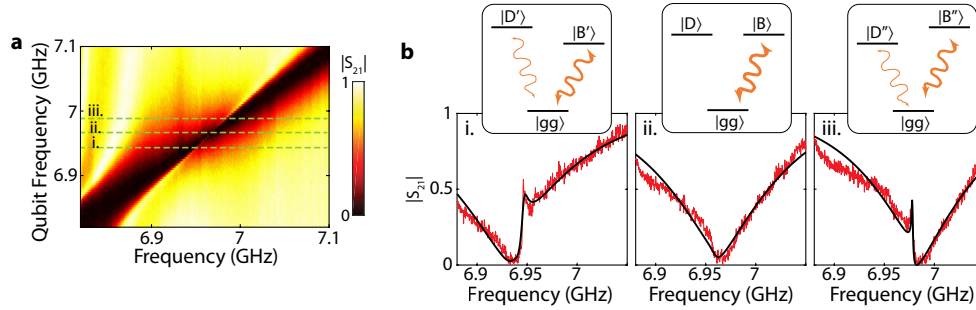


Figure E.10: Understanding the swirl pattern. **a**, Zoomed-in view of the swirl feature near 6.95 GHz of the experimental data illustrated in Fig. 6.3c. **b**, Transmission spectrum across two-qubit resonance for three different frequency tunings, corresponding to line cuts marked with green dashed lines on panel **a**. The insets to panel **b** show the corresponding level diagram with $|gg\rangle$ denoting both qubits in ground states and $|B\rangle$ ($|D\rangle$) representing the perfect bright (dark) state. The state notation with prime (double prime) in sub-panel i. (iii.) denotes the imperfect super-radiant bright state and sub-radiant dark state, with the width of orange arrows specifying the strength of the coupling of states to the waveguide channel. The sub-panel ii. occurs at the center of the swirl, where perfect super-radiance and sub-radiance takes place (i.e., bright state waveguide coupling is maximum and dark state waveguide coupling is zero). The black and red curves correspond to experimental data and theoretical fit, respectively.

remaining directionality with qubits on A (B) sublattice maintaining large coupling to port 2 (1), while showing small non-zero coupling to the opposite port.

Inside the upper bandgap

Inside the upper bandgap (7.485 GHz), the coupling of qubit-photon bound states to external ports decreases monotonically with the distance of the qubit site to the port, regardless of which sublattice the qubit is coupled to (Fig. E.9b). This behavior is similar to that of qubit-photon bound states formed in a structure with uniform coupling, where bound states exhibit a symmetric photonic envelope surrounding the qubit. Note that we find the external coupling to port 2 ($\kappa_{e,2}$) to be generally smaller than that to port 1 ($\kappa_{e,1}$), which may arise from a slight impedance mismatch on the connection of the device to the external wiring.

E.7 Probing band topology with qubits

Signature of perfect super-radiance

Here we take a closer look at the swirl pattern in the waveguide transmission spectrum—a signature of perfect super-radiance—which is discussed in Fig. 6.3c of Chapter 6. In Fig. E.10 we zoom in to the observed swirl pattern near 6.95 GHz, and three horizontal line cuts. At the center of this pattern (sub-panel ii. of Fig. E.10b),

the two qubits form perfect super-/sub-radiant states with maximized correlated decay and zero coherent exchange interaction [116, 147]. At this point, the transmission spectrum shows a single Lorentzian lineshape (perfect super-radiant state and bright state) with linewidth equal to the sum of individual linewidths of the coupled qubits. The perfect sub-radiant state (dark state), which has no external coupling, cannot be accessed from the waveguide channel here and is absent in the spectrum. Slightly away from this frequency, the coherent exchange interaction starts to show up, making hybridized states $|B'\rangle$, $|D'\rangle$ formed by the interaction of the two qubits. In this case, both of the hybridized states have non-zero decay rate to the waveguide, forming a V-type level structure [55]. The interference between photons scattering off the two hybridized states gives rise to the peak in the middle of sub-panels (i.) and (iii.) in Fig. E.10b.

The fitting of lineshapes starts with the subtraction of transmission spectrum of the background, which are taken in the same frequency window but with qubits detuned away. Note that the background subtraction in this case cannot be perfect due to the frequency shift of the upper passband modes under the presence of qubits. Such imperfection accounts for most of the discrepancy between the fit and the experimental data. The fit employs the transfer matrix method discussed in Refs. [118, 119, 147]. Here, the transfer matrix of the two qubits takes into account the pure dephasing, which causes the sharp peaks in sub-panels (i.) and (iii.) of Fig. E.10b to stay below perfect transmission level (unity) as opposed to the prediction from the ideal case of electromagnetically induced transparency [263].

Topology-dependent photon scattering on various qubit pairs

As mentioned in Chapter 6, when two qubits are separated by Δn ($\Delta n > 0$) unit cells, the emergence of perfect super-radiance (vanishing of coherent exchange interaction) is governed by Eq. (6.2). Although Eq. (6.2) is satisfied at the band-edges it does not lead to additional point of super-radiance because the non-Markovianity at these points do not lead to effective correlated decay [205]. Therefore, the perfect super-radiance takes place exactly $\Delta n - 1$ times in the trivial phase and Δn times in the topological phase across the entire passband. Chapter 6 shows the case of $\Delta n = 2$. Here we report similar measurements on other qubit pairs with different cell distance Δn between the qubits. Figure E.11 shows good qualitative agreement between the experiment and theoretical result in Ref. [55]. The small avoided-crossing-like features in the experimental data are due to coupling of one of the qubits with a local two-level system defect. An example of this is seen near 6.85 GHz of $\Delta n = 3$

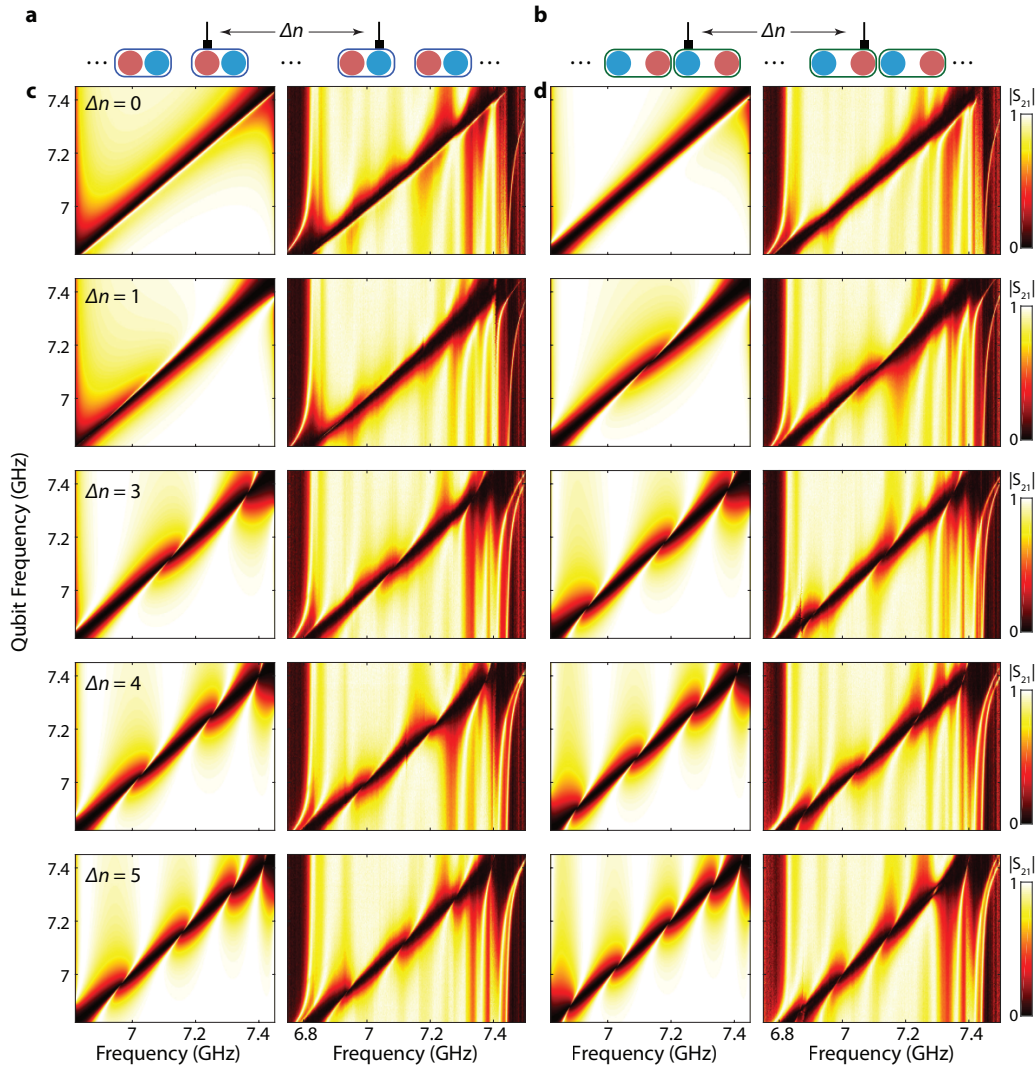


Figure E.11: Topology-dependent photon scattering on various qubit pairs. **a**, Schematic showing two qubits separated by Δn unit cells in the trivial configuration. **b**, Corresponding schematic for topological phase configuration. **c**, Waveguide transmission spectrum $|S_{21}|$ when frequencies of two qubits are resonantly tuned across the upper passband in the trivial configuration. **d**, Waveguide transmission spectrum $|S_{21}|$ for the topological configuration. For both trivial and topological spectra, the left spectrum illustrates theoretical expectations based on Ref. [55] whereas the right shows the experimental data.

in the topological configuration. For $\Delta n = 0$, there is no perfect super-radiant point throughout the passband for both trivial and topological configurations. For all the other combinations in Fig. E.11, the number of swirl patterns indicating perfect super-radiance agrees with the theoretical model.

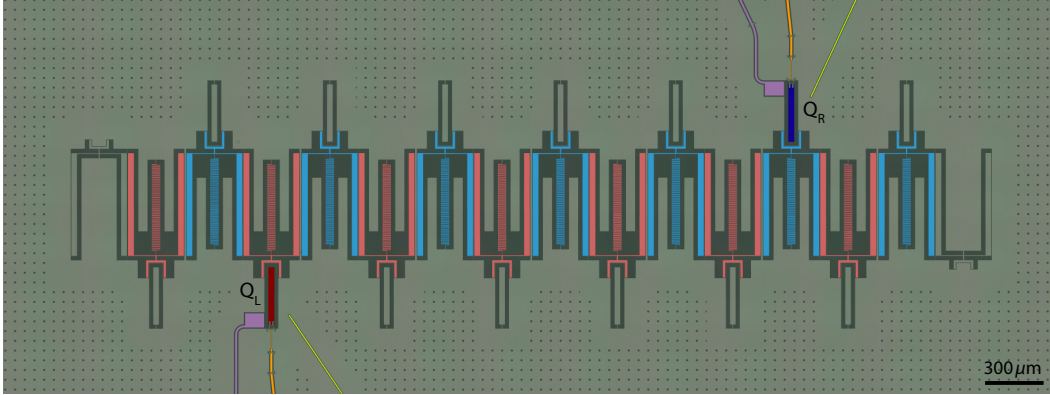


Figure E.12: Optical micrograph of Device II (false-colored). The device consists of a topological waveguide with 7 unit cells (resonators corresponding to A/B sublattice colored red/blue) in the topological phase, where the inter-cell coupling is larger than the intra-cell coupling. Two qubits Q_L (dark red) and Q_R (dark blue) are coupled to A sublattice of the second unit cell and B sublattice of sixth unit cell, respectively. Each qubit is coupled to a $\lambda/4$ coplanar waveguide resonator (purple) for dispersive readout, flux-bias line (orange) for frequency control, and charge line (yellow) for local excitation control.

Qubit	f_{\max} (GHz)	E_C/h (MHz)	$E_{J\Sigma}/h$ (GHz)	$g_E/2\pi$ (MHz)	f_{RO} (GHz)	$g_{RO}/2\pi$ (MHz)	T_1 (μs)	T_2^* (μs)
Q_L	8.23	294	30.89	58.1	5.30	43.5	4.73	4.04
Q_R	7.99	296	28.98	57.3	5.39	43.4	13.9	8.3

Table E.2: Qubit parameters on Device II. f_{\max} is the maximum frequency (sweet spot) and E_C ($E_{J\Sigma}$) is the charging (Josephson) energy of the qubit. g_E is the coupling of qubit to the corresponding edge state. The readout resonator at frequency f_{RO} is coupled to the qubit with coupling strength g_{RO} . T_1 (T_2^*) is the lifetime (Ramsey coherence time) of a qubit measured at the sweet spot.

E.8 Device II characterization and experimental setup

In this section we provide a detailed description of the elements making up Device II, in which the edge mode experiments are performed. The optical micrograph of Device II is illustrated in Fig. E.12.

Qubits

The parameters of qubits on Device II are summarized in Table E.2. The two qubits are designed to have identical SQUID loops with symmetric JJs. The lifetime and Ramsey coherence times in the table are measured when qubits are tuned to their sweet spot. Qubit coherence at the working frequency in the middle bandgap is also characterized, with the lifetime and Ramsey coherence times of Q_L (Q_R) at 6.829 (6.835) GHz measured to be $T_1 = 6.435$ (5.803) μs and $T_2^* = 344$ (539) ns,

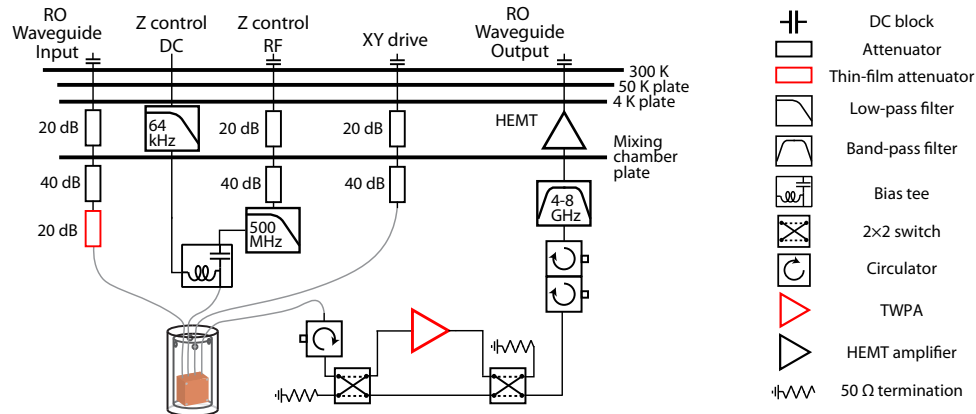


Figure E.13: Schematic of the measurement setup inside the dilution refrigerator for Device II. The meaning of each symbol in the schematic on the left is enumerated on the right. The level of attenuation of each attenuator is indicated with number next to the symbol. The cutoff frequencies of each filter is specified with numbers inside the symbol. Small squares attached to circulator symbols indicate port termination with $Z_0 = 50 \Omega$, allowing us to use the 3-port circulator as a 2-port isolator. The pump line for the TWPA is not shown in the diagram for simplicity.

respectively.

Metamaterial waveguide and coupling to qubits

The resonators in the metamaterial waveguide and their coupling to qubits are designed to be nominally identical to those in Device I. The last resonators of the array are terminated with a wing-shape patterned ground plane region in order to maintain the bare self-capacitance identical to other resonators.

Edge modes

The coherence of the edge modes is characterized by using qubits to control and measure the excitation with single-photon precision. Taking E_L as an example, we define the iSWAP gate as a half-cycle of the vacuum Rabi oscillation in Fig. 6.4d. For measurement of the lifetime of the edge state E_L , the qubit Q_L is initially prepared in its excited state with a microwave π -pulse, and an iSWAP gate is applied to transfer the population from Q_L to E_L . After waiting for a variable delay, we perform the second iSWAP to retrieve the population from E_L back to Q_L , followed by the readout of Q_L . In order to measure the Ramsey coherence time, the qubit Q_L is instead prepared in an equal superposition of ground and excited states with a microwave $\pi/2$ -pulse, followed by an iSWAP gate. After a variable delay, we perform the second iSWAP and another $\pi/2$ -pulse on Q_L , followed by the readout

of Q_L . An equivalent pulse sequence for Q_R is used to characterize the coherence of E_R . The lifetime and Ramsey coherence time of E_L (E_R) are extracted to be $T_1 = 3.68$ (2.96) μs and $T_2^* = 4.08$ (2.91) μs , respectively, when Q_L (Q_R) is parked at 6.829 (6.835) GHz. Due to the considerable amount of coupling g_E between the qubit and the edge mode compared to the detuning at park frequency, the edge modes are hybridized with the qubits during the delay time in the above-mentioned pulse sequences. As a result, the measured coherence time of the edge modes is likely limited here by the dephasing of the qubits.

Experimental setup

The measurement setup inside the dilution refrigerator is illustrated in Fig. E.13. The excitation of the two qubits is controlled by capacitively-coupled individual XY microwave drive lines. The frequency of qubits are controlled by individual DC bias (Z control DC) and RF signals (Z control RF), which are combined using a bias tee at the mixing chamber plate. The readout signals are sent into RO Waveguide Input, passing through a series of attenuators including a 20 dB thin-film attenuator developed in B. Palmer's group [157]. The output signals go through an optional TWPA, a series of circulators and a band-pass filter, which are then amplified by a HEMT amplifier (RO Waveguide Output).

Details on the population transfer process

In step i) of the double-modulation scheme described in Chapter 6, the frequency modulation pulse on Q_R (control modulation) is set to be 2 ns longer than that on Q_L (transfer modulation). The interaction strength induced by the control modulation is 21.1 MHz, smaller than that induced by the transfer modulation in order to decrease the population leakage between the two edge states. For step iii), the interaction strength induced by the control modulation on Q_L is 22.4 MHz, much closer to interaction strength for the transfer than expected (this was due to a poor calibration of the modulation efficiency of qubit sideband). The interaction strengths being too close between $Q_L \leftrightarrow E_L$ and $Q_R \leftrightarrow E_R$ gives rise to unwanted leakage and decreases the required interaction time in step ii). We expect that a careful optimization on the frequency modulation pulses would have better addressed this leakage problem and increase the transfer fidelity (see below).

The fit to the curves in Fig. 6.4e of Chapter 6 are based on numerical simulation with QuTiP [338, 339], assuming the values of lifetime (T_1) and coherence time (T_2^*) from the characterization measurements. The free parameters in the simulation

are the coupling strengths \tilde{g}_L , \tilde{g}_R between qubits and edge states, whose values are extracted from the best fit of the experimental data.

The detailed contributions to the infidelity of the as-implemented population transfer protocol are also analyzed by utilizing QuTiP. The initial left-side qubit population probability is measured to be only 98.4 %, corresponding to an infidelity of 1.6 % in the π -pulse qubit excitation in this transfer experiment (compared to a previously calibrated ‘optimized’ pulse). In the following steps, we remove the leakage between edge modes and the decoherence process sequentially to see their individual contributions to infidelity. First, we set the coupling strength between the two edge modes to zero during the two iSWAP gates while keeping the above-mentioned initial population probability, coupling strengths, lifetimes, and coherence times. The elimination of unintended leakage during the left and right side iSWAP steps between the edge modes gives the final transferred population probability of 91.9 %, suggesting $91.9 \% - 87 \% = 4.9 \%$ of the infidelity comes from the unintended leakage between edge modes. Also, as expected, setting the population decay and decoherence of the qubits and the edge modes to zero, the final population is found to be identical to the initial value, indicating that $98.4 \% - 91.9 \% = 6.5 \%$ of loss arises from the decoherence processes.